POLITECNICO DI MILANO

Doctoral programme in
Aerospace Engineering

Aerospace Science and Technology Department

DYNAMICS OF CYLINDRICAL CONVERGING SHOCK WAVES INTERACTING WITH CIRCULAR-ARC OBSTACLES

Doctoral dissertation of

Federica VIGNATI

Matr. 768533

Advisor:
Prof. Alberto M. A. GUARDONE
Tutor and Chair of the Doctoral Programme:
Prof. Luigi VIGEVANO

Year 2015 - XXVI Cycle

Ringraziamenti

L'è tutto sbagliato, l'è tutto da rifare
— GINO BARTALI

Si prendano n amici, m dei quali (con $m \,\middle|\, m/n \in (0.8, 1)$) aspiranti ingegneri e i rimanenti $n - m$ segretamente tali (siamo seri, non ci crede nessuno che possano non esserlo!). È solo questione di tempo prima che gli n soggetti inizino ad estendere i ben noti Principi di Conservazione a qualsiasi entità. Eccoci quindi al "Principio di Conservazione della Felicità (PCF)": La quantità totale di Felicità $\mathcal{F}$ presente in un dominio Ω (con $|\Omega|$ che varia da 1Å a ∞) corrisponde a una quota fissata.

Trascurando le sue interessanti ma deprecabili applicazioni, come quella suggerita dal "Corollario al PCF pseudo-stazionario" [I], il PCF dice chiaramente che, se una certa dottoranda ottiene un risultato soddisfacente, è meglio che non ci si abitui troppo. In alternativa, che se la dottoranda non ne azzecca una per un intervallo di tempo anche lungo, prima o poi qualche risultato arriverà. Da questo punto di vista il prof. Guardone si è dimostrato uno scienziato consumato, continuando a investire nel PCF, cioè nella dottoranda, anche quando le circostanze suggerivano che i risultati sarebbero arrivati, alla meglio, solo per $\tau \to \infty$ e che l'entropia prodotta nel frattempo avrebbe accelerato la fine dell'Universo di qualche milione di anni. Fosse anche solo per questo, Alberto, ti meriti un enorme "grazie" da parte mia.

Ma che dire dei Babbani, cioè coloro che, meno pratici in fatto di Princìpi, derivate e sommatorie, non conoscono il PCF? In attesa che Piero Angela dedichi una puntata alla divulgazione del PCF, i cari Babbani hanno trovato un modo altrettanto efficace per esprimere l'idea: fiducia. Grazie quindi a tutti coloro che illuminano la mia vita, sempre.

Grazie a mio marito Filippo, "il mio Filippino", che ogni giorno mi regala sorrisi a suon di incitamenti, di deliziosi post-it che nulla hanno da invidiare a The Order of the Stick e del suo esempio nell'affrontare la vita armato solo del suo sorriso, di Ombromanta e di un podetì. Dici sempre di sentirti troppo piccolo per migliorare il mondo, ma di sicuro migliori il mio.

[I] $\forall i \in \{\mathbb{N} \cap [0, N]\} \,\middle|\, (|x_i - x_0| \leq R)$, $\partial_\tau (\Sigma_i \mathcal{F}_i) \approx 0$: per ottenere un aumento immediato ($\partial_\tau \approx 0$) della propria Felicità $\mathcal{F}_0$, il soggetto 0 deve infastidire le N persone entro un raggio R, così che esse liberino i cosiddetti "felicitoni" (le particelle trasportatrici di Felicità) e il soggetto 0 li assorba, incrementando la propria.

Grazie alla mia grande famiglia, a quella vecchia e a quella nuova. Quasi cinque anni fa, per la mia laurea, ringraziavo i Fuchi "per avermi Supportata & Sopportata": mi accorgo di aver fatto spesso pendere la bilancia verso la seconda azione, eppure siete stati sempre capaci di farla tornare in equilibrio, aggiungendo ogni volta massicce dosi della prima.

Grazie alle mie sorelle, che vedo sempre come "le mie sorelline". Certo, ormai Aurora ci ospita nella [darsi un tono: mode on] sua casa nelle Dolomiti per le vacanze di Natale [darsi un tono: mode off] e Diletta, solo un mese fa, leggeva i ringraziamenti della sua tesi di laurea (occupando la rimanente parte delle vacanze di Natale), però sempre sorelline rimangono... Grazie a Matteo e Andrea: rendendo felici loro due, fate felice me.

Grazie ai miei suoceri e ai miei cognati: mi avete accolta nella vostra famiglia nel modo migliore, un "pòta" dietro l'altro. Parafrasando Platone, spesso abbiamo pensieri così diversi che ci sembra impossibile essere tutti spicchi che si incastrano nella stessa mela. E infatti preferisco di gran lunga mettere insieme uno spicchio di mela, una fettina di mandarino, due fragole e qualche acino d'uva: la macedonia è mooooooolto più saporita!

Grazie ad Alessandro e Francesco, i miei nipotini: siete davvero l'infinito in una noce! "I see babies cry and I watch them grow, they'll learn much more than I'll ever know": per quanto proprio conoscere qualcosa in più sia stata la mia sfida in questi anni, non posso che augurarvi proprio questo.

Grazie a tutto il resto della sempre grande famiglia: sapendovi ancora provati dall'ultima lettura dei ringraziamenti di tesi, credo che il modo migliore per dimostrarvi quanto vi voglio bene sia non aprire un ulteriore capitolo per citarvi uno per uno. Anche perchè, se mi perdonate la frase da Baci Perugina, sarebbe come provare ad applicare un'analisi discreta allo spettro dei colori dell'arcobaleno.

Grazie a coloro senza i quali avrei dovuto chiedere un altro paio d'anni di proroga: Parri e Aurora. Amici (certo, anche consiglieri, traslocatori, agenti immobiliari, accoglienti ospiti, pure (uno) figlioccio della cresima, ma soprattutto amici) ci fate sempre trovare aperta la porta della vostra casa per trascorrere insieme momenti così deliziosi che sembrano usciti dalla matita di Miyazaki. Che la serata sia a base di cena & zombi oppure di un'intensa sessione di C++, con voi ci sentiamo sempre a casa.

Grazie ai miei compagni di dottorato, con i quali mi sembra sempre di più di aver condiviso un'avventura donchisciottesca. A Tommaso, Seba, Willy, il Candidato, compagni dei primi anni. Al saggio Vincenzo e alla pelle d'oca che gli viene ogni volta che antepongo l'articolo ai nomi propri. A Alessandro, occhi di ghiaccio e cuore di salama da sugo. A Paolo, vicino di banco e a breve anche di casa, ansiolitico vivente e dalla rara cultura in tema di dinosauri, giochi di ruolo dal vivo e invenzioni inutili. A Giulio, "astro nascente dell'Aerodinamica" (cit.), che adora questa definizione tanto quanto apprezzerebbe il grana sulla pasta alle vongole. A Mirco (santo subito!) che, non contento di conoscere sette o otto linguaggi di programmazione, divide il suo tempo fra corsa, pesi, arrampicata e i Volumi Finiti in 5D: per piacere, aspetta qualche anno per trovare la soluzione in forma chiusa delle equazioni di Navier-Stokes o qui restiamo tutti a piedi. A Fabio Bocola e a Fabio-coi-boccoli, il primo stretto fra un lavoro che i Babbani definirebbero "vero", la famiglia, il dottorato e mille passioni, eppure sempre attento nel ricordarsi quello che ciascuno di noi ha per la testa, e il secondo aspirante fotomodello per le copertine dei romanzi rosa. A Samuele, e alla sua esperienza da zio. A Claudio, che sa trovare il lato positivo anche nelle invasioni di cavallette. To Kamal: keep smiling as you do now! A Giulio e a Marta, che erediterà la presidenza del Cynnamon Ultra Lovers Organization. A Mannarino e a Francesca, inconsapevoli e quanto mai geniali applicatori del PCF. A Valentina e Federico, con i quali sto finalmente vedendo la luce in fondo al tunnel: apprezzerete se vi dico "vi lovvo tutti dibbrutto". A Jakub e Louis, che mi fanno sentire una nonna con le loro domande sulla cura delle piante e sul lavoro a maglia. A Barbara, che sfoderando il suo sorriso più innocente demolisce una persona in tre parole, e a Michele, solitamente il suo obiettivo preferito, che si è sentito dare dell'hipster e del toy-boy ma che ogni volta condivide con noi le sue trovate (immancabilmente ma deliziosamente in stile hipster-toy-boy). A Paola e Andrea, come avrei fatto senza di voi?

Grazie agli amici che hanno affrontato il dottorato in parallelo al mio, magari a poche centinaia di metri di distanza, che però talvolta sembravano infinitamente di più. Ho assaporato ogni volta che siamo riusciti a incastrare gli impegni riuscendo a trovare il tempo per un pranzo insieme. Grazie ad Asto, con il suo sorriso barbuto e sincero (che ha scommesso sulla tesi in bianco e nero), a Simona, dall'entusiasmo contagioso, a Giò, con il suo umorismo nero, a Matteo, sempre capace di valorizzare il mio lavoro. Grazie a chi ha finito il dottorato da un po', ma resta sempre un raggio di sole nella Bovisa: a Damiano

e Lino (ehm, ragazzi, non voglio insistere, ma...), a Bino, a Andrea e alle sue colazioni, a Francesco ...

Grazie ai famosi n amici, di cui m ormai affermati ingegneri e n – m segretamente tali. Un adorabile effetto collaterale dell'avere per amici, da oltre metà della propria vita, persone come voi è che, dovessimo parlarci in binario, ci capiremmo benissimo. E se anche non ci parlassimo proprio, ci capiremmo lo stesso. Grazie bravaGiovannabrava, paziente quando non mi faccio sentire per un po' e contemporaneamente agguerrita con il suo avvitatore elettrico quando si tratta di difendermi, geniale nelle recensioni, che siano di romanzi (il suo blog http://bocconcinidicarta.com merita!), di tè o di smalti. Grazie al suo pazientissssssssimo Ciccino, a Guarni e a Fungo, grazie a Sara, a Maria e Terence (MI RACCOMANDO!), Alex, Federica, Mattia e Annamaria. Lucia, non vedo l'ora di leggere la saga di tutti noi!

Grazie agli amici, ospiti e volontari, di Cielo e Terra, soprattutto a coloro che hanno avuto molta pazienza e hanno sopperito alle mie assenze durante le mie lunghe latitanze dovute al dottorato. Mi emoziono a pensare a quello che fate, che stiamo facendo insieme, ogni volta. Grazie ragazzi.

Grazie a tutti coloro che hanno assecondato le mie passioni e le mie idee, anche quando sembravano così assurde e strampalate, come i ragazzi della Pro Loco di Rigosa, che si sono messi al lavoro organizzando la festa che sognavo consentendomi di sposare il mio Filippino anche da dottoranda.

Grazie a Contador, gatto arancione, vegetariano, cleptomane, amante del guinzaglio e instancabile fusatore.
Scrivere gli ultimi capitoli della tesi di notte, con il Filippino e Contador che provavano a farmi compagnia mentre bevevo litri di tè della Giovanna per stare sveglia è stata davvero una pacchia!
Bugia, crollavo dal sonno.
Però mi avete aiutata a farcela, grazie.

E grazie a tutti quelli che mi ricordano che, se anche esiste un PCF, molto probabilmente non è omogeneo: La quantità totale di Felicità $\mathcal{F}$ presente in un dominio Ω (ad esempio in una dottoranda) corrisponde a una quota fissata, che però può essere aumentata grazie a interventi esterni.

Contents

List of Figures

List of Tables

Notation

In the following, the letter $\mathcal{B}$ indicates a dummy variable. The two columns "GEO" and "TMD" of the following list separate geometrical and physic-thermodynamic variables. The position of the marker • indicates which category each variable belongs to.

Latin letters

	GEO	TMD	
$\hat{a}$		•	van der Waals equation pressure coefficient
A,B,C	•		vertices of the mesh element
$\hat{b}$		•	van der Waals equation covolume
c	•		obstacle chord
c_v		•	constant-volume specific heat
c_P		•	pressure coefficient
c_T		•	temperature coefficient
$d_r\mathcal{B}$	•		Finite-Differences discretization of $\partial\mathcal{B}/\partial r$
$d_\tau\mathcal{B}$	•		Finite-Differences discretization of $\partial\mathcal{B}/\partial\tau$
e		•	specific energy per unit mass

E^t	•	total specific energy per unit volume
h	•	slope
$\underline{\underline{I}}$		idendity matrix
J,K,L	•	set of mesh nodes
k_J	•	even/odd symmetry coefficient
$\hat{\ell}$	•	reference length
m	•	mesh element
$\underline{m}$	•	momentum
Mm	•	molecular mass
M_s	•	shock wave Mach number
n_c	•	number of components of a gas mixture
n_{obs}	•	obstacle number
P	•	pressure
q		(dummy)
r	•	radius
r_{LE}	•	obstacle leading-edge radius
R_s	•	shock wave radius
R_e	•	radius of the first node behind the shock
R_o	•	radius of the obstacle osculating circle
$\hat{R}$	•	mass-averaged gas constant
$\hat{\mathcal{R}}$	•	gas constant
s	•	shock speed
S	•	post-shock point

t	•		obstacle thickness
T		•	temperature
u		•	flow velocity
v		•	specific volume
w		•	speed of sound
(x_o, y_o)	•		center of the obstacle osculating circle
(x, y)	•		Triple Point coordinates
x	•		node position
y		•	molar fraction
Z		•	compressibility

Greek letters

	GEO	TMD	
α	•		self-similarity exponent
β_P		•	initial pressure ratio
γ		•	specific heats ratio of polytropic ideal gas
$\delta_{M-NQ,\,m}$	•		node M-segment $\overline{NQ}$ "distance with sign"
δ_γ		•	$\widehat{R}/\widehat{c}_v$
$\Delta\, q$	•		difference of q [I]
ϵ	•		threshold
ε			(dummy)
ζ	•		vector phase angle

[I] Δ applies to both the node spacing, the time step, the vertical Triple Point offset and the cautionary threshold of the radius

η • efficiency

θ_w • wedge angle

$\varkappa$ (dummy)

λ • cylindrical shock azimuth in polar coordinates

Λ • coefficients of a straight line explicit equation

ν (dummy)

ξ • elementary domain vertex angle π/n_{obs}

Ξ • coefficients of a conic curve implicit equation

ϖ (dummy)

ρ • density

ϱ (dummy)

σ • specific entropy per unit mass

$\varsigma_{MN,m}$ • inclusion coefficient of a node in the element m

τ • time

υ (dummy)

Υ • coefficients of the Triple Point trajectory

ϕ • obstacle azimuth in polar coordinates

Φ • temperature-dependent c_v term

χ • wedge angle of the Triple Point trajectory

ψ • generic azimuthal coordinate

ω (dummy)

Abbreviations

RR	Regular Reflection
IR	Irregular Reflection
MR	Mach Reflection
DiMR	Direct Mach Reflection
StMR	Stationary Mach Reflection
InMR	Inverse Mach Reflection
SMR	Single Mach Reflection
PTMR	Pseudo-Transitional Mach Reflection
TMR	Transitional Mach Reflection
DMR	Double Mach Reflection
vNR	von Neumann Reflection
i_s	incident shock
m_q	Mach stem originated at the q-th reflection
TP	Triple Point
RS	reflecting surface
RSW	reflected shock wave
1D	one-dimensional
2D	two-dimensional
FFR	Far Field Region
OR	Obstacle Region
FR	Focus Region

Indices

h	components of the mixture
j	probe along a radius
k	time step
l	Focus Region node
m	Obstacle Region element
M,N,Q	generic nodes
p	probes
z	vibrational temperature

Subscripts

a	alert
b	behind the shock
cr	gas critical point
d	numerical diaphragm
e	external
f	in front of the shock
i	internal
LE	leading edge
o	obstacle
P	pressure
s	secondary
tr	transition
T	temperature

TE	trailing edge
v	volume
vib	vibrational
w	wedge
0	in $r = 0$

Superscripts

abs	in an absolute reference system
cr	separating leading edge RR and MR
FD	Finite Differences
LE	leading edge
P	perceived
PL	power law
ref	reference
rel	in a relative reference system
RH	Rankine-Hugoniot
t	total
0	at $\tau = 0$

Accents

$\widehat{\mathcal{B}}$	$\mathcal{B}$ in dimensional units (dimensionless if unmarked)
$\widetilde{\mathcal{B}}$	$\mathcal{B}$ radius or time belonging to the power law curve

$\widehat{\mathcal{B}}$	$\mathcal{B}$ estimated from a fitting
$\mathcal{B}^*$	$\mathcal{B}$ evaluated in thermodynamic reference conditions
N'	symmetrical point of N
$\overline{\mathrm{NQ}}$	segment between N and Q
$\overset{\triangle}{\mathrm{MNQ}}$	triangle with vertices M, N and Q

Abstract

Cylindrical and spherical converging shock waves can be used to attain high energy concentration at the focus point, thus making them interesting for applications where high temperature and pressure are required, e.g. in Inertial Confinement Fusion (ICF). Unfortunately, converging shock waves suffer from corrugation instabilities which hamper the front regularity and reduce the shock intensity with respect to the axisymmetrical case.

The stabilization of the converging shock wave may be obtained by means of the so-called "shock reshaping", i.e. by changing the shock shape into a more stable one. Both numerical simulation and experimental measurements in the open literature point to the use of suitable shock-solid body interactions to reshape the converging waves into stable prismatic (for the cylindrical shocks case) or a polyhedral (for spherical implosions) ones.

The topic of this work is the numerical study of cylindrical implosions in air, interacting with lenticular obstacles. The reference configuration was proposed in M. Kjellander, N. Tillmark, N. Apazidis, "Thermal Radiation From A Converging Shock Implosion", Phys. of Fluids (2010), where wing-shaped obstacles are introduced to reduce the shock-obstacle losses. Lenticular obstacles, indeed, appear a good compromise between cylindrical and double-wedge obstacles, characterized by strong separation and losses.

Diverse obstacle geometries (number, position and thickness) and operating conditions (shock intensity and gas conditions) are considered in this work. Obstacles are symmetrical lenticular airfoils with a thickness-to-chord ratio t/c varying between 0.07 and 1 on thirteen levels. The considered number of obstacles n_{obs} is 0, 1, 4, 6, 8, 16 and 24. The obstacle leading edge radius r_{LE} is 7, 14 and 17.5.

Simulations are performed using the FlowMesh code, a solver for Euler equations over unstructured grids. The integration with a novel multi-domain approach provides faster and very accurate solutions.

Numerical results compare fairly well to theoretical models for the shock propagation and to available experimental results.

The Mach reflections occurring at the obstacle leading and trailing edges and over symmetry surfaces result in the polygonalization of the shock wave, which continues propagating inwards as a stable, polygonal shock. The leading edge reflections are duly studied and classified here for the first time in the case of cylindrical shock waves interacting with cylindrical obstacles. Diverse reflection patterns are observed and the influential parameters are identified. Local reflection types qualitatively agree with the classical criteria for pseudo-steady reflections around planar obstacles.

An analytic model for the description of the evolution of Regular Reflections is proposed. The dynamical transition of Regular Reflections into Mach Reflections during the shock propagation along

the obstacle is identifies and its dependence on geometric and fluid-dynamical factors is exposed. Diverse aspects of the Triple Point trajectory in Mach Reflections are studied, resulting in some empirical correlations.

Different shock patterns are observed after the leading edge reflection. Depending on the configuration and, therefore, on the resulting patterns, polygonal shock waves are observed with a time-dependent number of edges, switching among diverse n_{obs}, $2n_{obs}$, $3n_{obs}$ and $4n_{obs}$ configurations.

The largest temperature peak at the origin is obtained using a 16-obstacle array with the smallest thickness to length ratio, and located at $r_{LE} = 14$.

A general decreasing of the focusing effectiveness is highlighted by the study of the effects of the adopted thermodynamic model, if the van der Waals model is considered.

The applicability of the assumption of self-similarity of the shock temporal propagation is tested in conditions for which theoretical models are not available, by means of a fitting on numerical data. A novel method is used to detect the shock position in time in presence of very complex flow fields. Moreover, the effects of the thermodynamic model on the self-similarity exponent are evaluated.

The unsteady shock wave convergence is observed in the pressure-specific volume plane. One-dimensional results show an excellent accordance with Hugoniot adiabat. On the contrary, a departure of numerical data concerning two-dimensional shock waves from analytic curves is observed, due to fast but intense transient phenomena in correspondence of the shock reflections.

Key words: Numerical simulations; Converging shock waves; Lenticular obstacles; Ideal gas; Non-ideal gas; Shock reshaping.

Sommario

È noto che le onde d'urto convergenti cilindriche e sferiche possono essere impiegate per la forte concentrazione di energia nel punto di focalizzazione. Questa proprietà le rende interessanti per applicazioni in cui alte temperature e pressioni sono richieste, ad esempio per la Fusione a Confinamento Inerziale ("Inertial Confinement Fusion", ICF). Tuttavia, le onde d'urto convergenti sono affette da instabilità di corrugazione del fronte che ne riducono l'intensità rispetto al caso assialsimmetrico.

Come mostrato in letteratura, la stabilizzazione delle onde d'urto si può ottenere tramite il cosiddetto "reshaping", cioè modificandone la forma in una configurazione più stabile. Simulazioni numeriche e risultati sperimentali mostrano che, con un'adeguata interazione fra urti e ostacoli, si possono ottenere urti convergenti stabili di forma prismatica (per gli urti inizialmente cilindrici) o poliedrica (per urti sferici).

Oggetto di questo lavoro è lo studio tramite simulazioni numeriche di onde d'urto cilindriche convergenti in aria che interagiscono con ostacoli lenticolari. La configurazione di riferimento è quella descritta in M. Kjellander, N. Tillmark, N. Apazidis, "Thermal Radiation From A Converging Shock Implosion", Phys. of Fluids (2010), in cui urti cilindrici vengono resi poligonali dall'interazione con ostacoli aerodinamici al fine di ridurre le perdite dovute all'interazione urto/ostacolo. Gli ostacoli lenticolari appaiono infatti come un compromesso fra le caratteristiche degli ostacoli cilindrici e romboidali, che sono caratterizzati da separazione della corrente e perdite.

In questo lavoro si considerano diverse geometrie degli ostacoli (numero, posizione e spessore) e condizioni operative (intensità dell'urto e condizioni del gas). Gli ostacoli sono profili simmetrici ad arco di circonferenza con rapporto spessore/corda t/c che varia da 0.07 a 1 su 13 livelli. Il numero di ostacoli n_{obs} è 0, 1, 4, 6, 8, 16 a 24. Il raggio del bordo di attacco r_{LE} è pari a 7, 14 e 17.5.

Per le simulazioni numeriche si utilizza il codice FlowMesh per la soluzione delle equazioni di Eulero su griglie non strutturate. L'accuratezza e la velocità delle simulazioni sono incrementate dall'utilizzo di un nuovo metodo per il calcolo multi-domain.

Il confronto fra i risultati numerici con modelli teorici e risultati sperimentali mostra un buon accordo.

Le riflessioni di Mach ai bordi d'attacco e d'uscita degli ostacoli e lungo le superfici di simmetria causano la poligonalizzazione dell'onda d'urto, che continua a propagarsi verso l'interno. Le riflessioni al bordo d'attacco sono qui studiate e classificate secondo il tipo di riflessione e i parametri influenti. Il confronto fra i valori locali e i criteri di riflessione nel caso pseudo-stazionario mostra un accordo qualitativo.

Un modello analitico viene proposto per la descrizione dell'evoluzione delle riflessioni regolari. La transizione dinamica delle riflessioni regolari in riflessioni di Mach durante la propagazione di ogni urto viene descritta e correlata ai fattori geometrici e fluidodinamici. La traiettoria del punto triplo delle riflessioni di Mach viene studiata sotto vari aspetti e alcune correlazioni vengono proposte e discusse.

A valle della riflessione al bordo d'attacco degli ostacoli, vengono osservate diverse strutture fluidodinamiche. A seconda dei parametri imposti e, di conseguenza, delle strutture rilevate, si osservano urti poligonali con un numero di lati pari a n_{obs}, $2n_{obs}$, $3n_{obs}$ o $4n_{obs}$ e variabile nel tempo.

Il massimo valore di temperatura al punto di focalizzazione si ottiene con una schiera di 16 ostacoli con $t/c = 0.07$ e $r_{LE} = 14$.

Lo studio degli effetti del modello termodinamico mostra un generale scadimento dell'efficacia della focalizzazione dovuta a un'equazione termica di van der Waals.

Una regressione sui dati permette di valutare l'applicabilità dell'ipotesi di autosimilarità della propagazione dell'urto nel tempo, anche dove questa non viene garantita da modelli analitici. La posizione dell'urto viene ricavata istante per istante tramite un nuovo metodo adatto a considerare soluzioni molto complesse. Vengono valutati inoltre gli effetti del modello termodinamico e del numero di ostacoli sull'esponente di autosimilarità.

La propagazione instazionaria dell'urto viene osservata nel piano pressione–volume specifico. I risultati relativi a urti monodimensionali ricalcano perfettamente l'adiabatica di Hugoniot. Al contrario, dei brevi ma molto intensi transitori in corrispondenza delle riflessioni degli urti causano lo scostamento dei dati numerici dalle curve analitiche nel caso bidimensionale.

Parole chiave: Simulazioni numeriche; Onde d'urto convergenti; Ostacoli lenticolari; Gas ideale; Gas non-ideale; Poligonalizzazione dell'urto.

Introduction

Motivation

Converging shock waves

During the last decades, the problem of the focusing of converging shock waves has been generating an increasing interest in the scientific community, thanks to the possibility of attaining very high pressure, temperature and, in general, energy concentration at the focus point. The applications range from large-scale energy conversion to medical treatments, including a number of theoretical physics studies.

In Inertial Confinement Fusion (ICF) [1, 2, 3], light chemical elements (often Deuterium, ^{2}H and Tritium, ^{3}H) are contained in a spherical shell of solid fuel. Qualitatively speaking, when the fuel is ignited, a strong spherical shock wave propagates inwards and concentrates the fuel atoms within a very small radius. This method is known as "direct drive mode" [4], and consists in one of the two main ignition procedures. Provided that the kinetic energy (and therefore temperature) of the hydrogen isotopes nuclei is large enough to prevail against the reciprocal electrostatic repulsion, their nuclei fuse together. The fusion of Deuterium (whose nucleus consists of one proton and one neutron) and Tritium (made up one proton and two neutrons) results in the formation of an atom of Helium ^{4}He (with two protons and two neutrons in the nucleus) and in the emission of a neutron. Albeit the sub-atomic particles balance is respected, the mass results to be not conserved. Therefore, by virtue of the well known

mass–energy equivalence, an average amount of energy of about 18 MeV is released for each nuclear reaction. Due to the necessity to balance the electrostatic force, the focusing effectiveness of the imploding shock wave, quantified by the attained temperature at the focusing, is of paramount importance for the achievement of the nuclear fusion.

ICF represents a candidate for the ignition of nuclear-fusion based power plants. At this day, however, the application of ICF to the production of electric energy on large scale is still being studied. Unfortunately, ICF applies also in the military framework. In fact, one of the leading motivations which has boosted the study of strong imploding shocks is the research of a solution for the ignition of the so-called "H-bomb". The main principle of the nuclear-fusion bomb is to exploits the atomic energy without using fissile fuel, e.g. Uranium. A complete overview on ICF and its applications can be found in [4].

Another common application of converging shock waves—involving, of course, a much lower amount of energy—is lithotripsy, a medical treatment for the removal of kidney stones [5]. In this procedure, an acoustic pulse is used to focus a shock wave towards the calculus in order to break it in smaller pieces which can be processed by the organism.

In sonoluminescence experiments, a light emission is observed at the collapse of a cavitation bubble when the liquid is excited by an acoustic wave [6, 7]. Even if a theory fully explaining the phenomenon has not been proposed yet, one of the most complete models envisages the detachment of a strong perfectly-spherical implosion from the internal walls when the bubble radius reaches a critical value. This shock waves causes the formation of plasma at the center of the bubble, and the collision among free electrons result in the emission of a light spot. A review on the topic is in [8].

Converging shock waves are generated also during the explosion of a supernova: the violent outburst of material from the star is compensated by the onset of a pseudo-spherical converging shock wave, which travels from the surface of the star towards the center.

Shock wave instabilities

The role of converging shock waves in the applications observed above is to focus a very high amount of energy. Unfortunately, converging shocks are proved to suffer from surface instability, as highlighted in several studies [9, 10]. Shock instabilities can be triggered by diverse factors, and possibly gradually deteriorate the regularity of the shock front.

Analytical results for the prediction of the onset of instabilities were derived from linear models which account for the influence of real gas effects on the shock Hugoniot adiabat. In the so-called "D'yakov-Kontorvich corrugation instability" [11, 12], the perturbed shock front presents corrugations of increasing importance which eventually lead to the shock front splitting. The latter phenomenon is explained in detail in [13, 14].

In ICF applications, instabilities triggered by the density gradient were observed [15, 16, 17]. An instability of this kind is the "Rayleigh-Taylor instability", which is associated to layered fluids at rest accelerated by an uniform field, whose direction is opposite to the density gradient one [18, 19]. If the interface between the two fluids is perturbed, some so-called "fingers" of the heavier fluid propagate towards the lighter fluid normal to the separating surface, as illustrated in fig. I.1. Along the fingers lateral surfaces, a non-zero relative tangential velocity exists. The latter is indicated as the leading cause of the "Kelvin-Helmholtz instability", which causes the disappearance of the sharp interface between the two fluids and the onset of a mixing layer [20, 21]. For this reason, the occurrence of a Rayleigh-Taylor instability is associated to a further deterioration of the shock front surface (fig. I.2). Literature indicates that the Rayleigh-Taylor instability depends on the intensity of the accelerating field. For an impulsive acceleration, i.e. a shock wave, of the lighter fluid, the Rayleigh-Taylor instability degenerates into the so-called "Richtmyer-Meshkov instability", which is another type of surface instability. An example of Richtmyer-Meshkov instability is depicted in fig. I.3 [22, 23].

(a) (b)

Figure I.1: Example of Rayleigh-Taylor instability in two layered fluids, i.e. cold colored water above warm water.

The effect of these corrugation instabilities is that of decreasing the shock intensity during its propagation and, therefore, its effectiveness in energy focusing with respect to the stable case, which assumes the shock to remain one-dimensional axisymmetrical [24].

Solution to the instability problem: the shock reshaping

Several studies concerning converging shock waves have proved that shock front instabilities are an intrinsic feature of converging shock waves. Indeed, instabilities have been highlighted by a number of both numerical and experimental works, which focused on different implosion types and adopted diverse investigation methods ([25, 108, 27, 28, 29, 30, 31, 32, 33, 34]).

If on one hand the intrinsic instability of free cylindrical and spherical implosions makes them unsuitable for technical applications, on the other hand it also represents a possible solution. Indeed, it offers the possibility of directly controlling the shock front shape to prevent the onset of in-

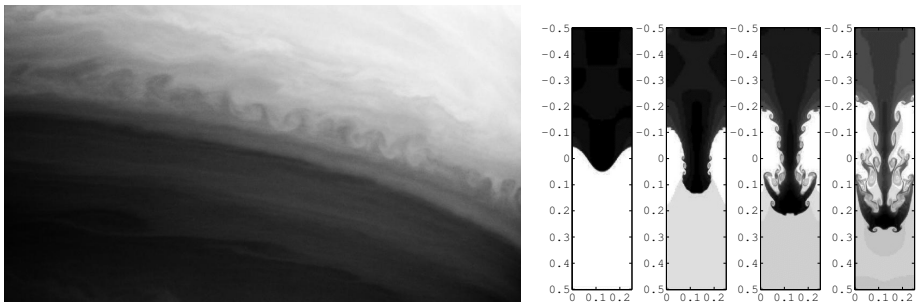

(a) (b)

Figure I.2: Examples of Kelvin–Helmholtz instability: (a) turbulent boundary between two latitudinal bands in Saturn's atmosphere (Image source: NASA/JPL/Space Science Institute, 2004) and (b) associated to Rayleigh–Taylor instability (Modified colors, image source: S. Li, H. Li, "Parallel AMR Code for Compressible MHD or HD Equations", Los Alamos Nat. Lab.).

stabilities. This result can be achieved by turning the shock wave into a prismatic (for initially cylindrical shocks) or a polyhedral (for spherical ones) shock.

This process, named "shock reshaping", can be carried out in diverse ways. A very promising way consists in forcing the shock to interact with a number of obstacles placed along its propagation path. The multiple reflections of the shock eventually modify its shape into a more stable one. For symmetrically arranged and suitably shaped obstacles, the final shock shape is prismatic, which corresponds to a more stable configuration [35, 36]. On the other hand, the obstacle arrangement is to be optimized to reduce losses due to shock–obstacle interaction [37, 38].

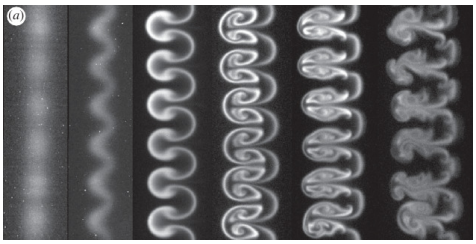

Figure I.3: Experimentally-generated Richtmyer-Meshkov instability observed by means of a high-resolution density-field image (Image source: K. Prestridge, G. Orlicz, S. Balasubramanian, B.J. Balakumar, "Experiments of the Richtmyer-Meshkov instability", Phil. Trans. Roy. Soc. A (2013)).

Shock reshaping: state-of-the-art and objectives

Overview

The reshaping of converging shock waves, for preventing the onset of surface instabilities, involves two main physical mechanisms, each of which represents a very interesting challenge.

The first one is the general focusing of converging shock waves. Unlike the case of planar shock waves, indeed, the computation of the solution in presence of a converging shock wave is more difficult, due to e.g. the non-uniform flow field. Theoretical, experimental and numerical works have provided a general knowledge on the problem. However, diverse research efforts are still being carried on to answer open questions on the focusing of cylindrical and spherical shock waves: does an exactly cylindrical implosion exist? How can it be generated? How does it propagate? Is it stable? Does it present some internal symmetry? What happens when it collapses into a single point? How can this phenomenon be investigated? How can it be exploited?

The second mechanism consists in the reshaping of a shock wave. On one hand it may seem natural to induce the reshaping of the shock through the interaction with some generic means, e.g. a solid wall, another shock wave, a field the shock wave is sensitive to, internal symmetry constraints, etc. On the other

hand, the proper choice of the procedure is non-trivial. Indeed, both the results and the investigation techniques depend on it, and therefore a number of questions arises: are all the interactions effective with any kind of shock wave? Which is the best technique to reshape a given type of shock wave? Which investigation methods are the most suitable to study the selected interaction? What factors influence the final result? Does the process generate relevant losses? Can the reshaping be modeled as a smooth process from a configuration to the next one, or must sudden transitions be accounted for? Does the selected technique assure the repeatability of the process? Is the reshaping stable with respect to small variations or do bifurcations occur? If the reshaping is achieved by means of a series of reflections, how to select and arrange the reflectors?

As mentioned above, these two physical mechanisms are coupled together in the investigation of the reshaping of a cylindrical converging shock wave and, therefore, also their mutual interaction must be accounted for.

In the following, the discussion on the state of the art is subdivided in accordance with the above classification of the two physical mechanisms which characterize the reshaping of a converging shock wave, i.e. the implosion in a gaseous medium and the reflection-induced reshaping of a shock wave. Eventually, the historical overview of the coupling between these two problems in the reshaping of a converging shock wave is presented.

The implosion problem

Converging shock waves have been studied for several years by means of theoretical, experimental and numerical approaches. Several assumptions can be performed on the structure of the implosion problem, such as the cylindrical or spherical symmetry of the converging shock waves, which allowed to obtain analytical solution of the governing equations.

The first relevant result was derived independently by Gud-

erley [39] in 1942 and by Butler [40] in 1954 for cylindrical and spherical shock waves, and consisted in the correlation between the shock radius R_S and time τ. This relation, hereafter referred to as "Guderley's law", provides a self-similar power law in the form

$$\frac{R_S}{\tilde{r}} = \left(1 - \frac{\tau}{\tilde{\tau}}\right)^{\alpha}$$

where $\tilde{r}$ and $\tilde{\tau}$ represent the initial shock radius and the total focusing time respectively, and α is the self similarity exponent. This law applies to imploding cylindrical or spherical shock waves in the proximity of the focus axis or point, respectively. The latter assumption, i.e. the applicability of the law to shock waves with a very small radius of curvature, is not in contradiction with its self-similarity nature. Indeed, it indicates that the power law applies only where the phenomenon is truly self-similar, that is where any phenomenon concerning the initial transient of the shock formation is completed. The self-similar solution is to be considered, indeed, a "limiting solution" of the general unsteady and non-self-similar propagation of the shock wave. Therefore, in the proximity of the focus point, the length scale associated to R_S differs enough from the radius of the shock in regions where transient phenomena are relevant, e.g. where the shock is generated.

Guderley's theory has been widely used in a number of applications and its validity and accuracy discussed during the years. As exposed in [41, 42], which report the derivation of the law based on dimensional analysis, the value of α depends only on the geometry of the shock wave (planar, cylindrical or spherical) and on the thermodynamics of the gas. In the mid-fifties, the works of Chester [43], Chisnell [44] and Whitham [45, 46] lead to the development of the so-called CCW method, which allowed to determine the value of α in the polytropic ideal gas case.

Some criticisms to Guderley's law are also reported, mainly concerning some discrepancies between predicted and measured values of the shock radius [47]. Furthermore, some more sophisticated models were proposed to increase the accuracy of the predictions on R_S [48], but confirming the general applicability of Guderley's law.

Another field of interest in the study of converging shock waves concerns the adopted method for the shock generation. In

literature [49], one can find the description of diverse techniques for the focusing of shock waves. In most cases, these works concern cylindrical or spherical shocks, which were generated by e.g. the instantaneous energy release [50] or the association with exploding waves [51, 52, 53]. In the numerical framework, the onset of a converging shock wave has been simulated also by means of the so-called "cylindrical piston" [54] method or by imposing a pressure and density circumferential discontinuity [55]. An alternative procedure consists in focusing a planar shock wave into a concave reflector [56].

A peculiar method is described in [57] and consisted in the reshaping of a planar shock wave propagating into a decreasing-size duct, whose section is modeled on the logarithmic spiral: in this case, therefore, the generated shock wave is not a whole cylindrical surface, but only a circular-arc. A discussion on this technique can be found in [58, 59, 60].

The propagation of converging shock waves and the domains of applicability of Guderley's law have been duly investigated by means of numerical simulations adopting diverse schemes, e.g. Finite Differences [61, 62], the CCW method [63], or Finite Volumes [64].

GOAL OF THIS WORK IN THE INVESTIGATION OF THE IMPLOSION PROBLEM One of the goals of the present work is to trace the shock position versus time for diverse shock intensities and thermodynamic conditions. The initial transient corresponding to the onset of the shock wave will be also observed.

To gain a further insight in the evolution of the post-shock flow field during the convergence, the thermodynamic conditions immediately downstream the shock wave will be evaluated at each time step. A comparison between the post-shock conditions and theoretical predictions will be used to assess the increase during time of the shock intensity.

The reshaping of shock waves

In this work, the method adopted for the reshaping of cylindrical imploding shocks will consist in the interaction with an

array of obstacles. Therefore, prior to the direct investigation of the reshaping, the reflection mechanism of a shock over an obstacle is recalled. Eventually, the effects of the application of these reflection to the reshaping are described in the following.

The reflection of shock waves

1. Reflection patterns The most promising and studied method to attain the reshaping of implosions consists in the forced reflection of the shock wave over one or more arrays of obstacles. Depending on the combination between fluid-dynamic properties (the shock Mach number, the gas behavior) and the geometry of the obstacles, a diverse set of reflection occurs and determine the final shape and stability of the shock, as illustrated in fig. I.4.

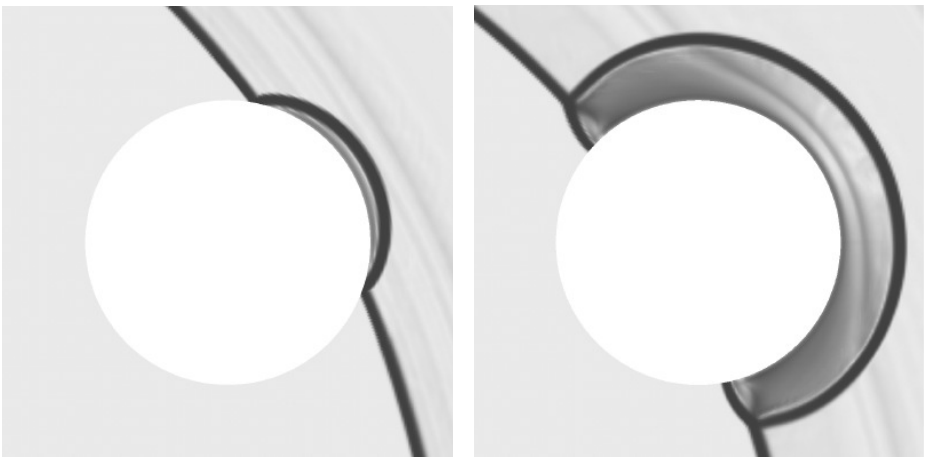

Figure I.4: Numerical Schlieren images of the impingement of the cylindrical converging shock wave at the leading edge of a cylindrical obstacle, highlighting the formation of the classical reflection patterns. The shock wave is converging towards the focus point located bottom-left outside of the figure boundaries. (Images source: V. Eliasson, "On focusing of shock waves", Ph.D. dissertation (2007).)

Albeit the study of the unsteady interaction between shock

waves and walls is—to this day—less complete than for the study of steady reflections, it is known that the interaction results in a number of reflections. Shock reflections exhibit diverse configurations, sketched in fig. I.5, depending on both geometrical and fluid-dynamical parameters.

In the so-called "pseudo-steady" interactions, the observed pattern depends only on the incident shock Mach number M_S and on the obstacle wedge angle θ_w^{LE}, both assumed constant, and can consist in a "Regular Reflection " (RR) or an "Irregular Reflection" (IR) [65]. The main difference between the two classes of reflections consists in the number of involved waves: a Regular Reflection includes only the incident shock and the reflected wave, whereas a further shock wave and a slip line—the latter necessary to the consistency of the system—make up an Irregular Reflection. For a long time, the second group was assumed to consists of "Mach Reflections" (MR) only, a structure including an incident shock, a reflected wave and a Mach stem, all intersecting at the so-called "Triple Point" (TP). According to Courant and Friedrichs [66], when the latter moves away from the reflecting surface, the reflection is Direct (DiMR). A Direct Mach Reflection can be a "Single" (SMR), ("Pseudo")"Transitional" ((P)TMR) [67] or "Double" (DMR) [68, 69] Mach Reflection. The distinction among the diverse types of Mach reflection is performed on the basis of the complexity of the structure resulting from the reflection, as described in the complete overview by Ben-Dor [70], along with transition criteria.

In fact, Irregular Reflections are not coincident with Mach Reflections, because an Irregular, SMR-like reflection pattern was observed in the diffraction of weak shock waves by extremely thin wedges. In these conditions, the diffraction of a Mach Reflection is excluded by theoretical models. This apparent contradiction, named the "von Neumann paradox", was solved with the introduction of an additional kind of non-Mach-type Irregular Reflection, namely the "von Neumann Reflection " [71, 72].

Based on theoretical considerations and on experimental and numerical evidences [73], the reflections listed above are the only possible detectable configurations in

the reflection of shock waves at the leading edge of planar wedges. Fig. I.5 is extracted from [70] and represents the classification of pseudo-steady reflections.

Analytical criteria derived for pseudo-steady shocks, e.g. length scale criterion [74], mechanical equilibrium criterion [75], sonic criterion [76] (actually, an improvement of the detachment criterium, as proved by [77]), [78], allow to determine the occurring reflection type depending on the combination between the incident shock Mach number and the leading edge wedge angle.

The generalization of pseudo-steady results obtained for planar shock waves interacting with planar geometries to the case of curved wave front interacting with curved wall is not trivial. Indeed, the non-constant propagation speed of converging shock waves [39, 54] and the positive convexity of both the shock and the obstacle make the reflection of implosions genuinely unsteady.

In the complete work of Takayama "et al." [79] on the diffraction of planar shock waves by cylindrical obstacles, the transition from Regular to Mach Reflections was observed [80]. In the same works, the influence of both the obstacles curvature radius and the leading edge wedge angle θ_w^{LE} on the transition delay was assessed. The observation of unsteady reflection allowed to observe the differences with respect to the pseudo-steady case. The direct comparison was performed thanks to the works on the shock polar curves [81], where it was demonstrated that, in a first degree of approximation, some unsteady shock diffractions can be treated as a sequence of pseudo-steady reflection.

To the authors' knowledge, no complete studies of the interaction of curved shock waves with curved obstacles is available.

2. Triple Point propagation For pseudo-steady shock reflections, closed analytical expressions of the Triple Point trajectory are available. The extension of the generated structure grows in time but it remains self-similar, and therefore it can be treated as a steady phenomenon by means of a Galilean transformation [70]. This allows to predict the trajectory of the single (in case of Single or Tran-

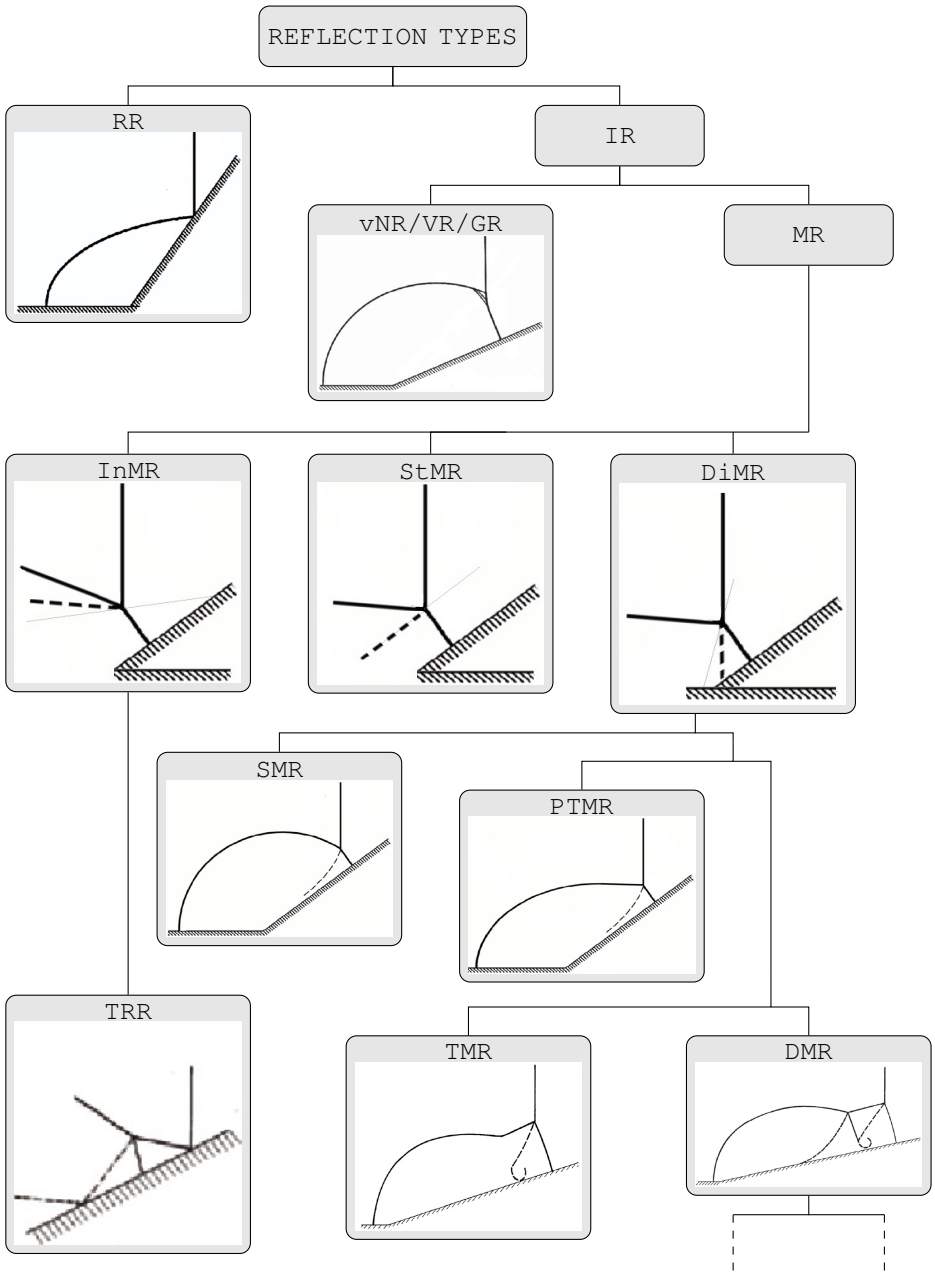

Figure I.5: Classification of pseudo-steady reflections (Images source: G. Ben-Dor, "Shock Wave Reflection Phenomena", ed. Springer (1991 and 2007 editions).)

sitional Mach Reflections) or multiple (for Double Mach Reflections) Triple Point. The prediction of the Triple Point trajectory is performed by means of pseudo-steady methods [82], and, due to the self-similarity assumption, it results in a linear correlation between the spatial coordinates.

When the wedge geometry is modified into a generic, curved obstacle, the conditions at the point of interaction change at any given time, the phenomenon becomes genuinely unsteady, and it has been mostly investigated by means of experiments or numerical simulations. One of the first works of the tracing of the Triple Point in unsteady reflections is attributed to Heilig [83], who studied the diffraction of planar shock waves over cylindrical obstacles and traced the Triple Point path for diverse obstacle radii.

The aforementioned works on unsteady reflections consider the trajectory of Triple Point of Mach Reflections generated by the transition of a Regular reflection. Therefore, the trajectories do not "macroscopically" originate from the obstacle leading edge. However, several theoretical and experimental works demonstrated that even for the so-called "genuine" Mach reflections—i.e. the Mach Reflections macroscopically generated at the leading edge as opposed to those resulting from Regular Reflections—the distance between the leading edge and the point of generation of the Triple Point is non-zero [84]. The existence of this transition layer, quantified in the order of some free mean paths, is attributed to viscous effects. For this reason, a "microscopic" effect exists, which causes a delay in the formation of the Triple Point also in the reflections which are macroscopically of genuine Mach-type. Other works assessed effects of the viscosity on the Triple Point propagation, as e.g. [85].

As already indicated [66] (see fig. I.5), three types of Mach Reflection are distinguished: "Direct" (DiMR, if the Triple Point moves away from the reflecting surface or reflecting wall), "Stationary" (StMR, if TP trajectory is parallel to the reflecting surface) and "Inverse" (InMR, if TP approaches the reflecting surface). The aforementioned study by Takayama "et al." on planar shocks imping-

ing over curved walls successively confirmed experimentally the existence of Direct, Stationary and Inverse Mach Reflections [79], highlighting the factors responsible of the transition and of the modulation of the Triple Point trajectory. In particular, the existence of Stationary and Inverse Mach Reflections was correlated to the concavity of the diffracting obstacle.

The Inverse Mach Reflection is a structure in which the Triple Point moves towards the reflecting surface and, therefore, it is necessarily a transient pattern. When the Triple Point reaches the reflecting surface, the Inverse Mach Reflection terminates and a new structure is generated. The latter is a complex shock-system, termed "Transitioned Regular Reflection" (TRR, see [86]) which is reported in fig. I.5.

In all the mentioned cases, the Triple Point is uniquely defined as the point where the incident shock, the reflected wave and the Mach stem merge. Some works on the diffraction of weak shock waves [87] suggest the possibility of defining a so-called "equivalent Triple Point" also in structures where it does not exists. In von Neumann Reflections, for example, the slope of the shock front varies continuously, i.e., the incident shock and the Mach stem are connected by means of a kink. Moreover, the region of the reflected wave in correspondence of the shock front is substituted by a compression band. For these two reasons, it is impossible to define a true Triple Point. On the contrary, the equivalent Triple Point is the point at the intersection between the leading band of the compression and the incident shock.

GOAL OF THIS WORK IN THE INVESTIGATION OF THE SHOCK REFLECTION PROBLEM The reflections occurring at the leading edge of circular-arc obstacles will be observed in this work. The goal is to subdivide the leading edge patterns and assess the resulting map with the criteria adopted for pseudo-steady reflections. The comparison with pseudo-steady results allows to define the differences introduced by the curvatures of both the obstacle and the shock wave.

The first expected difference with respect to the pseudo-

steady case concerns the definition of the domains where the diverse reflection patterns (Regular or Mach-types) occur. Unlike what happens in the pseudo-steady case, the parameters characterizing the Regular Reflection vary during time, and therefore their evolution will be presented. It is known that most unsteady Regular Reflections eventually become of Mach-type. Therefore, due to the aforementioned Regular Reflections evolution, this works aims at observing for the first time and duly discuss the transition of Regular into Mach Reflections of cylindrical converging shock waves over circular-arc obstacles.

Concerning Mach Reflections, an observation on the trajectory of the Triple Point will be performed.

Reshaping of cylindrical implosions

The first studies on the reshaping of converging shock waves dealt with the geometry-induces "self-reshaping" of polygonal [88] shock wave. The work adopted a simple version of the three-shock theory—the model used to describe the geometry and the flow field of a Mach Reflection—to demonstrate that a converging shock wave whose front is a regular polygon undergoes a continuous reshaping, due to the reciprocal Mach reflections of the edges over the symmetry diagonals. The process remains self similar, since it was demonstrated that the propagation of the polygonal shock edges can be conveniently described by the same power law as of a cylindrical axisymmetrical imploding shock wave. An extension to this work was provided several years later [89] with the three-dimensional reshaping of polyhedral shock waves. In the works of Schwendeman, the reshaping was induced by the internal symmetry of the shock waves, and it does not need to be triggered by external agents. This feature of regular-polygonal shock waves was verified also by experimental works [90, 91].

On the contrary, the reshaping of initially cylindrical shock waves requires the introduction of disturbances in the flow field, with the purpose of causing a series of reflections resulting in a final polygonal shock shape. This possibility has been widely explored in a number of numerical and experi-

mental works.

The reshaping by means of polygonal reflectors is described in [92]. This method, in accordance with the reported results, does not appear to be a good candidate.

Currently, the most promising solution appears to be the adoption of arrays of obstacles, which cause a number of Mach Reflections, resulting eventually in a polygonal shock wave [93, 94]. Indeed, diverse theoretical, numerical and experimental investigations [97, 36] demonstrated that if an array of obstacles is located along the shock path, the interaction between the shock wave and the obstacles can possibly result in the reshaping of the shock geometry into a more stable configuration. In particular, the resulting reshaped shock is represented by a polygon whose edges number either corresponds to the obstacles number or dynamically oscillates between once and twice this number, as depicted in fig. I.6.

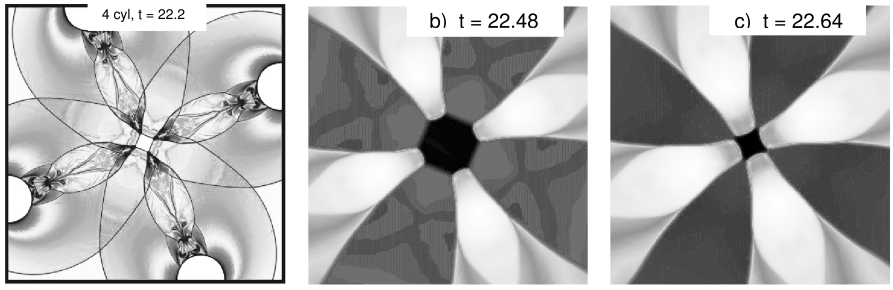

Figure I.6: (a) Numerical Schlieren image and (b)–(c) pressure contours (close up in correspondence of the focus point) of the flow generated by the diffraction of a cylindrical implosion by 4 cylindrical obstacles. Time increases from left to right, showing the definition of a square shock wave and its transition into an octagonal and eventually into a rotated square due to the trailing edge Mach Reflections. The shock wave is converging in diatomic gas with initial Mach number of 2.4. The diffraction is generated by 4 cylindrical obstacles with a diameter of 15 mm located at 46.25 mm from the focus point. (Modified colors, images source: V. Eliasson, W.D. Henshaw, D. Appelö, "On cylindrically converging shock waves shaped by obstacles", Physica D (2008).)

The drawback of the shock reshaping technique is that non negligible losses occur, that reduce the shock strength. This

implies that a relevant task in the design of the array configuration is the identification of a suitable compromise between front stability and shock effectiveness [94, 37]. This identification represents a complex problem, as it depends nonlinearly on a number of factors, e.g. a-priori-set parameters, fluid-dynamic structures generated during the reflections [95] or reciprocal interactions among the shock waves [96].

More recently, Apazidis "et al." [97] individuated a simple but efficient technique for the reshaping of cylindrical imploding shocks. It consists in adopting lenticular obstacles, i.e. symmetric aerodynamic profiles with sharp leading and trailing edge. Results in [97] show that on one hand the described configuration produces a polygonal shock (as reported in fig. I.7) and, at the same time, it reduces the interaction losses, generating only a very small recirculation region at the obstacle trailing edges.

GOAL OF THIS WORK IN THE INVESTIGATION OF THE RESHAPING PROBLEM Moving from the observation concerning the higher efficiency of lenticular obstacles with respect to cylindrical ones, this work will explore the interaction between cylindrical converging shock waves and circular-arc obstacles, in the perspective of assessing the effects of the obstacle geometrical parameters on the shock reflections and, eventually, on the effectiveness of the energy focusing.

Furthermore, the assessment on the effects of the thermodynamic model on the shape and intensity of the reshaped shock is another goal of this thesis.

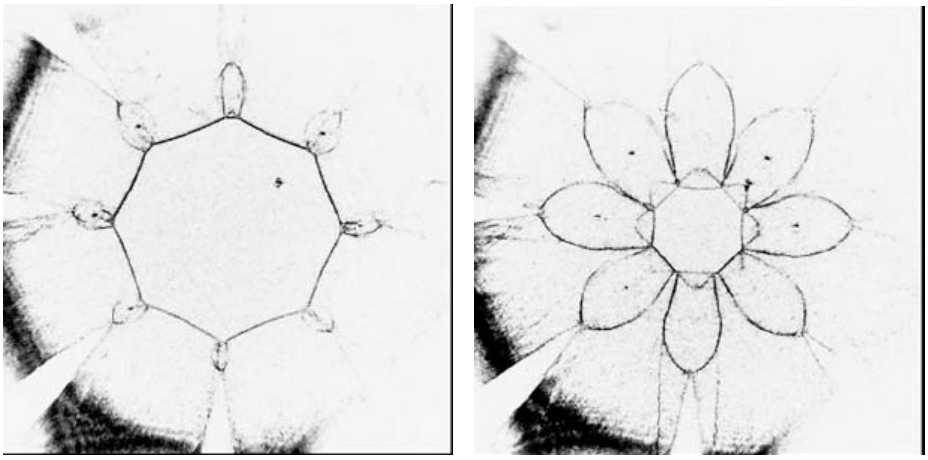

(a) time-to-focusing = 11μs (b) time-to-focusing = 3.9μs

Figure I.7: Experimental Schlieren images of the reshaping of a cylindrical shock wave by 8 lenticular flow dividers. Time increases from left to right, showing the definition of an octagonal shock wave and its following rotation due to the trailing edge Mach Reflections. The shock wave is converging in low-pressure air with initial Mach number of 2.7. The diffraction is generated by 8 lenticular obstacles with a chord of 50 mm, leading edge radius of 70 mm and thickness-to-chord ratio of 0.14. (Inveted colors, images source: M. Kjellander, N. Tillmark, N. Apazidis, "Thermal radiation from a converging shock implosion", Phys. of Fluids (2010).)

Thesis structure

This works moves from the configuration described in [97], and it will investigate different geometrical and operational configuration to assess their influence on the shock reshaping. The thesis is structured as follows:

1. The first chapter, "Numerical simulation of converging shock waves: flow features and methodology", will describe the adopted methodology. As it will be better detailed within the chapter, the symmetry of the obstacle layout allows to reduce the computational domain, and to compute the flow only in a sub-domain, that is a circu-

lar sector delimited by symmetry boundaries. The physics of the cylindrical implosions reshaping will be briefly recalled. Based on experimental results [91], viscous effects will be assumed to be confined only in the boundary layer [98], resulting in the possibility of describing the flow field by means of Euler equations. The choice of exploring the effects of multiple thermodynamic models [100] will allow on one hand to compare numerical results with available references, which mostly concern polytropic ideal gas, and on the other hand to assess real gas effects [101]. Eventually, the setting of the initial conditions will be described.

2. The second chapter, "Multi-domain simulation of the shock reshaping process", concerns the description of two numerical tools developed to provide a more efficient computation of the flow field and of relevant quantities.

   The first tool is a new multi-domain approach [99] which allows to exploit the geometric features of the shock waves in the diverse regions of the computational domain. The peculiarity of this method is that it allows to reconstruct the solution also outside the boundaries of the computational sub-domains. Part of the method is inspired by general studies on converging shock waves, which highlight some features of the phenomenon which are exploited in the multi-domain approach [102, 103].

   The second tool is a technique which allows to trace the shock position also in presence of very complex flow fields. The knowledge of the shock position will be used also to trigger the switch among the domains in the multi-domain approach. For this reason it is formulated to analyze a solution provided by the two Finite Volume solvers for Euler equations [104, 105, 106, 107], i.e., a one-dimensional axisymmetrical and a two-dimensional Cartesian solution.

3. The first group of numerical results will be described in chapter "Cylindrical shock reflection over circular-arc obstacles". To gain a further insight in the diffraction of cylindrical implosions over circular-arc obstacles, the patterns generated at the reflection of the converging shock wave over the obstacle leading edge will be

analyzed.

Diverse reflection types will be identified and classified, depending on the combination between the obstacle geometry and flow conditions generating each reflection, and results will be assessed with the predictions of pseudo-similar models.

Diverse observations will be performed on each family of reflections, i.e. Regular and Mach Reflections. A simple analytical model will be derived for the first ones, and the Regular–Mach transition observed and correlated to the diverse factors. The Triple Point trajectory will be traced for genuine Mach reflections, and an empirical law will be derived by means of a fitting on numerical data.

4. The shock reshaping and convergence process in polytropic ideal gas will be analyzed in chapter "Shock reshaping and focusing in dilute gas". The optimal configuration will be assessed, i.e. the one producing the largest values of pressure and temperature at the focus point. The complex shock-induced flow field will be described, and observed phenomena will be qualitatively correlated to the diverse factors.

5. The last chapter will focus on non-ideal gas effects on cylindrical and polygonal imploding shocks [108, 109, 110, 111, 112], comparing gas in dilute and dense conditions. A systematic investigation on the shock convergence, reshaping and focusing will be performed in accordance with each adopted thermodynamic model. The results will concern:

   - pressure and temperature values attained at the focus point.
   - the determination of the self-similarity exponent α for the diverse thermodynamic models by means of a fitting on numerical data. For one-dimensional shock waves, the hypotheses for the application of Guderley's law are completely satisfied, and therefore the numerically determined value of α is a genuine self-similarity exponent, as discussed by [113] and [114]. For generic two-dimensional shock waves, on the contrary, the possibility of describing the shock wave

average radius versus time by means of a power-law is not proved on a theoretical background. However, it was observed [97] that the functional form of Guderley's law applies satisfactorily also to the description of the propagation of two-dimensional shock waves. For this reason, the "pseudo-self-similarity exponent" will be derived also for two-dimensional shock waves, and it will be correlated to geometrical and thermodynamic parameters.

- the evolution of the post-shock thermodynamic conditions during the shock convergence. For both one-dimensional and two-dimensional shock waves, the trajectory of the post-shock state will be traced in the pressure-specific volume plane and assessed with the analytic Hugoniot adiabat. Since the Hugoniot adiabat applies across one-dimensional normal shock waves, this comparison will allow to assess the relevance of the regions of the flow field where two-dimensional effects are the most relevant.

Chapter 1

Numerical simulation of converging shock waves: flow features and methodology

> With you, everything is gas
> — THE LION KING

The approach to the numerical study of converging shock waves is described here. As it will be detailed in the next chapters, due to the strong sensitivity of results to all the investigated factors, a definitional step is necessary at the beginning. The main features of the shock reshaping are therefore briefly described here: the so-called "reference condition" is introduced, as well as the most relevant steps of the shock reflection, reshaping and convergence. The fluid-dynamical structures are defined, either by recalling conventional names or by means of "ad-hoc" designations. The second section is dedicated to the description of the numerical modeling of the physical phenomena: the governing equations, the thermodynamic model and the initial conditions setting are explained in this framework.

1.1 Converging shock-obstacle interaction

The physics of the shock reshaping is briefly recalled in this section. In the beginning, the so-called "reference con-

figuration", i.e. the one adopted in [97], is described, and the definitions of the diverse variables are provided. The list of steps necessary to define the shock reshaping is the object of sec. 1.1.2.

1.1.1 Reference configuration

The main features of the shock–obstacle interaction are presented in this section for the "reference configuration" described in Ref. [97]. The test rig adopted to perform the experiments in [97] is illustrated in fig. 1.1.

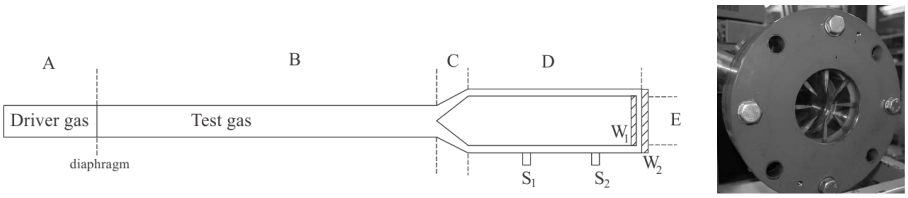

Figure 1.1: Experimental test rig adopted in Ref. [97]. (a) Schematic drawing of the shock tube: (A) driver section, (B) inlet pipe, (C) transformation section, (D) annular tube, (E) test section. S_1 and S_2, shock sensors; W_1 and W_2, glass windows framing the test section. (b) Photograph of the test section with the profiles installed in the chamber. (Images and captions source: M. Kjellander, N. Tillmark, N. Apazidis, "Thermal radiation from a converging shock implosion", Phys. of Fluids (2010)).

The geometry of the reshaping chamber is depicted in figure 1.2, where the three-dimensional cylindrical shock front is represented in a two-dimensional plane that is normal to the shock axis. In figure 1.2, the dashed line indicates the shock position before its impingement at the obstacle leading edges. As it moves towards the origin, the shock interacts with the array of obstacles with lenticular shape which are arranged around the origin in a symmetric fashion.

Thanks to the symmetric arrangement of the obstacles, the shock dynamics can be conveniently described in a reduced do-

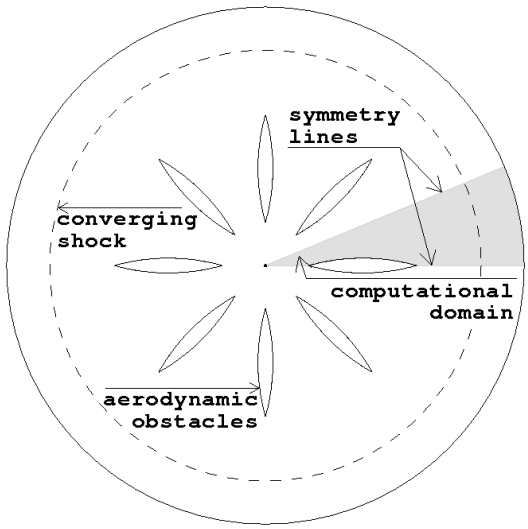

Figure 1.2: Physical domain of propagation and reshaping of the converging shock wave for the reference configuration. The gray region is the computational domain.

main (the gray area in figure 1.2) which is delimited by two symmetry boundaries: for convenience, the one which crosses the obstacle is termed "lower symmetry line", whereas the opposite is named "upper symmetry line". The angle ξ, defined as the "vertex angle" and delimited by the two symmetry lines and with a vertex in the focus point, spans an angular sector of π/n_{obs}—where n_{obs} is the number of obstacles. In sec. 2.1, where computational domains characterized by vertex angles different from π/n_{obs} are also used, the domain with $\xi = \pi/n_{obs}$ is referred to as the "elementary domain"; in the following chapter, if not specified otherwise, the vertex angle corresponds to the elementary one $\xi = \pi/n_{obs}$.

A non-trivial consideration concerns the actual symmetry of the polygonal shock. Previous theoretical and experimental works [97] demonstrate that the polygonal shock is a stable configuration against surface corrugations, but less with respect to small deviations from symmetry in the obstacle layout. However, it was observed in the same works that even in case of

non-perfectly symmetrical final configuration, the deviation of the reshaped shock shape from the symmetrical one remains small. In this work, on the contrary, the use of a symmetric computational domain implicitly forces the reshaped shock to remain perfectly symmetric, and therefore results concern the symmetrical case only, where no deviation from symmetry takes place.

Geometrical variables are made non dimensional with respect to the reference length $\hat{\ell} = 0.01\,\mathrm{m}$ and, unless differently specified, all the quantities (both geometrical and fluid-dynamical) are to be hereafter intended as non-dimensional. Dimensional quantities, on the contrary, are marked with the symbol $\widehat{\ }$.

The flow Reynolds number Re is evaluated using the obstacle chord as characteristic length and the dynamic viscosity of air at standard temperature. The obtained Reynolds number, for all the simulations, ranges from 10^6 to 10^7. In accordance with the boundary layer theory [98], such a range for Reynolds number allows to neglect the influence of the viscosity but directly in the boundary layer. The latter, due to the—mostly—aerodynamic shape of obstacles, remains confined to a small region near the wall. This allows to simulate a non viscous flow, with the consequent possibility to disengage the results from the space scale and to use dimensionless variables. The applicability of this assumption is confirmed also by the adoption of an Eulerian code by reference authors [97].

In accordance with [97], the obstacle chord is $c = 5$. The reference distance of the leading edge from the focus point is $r_{LE}^{ref} = 7$. The dimensionless obstacle maximum thickness-to-chord ratio is $t/c^{ref} = 0.14$. The Mach number M_S of the impinging shock is equal to 2.7 when the shock wave is about to first interact with the obstacle, namely, at $r = r_{LE}^{ref} + 1$. Note that the shock Mach number M_S and hence the shock strength increase as the shock front converges towards the origin.

1.1.2 Shock-reshaping steps

According to Ref. [97], in the reference configuration the reshaping process is characterized by three main interactions with the obstacle, which are illustrated in figure 1.3.

The first reflection, termed "primary reflection", takes place at the obstacle leading edge (first step, figure 1.3(a)). As it is well known for planar shocks [70]—and as it will be confirmed in chap. 3 also for cylindrical shocks—, for small values of t/c a Mach Reflection occurs at the leading edge, generating a Triple Point where the unperturbed portion of the incident shock, a reflected wave (termed "wave A") and a Mach stem merge. The aforementioned Triple Point, generated at the leading edge, will be in the following termed "leading edge Triple Point " or "first Triple Point". For increasing values of t/c, the leading edge reflection is of Regular type (see [93]); however it is verified that, while the shock is crossing the obstacle, the Regular reflection always terminates into a Mach reflection. Therefore, regardless of the reflection type occurring exactly in correspondence of the obstacle leading edge, the cylindrical shock reshaping is always obtained by means of a number of Mach reflections. Note that the three-shock theory, which predicts the diverse reflection patterns, strictly applies to pseudo-steady shocks, but it is qualitatively in good agreement with results obtained in the investigation of some types of unsteady reflections [79]. The reflections explored in the present work represent an extension of the ones included in [79], accounting for also curved shock fronts. An accurate description of the leading edge reflection types and of the transition from Regular to Mach-type will be provided in chap. 3.

Due to the phenomenon unsteadiness, the three-wave system evolves in time: while the incident shock continues propagating inwards, the Triple Point moves far from the obstacle, and eventually approaches the symmetry line between two obstacles (second step, figure 1.3(b)).

Afterwards, the Mach stem generated by the leading edge reflection impinges against the symmetry line, and undergoes a "secondary reflection" of Mach type, which generates an additional three-shock structure including a new Mach stem and a reflected wave ("wave B", third step, figure 1.3(c)). Af-

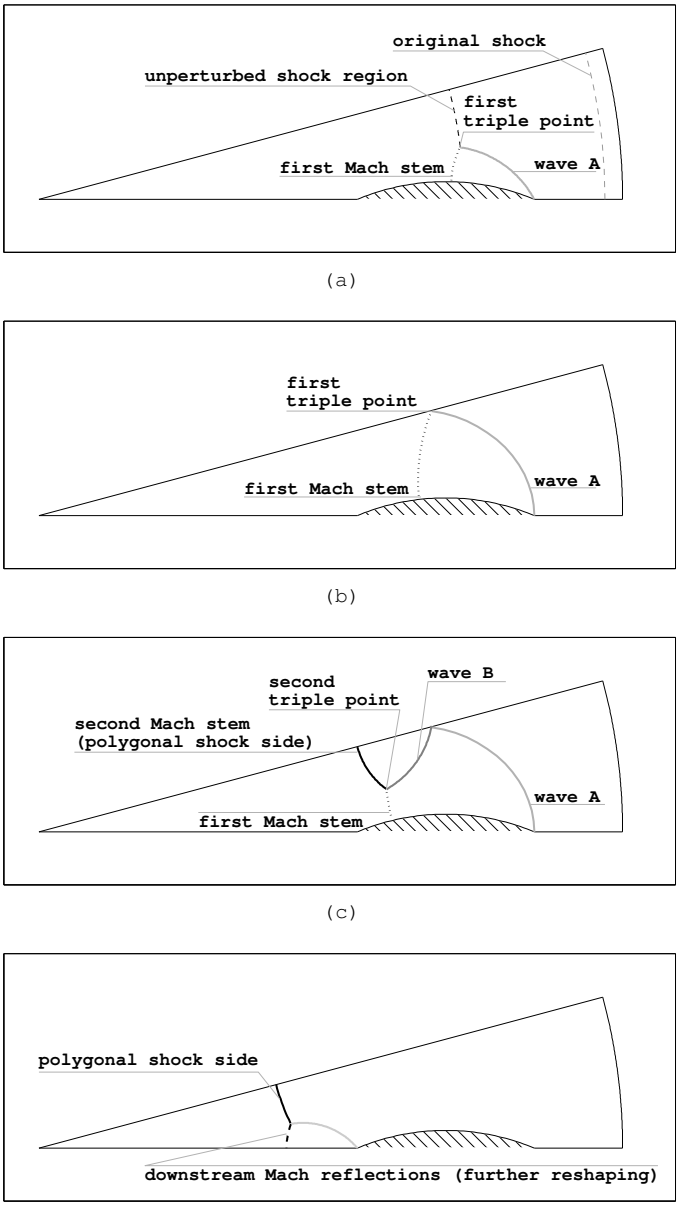

Figure 1.3: Relevant features of the basic reflections causing the shock reshaping in the reference condition.

ter the secondary Triple Point reaches either the obstacle or the bottom symmetry line (figure 1.3(d)), the converging shock consists of a n_{obs}-edges polygonal wave. Each side of the wave originates from the secondary Mach stem.

The reshaping process may now be considered concluded, but the combination of geometrical and fluid-dynamic factors may possibly results in further Mach reflections over the symmetry lines downstream the obstacles or on the obstacle itself.

Both Mach stems exhibit a small outward curvature, similarly to what observed in Direct Mach Reflections (DiMR), but this concavity is negligible in the considered conditions and therefore the reshaped shock is assumed to be a polygonal one.

The four described steps, observed experimentally by [97], are present in all the explored configurations, but it must be kept into account that, in general, the combinations of geometrical factors, operating conditions and thermodynamic model cause as many patterns as configurations are.

1.2 Numerical model

In the following, model adopted to describe the imploding shock waves and their reshaping is briefly outlined. It concerns the governing equations, the thermodynamic models and the set of initial conditions, respectively.

1.2.1 Governing equations

Under the inviscid flow assumption, the flow field is computed by means of classical Euler equations,

$$\begin{cases} \dfrac{\partial \rho}{\partial \tau} + \nabla \bullet \underline{m} = 0, \\ \dfrac{\partial \underline{m}}{\partial \tau} + \nabla \bullet \left(\dfrac{\underline{m} \otimes \underline{m}}{\rho} + P \underline{\underline{I}} \right) = 0, \\ \dfrac{\partial \left(E^t \right)}{\partial \tau} + \nabla \bullet \left(\dfrac{\underline{m}}{\rho} \left(E^t + P \right) \right) = 0, \end{cases} \tag{1.1}$$

where τ, ρ, $\underline{m}$, P and E^t indicate the dimensionless time, density, momentum, pressure and total specific energy per unit volume, respectively. It is to be remembered that the domain reduction described in sec. 1.1 allows to set the problem in a two-dimensional framework. For the definition of non-dimensional quantities, please refer to sec. 1.2.2.

1.2.2 Description of the adopted thermodynamic models

The closure of the system of governing equations requires the description of the thermodynamic behavior of the operating fluid, and therefore an equation of state for the pressure and a model for the constant volume specific heat c_v [100].

It is recalled that all thermodynamic properties of a single-phase mono-component fluid made up of a "large" mole number at thermodynamic equilibrium can be obtained from the so-called "fundamental equation",

$$\hat{e} = \hat{e}\left(\hat{\sigma}, \hat{v}\right), \tag{1.2}$$

where $\hat{e}$, $\hat{\sigma}$ and $\hat{v}$ represent respectively the specific internal energy, entropy and volume per mass unit. Only $\hat{e}$ and $\hat{v}$ can be directly expressed as functions of the conservative variables $\left(\rho, \underline{m}, E^t\right)$,

$$\hat{e} = \frac{E^t}{\rho} - \frac{1}{2}\left(\frac{|\underline{m}|}{\rho}\right)^2, \tag{1.3a}$$

$$\hat{v} = \frac{1}{\rho}. \tag{1.3b}$$

In postulatory thermodynamics [115, 116], the temperature $\hat{T}$ and the pressure $\hat{P}$ are defined as

$$\hat{T} = \left(\frac{\partial \hat{e}}{\partial \hat{\sigma}}\right)_{\hat{v}}, \tag{1.4a}$$

$$\hat{P} = -\left(\frac{\partial \hat{e}}{\partial \hat{v}}\right)_{\hat{\sigma}} \tag{1.4b}$$

and therefore the fundamental relation, eq. (1.2), can be rewritten as

$$\hat{P} = \hat{P}\left(\hat{T}, \hat{v}\right), \tag{1.5}$$

which is called "thermal equation" or "pressure equation of state". Eq. (1.5) implies that the thermodynamic state of the system can be described by means of so-called "intensive variables", i.e. quantities which do not depend on the mass or on the volume of the system. On the contrary, it does not give informations on the functional form of the relation between the pressure and temperature and specific volume. This functional form depends on the selected thermodynamic model, and therefore the choice of the functional expression of eq. (1.5) represents the first condition which defines the thermodynamic model.

The sole eq. (1.5) is not sufficient to close the system of governing equations, as it introduces a new variable with respect to the system (1.1), i.e. the temperature. Therefore, a further equation is added to the system, which can be obtained from eq. (1.2). By expressing entropy as $\hat{\sigma} = \hat{\sigma}\left(\hat{T}, \hat{v}\right)$, the energy can be rewritten as $\hat{e} = \hat{e}\left(\hat{v}, \hat{\sigma}(\hat{T}, \hat{v})\right)$, and its derivative with respect to the first variable is expressed as

$$\left(\frac{\partial \hat{e}\left(\hat{v}, \hat{\sigma}(\hat{T}, \hat{v})\right)}{\partial \hat{v}}\right)_{\hat{T}} = \left(\frac{\partial \hat{e}}{\partial \hat{v}}\right)_{\hat{\sigma}} + \left(\frac{\partial \hat{e}}{\partial \hat{\sigma}}\right)_{\hat{v}} \cdot \left(\frac{\partial \hat{\sigma}}{\partial \hat{v}}\right)_{\hat{T}}. \tag{1.6}$$

The integration of this expression with respect to the specific volume leads to

$$\hat{e}\left(\hat{T}, \hat{v}\right) = \hat{e}^{*} + \Phi\left(\hat{T}\right) + \int_{\hat{v}^{*}}^{\hat{v}} \left[\left(\frac{\partial \hat{e}}{\partial \hat{v}}\right)_{\hat{\sigma}} + \left(\frac{\partial \hat{e}}{\partial \hat{\sigma}}\right)_{\hat{v}} \cdot \left(\frac{\partial \hat{\sigma}}{\partial \hat{v}}\right)_{\hat{T}}\right] \mathrm{d}\hat{v}, \tag{1.7}$$

where the variables marked with * are constant terms. Therefore, the terms $\hat{e}^{*}$ and $\Phi\left(\hat{T}\right)$ play the role of "integration constants" since the integration is performed only with respect to $\hat{v}$.

Recalling eq. (1.4) and thanks to Maxwell's relation stemming from Helmholtz free energy

$$\left(\frac{\partial \hat{\sigma}}{\partial \hat{v}}\right)_{\hat{T}} = \left(\frac{\partial \hat{P}}{\partial \hat{T}}\right)_{\hat{v}}, \tag{1.8}$$

the specific internal energy becomes

$$\hat{e}\left(\hat{T}, \hat{v}\right) = \hat{e}^* + \Phi\left(\hat{T}\right) + \int_{\hat{v}^*}^{\hat{v}} \left[-\hat{P} + \hat{T}\left(\frac{\partial \hat{P}}{\partial \hat{T}}\right)_{\hat{v}}\right] d\hat{v}. \tag{1.9}$$

The constant-volume specific heat, defined as

$$\hat{c}_v = \left(\frac{\partial \hat{e}}{\partial \hat{T}}\right)_{\hat{v}}, \tag{1.10}$$

therefore, becomes

$$\begin{aligned} \hat{c}_v &= \frac{d\Phi\left(\hat{T}\right)}{d\hat{T}} + \int_{\hat{v}^*}^{\hat{v}} \left[-\left(\frac{\partial \hat{P}}{\partial \hat{T}}\right)_{\hat{v}} + \left(\frac{\partial^2 \hat{P}}{\partial \hat{T}^2}\right)_{\hat{v}} + \left(\frac{\partial \hat{P}}{\partial \hat{T}}\right)_{\hat{v}}\right] d\hat{v} \\ &= \frac{d\Phi\left(\hat{T}\right)}{d\hat{T}} + \int_{\hat{v}^*}^{\hat{v}} \left(\frac{\partial^2 \hat{P}}{\partial \hat{T}^2}\right)_{\hat{v}} d\hat{v} \end{aligned} \tag{1.11}$$

As resulting from eq. (1.11), the expression of c_v includes two terms: the first one is a function of the temperature, whereas the second depends on the relation between P, T and v, that is the thermal equation. This implies that the c_v functional expression, which represents the second condition defining the thermodynamic model, cannot be a completely arbitrary function, as it must be consistent with the adopted pressure equation of state.

In the following, for both the pressure equation of state and the constant volume specific heat, two possible independent descriptions are adopted; therefore, four thermodynamic models are explored. The reference one is the so-called "polytropic ideal gas model", which allows to compare numerical results with theoretical predictions and a number of experimental results available in literature. Other thermodynamic models are devised from the polytropic ideal gas one, to provide better descriptions of the flow field when the shock approaches the focus point, and the temperature and specific volume considerably increase [42] and jeopardize the validity of the polytropic ideal gas assumption. The other three descriptions of the thermodynamic behavior of the gas consist in the alternative combinations of the pressure equation of state and c_v model, respectively.

1.2.2.1 Pressure equation of state

This work analyzes air modeled as a simple mixture of diatomic gases, i.e. Nitrogen, $y_{N2} = 79\,\%$ and Oxygen, $y_{O2} = 21\,\%$, with y_h the molar fraction of the h – th component. Argon, water steam, carbon dioxide and impurities—which in atmospheric air make up to 1 % of the overall composition—are neglected, so that the thermodynamics can be treated by means of simple models. In the following, the two adopted equations of state for the pressure are discussed.

1. To describe the thermodynamic properties of air, the so-called "ideal gas" model is first adopted in the simulations. In accordance with the ideal gas model, the equation of state for the (dimensional) pressure is

$$\hat{P} = \hat{\rho} \cdot \hat{R}\hat{T}, \tag{1.12}$$

being $\hat{T}$ the dimensional temperature and $\hat{R}$ the mass-averaged gas constant:

$$\hat{R} = \frac{\hat{\mathcal{R}}}{\hat{M}m}, \tag{1.13}$$

where $\hat{\mathcal{R}}$ is the gas constant. $\hat{M}m$ indicates the molecular mass of the mixture, and it is evaluated from the average of the molecular masses of the n_c single components,

$$\hat{M}m = \sum_{h=1}^{n_c} \left(\hat{M}m_h \cdot y_h \right). \tag{1.14}$$

Eq. (1.12) derives from Boyle's, Charles' and Gay-Lussac's laws [100]. For diatomic gases and their mixtures, the validity of these laws is experimentally verified provided that

$$\frac{\hat{M}m}{\hat{\rho}} > 5 \, \frac{m^3}{kmol}. \tag{1.15}$$

The condition (1.15) is here respected by the initial state, since the minimum $\hat{M}m/\hat{\rho}$ in the flow field prior the reshaping is about 41 in the most critical case, which justifies the adoption of the ideal gas model.

2. Real gas effects arise due to non-linearities of the equation of state: the van der Waals model is adopted for the evaluation of the pressure [117]:

$$\hat{P} = \frac{\hat{R}\hat{T}}{\hat{v} - \hat{b}} - \frac{\hat{a}}{\hat{v}^2}, \tag{1.16}$$

with $\hat{a}$ and $\hat{b}$ the gas-dependent coefficients which account for long-radius attractive forces and short-radius repulsive forces, respectively:

$$\hat{a} = \frac{27}{64}\frac{\hat{R}^2\hat{T}_{cr}^2}{\hat{P}_{cr}}, \tag{1.17a}$$

$$\hat{b} = \frac{1}{8}\frac{\hat{R}\hat{T}_{cr}}{\hat{P}_{cr}}. \tag{1.17b}$$

The van der Waals model has been selected because it consists in the simplest deviation from the ideal gas model, while at the same time it allows to account for real gas effects with only a small computational overload. Moreover, in a van der Waals equation of state, the temperature dependence from the pressure is linear, as in the ideal gas model. Therefore, in accordance with eq. (1.11), the van der Waals equation can be consistent with the same $\hat{c}_v$ models chosen for the ideal gas. Therefore, it is possible to observe the effect of different models for $\hat{c}_v$, both for ideal and for a van der Waals gas, and to disengage them from the pressure equation of state.

The main drawback of van der Waals model, as of other two-parameter equations of state, is in the evaluation of critical variables: the compressibility at the critical point is $Z_{cr} = 0.375$, and therefore the critical specific volume is fixed and can be calculated as:

$$\hat{v}_{cr} = \frac{Z_{cr}\hat{R}\hat{T}_{cr}}{\hat{P}_{cr}}. \tag{1.18}$$

The comparison between results of eq. (1.18) and very accurate measurements [118] on oxygen and nitrogen, reported in table 1.1, show some difference in the values of $\hat{v}_{cr}$ and therefore of Z_{cr}. However, being in the framework of a phenomenological analysis, it was decided to maintain the van der Waals model to investigate real gas effects.

		N_2		O_2	
		theor.	exp.	theor.	exp.
$\widehat{v}_{cr} = \frac{Z_{cr}R\widehat{T}_{cr}}{\widehat{P}_{cr}}$	$\times 10^{-3}\left[\frac{m^3}{kg}\right]$	3.807	<u>3.215</u>	2.864	<u>2.342</u>
$Z_{cr} = \frac{\widehat{P}_{cr}\widehat{v}_{cr}}{R\widehat{T}_{cr}}$		<u>0.375</u>	0.288	<u>0.375</u>	0.291

Table 1.1: Comparison between theoretical and experimental values of $\widehat{v}_{cr}$ and its derived thermodynamic parameters. Marked entries indicate the imposed or measured quantities, whereas plain text indicated a posteriori calculated quantities.

1.2.2.2 Constant-volume specific heat

With reference to eq. (1.11), depending on the pressure equation of state, diverse c_v models can be derived.

The term $\left(\partial^2\widehat{P}/\partial\widehat{T}^2\right)_{\widehat{v}}$ is evaluated for the two diverse equations of states,

$$\left(\frac{\partial^2\widehat{P}}{\partial\widehat{T}^2}\right)_{\widehat{v}} = \left(\frac{\partial^2\left(\widehat{R}\widehat{T}/\widehat{v}\right)}{\partial\widehat{T}^2}\right)_{\widehat{v}} = 0 \qquad (1.19a)$$

(for ideal gas)

$$\left(\frac{\partial^2\widehat{P}}{\partial\widehat{T}^2}\right)_{\widehat{v}} = \left(\frac{\partial^2\left(\widehat{R}\widehat{T}/\widehat{v}-\widehat{b}-\widehat{a}/\widehat{v}^2\right)}{\partial\widehat{T}^2}\right)_{\widehat{v}} = 0 \qquad (1.19b)$$

(for van der Waals gas)

Therefore, for both ideal and van der Waals gas, the integrand function in eq. (1.11) is null. Therefore, the constant-volume specific heat is made up of only the temperature-dependent term,

$$\widehat{c}_v = \frac{d\Phi\left(\widehat{T}\right)}{d\widehat{T}} \qquad (1.20)$$

This implies that the consistency of the thermodynamic model is provided by a c_v depending at most on the temperature.

For the actual selection of the $\widehat{c}_v$ model, the range of temperatures resulting from the simulations must be considered. The lowest temperature attained during all the implosion process corresponds to that of the gas at rest upstream the shock [41]. In the present work, the upstream state temperature is arbitrarily set to the standard ambient temperature 298.15 K. This temperature is much higher than 30 K, which corresponds to the minimum temperature for which the molecules rotational degrees of freedom can be considered fully excited. Therefore, the considered thermodynamic models must consider the contribution of the rotational degrees of freedom.

1. A so-called "polytropic", i.e. constant specific heat, model is first used to model the constant-volume specific heat of air up to the focusing of the shock wave. The constant specific heat is evaluated on the basis of the equipartition principle applied to diatomic gases:

$$\widehat{c}_v = \frac{5}{2}\widehat{R}, \tag{1.21}$$

   and it is made dimensionless with $\widehat{R}$.

   The adoption of a polytropic ideal gas model allows to perform local comparisons between numerical results and theoretical models, mainly dealing with ideal equations of state for gas upstream the shock in dilute conditions. Moreover, the reference experiment [97] is performed in conditions of upstream dilute air, too.

   A further advantage is that, combined with the ideal gas equation of state for the pressure, the polytropic ideal gas, that is the so-called "perfect gas model". In the latter, also the constant-pressure specific volume is a constant. Therefore, the ratio between the constant pressure and volume specific heat is a constant term, named γ.

2. To better account for high temperature effects, both in ideal and van der Waals gases, the constant-volume specific heat is estimated in accordance with the harmonic oscillator model, which accounts for vibrational energy as an additional temperature-dependent term to be added

to internal energy:

$$\begin{aligned}\hat{e}(\hat{T}) &= \hat{e}^* + \hat{c}_v\hat{T} + \hat{R}\sum_{h=1}^{n_c}\left(x_h \cdot \hat{e}_h\right) \\ &= \hat{e}^* + \hat{c}_v\hat{T} + \hat{R}\sum_{h=1}^{n_c}\left(x_h \cdot \sum_{z=1}^{n_{zh}} \frac{\hat{T}_{zh}}{e^{\hat{T}_{zh}/\hat{T}} - 1}\right),\end{aligned} \tag{1.22}$$

where $\hat{e}_h$ is the vibrational contribution to the internal energy of the h – th component, weighted on its mass fraction x_h, and $\hat{T}_{zh}$ is the z – th vibrational temperature of the of the h – th component, too. Since both oxygen and nitrogen are diatomic gases, the relative motion between the two atoms of each molecule has one degree of freedom only. Therefore, only one vibrational mode for each component is activated, resulting in a number of vibrational temperatures $n_{z,O2} = n_{z,N2} = 1$. In the following, therefore, vibrational temperature of nitrogen and oxygen will be indicated as $T_{vib,N2}$ and $T_{vib,O2}$, respectively.

This model describes the departure, in correspondence of each $\hat{T} \approx 0.25 \cdot \hat{T}_{zh}$, of the harmonic $\hat{e}(\hat{T})$ from the corresponding value of energy calculated by means of a polytropic model. This implies that, even though the flow field maximum temperature does not exceed the minimum vibrational temperature, a certain contribution to the internal energy is anyway provided by the molecules vibrational degrees of freedom, and should be taken into account.

Other effects which occur for increasing temperature are neglected. With reference to [70], indeed, dissociational effects in nitrogen have no relevance on the shock reflections for $M_S < 7$ (much larger than the reference case, which has, at the leading edge, $M_S^{LE} = 2.7$) and therefore, a fortiori, also other effects occurring at higher temperature—electronic excitation and ionization—can be ignored.

It must be noted that the polytropic ideal gas is a suitable model for predicting the shock propagation and reshaping, but it suffers from severe limitations in the simulation of the last part of the process, when the focusing takes place, because it cannot keep into account the ionization process and

the chemical reactions. Nevertheless, the maximum temperature values attained at the origin are correlated with the average intensity of the shock evaluated in a region near the focus point but still in the field of validity of the thermo-chemical equilibrium assumption. The good agreement between the two sets of data suggests that, even if the simple thermodynamical model cannot capture the actual values of pressure and temperature at the focus point, it gives an indication on which configurations are more suitable to produce the most effective shock focusing.

In the following, each thermodynamic model will be identified by a code in figures and tables. The first letter indicates the model adopted for the constant volume specific heat, i.e. "P" for polytropic and "H" for harmonic c_v. The second group of letter, separated from the first by a "-", represents the equation of state: "IG" is for ideal gas and "VdW" for van dwe Waals gas. Therefore, e.g. the polytropic ideal gas is P-IG, and the harmonic van der Waals gas is H-VdW.

1.2.2.3 Non-dimensionalization of variables

Geometrical variables, as indicated in section 1.1.1, are made dimensionless with respect to the reference length $\widehat{\ell}$. The treatment of fluid-dynamic variables requires other reference quantities to be set.

The pressure is made dimensionless with respect to the critical pressure and the temperature with respect to $\widehat{T}_{cr}$, being $\widehat{T}_{cr} = 132.65\,K$ and $\widehat{P}_{cr} = 3.872 \times 10^6\,Pa$ the critical temperature an pressure of air. Other fluid-dynamic variables are consequently made non-dimensional as reported in tab. 1.2, where $\widehat{w}$ and $\widehat{\underline{u}}$ indicate respectively the speed of sound and the flow velocity.

It must be noted that results presented do not correspond to the output of numerical simulations. Indeed, in the adopted softwares, the temperature is made dimensionless with $Z_{cr}\widehat{T}_{cr}$, where $Z_{cr} \neq 1$ for non ideal equations of state. Therefore, to compare numerical results obtained by means of different thermodynamic models, all the variables whose non-

ρ	T	e	h	w	$\underline{u}$	τ
$\widehat{\rho}\cdot\frac{\widehat{R}\widehat{T}_{cr}}{\widehat{P}_{cr}}$	$\frac{\widehat{T}}{\widehat{T}_{cr}}$	$\frac{\widehat{e}}{\widehat{R}\widehat{T}_{cr}}$	$\frac{\widehat{h}}{\widehat{R}\widehat{T}_{cr}}$	$\frac{\widehat{w}}{\sqrt{\widehat{R}\widehat{T}_{cr}}}$	$\frac{\widehat{\underline{u}}}{\sqrt{\widehat{R}\widehat{T}_{cr}}}$	$\widehat{\tau}\cdot\frac{\sqrt{\widehat{R}\widehat{T}_{cr}}}{\widehat{\ell}}$

Table 1.2: Definition of dimensionless quantities by means of critical quantities $\widehat{P}_{cr}$ and $\widehat{T}_{cr}$ and of the reference length $\widehat{\ell}$.

dimensionalization involves the critical temperature must be properly rescaled. For results obtained under the ideal gas assumption, of course, the dimensionless quantities defined in tab. 1.2 are coincident with the ones used in the numerical simulations; similarly, the same dimensional pressure corresponds to the same dimensionless one for all the considered thermodynamic models.

1.2.3 Initial conditions setting

In the reference experimental configuration, the cylindrical shock wave in fig. 1.2 results from the reshaping into a cylindrical shape of a planar shock wave, which is generated within a straight-axis shock tube. The reshaping occurs by forcing the shock through a duct at the closed end of the shock tube, as depicted in fig. 1.1. Further details can be found in ref. [97].

In the numerical experiments, the cylindrical converging shock is generated by the imposition of an axisymmetrical pressure step upstream the obstacle, separating an internal ($_i$) from an external region ($_e$); the initial gas speed is everywhere zero in the domain, i.e. $\underline{u}_i^0 = \underline{u}_e^0 = 0$. The initial state problem, therefore, can be considered a "cylindrical shock tube".

The internal state is the same as in [97], and it is maintained constant for all the simulations. In accordance with reference values, it is identified by pressure P_i^0 and density ρ_i^0:

$$P_i^0 = \frac{10^4\,\mathrm{Pa}}{\widehat{P}_{cr}} \qquad T_i^0 = \frac{298.15\,\mathrm{K}}{\widehat{T}_{cr}} \qquad \rho_i^0 = \frac{P_i^0}{T_i^0}. \tag{1.23}$$

The initial external pressure P_e^0 depends on the parameter $\beta_P = P_e^0/P_i^0$ and the corresponding density ρ_e^0 is computed from Hugoniot adiabat for a polytropic ideal gas as

$$\rho_e^0 = \rho_i^0 \cdot \frac{\left(\frac{\gamma+1}{\gamma-1}\right)\beta_P + 1}{\left(\frac{\gamma+1}{\gamma-1}\right) + \beta_P}, \qquad (1.24)$$

where it is recalled that γ is the specific heat ratio for diatomic perfect gases, and for air is assumed to be $\gamma = 1.4$.

The evaluation of ρ_e^0 in eq. (1.23) is performed in accordance to the ideal gas model; however, it has been decided to initialize all the simulations, regardless of the thermodynamic model, with the same numerical values of pressure and density in the internal and in the external states. Necessarily, the external state belongs to the Hugoniot adiabat only in the polytropic ideal gas case. This initialization procedure, which forces the same initial values, allows to explore the effects of the thermodynamics on a problem with exactly the same initial conditions.

Note that due to the curvature of the shock wave, the post-shock state changes in a continuous way as the shock moves towards the origin. The above initial conditions, therefore, result in the formation of a three-wave system including the converging shock wave, a converging contact discontinuity and a diverging rarefaction wave. Indeed, unlike pseudo-steady shock waves, which divide the domain into two regions where the solution is uniform both in space and in time, cylindrical shocks satisfy Rankine-Hugoniot (RH) jump conditions only locally across the shock. Therefore, the initialization of the solution of a flow field induced by a planar shock is a simple task, and it can be directly performed thanks to the algebraic, uncoupled Rankine-Hugoniot conditions. On the contrary, to know the solution behind the shock at any time step in the case of a cylindrical implosion, it is mandatory to simulate the onset of the shock wave. This is achieved by simulating the breaking of the numerical "diaphragm" of the cylindrical shock tube. At the diaphragm breaking, a three-waves system is generated, consisting in the shock, in a contact discontinuity and a rarefaction wave.

The rarefaction wave moves outwards and the contact discontinuity is slower than the shock; therefore to obtain an

isolated convergent shock wave it suffices to locate the initial pressure step sufficiently far from the obstacles.

It was observed that, for the explored gas and Mach number range, the minimum distance between the pressure step and the center corresponds to at least five times the chord of the obstacles, but may extend up to twenty times, resulting in a dramatic increase of computational times. The adopted solution consists in the adoption of a multi-domain approach, which is very suitable to reduce the overall computational time of the simulation. Details on the method and a discussion of the results will be provided in chapter 2.

Chapter 2

Multi-domain simulation of the shock reshaping process

> Without any underlying symmetry properties, the job of proving interesting results becomes extremely unpleasant. The enjoyment of one's tools is an essential ingredient of successful work.
> — DONALD KNUTH, THE ART OF COMPUTER PROGRAMMING

In this chapter, a novel multi-domain procedure for the simulation of the reshaping process is detailed. The method is used to overcome the trade-off between the reduction of the large calculation times and the quality of the results: indeed, to accurately capture the diverse spatial scales of the problem, the computational domain is divided into three subdomains, (see sec. 2.1). In the first region, i.e. the "Far Field Region", the cylindrical shock propagation prior the interactions with the obstacles is simulated under the axisymmetric one-dimensional approximation. A two-dimensional simulation is carried out to compute the flow during the shock-obstacle interaction, as well as the polygonal shock convergence, in the "Obstacle Region"; the initial conditions for the simulations in the Obstacle Region are obtained by interpolating the solution from the Far Field Region. Eventually, the numerical simulations of the shock focusing are preformed on a domain describing the small region surrounding the focus point, namely the "Focus Region". The solution on the Focus Region is initialized with the solution computed on the Ob-

stacle Region. The two interpolations—between the Far Field and the Obstacle Region and between the Obstacle and the Focus Region—are performed on small overlapping regions between the pairs of sub-domains.

The termination of the simulation on one sub-domain and the following interpolation of the solution onto the following one requires the knowledge of the shock position R_S in time. For this purpose, a novel method for the detection of the shock position is developed: it consists of an extension of Payne's method to more irregular shock waves, i.e. unsteady, two-dimensional and generating complex non-uniform flow distributions. The method, presented in sec. 2.2 is widely used in this work, both for the triggering of the multi-domain technique and for the investigation of the physics of the converging shock reshaping.

The sub-domain switch is triggered by the shock radius resulting from the shock-position-detection algorithm. Moreover, the latter is formulated to detect the shock by analyzing the flow field computed by the numerical solver adopted in each sub-domain. For this reason, these two tools should be described in a coupled way. However, to highlight the specific features of each method, in the following they will be discussed separately.

2.1 Multi-domain method

In the design of the numerical model for simulations, in general, one has to deal with diverse requirements: the accuracy of the solution, the detail level of the model and, possibly, the reduction of the computational burden, etc. Unfortunately, these requirements often counter each other. Indeed, an accurate description of the solution usually implies large computational times; similarly, the approximation of the real phenomenon with a model introduces some inaccuracies. The development of a strategy which allows to speed-up the calculations without compromising the quality of the solution is the goal of this chapter.

In the framework of the simulation of implosions reshaping, this trade-off appears to be very important. Fortunately, thanks to the geometrical consideration discussed in chap. 1, it is not necessary to compute the whole flow field. Indeed, the problem of the reshaping of cylindrical converging shock waves is characterized by a high level of symmetry, both before and during the reshaping. Therefore, it is possible to compute the flow only in the elementary domain (the gray area in fig. 1.2), defined in sec. 1.1 as the circular sector delimited by two symmetry lines, and whose angle in the origin is $\xi = \pi/n_{obs}$. The reduction of the computational domain to the elementary domain offers a relevant improvement in the calculation speed, while the obtained solution is sufficient to describe the global flow field generated by the shock convergence and reshaping thanks to the symmetry of the problem.

In addition to the exploitation of the periodicity along the azimuthal coordinate, a multi-domain approach is adopted to reduce the computational cost of the simulations and circumvent the limitations introduced by the chosen numerical model. These limitations arise from the inclusion of fictitious, additional physical phenomena and from numerical artifacts.

The first ones are phenomena correctly described by the numerical simulations, but whose onset is due only to the model. For example, the simulation the shock generation by means of a circular pressure step upstream the obstacles (described in sec. 1.2.3) can be recast to a particular case of "cylindrical Riemann problem" of gasdynamics [119], which is known to cause the onset of two further waves. The latter, for the adopted set of initial conditions, are a contact discontinuity and a rarefaction wave. These two collateral waves behind the cylindrical shock are consistent with the physical model, but they cannot be observed in experimental investigations, where the (three-dimensional) shock generation is achieved by means of different techniques (as detailed in sec. "The implosion problem" of the Introduction).

The second type of side-effects, i.e. spurious numerical effects, on the contrary, is unphysical and include, for example, numerical oscillations in the proximity of shock waves.

Dealing with physical side-effects is a quite simple task if the approach is not a black box one, that is if the knowledge of the physics of the explored mechanisms allows to pre-

dict at least a qualitative behavior. In the example above, the onset of the collateral waves is expected, and therefore the numerical solution concerning the convergence of the shock wave—which is the only wave under scrutiny—is relevant only in the internal region with respect to the radius of the contact discontinuity [103]. On the contrary, numerical side-effects result in a loss of accuracy of the solution, and depend not only on the physical model, but also on the adopted numerical method. Therefore, to overcome numerical side-effects, the combination between the physical model and the numerical method must be changed.

The shock propagates into still gas with a larger velocity than the speed of sound. Therefore, the presence of downstream obstacles cannot be influential on the shock conditions before the interaction. For this reason, it is possible to define three different regions separated both in space and in time during the reshaping. The domain is therefore divided into three sub-domains, i.e. the regions respectively upstream, in proximity and far downstream the obstacle, as exposed in fig. 2.1.

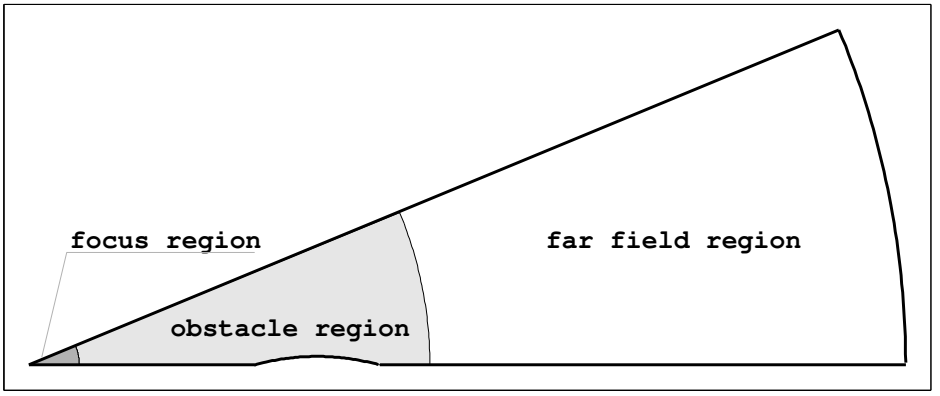

Figure 2.1: Sketch of the partition into three parts of the computational domain: from right to left, the “Far Field Region”, the “Obstacle Region” and the “Focus Region”.

2.1.1 Multi-domain formulation on the three sub-domains

Far upstream the obstacle, the cylindrical shock is originated and propagates inwards. The one-dimensional axisymmetrical simulation of the shock propagation in this zone, namely the "Far Field Region" (FFR), is described in section 2.1.1.1. The two-dimensional shock-obstacle interaction and the resulting reshaping are detailed in section 2.1.1.2, which describes the reflections taking place in the "Obstacle Region" (OR). Finally, the polygonal shock focusing is simulated on a two-dimensional computational domain which includes the origin, that is the "Focus Region" (FR): the latter simulation and the interpolation technique which allows the initialization of this calculation are illustrated in section 2.1.1.3.

2.1.1.1 Far Field Region

If the shock is assumed to be initially stable, an axisymmetric model can be used up to the obstacle leading edges. The shock propagation before the reshaping can be determined by means of one-dimensional axisymmetrical calculation. The initial conditions consist in the aforementioned cylindrical shock-tube problem, i.e. a flow field in quiet where a pressure and density step is imposed.

Such an initial condition results in the formation of the converging shock as well as a contact discontinuity moving towards the focus point and an outwards propagating rarefaction wave. Besides the flow variation across these waves, unlike the planar shock propagation, the radial distribution of the flow quantities is not uniform and time-dependent. For this reason, albeit some analytical solutions are available [54], to account for the effects of non-polytropic, non-ideal thermodynamic models and of the initial transients, the flow field is computed by means of numerical simulations. Although the region upstream the obstacle is not involved in the reshaping process, the initial pressure step must be set far enough from the leading edges to let the necessary time for the shock front to be reshaped and reach the origin before the contact discontinuity interacts with the obstacles.

Preliminary simulations were performed to assess the minimum distance r_d between the numerical diaphragm and the center: it was observed that, in the explored range of pressure and density, for $r_{LE} = r_{LE}^{ref}$ the minimum distance corresponds to five times the chord of the obstacles; however, when r_{LE} is increased, r_d must increase too. In particular, for the highest explored value of r_{LE} (see chap. 4 for details), the value increases up to fifteen to twenty times depending on β_P. This means that the size of the computational domain should be much larger than the simple region where the reshaping and the focusing take place, and that a very large computational time would be required for the full two-dimensional simulation of the formation and propagation of the waves upstream the obstacles which are of no interest for the problem under scrutiny.

This problem is overcome by means of a two-steps method. In the first step, the formation and propagation in the far field of the three-wave system generated by the pressure and density step is simulated by means of a dedicated Finite Volumes solver for the Euler equations in a cylindrical coordinates system, described in [105, 120]. Fig. 2.2 depicts the solution of the shock wave generated by a discontinuity with a pressure ratio $\beta_P = 16$ at a radius $r_d = 25$. The solution is computed over a uniform mesh of 2300 nodes, corresponding to a nodes-spacing $\Delta x = 0.01$. With reference to the figure, this method computes a one-dimensional axisymmetric solution with a very good compromise between the accuracy and the reduction of the computational time with respect to the corresponding two-dimensional solution (the time saving consists indeed of about 95 % with respect to the full two-dimensional simulation).

During the second step, the solution itself is analyzed: when the shock approaches the obstacle leading edge, the one-dimensional simulation terminates and the solution is used to initialize the two-dimensional simulations in the Obstacle Region. However, a portion of the one-dimensional solution is removed, that is the region of the shock tail including the contact discontinuity and the rarefaction wave. This allows to set the diaphragm in correspondence of $r_d = 5c$ even for $r_{LE} > r_{LE}^{ref}$: when the shock approaches the obstacle leading edge radius, the contact discontinuity and the rarefaction wave are far enough from the shock wave to fall out of the Obstacle Region domain

boundaries.

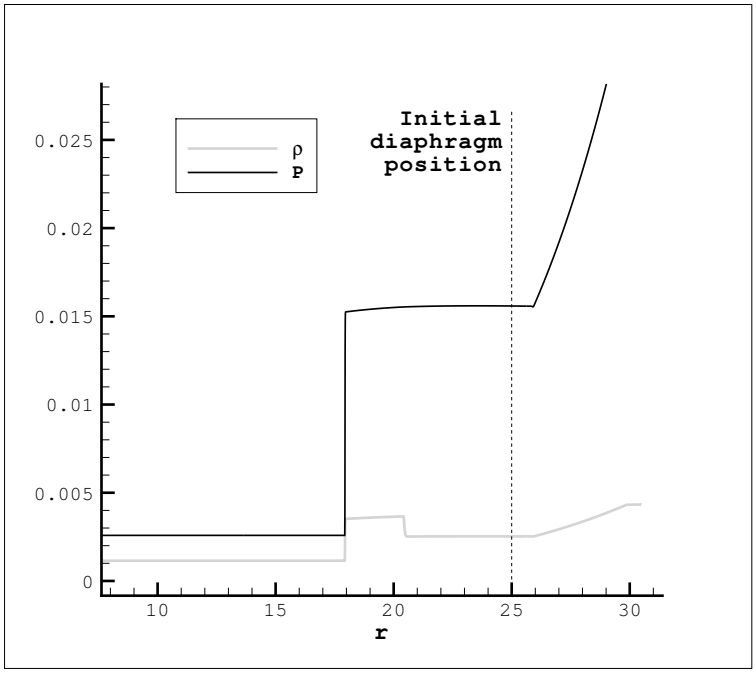

Figure 2.2: Pressure and density one-dimensional radial distribution at a dimensionless time of 2.5×10^{-2} after the breakup of a numerical diaphragm located in $r_d = 25$ with $\beta_P = 16$, corresponding to the reference value. From left to right, the shock wave, the contact discontinuity and the rarefaction are visible. The simulation is performed on a uniform grid, $\Delta x = 0.01$.

The termination of the one-dimensional simulation—and the following switch to the corresponding two-dimensional one—is triggered by the shock passage by a pre-determined radius. Indeed, when the shock is approaching the obstacle leading edge, i.e. in $r_{1D\,end} = r_{LE}^{ref} + \Delta r$, the calculation is stopped and the interpolation of the solution over the Obstacle Region domain is performed. Δr is an arbitrary quantity, usually $\Delta r = 1$, set to prevent the cut-off of a part of the solution in correspondence of the shock. As it is well known, artificial viscosity in shock-capturing numerical methods [104, 121, 122], results in a spreading of the shock wave over multiple nodes,

although it consists in a first-type discontinuity in the Euler equations framework. Therefore, its numerical representation is a continuous ramp of finite amplitude, and the flow field presents slight perturbations also in front of the average shock position R_S. These perturbations are part of the numerical solution, and therefore the one-dimensional simulation must be terminated before $R_S = r_{LE}^{ref}$ as a precautionary measure.

The actual detection of the shock position is performed by means of a novel method, based on Payne's. A detailed description of the method will be provided in sec. 2.2.

2.1.1.2 Obstacle Region

The reshaping process is investigated by means of a fully two-dimensional simulation performed on the sub-domain depicted in fig. 1.2, namely the elementary domain defined in sec. 1.1.1. The multi-domain approach allows to exclude from the computational domain the tail of the distribution of density, momentum and total energy far upstream the obstacles, that include phenomena of no relevance such as the contact discontinuity and the rarefaction wave and, consequently, to reduce the number of nodes and the required computational time. This is accomplished by initializing the two-dimensional calculations with the linear interpolation on the Obstacle Region mesh of the solution of the previous one-dimensional axisymmetrical simulation. Boundary conditions of the external boundary are of non-reflecting type.

In order to capture the complete time-dependent reshaping process, it is necessary to include in the Obstacle Region not only the portion strictly surrounding the obstacle, but also a significant zone downstream. The Obstacle Region, therefore is defined as $[r_{min}, r_{max}] \times [0, \xi]$, being r_{min} the internal boundary radius and $r_{max} > r_{LE}^{ref} + \Delta r$, to include a small overlapping area with the Far Field Region, necessary to the interpolation.

Figure 2.3 illustrates the correspondence of the density

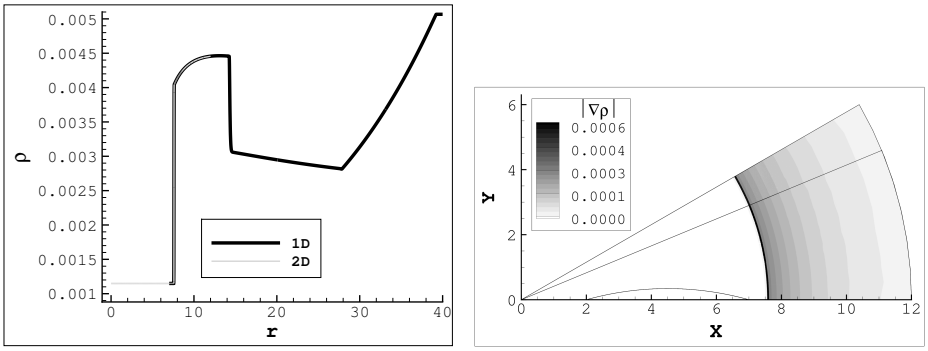

(a) (b)

Figure 2.3: Results of the simulations of the propagation of a shock generated by an initial discontinuity located at $r_d = 25$, with a pressure ratio $\beta_P = 16$. The simulation is performed on a uniform grid, $\Delta x = 0.01$, and the solution is for a dimensionless time of 0.05 after the numerical diaphragm breakup. (a) Density profiles in the area of overlapping between the one-dimensional simulation (black) and a radial section of the initialized two-dimensional simulation (gray) at the beginning of the simulation of the Obstacle Region. (b) Numerical Schlieren on the initial condition imposed on the two-dimensional domains (bottom: $n_{obs} = 8$, top: additional part for $n_{obs} = 6$), showing the possibility of using the same one-dimensional solution for the initialization of diverse two-dimensional simulations.

profiles between the one-dimensional solution and a radial section of the two-dimensional case in the overlapping zone. The interpolation between the Far Field Region and the Obstacle Region is a simple task, due to the fact that the source one-dimensional and ordered grid is uniform: the relative position of old and new nodes is immediately calculated by comparing their radial coordinates only.

The advantage offered by this interpolation is two-fold: on one hand the simulation of each single problem is faster with respect to a fully two dimensional simulation; on the other hand, each one-dimensional simulation can be used for the initialization of several two-dimensional simulations, which share the same initial conditions and differ from each other only because of the obstacles geometrical parameters.

Fully two-dimensional numerical simulations are carried out using the FlowMesh code, developed at the Department of Aerospace Science and Technology of Politecnico di Milano [106, 107]. The solver is a standard Finite-Volume unstructured-grid solver; the unsteady Euler equations for compressible inviscid flows are solved by using a high-resolution flux (centered and Roe scheme, van Leer limiter, see [104]) and by using the Backward Euler implicit time integration scheme. The latter is only first-order accurate and was preferred over the e.g. second- and third- order Backward Differentiation Formulas for robustness.

The construction of the mesh for the discretization of the Obstacle Region is performed by the program UMesh2D [123], based on Delaunay triangulation of a set of points recursively inserted by means of the Voronoi segment technique [124]. In the mesh produced, all the elements are triangles with at most one edge on a boundary of the domain.

The switch from the simulation on the Obstacle Region to the Focus Region is triggered by the shock position. The detection of the two-dimensional shock location is performed by means of a novel method, which will be duly described in sec. 2.2.

2.1.1.3 Focus Region

Due to the adopted mesh generator for the discretization of the Obstacle Region [123], the triangular mesh elements have either zero or one edges on a computational domain boundary. For this reason, if $r_{min} = 0$—that is if the Obstacle Region includes the focus point—there must be at least two elements with a vertex in the origin. As discussed in section 1.1, the angle ξ of the elementary domain is $\xi = \pi/n_{obs}$, resulting in triangular elements at the origin associated to a minimum angle of about $\xi/2 = \pi/2n_{obs}$. As such, in cases with several obstacles, the elements in the origin present an excessively large aspect ratio, which can jeopardize the accuracy of the calculation. This has been verified in preliminary numerical simulations especially from twenty four obstacles up. The simulation of the focusing is therefore performed on a dedicated domain, namely the "Focus Region", which includes the a close-up of the zone where all the

edges of the polygonal shock collapse and a small overlapping region with the Obstacle Region.

The angular size of the computational domain related to this third simulation is not of π/n_{obs}, as in the Obstacle Region, but an integer multiple of it, in order to avoid overstretched elements at the origin. If on one hand this results in a computational domain larger than theoretically necessary—the reproduction of the elementary sub-domain decreases the positive effect of the symmetry—on the other hand numerical errors due to the overstretched elements can lead to a significant reduction of the accuracy or even prevent to obtain meaningful results.

Figure 2.4 illustrates the comparison between the vertex element angles without and with a multi-domain approach in a twenty-four-obstacle case. It is observable that even though the vertex cutoff does not affect the grid on a macroscopic scale (see, e.g, fig. 2.4(c)), the difference becomes relevant close to the origin (pictures 2.4(b) and 2.4(d)).

The simulation over this domain is initialized by means of a linear interpolation of the solution coming from the Obstacle Region. The angle in the origin of the Focus Region domain is an integer multiple of π/n_{obs}, usually $\pi/2$. Figure 2.5—illustrating the local improvement in the quality of the mesh in correspondence of the origin in the multi-domain case—and results in the following refer to a domain of the Focus Region spanning 2π for higher clarity.

The solution in the Focus Region is initialized by means of a linear interpolation from the Obstacle Region. This requires the detection of the correspondence between the new grid and the old mesh which, unlike the 1D-2D case, cannot be direct, because of the use of unstructured grids for two dimensional simulations. It is therefore necessary, for each Focus Region node, to determine its parental element in the Obstacle Region mesh.

This problem, namely the “grid tagging”, belongs to the computational geometry branch of topology. For the specific nomenclature, please refer to [125]. The algorithm to deter-

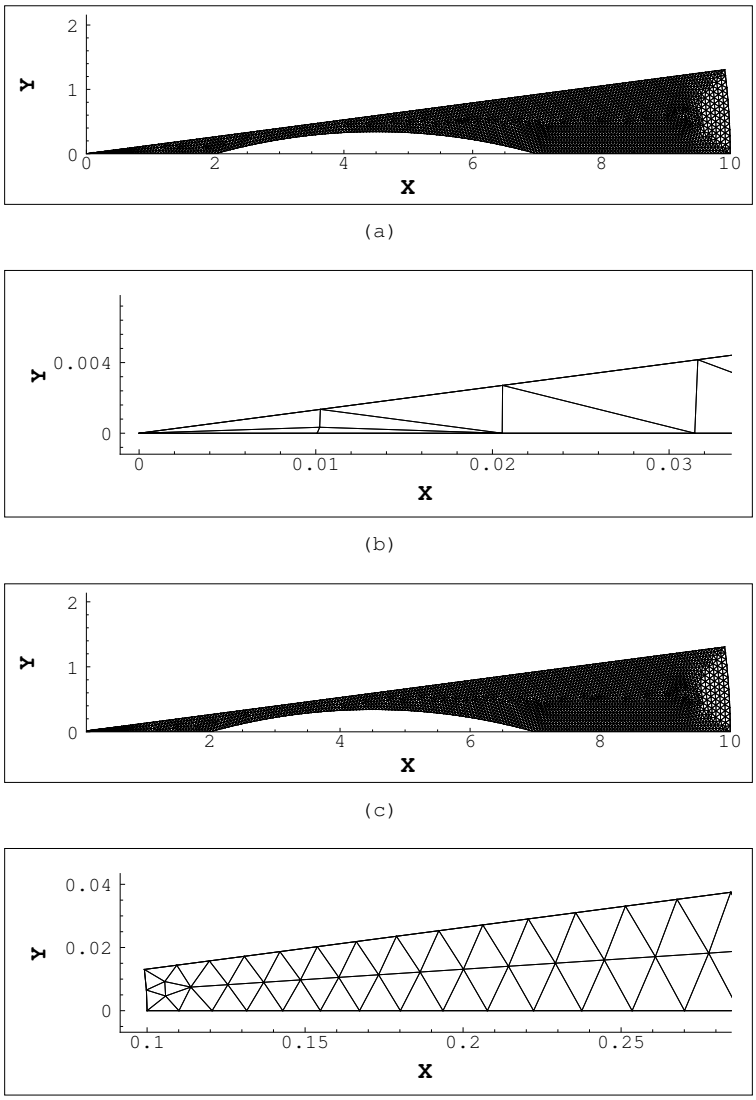

Figure 2.4: Obstacle Region sub-domains, (a) including the focus point and (c) with cut-off before the focus point. Close up in correspondence of the vertex (b) of the stretched elements and (d) of the higher quality mesh. For all, $n_{obs} = 24$ (the grid spacing of figs. (a) and (c) is larger than the one actually adopted for visual clarity).

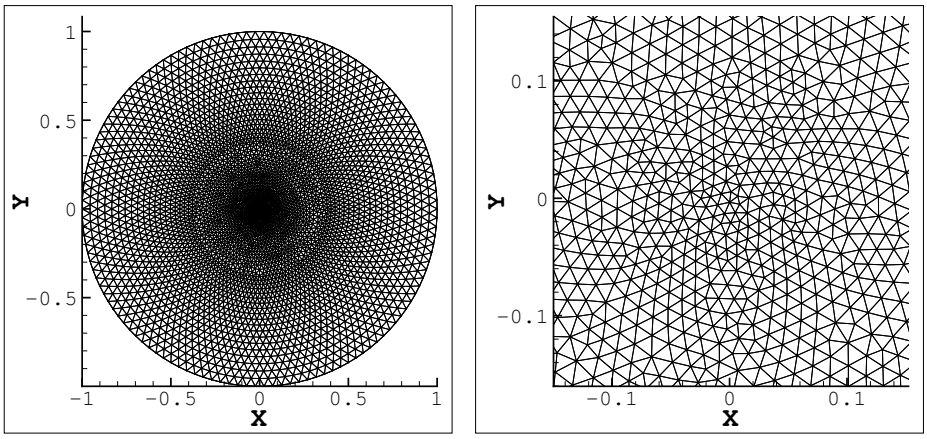

Figure 2.5: Focus Region mesh (2π case) and close-up in correspondence of the focus point.

mine the correspondence detection is taken from former works on grid adaptation [126], based on a-posteriori Collision Detection techniques [127]. Indeed, for unstructured meshes of non-monotone elements [125], the solution is non-trivial, and therefore the algorithm recalls the non-hierarchical image-based two-dimensional virtual ray casting method.

For symplectic mesh elements, the whole algorithm for the correspondence detection and for the solution initialization is described in the following:

1. For each node J of the new grid, it is determined which part of the Focus Region computational domain it belongs to. With reference to fig. 2.6, the intersection between the Obstacle Region and the Focus Region outlines three areas: zone I represents the area the shock has not reached yet at the end of the Obstacle Region simulation, zone II is the overlapping between the two regions—where, therefore, the solution is known—and zone III identifies the part of the domain where the solution is not known, but can be evaluated by virtue of the symmetry of the problem.
   Four quantities are now defined: r_{min} is the radius of the

inner boundary of the Obstacle Region, whereas r_{max} is the radius of the outer boundary of the Focus Region. The elementary domain spans from ψ_{min}, usually 0, to $\psi_{max} = \psi_{min} + \xi$. The case of $r_J > r_{max}$, corresponding to the gray area in fig. 2.6, is not discussed, because the goal of this third part of the simulation is to investigate only the focusing of the shock, and does not need to take into account the flow in the Far Field Region. The attribution of J

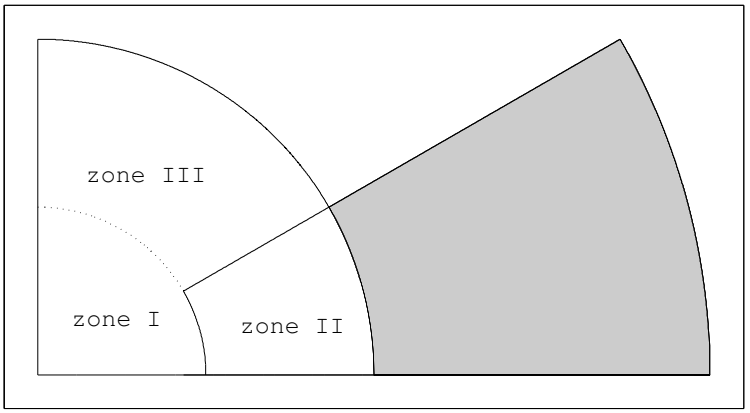

Figure 2.6: Sketch of the subdivision of the Focus Region domain into three areas, requiring different treatments (relative proportions among the three zones exaggerated for clarity purposes).

to the correct zone is accomplished by comparing the polar coordinates of point J (r_J, ψ_J) with the boundary ones $[r_{min}, r_{max}]$ and $[\psi_{min}, \psi_{max}]$ of the Obstacle Region domain.

(a) If $r_J \leq r_{min}$, J belongs to zone I and it is possible to skip the interpolation stage and directly attribute to J the solution corresponding to the initial internal state, being J still unaffected by the shock passage. No other operation is required for the initialization of the solution on J:

$$\begin{cases} \rho_J = \rho_i^0, \\ \underline{m}_J = 0, \\ E_J^t = E_J^{t,0}. \end{cases} \qquad (2.1)$$

(b) Otherwise, if J belongs to zone II, the fictitious coordinates (x'_J, y'_J) which will be used later for the coupling of J with its parental element are assumed to correspond to its actual coordinates (x_J, y_J).

(c) Eventually, for J located in zone III, that is if $r_J \in [r_{min}, r_{max}]$ but $\psi_J \notin [\psi_{min}, \psi_{max}]$, considerations on the symmetry apply: the integer parameter k_J is calculated as

$$k_J = \left\lceil \frac{\psi_J}{\xi} \right\rceil \tag{2.2}$$

and therefore the fictitious polar coordinates (r'_J, ψ'_J), as reported in fig. 2.7, are attributed as follows:

i. For $k_J \,\%\, 2 = 1$, the symmetry to be applied is rotational—i.e. a reflection applied for an even number of times—and therefore

$$(r'_J, \psi'_J) = (r_J, \psi_J - (k_J - 1) \cdot \psi_{max}) . \tag{2.3}$$

ii. For $k_J \,\%\, 2 = 0$, the symmetry is a simple reflection, and therefore

$$(r'_J, \psi'_J) = (r_J, k_J \cdot \psi_{max} - \psi_J) . \tag{2.4}$$

After this transformation, fictitious Cartesian coordinates can be computed:

$$(x'_J, y'_J) = (r'_J \cdot \cos(\psi'_J),\ r'_J \cdot \sin(\psi'_J)) . \tag{2.5}$$

The point whose coordinates correspond to (x'_J, y'_J) will be denoted as J' in the following.

2. For each element m of the Obstacle Region mesh, the three parameters $\delta_{A-BC,\,m}$, $\delta_{B-CA,\,m}$ and $\delta_{C-AB,\,m}$ are evaluated:

$$\delta_{A-BC,\,m} = \frac{\Lambda_{BC,1} \cdot x_A - y_A + \Lambda_{BC,0}}{\sqrt{\Lambda_{BC,1}^2 + 1}}, \tag{2.6a}$$

$$\delta_{B-CA,\,m} = \frac{\Lambda_{CA,1} \cdot x_B - y_B + \Lambda_{CA,0}}{\sqrt{\Lambda_{CA,1}^2 + 1}}, \tag{2.6b}$$

$$\delta_{C-AB,\,m} = \frac{\Lambda_{AB,1} \cdot x_C - y_C + \Lambda_{AB,0}}{\sqrt{\Lambda_{AB,1}^2 + 1}}, \tag{2.6c}$$

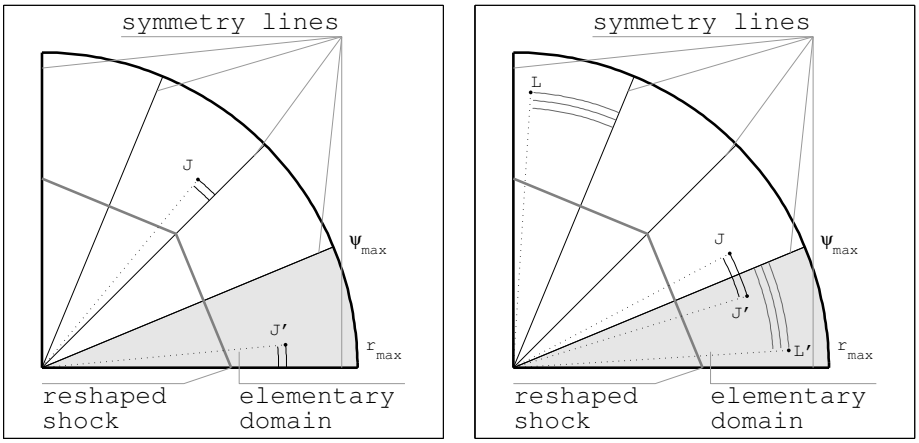

Figure 2.7: (a) Rotational and (b) reflectional symmetries depending on k_J (and k_L) which allow to compute the fictitious coordinates of the Focus Region nodes. The gray areas represent the overlapping region with the Obstacle Region, whereas while areas belong to the Focus Region only.

where $\Lambda_{MN,1}$ and $\Lambda_{MN,1}$ represent respectively the angular coefficient and the ordinate-intercept of the straight line passing by each couple of vertexes M, N of the element m, and (x_Q, y_Q) are the coordinates of point $Q \notin \overline{MN}$, that is the element third vertex, as reported in fig. 2.8.

Consequently, $\delta_{Q-MN,\,m}$ is a "distance with sign" between the vertex Q and the opposite edge $\overline{MN}$ of the triangular mesh.

3. For each node J, the same definition of the parameters $\delta_{J'-MN,\,m}$ is applied to evaluate the "distance with sign" between J' and each edge $\overline{MN}$ belonging to the element m of the

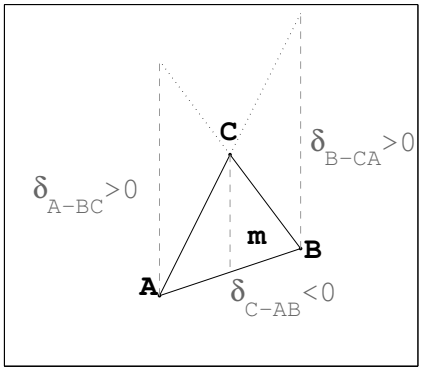

Figure 2.8: Definition of the three parameters $\delta_{A-BC,\,m}$, $\delta_{B-CA,\,m}$ and $\delta_{C-AB,\,m}$ of element m of the Obstacle Region mesh.

Obstacle Region mesh:

$$\delta_{J'-BC,\,m} = \frac{\Lambda_{BC,1}\cdot x'_J - y'_J + \Lambda_{BC,0}}{\sqrt{\Lambda_{BC,1}^2 + 1}}, \tag{2.7a}$$

$$\delta_{J'-CA,\,m} = \frac{\Lambda_{CA,1}\cdot x'_J - y'_J + \Lambda_{CA,0}}{\sqrt{\Lambda_{CA,1}^2 + 1}}, \tag{2.7b}$$

$$\delta_{J'-AB,\,m} = \frac{\Lambda_{AB,1}\cdot x'_J - y'_J + \Lambda_{AB,0}}{\sqrt{\Lambda_{AB,1}^2 + 1}}. \tag{2.7c}$$

With reference to fig. 2.9, depending on the relative position between J and m, the signs of $\delta_{J'-MN,\,m}$ may assume diverse values:

4. For each J, the three products are calculated:

$$\varsigma_{BC,m} = \delta_{A-BC,\,m}\cdot\delta_{J'-BC,\,m}, \tag{2.8a}$$

$$\varsigma_{CA,m} = \delta_{B-CA,\,m}\cdot\delta_{J'-CA,\,m}, \tag{2.8b}$$

$$\varsigma_{AB,m} = \delta_{C-AB,\,m}\cdot\delta_{J'-AB,\,m}. \tag{2.8c}$$

In accordance with the theorem of Jordan's curve applied to the definition of a triangle, it is immediate that, if

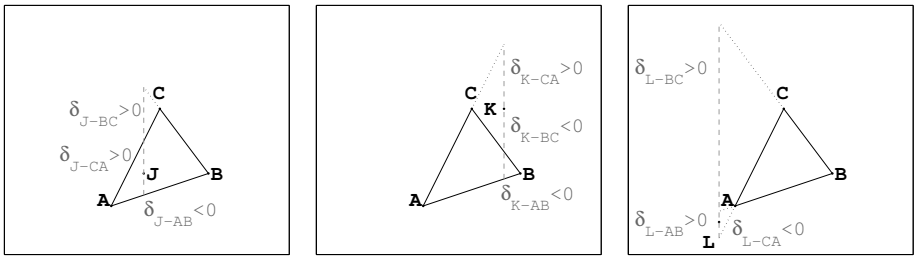

Figure 2.9: Definition of the three parameters $\delta_{J'-BC,\,m}$, $\delta_{J'-CA,\,m}$, $\delta_{J'-AB,\,m}$ of element m of the Obstacle Region mesh: the case reported in (a) is related to the match between the element and the node; vice versa, (b) and (c) illustrate the case of no correspondence.

there exists at least one $\varsigma_{MN,m} < 0$, so J' does not belong to m. Otherwise, the node J' is internal to the element m of the Obstacle Region grid, and therefore it inherits its solution and passes it to J. The criterion is

$$\left(\min\left(\varsigma_{MN,m}\right) \geq 0\right) \Longleftrightarrow \left(J' \in m\right). \tag{2.9}$$

Particular care is to be taken for boundary nodes in special cases, i.e. if the domain boundaries are curved, as illustrated in fig. 2.10. In these cases, the inclusion criterion expressed in (2.9) is relaxed to prevent the lack of detection of the correct parental element. The general criterion becomes

$$\left(\min\left(\varsigma_{MN,m}\right) \geq \epsilon\right) \Longleftrightarrow \left(J' \in m\right), \tag{2.10}$$

where $\epsilon < 0$ is a tolerance. The initial value of ϵ, i.e. ϵ_{start}, is very close to zero, and iteratively amplified until either a correspondence is found or it reaches a limit value ϵ_{limit}. This latter case results in a error message. This occurrence has never manifested in any of the considered test cases, where the adopted meshes were fine enough to bound the error introduced by the spatial discretization within the maximum tolerance.

5. The reconstruction of the solution on the Focus Region domain is accomplished by means of a linear interpolation on

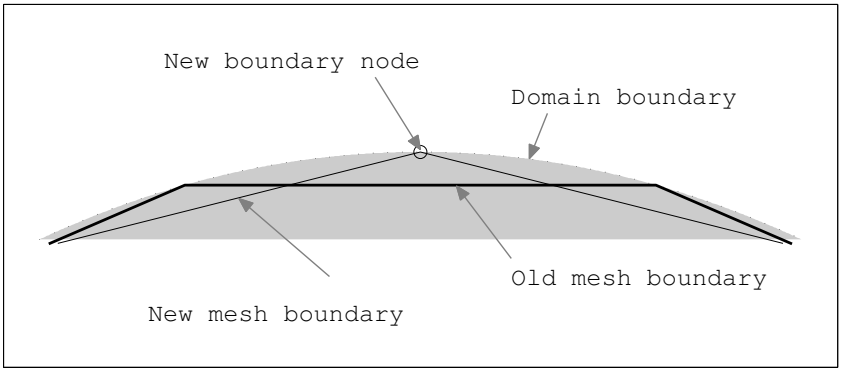

Figure 2.10: Example of missing of a boundary node (○) over the boundary discretization (dimensions exaggerated for clarity).

the coordinated of J' from the vertices of the corresponding element m. Density and total specific energy, being scalar quantities, are directly interpolated. On the contrary, the momentum requires a specific treatment.

Indeed, if the node J belongs to zone III, its coordinate ψ_J is transformed as described at the point (1c); moreover, it is mandatory to keep into account that the same transformation applies also to the vector phase angle $\zeta_{\underline{m}}$, while the modulus $|\underline{m}|$ remains unaffected by the rotation.

To reconstruct the correct tangential component, it is necessary first to interpolate the Cartesian expression of the vector, and then compute the polar components: this provides the direction that the vector would assume if J actually belonged to zone II, like J'. Eventually, it is necessary to recast the real vector phase depending on the value of k_J:

$$\begin{cases} \rho_J = \rho_{J'} \\ E_J^t = E_{J'}^t \\ |\underline{m}_J| = |\underline{m}_{J'}| = \sqrt{\left(m_{x,J'}\right)^2 + \left(m_{y,J'}\right)^2} \\ \zeta_{\underline{m},J} = (-1)^{k_J+1}\zeta_{\underline{m},J'} + \left[k_J - \dfrac{1-(-1)^{k_J}}{2}\right]\psi_{max} \end{cases} \tag{2.11}$$

with $\zeta_{\underline{m},J'} = \arctan\left(m_{y,J'}/m_{x,J'}\right)$.

A sketch of the union of the three computational sub-domains is reported in fig. 2.11

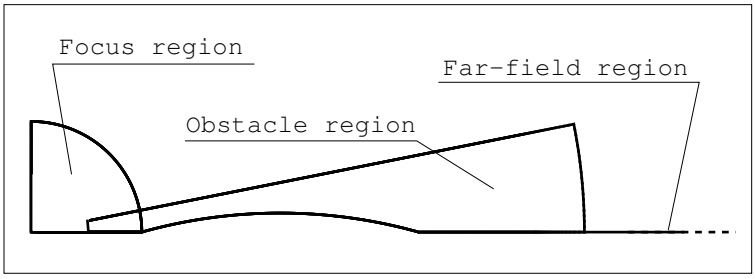

Figure 2.11: Sketch of the union of the three sub-domains adopted in the multi-domain approach: from right to left, the one-dimensional axisymmetrical Far Field Region, the two-dimensional elementary Obstacle Region and the two-dimensional Focus Region. Relative proportions are exaggerated for clarity.

Figure 2.12 illustrates a flowchart which summarizes the symmetry-exploiting interpolation.

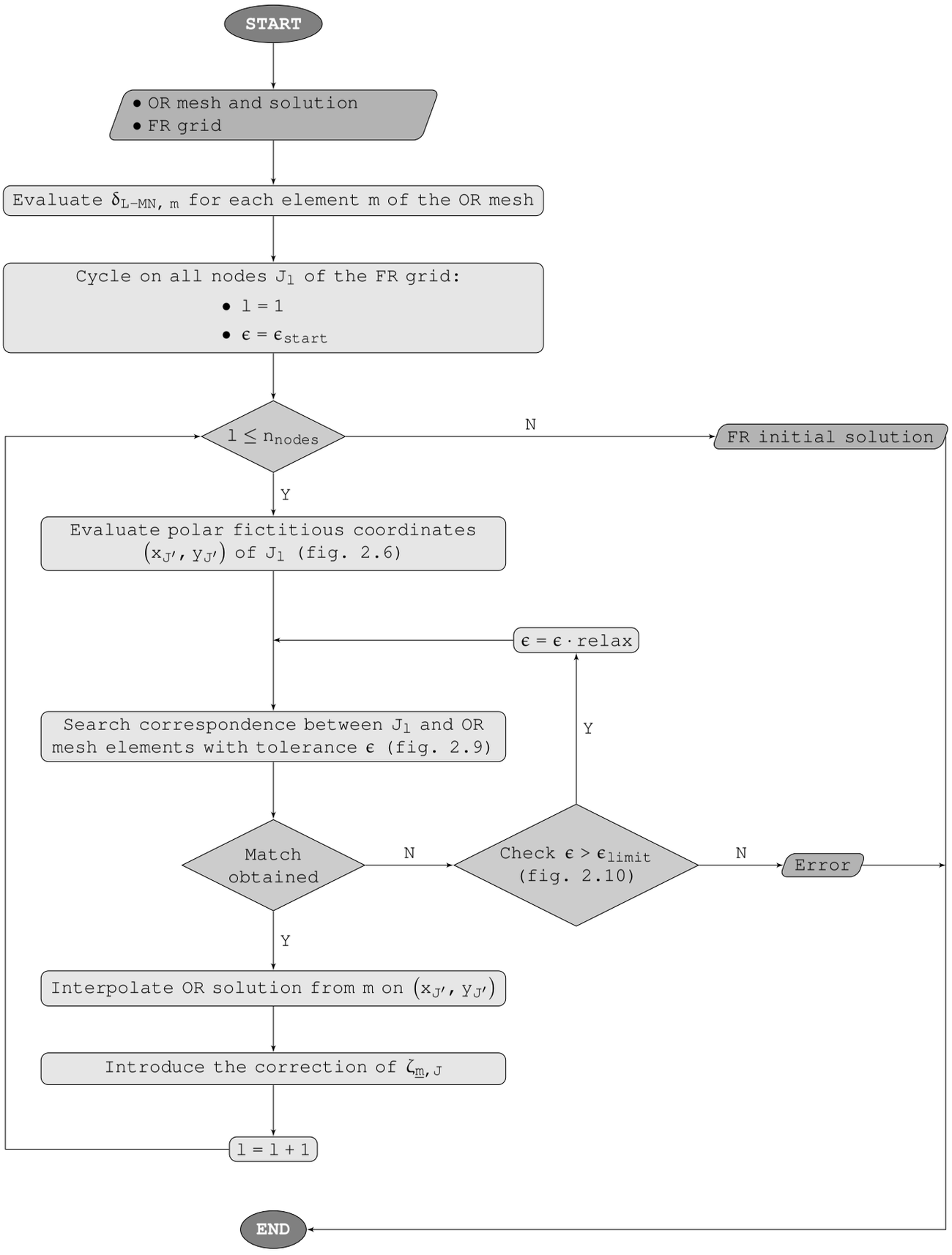

Figure 2.12: Flowchart of the algorithm for the interpolation from the solution obtained in the reshaping region to the grid to be used to explore the focusing.

2.1.2 Verification of the multi-domain procedure

Numerical results obtained with the multi-domain procedure are presented in this section, to assess the effectiveness of the approach. This is achieved by comparing the multi-domain solution with simulations performed on full domains and, when available, analytical solutions. Moreover, the computational times of the simulations and associated to the domain interfaces are reported.

All the reported results are related to the reference condition, i.e shocks generated by the imposition of a density and pressure step with $\beta_P = 16$ located at $r_d = 25$, and obstacles with $t/c = 0.14$ and $r_{LE} = 7$. Diverse values of n_{obs} are observed, i.e. 4, 8, 16 and 24. On the one hand, the number of obstacles n_{obs} is the factor determining the necessity to split the two-dimensional region into the Obstacle and the Focus Region. On the other hand, if the grid spacing is constant, n_{obs} is directly influential onto the number of grid nodes, and therefore to the computational burden of the interpolations.

The adopted thermodynamic model for the present calculations is the polytropic ideal gas one. The computational time used by the domain interface procedure does not depend on the thermodynamic model, in contrast to what happens for the simulations. Preliminary simulations indicate that simulations performed with the polytropic ideal gas model are in general faster than computations regarding the same geometry and initial conditions but with non-ideal or non-polytropic models. Therefore, the relative cost of the tagging and of the interpolation, with respect to the whole simulation, is higher in case of polytropic ideal gas. The polytropic ideal gas model, for this reason, is the most severe one to test the multi-domain procedure.

The reported calculations were performed on a single core of a six-core Xeon 2.66 GHz CPU, with 2 GB RAM.

2.1.2.1 One-dimensional/two-dimensional interface

A first comparison concerns the computational times required by the simulations of the shock formation and reshaping, with and without the multi-domain approach, in the cases of eight and sixteen obstacles. Results are reported in tab. 2.1. In all four cases , the two-dimensional domains are discretized by means of triangular grids with a non-dimensional edge size $\Delta x = 0.01$. The computational times are scaled using the time required for the simulation of the Obstacle Region only (marked cell in Table 2.1) for $n_{obs} = 8$. The time required by the interpolation from the one-dimensional to the two-dimensional domain is not explicitly reported because it is about 4 orders of magnitude smaller, and therefore negligible, regardless of Δx.

Ref. time = 674 min		8 obstacles	16 obstacles
1D + 2D	1D	0.13	
	2D	1	0.58
	total	1.13	0.71
2d only		28.69	15.89

Table 2.1: Computational time relative to the simulation of the shock wave in the Far Field and in the Obstacle Region ($\beta_P = 16$, $r_{LE} = 7$, $t/c = 0.14$).

Fig. 2.13 illustrates the correspondence between the solutions obtained by means of a multi-domain approach and a two-dimensional calculation only. They depict the flow field in the Obstacle Region when the obstacle is about to reach the internal boundary. Reflections are generated by an array of 16 obstacles, which provide a more severe benchmark due to the stronger disturbance introduced with respect to $n_{obs} = 8$.

The differences, both in the pressure profile along the upper symmetry boundary and in the density contours, are negligible, as shown also in fig. 2.3, which illustrates the initialization of the two-dimensional calculation.

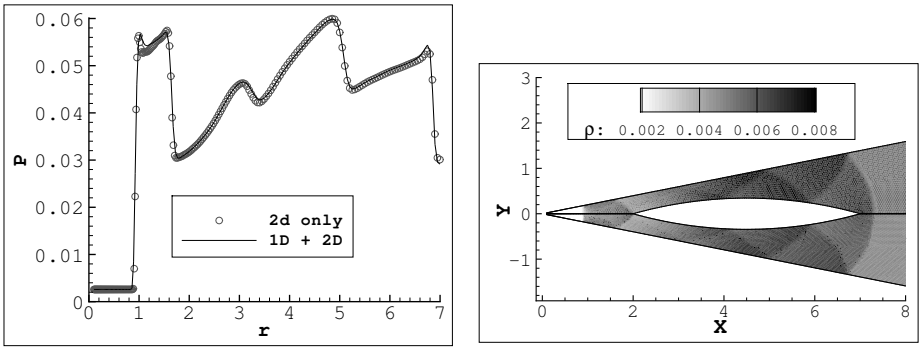

(a) (b)

Figure 2.13: Correspondence between a full two-dimensional (○, top) and a multi-domain simulation (full line, bottom) at the end of the computation in the Obstacle Region: (a) pressure profiles on the upper symmetry boundary and (b) density contours in the domain. Results are reported at a dimensionless time-to-focusing of about 0.2 and concern the reshaping of a cylindrical shock wave with Mach number at the impingement of $M_S = 2.7$ due to the interaction with an array of 16 obstacle of reference geometry. The simulations are performed on meshes with a grid spacing of $\Delta x = 0.01$, consisting of about 50000 nodes for the two-dimensional domain representing the Obstacle Region in the multi-domain simulation.

2.1.2.2 Two-dimensional/two-dimensional interface

Figure 2.14 shows the simulation of the reshaping of a shock by means of four obstacles: in this case the high angle of the domain in correspondence of the focus point ($\pi/2$) allows to obtain regular elements everywhere. Therefore, the results of simulations performed on this domain can be used to explore the goodness-of-fit between the two cases, respectively with and without interpolation.

Table 2.2 provides a comparison among the overall computational times required for the simulation of the reshaping and focusing depending on the size of the elements; in all the cases reported below the final grid consists of a quarter circle, with unitary radius. The times related to the interface (reference grids, $\Delta x = 0.01$) are 36 s and 31 s (respectively for

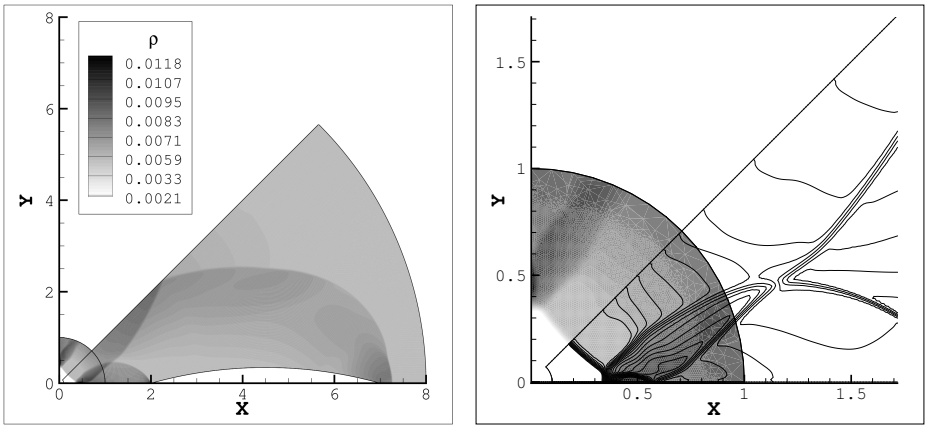

(a) (b)

Figure 2.14: Density profiles for $n_{obs} = 4$: (a) coupling between the result of the simulation of the Obstacle and the Focus Region ($\pi/2$ case) and (b) close-up of the two domains overlapping zone (contours represent the interpolated solutions, isopycnic lines the old one). Results are reported at a dimensionless time-to-focusing of about 0.1 and concern the reshaping of a cylindrical shock wave with Mach number at the impingement of $M_S = 2.7$ due to the interaction with an array of 4 obstacle of reference geometry. The simulations are performed on meshes with a grid spacing of $\Delta x = 0.01$, consisting of about 200000 nodes for the Obstacle Region domain.

eight and sixteen obstacles), whereas for the simulation of the reshaping 24 minutes and 28 minutes.

It can be observed that the additional time introduced by the interpolation is always negligible with respect to the computational time required by the simulation of the shock reshaping.

The vertex angle of the Focus Region is larger than $\xi = \pi/n_{obs}$, and therefore the computational time corresponding to the simulation of the Obstacle Region is larger that the corresponding time of a simulation carried out on an elementary domain. However, the global time for the two-dimensional simulations—reshaping and focusing—must be compared with the time required by the the calculation in the alternative possible configuration, that is the simulation of the reshaping and focusing on a single non-elementary domain, which is always

larger.

Δx	8 obstacles			16 obstacles		
	OR	interpolation	FR	OR	interpolation	FR
0.007	6.96	2.32×10^{-3}	0.07	4.02	1.01×10^{-3}	0.08
0.01	1	8.90×10^{-4}	0.04	0.7	7.67×10^{-4}	0.04
0.05	0.09	1.02×10^{-4}	0.02	0.08	9.72×10^{-5}	0.02
0.1	0.08	8.51×10^{-5}	0.01	0.06	7.16×10^{-5}	0.01

Table 2.2: Computational times relative to the simulation of the reshaping (Obstacle Region domain, OR) and the focusing (Focus Region domain, FR), and to the intermediate interpolation of the solution ($\beta_P = 16$, $r_{LE} = 7$, $t/c = 0.14$).

The result of the interpolation from a sixteen-obstacle-case to a 2π final computational domain is shown in figure 2.15; the Obstacle Region is the slice on the right side with black edges. The external radius of the Focus Region domain is exaggerated to highlight the goodness-of-fit between the original and interpolated solutions. The analogous result is reported in fig. 2.16, concerning an eight obstacles case.

Figs. 2.15 and 2.16 report density (a) and velocity modulus (b): this allows a double check on the accuracy of the grid tagging and of the solution interpolation. Indeed, the density is a quantity directly interpolated, whereas the velocity is evaluated a posteriori as $|\underline{u}| = |\underline{m}|/\rho$, and therefore includes interpolation errors on both ρ and $|\underline{m}|$. Moreover, stream traces reported in fig. 2.15(b) indicate a good application of the correction on the phase of vectorial quantities described at point 5 of sec. 2.1.1.3.

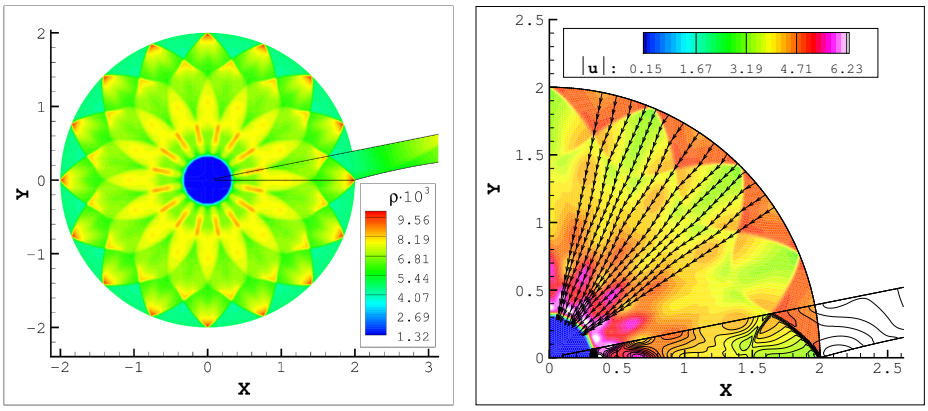

(a) (b)

Figure 2.15: (a) Density field and (b) velocity modulus in the overlapping zone between the Obstacle Region and the Focus Region domains, for n_{obs} = 16 and reference M_s and obstacle geometry. Results are reported at a dimensionless time-to-focusing of about 0.1. The simulations are performed on meshes with a grid spacing of Δx = 0.01, consisting of about 50000 nodes for the Obstacle Region domain.

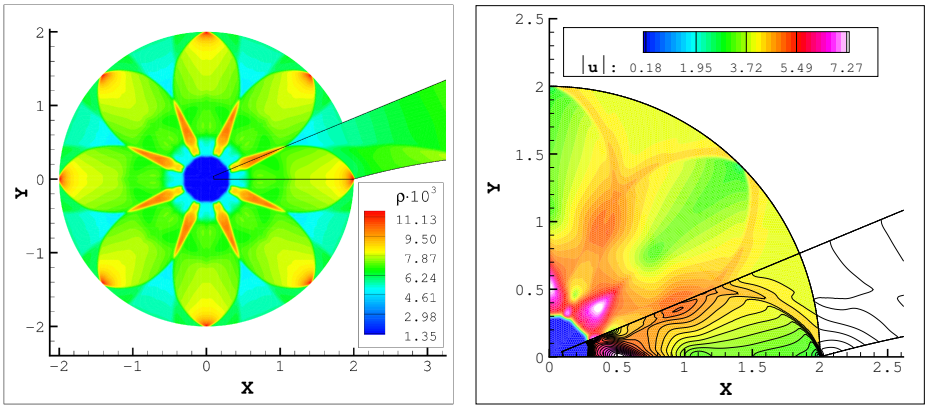

(a) (b)

Figure 2.16: (a) Density field and (b) velocity modulus in the overlapping zone between Obstacle Region and the Focus Region domains, for reference conditions. Time-to-focusing of about 0.1, Δx = 0.01, (about 100000 nodes for the Obstacle Region domain).

It is worth noticing that a side advantage offered by the simulation of the reshaping of converging shocks by means of this procedure is the possibility of observing the influence of small deviations from the symmetry. It is in fact possible to observe that, when symmetry conditions are not imposed any more along physical symmetry lines, i.e. with non-elementary domains, the simulations continue to produce symmetrical polygonal shocks.

2.2 Detection of the shock passage and position

Within this work, to trace the shock location in time is a recurring necessity. This means either to know the shock position at a given time or to detect the occurrence of the shock passage by a given point.

For this reason, a method has been developed and it is described in the following. The procedure is applied within this work for a number of purposes, e.g. the multi-domain method described in 2.1, the verification of the numerically computed shock position against theoretical and experimental results (chap. 4) and the observation of the effects of the thermodynamic model on the propagation of the cylindrical and polygonal shocks performed in chap. 5.

The evaluation of the shock position is performed by means of a novel method, based on Payne's. The original procedure developed by Payne [61] for one-dimensional shock waves assumes the shock position R_s to be in correspondence of the average pressure across the jump:

$$P(R_s) = \frac{P_b + P_f}{2} \tag{2.12}$$

where subscripts $_f$ and $_b$ mean respectively in front and behind the shock. According to [54] and others, for one-dimensional isolated implosions with monotone trend of pressure behind the shock, P_b and P_f are to be taken respectively as the maximum and the minimum pressure values in the close proximity of the shock front. For shock waves converging in a uniform medium, P_f can be simply evaluated as $P_f = P(r = 0)$. For reshaped implosions, to account for the strong non-uniformity of the shock-induced

flow field, some modifications to Payne method are introduced for the first time in this work. The main features the procedure has to deal with are:

- The two-dimensional shock shape: with reference to fig. 2.17, which depicts the numerical simulation of the reflection in reference conditions and $n_{obs} = 4$, the evaluated shock radius may vary a lot along the azimuthal coordinate. In the example figure, the difference between the minimum and maximum radii (evaluated respectively along the obstacle and the upper symmetry boundary) is of about 6 %.

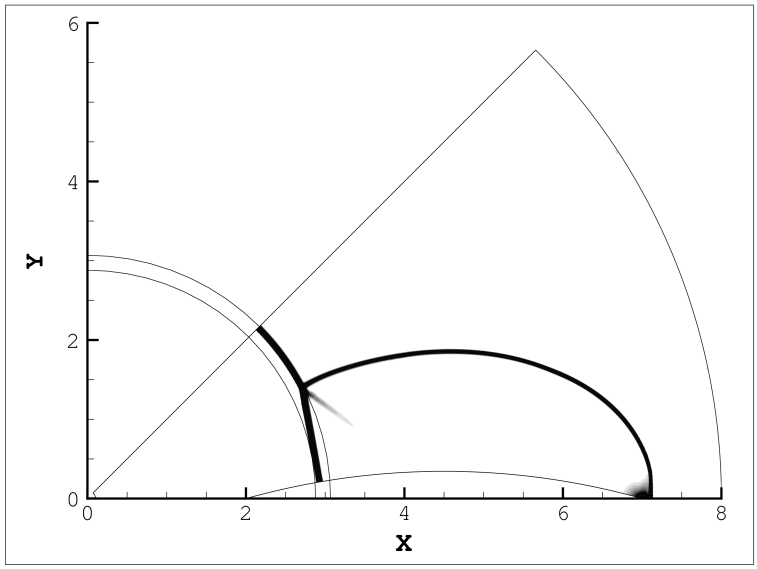

Figure 2.17: Numerical Schlieren of a reflection in reference conditions (with $n_{obs} = 4$) highlighting the high variance of the shock radial position with respect to the azimuthal coordinate.

- The complex shock-induced flow field, which makes the choice of the post-shock state non-unique, both for pressure and for other quantities. The post-shock distribution, indeed, presents several jumps—previous shock reflections, contact discontinuities generated in correspondence of the triple points, etc—so that the maximum

pressure value is not necessarily in correspondence of the shock wave. The solution to this problem is not a simple task: indeed, for pressure distribution similar to the one represented in fig. 2.13(a), P_b corresponds to the minimum-radius local maximum of pressure, which can be easily detected by windowing the pressure distribution. On the contrary, for diverse configuration P_f may continue to grow in a continuous way even behind the shock. This is depicted in fig. 2.18, which illustrates the pressure and the density in correspondence of the upper symmetry boundary ($\beta_P = 27$, $n_{obs} = 16$, $t/c = 0.21$, $r_{LE} = 17.5$): even if the shock is located at $x \approx 4.5$, the first local pressure maximum is in $x \approx 5$.

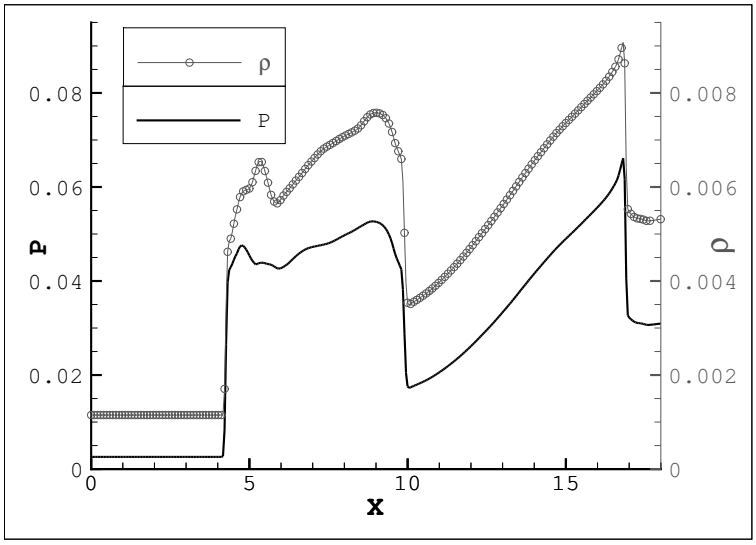

Figure 2.18: Non monotone pressure and density trend behind the shock: the location of the maximum of P is not in correspondence of the shock.

- The necessity of two criteria, one for the detection of the shock passage by a given point (which is necessary in the multi-domain procedure, as described in sec. 2.1) and one to trace the shock position at a given time (as in Payne's method) for the comparison between numerical, theoretical and experimental results.

Each of these tasks is solved with a novel technique described in secs. 2.2.1 and 2.2.2.

2.2.1 Shock position at a given time

At each azimuth, i.e. along each radius, and at each time step τ_k, an array of n_p equally distributed probes measures the pressure value $P_{j,k}$—with j the probes index—and evaluates the following quantities:

$$d_r P_{j,k} = \frac{P_{j,k} - P_{j-1,k}}{r_j - r_{j-1}} \qquad j = 2, n_p \qquad (2.13a)$$

$$d_r^2 P_{j,k} = \frac{P_{j+1,k} - 2P_{j,k} + P_{j-1,k}}{\left(r_j - r_{j-i}\right)^2} \qquad j = 2, n_p - 1 \qquad (2.13b)$$

which represent the first and second order Finite Differences of pressure along the radius (identified by subscript $_r$). The index $_k$ identifies he time level.

With reference to fig. 2.19, at any time step and for a given azimuth, a variety of pressure profiles can be encountered across the shock. The common features among these pressure distributions are that the shock is compressive and that the ramp approximating the shock has increasing slope near the shock base. Figure 2.20 represents a numerical pressure spatial distribution, highlighting the inflection point near the midpoint of the shock-approximating ramp. The figure depicts the pressure along the upper symmetry line of a reshaped shock in reference conditions, governed by the polytropic van der Waals gas model.

For a fixed azimuth, therefore, $R_s(\tau_k)$ is obtained as the minimum radius of the probe j where all the following conditions are satisfied:

$$d_r P_{j,k} > 0 \qquad \text{(compression shock)}, \qquad (2.14a)$$

$$d_r^2 P_{j,k} \leq 0 \qquad \text{(inflection point or peak)}, \qquad (2.14b)$$

$$P_{j,k} - P_i > \epsilon' \qquad \text{(numerical oscillations)}. \qquad (2.14c)$$

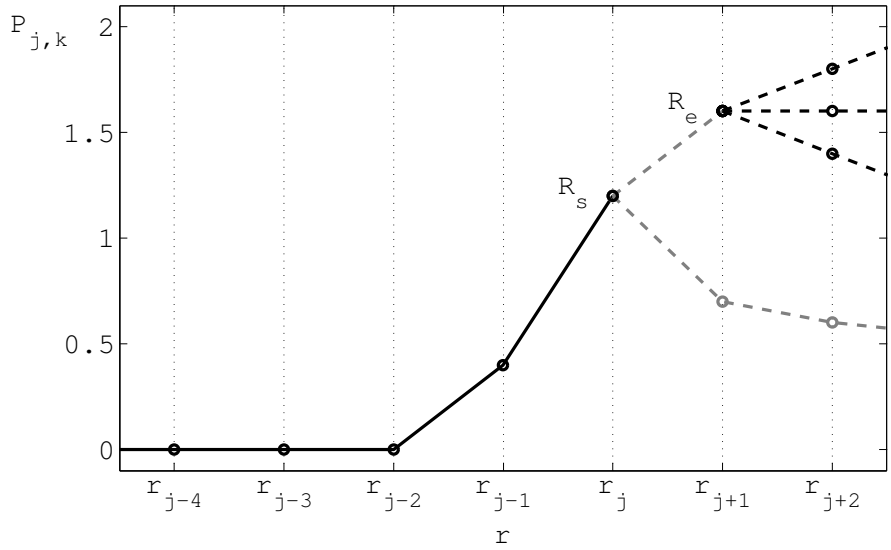

Figure 2.19: Sketch of the possible pressure profile along the radius for given azimuth and time. Solid black lines represent the common part of the pressure distribution, dashed lines the various detectable trends.

It must be noted that first-order derivatives are approximated by means of Backward Finite Differences, whereas Centered Finite Differences are used to discretize second-order derivatives (2.13). This choice is motivated by two possible pressure distributions along the ramp which approximates the numerical shock: it can either present an inflection point (upper gray dashed line in fig. 2.19) or it can have always increasing slope until a peak value (lower gray dashed line). In the first case, the inflection point is assumed to represent the shock position because in most cases it is near the ramp midpoint; in the second case, the shock is assumed to be located in correspondence of the peak. Both these configurations are well described by the conditions (2.14a) and (2.14b).

The third condition is included to identify numerical oscillations, which would cause the detection of false positives in correspondence of tiny high frequency pressure oscillations in the unperturbed region of the domain. Therefore, a further condition is required on the value of $P_{j,k}$, i.e. (2.14c), which

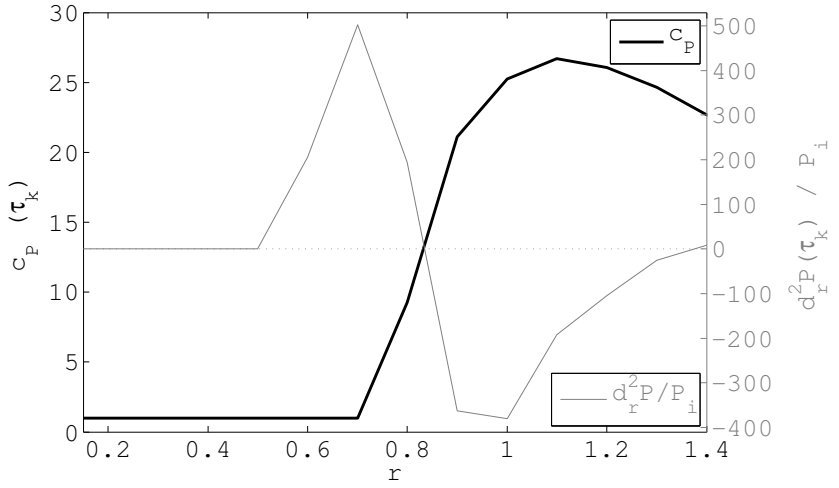

Figure 2.20: Pressure ratio P/P_i versus radius measured by probes along the lower symmetry boundary at time-to-focusing of 0.04 with respect to the total time-to-focusing from the leading edge reflection (reference conditions).

must differentiate from P_i by a threshold $\epsilon' > 0$ which depends on the shock intensity.

The procedure described aboves allows to detect the position of a shock wave along a radius, i.e. either a one-dimensional shock wave or a two-dimensional shock along a fixed azimuthal coordinate. The radius of the front of a two-dimensional shock wave, on the contrary, depends on the azimuthal coordinate, and therefore the method must be exended to the two-dimensional case. According to [97], the extension to two-dimensional shock is straightforward: the shock position at a given time step is obtained by averaging among the diverse shock positions detected at different azimuth.

The main advantage of the above procedure is the strong stability, because it is based on the solution in front of the shock, and therefore does not require the knowledge neither of P_b, nor of the radius where $P = P_b$, which suffer from higher uncertainty. It might be necessary, however, to trace R_e, defined as the radius of the first node immediately behind the

shock.

Note that, in general, $R_e \neq R_s$, since the shock front has a finite thickness due to the numerical viscosity. As for R_s, due to the presence of a non-uniform, non-monotone shock tail, the detection of R_e requires a special treatment. With reference to fig. 2.19, four possible configurations of shock tail are detectable. In the first one, represented by the lower gray line: the concavity of the pressure profile along the shock is positive until $r = R_s$. In this case the conditions immediately behind the shock are in correspondence of the peak, and therefore $R_e \equiv R_s$. On the contrary, if the shock profile exhibits an inflection point (upper gray line in fig. 2.19) the pressure distribution in the shock tail immediately behind the shock can be either monotonically decreasing, or it presents a plateau or eventually continue growing (black dashed lines). In all the above situations, however, a common feature is observed. Indeed, the curvature of the pressure profile assumes the largest value in $r = R_e$ with respect to the surrounding nodes. The shock curvature is here well approximated by its concavity, which allows to rewrite the above requirement into a problem of local maximum of the absolute value of the second derivative in the neighborhood of R_s.

Therefore, R_e is located in correspondence of the probe where it is verified that:

$$R_e \geq R_s, \tag{2.15a}$$

$$d_r^2 P_{j,k} < 0 \quad \text{(negative concavity)}, \tag{2.15b}$$

$$d_r^2 P_{j,k} < \min\left(d_r^2 P_{j+1,k},\ d_r^2 P_{j-1,k}\right) \quad \text{(largest function curvature)}. \tag{2.15c}$$

In the detection of R_e, no oscillations treatment is required.

The knowledge of R_s allows to perform comparisons between the numerical shock position (as in section 2.1.2.2) and to restrict the range where R_e is searched, with the consequent improvement of the accuracy of the result. R_e, on the contrary, is used to determine the shock Mach number (see chap. 4) and the shock propagation along the thermodynamic $P - v$ plane in chap. 5.

2.2.2 Shock passage by a given point

As stated before, the domain switch in the multi-domain approach is triggered by the passage of the shock by a given "alert radius" r_a. In this case, therefore, it is necessary to monitor the state of this point at diverse time steps, and to set a criterion to determine the occurred shock passage.

Two solutions can be adopted. The first one corresponds to the so-called "a posteriori" method, in accordance with the nomenclature adopted in the studies on the Collision Detection [127]. It consists in determining the shock position at each time step by means of the method previously described, and to define the time of occurred passage τ_s such that

$$R_s(\tau_s) = r_a . \tag{2.16}$$

Due to the temporal discretization of the solution, however, in most cases the alert radius is expected to fall between the shock positions detected in two consecutive time steps, i.e. $r_a \in \left[R_s(\tau_{k+1}), R_s(\tau_k)\right]$. At best, τ_s can be defined as a weighted average between the last time step prior to the shock passage and the first time step after the occurrence of the passage:

$$\tau_s = \tau_k \cdot \frac{r_a - R_s\left(\tau_k\right)}{R_s\left(\tau_{k+1}\right) - R_s\left(\tau_k\right)} + \tau_{k+1} \cdot \frac{R_s\left(\tau_{k+1}\right) - r_a}{R_s\left(\tau_{k+1}\right) - R_s\left(\tau_k\right)} . \tag{2.17}$$

In the multi-domain framework, the solution used to initialize the simulation on the following domain is, for caution, the one evaluated at τ_k, hereafter named τ_k'. The error can be minimized by placing a huge number of probes in the domain, and by adopting a very fine time step, but both these solutions cause a relevant growth of computational times.

Moreover, it can be noted that R_s is not the best candidate, because it is located near the midpoint of the ramp approximating the shock. As described in sec. 2.1.1.1, the artificial viscosity causes the spread of the shock over multiple nodes. Even for fine grids, the ramp which approximates the shock wave can have a non-negligible amplitude, and therefore a certain amount of time (significantly more than one time step) elapses between the beginning of the shock passage and the instant detected by eq. (2.17). If the shock detection is used to trigger

the computational domain switch in the multi-domain approach, the simulation must be stopped at most at the beginning of the shock passage, and therefore R_s cannot be adopted to identify the transit of the shock.

The second and most eligible method is based on the monitoring of the temporal evolution of the solution in r_a: even in this case, the pressure shows very different trends depending on the geometry and the operating conditions, but some common features can be still identified. These are the compressive nature of the shock and the presence of an inflection point, as illustrated in fig. 2.21.

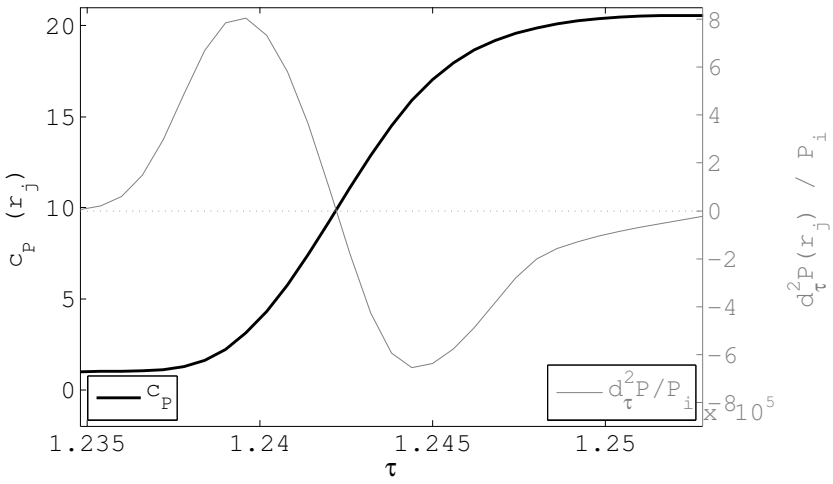

Figure 2.21: Pressure ratio P/P_i versus time measured by a probe located in (0.8, 0.0) (reference conditions).

Similarly to the detection of R_s, the following quantities are defined, which approximate the first and second partial derivatives of the solution with respect to time (identified

by the subscript τ):

$$d_\tau P_{j,k} = \frac{P_{j,k+1} - P_{j,k-1}}{\tau_{k+1} - \tau_{k-1}}, \tag{2.18a}$$

$$d_\tau^2 P_{j,k} = \frac{P_{j,k+1} - 2P_{j,k} + P_{j,k-1}}{\left(\tau_{k+1} - \tau_{k-1}\right)^2}. \tag{2.18b}$$

The shock passage time τ_s' is the minimum time where the following conditions are satisfied:

$$d_\tau P_{j,k} > 0, \tag{2.19a}$$

$$d_\tau^2 P_{j,k} \leq 0, \tag{2.19b}$$

$$P_{j,k} - P_i > \epsilon'', \tag{2.19c}$$

with the sole distinction that also the first order finite difference is centered.

By comparing figs. 2.20 and 2.21, the choice of adopting τ_s' as representative of the time of passage of the shock—corresponding to the inflection in the pressure temporal profile—appears to be more precautionary than the choice of the time for which $R_s \equiv r_a$.

A further cautionary measure is adopted when the detection of τ_s applies to trigger the domain switch in the multi-domain framework: the solution adopted to initialize the following simulation is the one evaluated at

$$\tau_s = \tau_s' - \left|\tau_s' - \tau_k'\right|, \tag{2.20}$$

which individuates the beginning of the pressure ramp in time.

The above procedure describes the detection of a shock passage in the one-dimensional framework.

The extension to the two-dimensional case, due to the practical application of this method, cannot be performed similarly to the analogous two-dimensional extension of the procedure for the radius evaluation at a given time, i.e. by computing the arithmetic mean among the τ_s evaluated at different azimuthal coordinates. As depicted in fig. 2.17, indeed, the spatial variance of the shock radii is very large. While testing the proposed method, it was observed that the temporal

difference between the average and the minimum computed τ_s, was large enough to span a whole ramp of pressure in time.

In the analysis of two-dimensional simulations, therefore, the procedure provides to place an array of probes in $r = r_a$ at diverse azimuthal coordinates and to monitor the solution on each of them. The simulation must be stopped as soon as the first of them detects the passage of the shock in accordance with eq. (2.20), i.e. at $\tau = \min_{\psi} \left(\tau_s \left(\psi \right) \right)$.

2.2.3 Verification of the multi-domain approach combined with the shock detection method

To check the validity of the multi-domain approach together with the novel method for the detection of the shock passage, the twenty-four obstacle case is analyzed. Unlike the eight- and sixteen-obstacle cases described in sec. 2.1.2.2, when $n_{obs} = 24$, the poor quality of the elements in the origin prevents to obtain sufficiently accurate solutions. Therefore, the solution obtained by means of the multi-domain approach cannot be directly compared to the one obtained to a single, elementary domain. For this reason, the reference case used for the comparisons is the simulation performed on a domain which includes two obstacles, in order to reduce the aspect ratio of the elements at the origin (named "doubled domain", see figure 2.22). It must be noted that the straight discontinuity perpendicular to the bisecting line at $r \approx 9$ (fig. 2.22(a)) is the Mach stem of the mutual Mach reflection of waves A generated by the two obstacles. This is evident in fig. 2.22(b), which reports the pressure gradient magnitude: if the density jump were actually the contact discontinuity originated at the numerical diaphragm breakup, the related pressure jump should be almost null, being the one-dimensional axisymmetrical slip line isobaric.

The shock position, evaluated by means of the novel method described in sec. 2.2, is plotted as a function of time in fig. 2.23. The shock position obtained by the multi-domain simulation is compared to those provided respectively by experimental data from the reference case, a calculation performed on

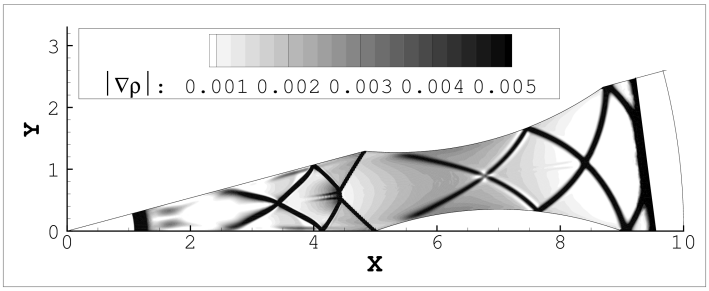

(a)

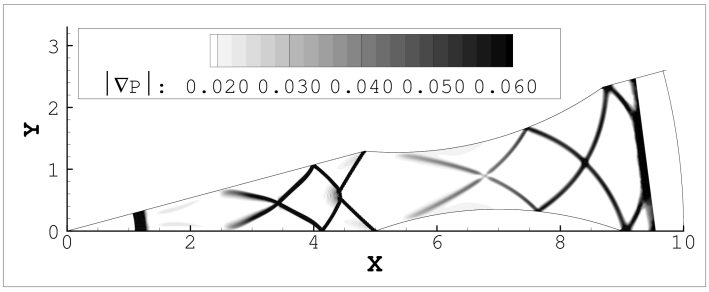

(b)

Figure 2.22: (a) Numerical Schlieren and (b) pressure gradient magnitude of the twenty-four obstacle case on a doubled domain. Results are reported at a dimensionless time-to-focusing of about 0.2 and concern the reshaping of a cylindrical shock wave with Mach number at the impingement of $M_S = 2.7$ due to the interaction with an array of 24 obstacle of reference geometry. The simulations are performed on meshes with a grid spacing of $\Delta x = 0.01$, consisting of about 60000 nodes.

an elementary domain without the multi-domain approach and a self-similar solution in the form described in the Introduction, at sec. "The implosion problem" [39]. In accordance with [88, 97], indeed, the convergence of polygonal shocks with a certain degree of symmetry is ruled by a power law, whose exponent α weakly depends on the thermodynamic model and on the shock shape. Due to the large number of obstacles, α is expected to be very close to the Guderley's cylindrical shock's (0.834), which is indeed adopted for the assessment.

Figure 2.23 depicts a comparison among the analytical solution (full line) and the results of the simulations: it can

be observed that the multi-domain approach and the simulation performed on the doubled domain provide very close solutions (the small deviation from Guderley's solution can be attributed to the non perfect circularity of the shock front). On the contrary, closer to the focusing, the simulation on the poor quality grid deviates significantly from reference values.

Results in fig. 2.23 allow to observe that both the multi-domain approach and the method for the shock position detection provide good results. Indeed, the solution computed on the doubled domain (indicated by the symbol *), initialized by means of the interpolation from the one-dimensional simulation, shows good accordance with Guderley's law. This indicates the accuracy of both the one-dimensional/two-dimensional domain interface and the shock position detection. The two-dimensional/two-dimensional domain interface can be assessed by observing the solution computed by means of the multi-domain approach (symbol O in figure), which presents a satisfactory overlapping with the reference case, i.e. the solution computed on the doubled domain.

For the same case, the pressure ratios at the focus point P_0/P_i are plotted as functions of time in figure 2.24. The accordance among the results of the simulations performed on the doubled domain and those obtained by means of the multi-domain approach is very good, whereas the sharp domain underestimates the peak value of the pressure, and poorly captures its trend along time. It must be observed that the value of ξ of the Focus Region does not affect the quality of the solution, provided it is sufficiently large ($\pi/2$ and $\pi/12$ in figure).

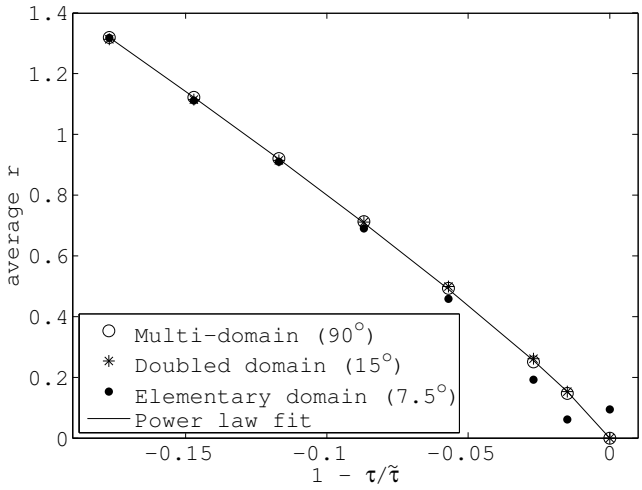

Figure 2.23: Shock position as function of normalized time: comparison between Guderley self-similar solution (full line) and the results of the calculations performed on the doubled domain (∗), with the multi-domain approach (○) and on the elementary domain (•) ($\beta_P = 16$, $t/c = 0.14$, $r_{LE} = 7$, $n_{obs} = 24$).

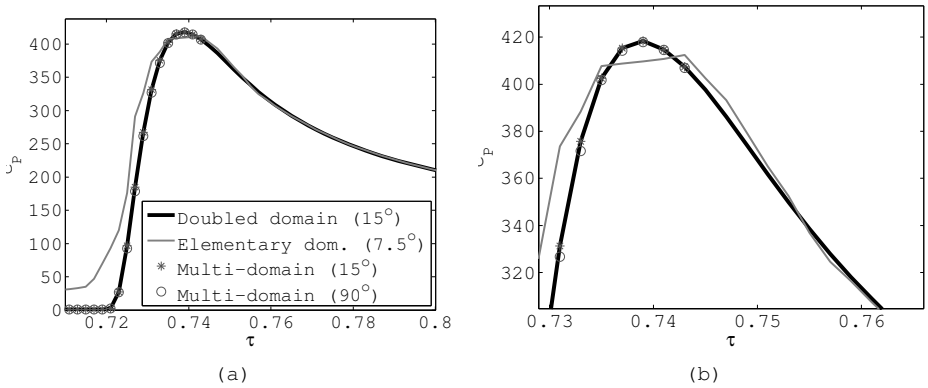

Figure 2.24: (a) P_0/P_i at the focus point versus time calculated with diverse methods: doubled domain (full black line), multi-domain approach with vertex angle of $\pi/2$ (○), multi-domain with vertex angle of $\pi/12$ (∗) and elementary domain (full gray line). (b) Magnification in correspondence of the pressure peak ($\beta_P = 16$, $t/c = 0.14$, $r_{LE} = 7$, $n_{obs} = 24$).

Chapter 3

Cylindrical shock reflection over circular-arc obstacles

> [...] a practice has crept into the highest ranks of the polygons of having their children, when barely a month old, reshaped in the state clinic. The frame is broken in many pieces, which increases the many-sideness. This operation is exceptionally dangerous—only a small percentage of the children survives it. But parental vanity drives the aristocrats to subject nearly all the children to it.
> — DIONYS BURGER, SPHERELAND

This chapter is dedicated to the phenomenological description of the reflection of curved shocks waves over curved walls.

Before approaching the investigation of the reshaping and focusing of implosions, which will be treated in detail in chaps. 4 and 5, a study on the reflection phenomenology is performed. Focusing on the physics of the reflection, indeed, is useful to determine parameters having an explicit influence on the polygonalization and, eventually, to isolate the range of each parameter for which the reshaping can be actually achieved.

In the first section of the chapter, the setup of numerical

experiments is described, in terms of Design of Experiments and assessment of the spatial and temporal discretization.

In the following, the leading edge reflections are presented and classified in accordance with the classical nomenclature [70]. In fact, even if the reflection of cylindrical converging shock waves over convex obstacles is a genuinely unsteady phenomenon, numerical results presented in this chapter evidence the onset of all the reflection types predicted by the theory of pseudo-steady reflections at the obstacle leading edge, although for different combinations of wedge angles and incident shock Mach number. The differences with respect to pseudo-steady results [70]—dealing with both straight shock waves and planar reflecting surfaces—and previous investigations on unsteady reflections [79] are due to the combined effects of the shock curvature—and related unsteadiness—and of the varying wedge angle and radius of curvature. These factors responsible for the unsteadiness of the reflection are partially accounted for in the third section, where a simple model for the description of the dynamics of unsteady regular reflections is proposed. Numerical results are in good accordance with the proposed model.

It is moreover observed that the unsteadiness of the reflection results in different leading edge reflection patterns and on the delay of the Regular-Irregular Reflection transition with respect to pseudo-steady results; these results will be presented in the fourth section. The comparison between numerical results and literature highlights that on one hand all the reflection patterns and bifurcations which are known to occur in pseudo-steady reflections are observed also for unsteady reflections due to curved geometries. On the other hand, the effect of the leading edge wedge angle and of the obstacle curvature on the delay of the Regular-Irregular Reflection transition depart significantly from pseudo-steady results.

Eventually, for Mach reflections, the tracing of the Triple Point trajectory is performed. Results are correlated with both geometrical and fluid-dynamical factors, such as the obstacle maximum thickness-to-chord ratio, the leading edge distance from the focus point of the implosion and the shock Mach

number at the impingement. Diverse polynomial interpolations are performed on the Triple Point coordinates, and a pseudo-linear trend is observed between the obstacle thickness and the polynomial coefficients. A non monotone trend is observed for the trajectory, which suggests the possibility of the onset of Inverse Mach reflection also over convex obstacles. The features of the Triple Point trajectory are discussed in the last section.

3.1 Description of the numerical experiments

3.1.1 Design of Experiments

To investigate the physics of the leading edge reflection of the cylindrical converging shock wave over lenticular obstacles, the considered parameters are the obstacle thickness-to-chord ratio t/c, the obstacle leading edge radius r_{LE} and the Mach number of the shock when it approaches the leading edge M_s^{LE}.

The number of obstacles n_{obs} is not taken into account in this section. Only the interaction between a cylindrical implosion and one curved wall, which is equivalent to the case of $n_{obs} = 1$ is considered here, because of the local character of the phenomenon and of the scale invariance of Euler equations. Indeed, the results can be extended to the leading edge reflection for any n_{obs} value, because when the cylindrical implosion interacts with an array of obstacles, the leading edge reflection pattern is simply replicated $2n_{obs}$ times along the azimuthal coordinate. The reason is that, when observing the polygonal reshaping of a shock, the presence of other obstacles in the array cannot be influential on each single leading edge reflection until the leading edge-generated Triple Point reaches the upper symmetry boundary. Therefore, the leading edge reflection type cannot be influenced by the number of obstacles. The influence of n_{obs} on the reflection pattern is limited to determining when the leading edge-generated Triple Point is reflected over the upper symmetry line.

In accordance with the description of the parameters provided in sec. 1.1.1, the obstacle chord is fixed, i.e. $c = 5$. For this reason, since the obstacle profile is defined as a circular-arc, the obstacle geometry is fully defined by the parameter t/c only.

As it is well known, pseudo-steady reflections are influenced only by the wedge angle θ_w and by the incident shock Mach number, which are both assumed to remain constant. In the reflection of planar shock waves over circular-arc obstacles [79], the sole leading edge wedge angle θ_w^{LE} was proved to be insufficient to define the type of leading edge reflection and its evolution during time. In the same reference, also the obstacle radius of curvature R_O was found to be influential on the evolution of the shock wave reflection. In the present work, θ_w^{LE} and R_O both depend only on the value of t/c as follows:

$$\theta_w^{LE} = \frac{1}{2}\left[\pi - \arctan\left(\frac{1}{t/c} - t/c\right)\right], \tag{3.1a}$$

$$R_O = \frac{c}{4}\left(t/c + \frac{1}{t/c}\right). \tag{3.1b}$$

Numerical simulations were performed in two steps: during the first step, a coarse factorial design of experiments helped to determine the regions where more relevant results could be observed. Based on this preliminary analysis, further levels have been added to the factors, to gain a further insight in the Regular-Irregular Reflection transition boundaries. Data reported here and results in secs. 3.2 and following concern the final, refined, factorial design, summarized in tab. 3.1 and for this reason the factors levels can be non-uniformly distributed.

The value of t/c is varied on thirteen levels, corresponding the latter to the cylindrical case:

$$t/c = 0.07 \cdot (1, 2, 3, 4, 5, 6, 6.5, 7, 8, 9, 11, 13)\ , 1. \tag{3.2}$$

The shock intensity is proportional to the value of M_s evaluated at a brief distance upstream the obstacle leading edge. M_s is linearly varied on ten levels, from 2.2 to 6.7. Each of

Thickness-to-chord ratio	t/c	0.07, 0.14, 0.21, 0.28, 0.35, 0.42, 0.445, 0.49, 0.56, 0.63, 0.77, 0.91, 1
Leading edge coordinate	r_{LE}	7, 14, 17.5
Initial pressure ratio	β_P	11, 16, 27, 36, 48, 60, 75, 90, 110, 130

Table 3.1: Test matrix for the numerical experiments. Considered parameters are the thickness-to-chord ratio t/c, the radial coordinate of the obstacle leading edge r_{LE} and the initial pressure ratio β_P. In all tests, the operating fluid is air in standard conditions, with $\gamma = 1.4$.

these levels of M_S correspond to a value of β_P. The initial pressure ratio values are not uniformly distributed, since they are selected to generate shock waves having equally distributed leading edge shock Mach number M_S^{LE} at r_{LE}^{ref}. The obstacle is located in three positions, corresponding to $r_{LE} = 7$, 14 and 17.5. The effect of the position on the reflection is twofold: by varying r_{LE}, on the one hand the effect of the shock curvature on the reflection can be accounted for, and on the other hand the effects of M_S and β_P are disengaged.

The thermodynamics is described by a polytropic ideal gas model: for van der Waals or non-polytropic gases, experimental and theoretical data are not available, and therefore numerical results cannot be compared with literature ones. Some studies concerning high temperature effects on the reflection pattern are available, but they are not of practical use here, since not only they concern pseudo-steady reflections, but also do not separate the effects of molecular internal vibrations from other high temperature phenomena.

The numerical experiments are distributed on a full factorial design, for an overall number of 390 treatments, as reported in tab. 3.1.

3.1.2 Numerical simulations settings

The computational domain and its spatial discretization are described in this section.

3.1.2.1 Computational domain

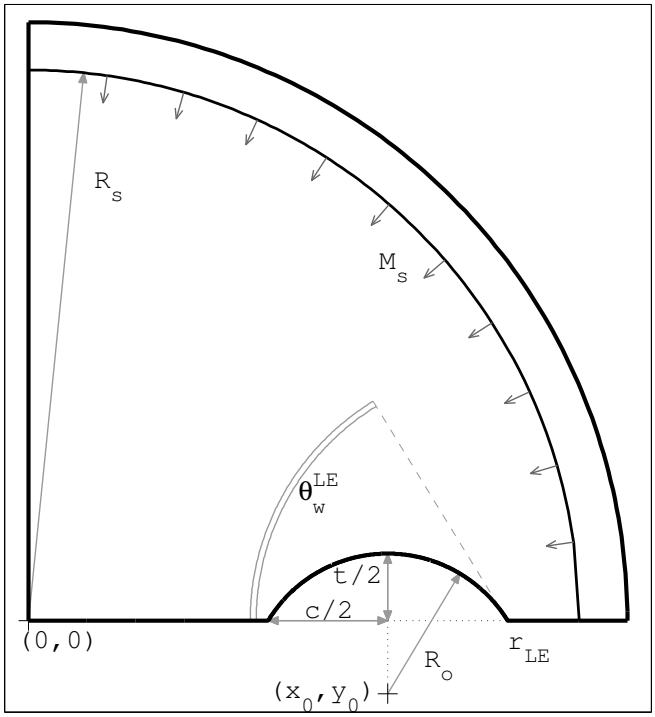

Figure 3.1: Sketch of the computational domain , spanning over an angle $\xi = \pi/2$, and of geometrical features. A half-obstacle is represented, with leading-edge radius r_{LE} and leading-edge wedge angle θ_w^{LE}, depending the thickness-to-chord ratio t/c. The obstacle profile is a circular-arc, with center in (x_0, y_0) and radius R_o. The shock is depicted before the reflection, at a radius $R_s > r_{LE}$, converging towards the focus point $(0, 0)$ with a Mach number M_s.

A sketch of the computational domain is illustrated in fig. 3.1. The vertex angle spans $\pi/2$ because, as already stated, n_{obs}

is not considered, and therefore the elementary domain cannot be defined. However, two considerations can be performed: on one hand, the obstacle has a finite radius of influence in the domain. For this reason, the region of the domain not reached by the Triple Point can be neglected, which allows to cut-off the second and third quadrants. Moreover, the horizontal axis is still a symmetry line, resulting in a final computational domain spanning the first quadrant, with $\xi = \pi/2$.

Due to the constant value of $\xi = \pi/2$, which guarantees high-quality mesh elements in correspondence of the domain vertex, the last step of the multi-domain approach is skipped. Therefore, the reflection and the focusing are computed on a unique computational domain which includes the focus point, and only the coupling between the one-dimensional and the two dimensional domains in performed.

3.1.2.2 Determination of the grid spacing

Simulations are performed on fixed grids of triangular elements with maximum edge length $\Delta x = 0.01$, with local a-priori refinements in correspondence of regions where larger gradients of the solution are expected, e.g. in correspondence of the obstacle leading edge and along the obstacle boundary. Selecting the best discretization in space and time is of fundamental importance, because it must satisfy the trade off between the necessity of reducing the computational times and obtaining a sufficiently accurate solution, since in some cases a very weak difference between diverse reflection patterns is observed. To determine the adopted value of Δx, a number of simulation with decreasing grid spacing has been performed, until flow field qualitative features could be captured with sufficient accuracy, and it did not exhibit a dependence on Δx. Figure 3.2 compares the solutions obtained with a uniform grid with $\Delta x = 0.01$ (3.2(a)) and a mesh with local refinements, up to $\Delta x = 0.001$ (3.2(b)). In both cases the reflection appears to be a Transitional Mach Reflection, but thanks to the grid refinement it is possible to observe the pattern more in detail. Tests with finer grid show that further mesh refinements do not provide significant improvements in the accuracy of the

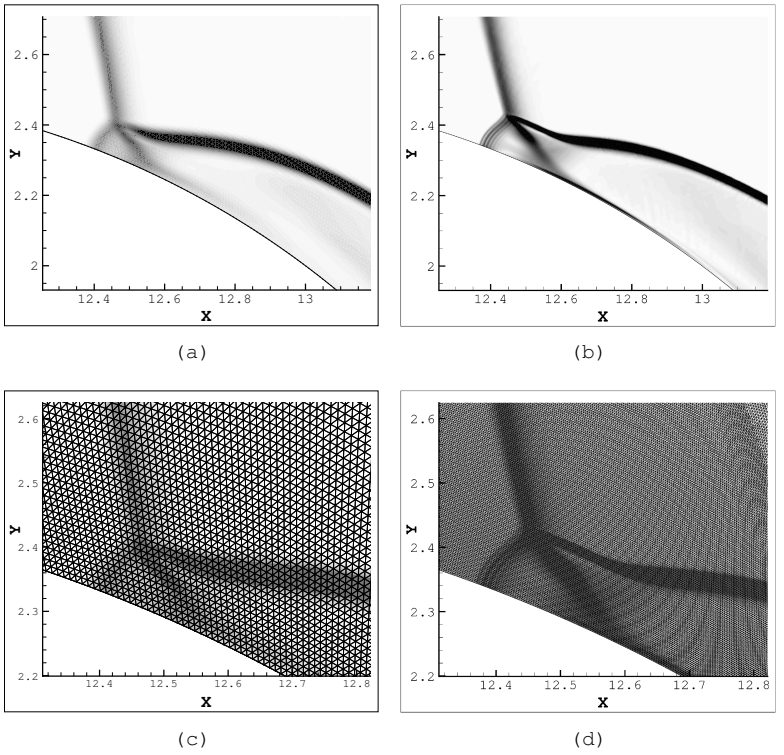

Figure 3.2: Numerical Schlieren in correspondence of a circular obstacle leading edge: (a) uniform grid (b) and local refinement, with the corresponding meshes in figs. (c) for uniform $\Delta x = 0.01$ and (d) for refined Δx up to 0.001 ($\beta_P = 130$, $t/c = 1$, $r_{LE} = 14$).

flow field description.

A similar procedure is adopted to determine the time step $\Delta\tau$, based on successive refinements of the temporal resolution until convergence. For the analysis of leading edge patterns, the adopted time step is $\Delta\tau = 10^{-3}$.

It must be noted that the aforementioned values of Δx and $\Delta\tau$ are valid only for the numerical simulations illustrated in this chapter. During the preliminary analyses phase of this work, it has been verified that the simulation of shock waves reshaping is more demanding in terms of spatial and temporal

resolution, and therefore a different discretization must be adopted for the numerical simulations presented in chaps. 4 and 5.

All the simulation results reported in this chapter are obtained by means of calculations performed on meshes with maximum grid spacing $\Delta x = 0.01$ and local refinements up to $\Delta x = 0.001$.

3.2 Leading edge reflections

3.2.1 Overview on the detected reflection patterns

According to well known theoretical and experimental results, the reflection of a planar shock wave over either planar or curved obstacles can result in a multiple number of patterns [70]. The main subdivision concerns the number of waves belonging to the structure that arises within the reflection.

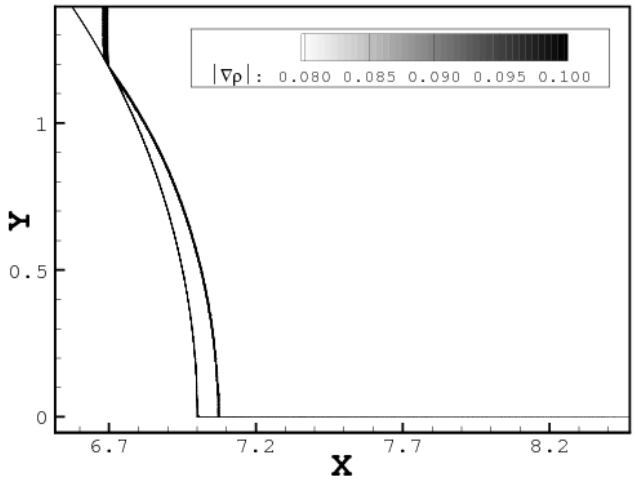

Figure 3.3: Numerical Schlieren image highlighting a Regular Reflection of a cylindrical implosion with $M_s^{LE} = 6.7$ over a cylindrical obstacle ($r_{LE} = 7$, time after the numerical diaphragm breaking $\tau = 0.25$).

When only the original, i.e. the "incident", and a "reflected" shock are detected, the reflection is Regular; these two waves merge into a point belonging to the reflecting surface called Reflection Point. Usually, a Regular Reflection occurs for very large values of θ_w^{LE}, as illustrated in fig. 3.3, which depicts the reflection over a cylindrical obstacle with $\theta_w^{LE} = \pi/2$ (the other parameters which define this treatment are $M_S^{LE} = 6.7$ and $r_{LE} = 7$).

On the contrary, when a further shock, namely a "Mach stem", and a slip line are generated at the reflection, the reflection is named Mach Reflection, and the Reflection Point becomes a Triple Point (indicated as TP). This reflection type is the most interesting for the purposes of this work, both because it allows to achieve the reshaping—the polygonal edges are just made up of the Mach stems—and because it can result in a number of interesting patterns.

Fig. 3.4 reports numerical results of four simulations of the reshaping of cylindrical shocks with $M_S^{LE} = 6.7$ in $r_{LE} = 7$ over variable t/c obstacles. For all the four depicted configurations, the reflection is Mach-type, but the patterns behind the Triple Point differ from each other. It is known, indeed, that Mach Reflections allow diverse sub-categories, depending on the complexity of the resulting structure.

In the framework of pseudo-steady reflections, it is well known that three main Mach Reflection types can be identified [70]. As duly described in [70], a qualitative trend is observed between θ_w^{LE}, M_S^{LE} and the complexity of the shock structure. Indeed, for low values of θ_w^{LE} and M_S^{LE}, the reflected shock consists in a single continuous shock—which can be either attached or not to the obstacle leading edge—and the resulting structure is therefore named "Single Mach Reflection" (SMR), which is the simplest configuration for Mach Reflections. The reference configuration described in chap. 1 and the one reported in fig. 3.4(a) are two examples of Single Mach Reflection observed in the reflection of a cylindrical shock wave over a circular-arc obstacle.

For slightly larger values of θ_w^{LE} or M_S^{LE} a structure with increasing complexity is generated: the reflected shock, indeed, presents a kink, where the two branches of the reflected

shock merge, a straight one—between the Triple Point and the kink—and the classical curved one—between the kink and the obstacle leading edge. This type of reflection is named "Transitional Mach Reflection" (TMR). In the region between the Mach stem and the reflected shock, a compression band is observed along the kink. An example of Transitional Mach Reflection of a cylindrical implosion occurring at the leading edge of a circular-arc obstacle is illustrated in fig. 3.4(c).

Eventually, for even larger values of θ_w^{LE} or M_S^{LE}, the most complex shock structure is observed: the compression band coalesces into a shock wave, and the kink collapses into a single point. The latter, therefore, is termed "secondary Triple Point", whereas the former is identified as "second reflected wave" (not to be confused with the secondary reflection described in chapter 1, which occurs on the upper symmetry boundary). A so-called "Double Mach Reflection" (DMR) generated by the unsteady reflection of a converging shock wave over a circular-arc obstacle is shown in fig. 3.4(d). From pseudo-steady reflection theories, when θ_w^{LE} is further increased from the values characterizing a Double Mach Reflection, regardless of M_S^{LE}, obtaining a Mach Reflection becomes impossible, and the leading edge reflection is Regular.

In addition to these three main Mach Reflection types, a further reflection pattern is known to occur in pseudo-steady reflections, that is the "Pseudo-Transitional Mach reflection". For intermediate combinations of M_S^{LE} and θ_w^{LE} between the Single Mach Reflection and the Transitional Mach Reflection ones, a structure whose reflected wave is characterized by both a null concavity in correspondence of the Triple Point (typical of Transitional Mach Reflections) and a constant-sign concavity (a feature of Single Mach Reflections) can be observed. Since it shares characteristics of both these reflection types, it is termed Pseudo-Transitional Mach Reflection. A Pseudo-Transitional Mach Reflection generated by a cylindrical shock/lenticular obstacle reflection is depicted in fig. 3.4(b).

The observation of diverse Mach Reflection types originated at the leading-edge reflection of cylindrical converging shock waves over circular-arc obstacles has been recorded for the first time in this thesis work.

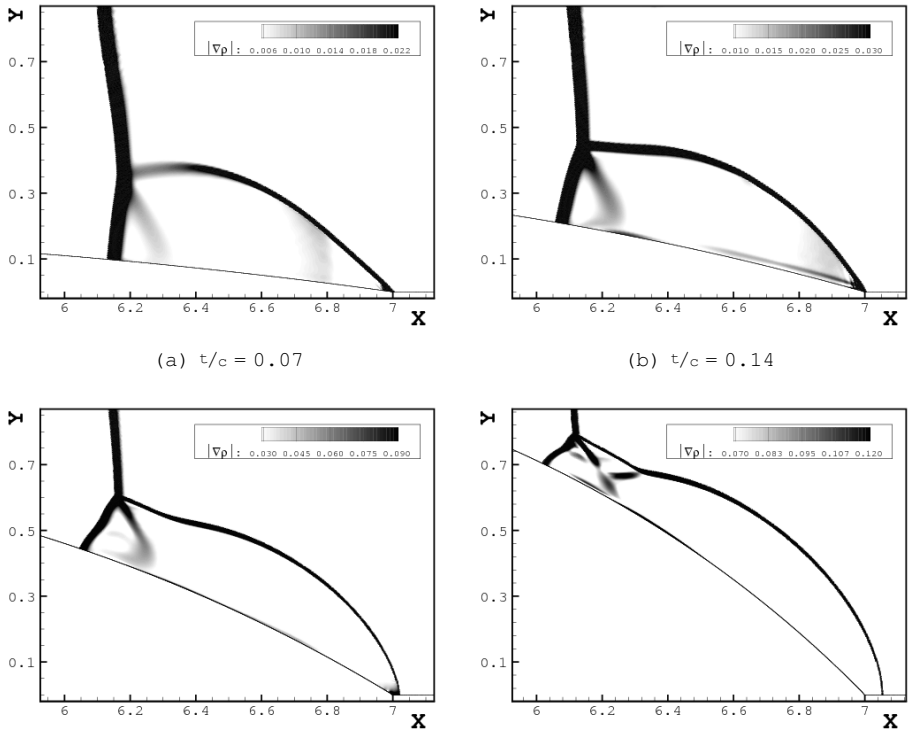

(a) $t/c = 0.07$ (b) $t/c = 0.14$

(c) $t/c = 0.28$ (d) $t/c = 0.42$

Figure 3.4: Numerical Schlieren images highlighting diverse patterns of Mach Reflections of cylindrical implosions over circular-arc obstacles: (a) Single, (b) Pseudo-Transitional, (c) Transitional, and (d) Double Mach Reflection are obtained with $M_S^{LE} = 6.7$ at $r_{LE} = 7$, for different t/c values (time after the numerical diaphragm breaking $\tau = 0.25$).

It is worth noticing that all the reflections reported in figs. 3.3 and 3.4 concern incident shock waves with $M_S^{LE} = 6.7$ in $r_{LE} = 7$, corresponding to $\beta_P = 130$, and differ from each other only because of t/c. This is in accordance with pseudo-steady results: in general, for a given M_S^{LE}, the lower is t/c, the less complex is the resulting shock structure.

Regular and Mach Reflections cover all the known reflection types of shock waves with $M_S^{LE} \geq 2$. However, it is known from the theory of pseudo-steady shocks that for small perturbations (which means both weak shocks and thin wedges), a non-regular shock structure results from the shock reflection which is although incompatible with analytical relations describing a Mach Reflection [71]. More accurate analyses [72] revealed that this waves system, known as "von Neumann Reflection" (vNR), consists in a structure similar to a Mach Reflection, but with a gradual bending of the incident shock and of the Mach stem rather than a single point of intersection, that is indeed the Triple Point. For this reason, all the four-wave reflection patterns, i.e. Mach Reflections and general weak shock reflections, will be indicated as Irregular Reflections.

The numerical experiments in this work are designed to obtain $M_S > 2$ at $r_{LE} = r_{LE}^{ref}$. However, with reference to tab. 3.1, the extension of the factorial design to $r_{LE} > r_{LE}^{ref}$ produces some configurations with an incident shock Mach number lower than 2, generating reflections of unclear type on obstacles with the lowest t/c. Indeed, it is not clear yet whether these reflections are actually Single Mach Reflections or weak reflections, e.g. von Neumann Reflections. Indeed, the detection of the structure of a weak reflection would require an ultrafine grid and the detailed analysis of the complex region of the equivalent Triple Point. For this reason, this work only focuses on strong shocks, and simply records the occurrence of a structure similar to a von Neumann Reflection. The difference between a Single and a possible von Neumann Reflection is depicted in fig. 3.5, regarding the diffraction of a shock with $M_S^{LE} = 1.9$, $r_{LE} = 17.5$ and $t/c = 0.07$.

The realm of weak reflections includes diverse reflection patterns, including von Neumann Reflections. Further works on the realm of weak shock reflections [87, 128] suggest the existence of further reflection patterns for weak shock waves, such

as Guderley Reflections [129] and Vasil'ev Reflection [130].

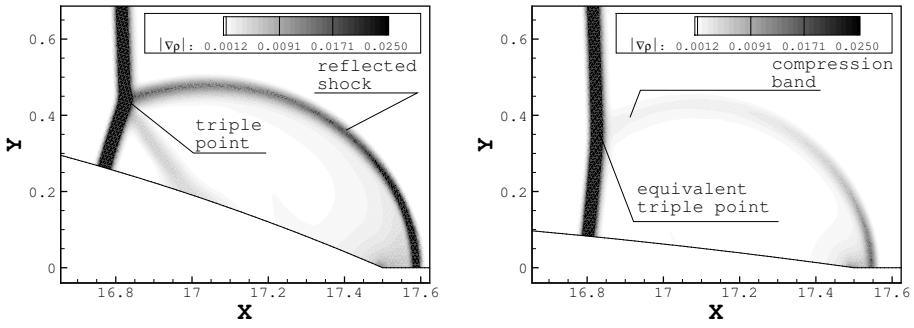

Figure 3.5: Numerical Schlieren of (a) Single Mach Reflection and (b) possible von Neumann Reflection at the leading edge of different thickness obstacles ($\beta_P = 11$, $r_{LE} = 17.5$, resulting in a $M_S^{LE} = 1.9$). The Irregular Reflection suspected to be a von Neumann Reflection is obtained with $t/c = 0.07$, whereas the Single Mach Reflection is generated over an obstacle with $t/c = 0.21$.

For the explored range of parameters, the detected patterns correspond to the five reflection types reported in figs. 3.3 and 3.4, in accordance to analytical predictions for pseudo-steady shocks. If the possibility of considering von Neumann Reflections is included, the sixth investigated pattern is the one depicted in fig. 3.5(b).

A summary of the classification of pseudo-shock reflection patterns, which are the basis for comparison for unsteady results, is provided in the Introduction, in the form of a flowchart. The summary is from the complete survey [70], the reader is addressed to.

3.2.2 Regions of occurrence of diverse reflection types

The classical approach to the determination of shock reflection types, adopted also for steady, pseudo-steady and some unsteady cases (see e.g. [131]), consists in classifying the shock configurations on the M_S^{LE}-θ_w^{LE} plane. Each combi-

nation of leading edge shock Mach number M_S^{LE} and leading edge wedge angle θ_w^{LE} results in one of the aforementioned reflection types, and therefore the plane is partitioned along transition lines, in accordance with classical criteria, [74, 75, 77].

The same classification is applied here for the first time to the diffraction of cylindrical shocks over circular-arc obstacles: the diverse types of leading edge reflections are reported in fig. 3.6, arranged by M_S^{LE} and θ_w^{LE}. The first parameter includes the effects of β_P and r_{LE}. It is known, indeed, that the intensity of the shock wave depends on the initial pressure ratio β_P. Moreover, in accordance with Guderley's theory, the shock speed increases as the shock wave approaches the focus point. Therefore, the Mach number at the leading edge reflection of each shock wave depends on the radius of the obstacle leading edge. The value of θ_w^{LE}, on the contrary, depends directly on t/c, and therefore the influence of all the geometrical factors and operating conditions is accounted for. Data appear to be more concentrated for $M_S^{LE} \in [2, 3]$ because for $\beta_P = 11, 16, 27$ the reflection types are plotted also for $r_{LE} = 14$ and $r_{LE} = 17.5$.

Full lines represent the partition of the plane by the reflection type in accordance with the set of criteria formulated by Ben dor et al. [70], derived from the length scale criterion [74, 73], assumed as reference. The theory was developed under the pseudo-steadiness assumption, and therefore it does not strictly apply to this context, where two unsteadiness sources are present, i.e. the obstacle profile and the shock curvature. However, as suggested in several works [81, 79], to a first approximation, the unsteady shock diffraction can be interpreted also as a sequence of steady states, each described by the above models. In reference literature, this assumption was proved to be valid if applied to the generic description of the "incipient" unsteadinesses. The latter refers to phenomena which depart weakly from the self-similar behavior, e.g. the leading edge reflection of planar shock over curved walls when the shock advancement has covered a small percentage of the obstacle chord [78, 79, 132]. On the contrary, the approximation of unsteady phenomena with a sequence of steady ones suffers from severe limitations in capturing truly unsteady

behaviors, such as the shock dynamics, evolving transitions and hysteresis [78, 79]. Therefore, its use is limited to the comparison of leading edge reflection types.

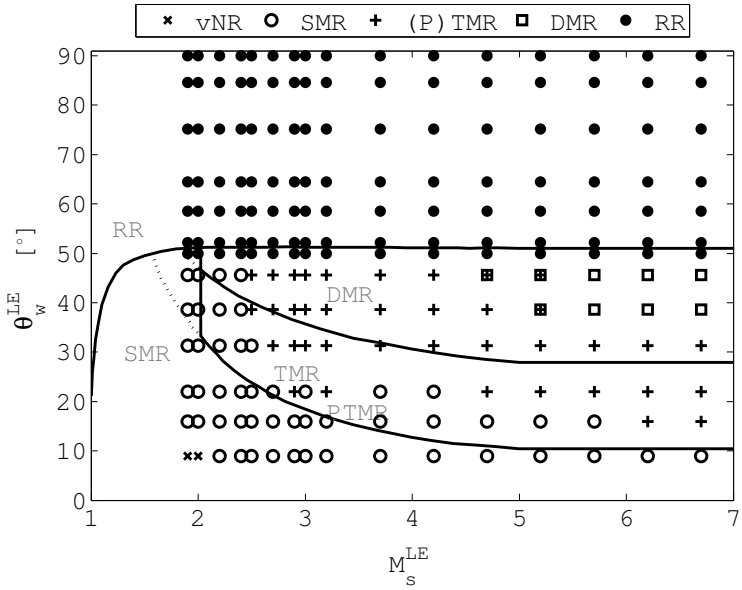

Figure 3.6: Leading edge reflection types, depending on the diverse values of M_s^{LE} and θ_w^{LE}. Solid lines indicate the partition of the θ_w^{LE}-M_s^{LE} plane in the regions of occurrence of the diverse leading-edge reflection patterns in the pseudo-steady case. The diverse symbols represent different reflection types of cylindrical converging shock waves over circular-arc obstacles. Where two different symbols overlap, the distinction between the two types of reflection is not clear.

As already stated in the description of figs. 3.3 and 3.4, all the reflection types predicted by pseudo-steady criteria for the explored range of M_s^{LE} and θ_w^{LE} can be observed also in the investigation of the interaction between curved shocks and obstacles: Regular Reflection and Single, (Pseudo-)Transitional, and Double Mach Reflection.

The comparison between the transition lines of pseudo-steady reflections and numerical results in fig. 3.6 reveals a peculiar fact: for a given θ_w^{LE}, the M_s^{LE} which separates two diverse regions on the plane for unsteady reflections is higher that the corresponding one relative to the pseudo-steady case.

The systematic occurrence of this phenomenon at each transition may suggest that, in each region of the plane, the less complex reflection type in the unsteady case is persistent even in the range of Mach numbers where the more complex type would be expected according to pseudo-steady theories.

The persistence of this simpler configuration, on the contrary, is not observed when analyzing the transitional wedge angles. Indeed, both the qualitative trend of transition lines and quantitative values of the transition wedge angles remain the same as for pseudo-steady shock reflections. In the pseudo-steady case, indeed, the transitional wedge angles as function of M_s^{LE} show a convergence towards an asymptotic value for increasing M_s^{LE}. With reference to fig. 3.6, this convergence can be observed also in the reflection of cylindrical shocks over circular-arc obstacles. The quantitative comparison, therefore, is performed on the asymptotic values, and it shows good accordance.

In particular, the asymptotic value of θ_w^{LE} separating the onset of Regular Reflections and Mach Reflections at the leading edge is termed "critical leading wedge angle" or θ_w^{cr}: for the reflection of cylindrical converging shocks over circular-arc obstacles it is observed that θ_w^{cr} remains close but slightly smaller than the corresponding one for pseudo-steady reflections, which ranges from 49° to 51°, depending on the adopted criterion. This means that the onset of an unsteady Mach Reflection at the leading edge is impossible when $\theta_w^{LE} > 48^\circ$. In this case, when a Regular Reflection occurs at the leading edge, a transition from Regular to Mach Reflection is observed to take place during the shock propagation along the obstacle. This phenomenon is discussed in sec. 3.4.

The classification of the leading edge reflections in Irregular (to include both Mach Reflections and the possible weak shock reflections) and Regular Reflection shows a net subdivision on the basis of the value of t/c—which is correlated to θ_w^{LE} by means of eq. (3.1a).

Therefore, results of numerical simulations over obstacles with $t/c \geq 0.445$ will be used to investigate the evolution of a Regular Reflection (in sec. 3.3) and to assess the delay in the dynamic transition from Regular Reflection to Mach Reflection (in sec. 3.4). This transition, indicated as RR $\longrightarrow$ MR

in the following, was observed in the investigation of the diffraction of straight shock waves over cylindrical obstacles [79, 84]: these works show that the transition occurs when θ_w reaches a "transitional wedge angle" θ_w^{tr}, which is in general lower than θ_w^{cr}.

Eventually, the configurations which generate a Mach Reflection immediately at the leading edge allow the tracing of the Triple Point trajectory in space, and to assess the diverse geometrical and fluid-dynamical parameters on its propagation.

3.3 Regular Reflection of cylindrical shock waves over circular-arc obstacles

In the Regular Reflection of cylindrical shocks over circular-arc obstacles, the combination between the values of the local shock Mach number and the angle of the reflecting wall perceived at any given time (namely, the "perceived wedge angle", or θ_w^P) changes during time with the shock propagation along the obstacle profile, whereas in the pseudo-steady case it is fixed. θ_w^P is defined as the angle whose edges consist of the obstacle tangent line and the shock radius, both originated from the Reflection Point.

3.3.1 Derivation of the $\theta_w^P - M_S$ correlation

An analytical correlation between M_S and θ_w^P is derived in the following, based on Guderley's law and geometrical considerations. The first is used to express the local shock Mach number as a function of R_S, whereas geometrical properties allow to recast angular values to absolute and shock-obstacle relative positions.

The plane θ_w^{LE}-M_S^{LE}, therefore, can be interpreted as the "initial configuration" of Regular Reflections, since at the beginning of the reflection $\theta_w^P \equiv \theta_w^{LE}$ and $M_S \equiv M_S^{LE}$. Starting from the leading edge configuration, each Regular Reflection will propagate on a generic θ_w^P-M_S plane along a trajectory defined by the law derived in the following.

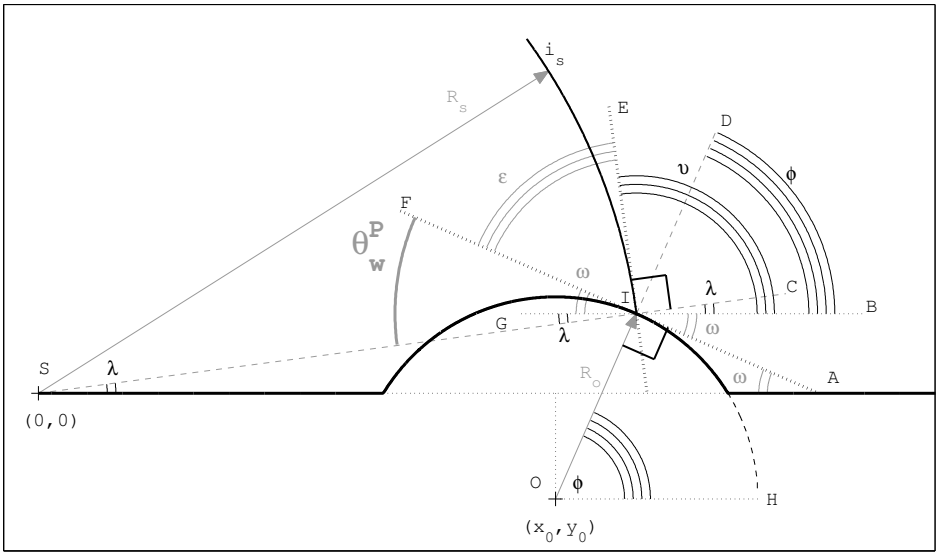

Figure 3.7: Definition of the angles adopted in the model of temporal evolution of the combinations $\theta_w^P - M_s$ in a Regular Reflection (the reflected wave is not reported for clearer visibility). The thick solid line represents the reflecting wall, that is the union of the obstacle and the lower symmetry line. The incident shock wave i_s is represented at a generic radius R_s converging with a Mach number of variable value M_s. The angle θ_w^P is the wedge angle perceived by the shock wave during its convergence, which varies in time to account for the variable slopes of the shock waves and of the obstacle at the Reflection Point. λ is the azimuthal coordinate of the shock wave in a polar coordinate system. The angle ϕ is the polar angle of the obstacle, centered in the center of the obstacle osculating radius.

With reference to fig. 3.7, θ_w^P can be expressed as a function of the two angles ϕ and λ. These angles represent respectively the azimuthal coordinates of the obstacle and of the shock wave in a polar coordinate system. ϕ and λ are reciprocally linked through the generic angles υ and ω. The latter two are the angles formed with the horizontal line by the lines tangent respectively to the shock wave and to the obstacle at the Reflection Point, named I. ε is a dummy angle used only for the derivation of eq. (3.14). The two points S and O indicate the focus point and the center of the obstacle obsculating circle, respectively. Other latin uppercase letters in fig. 3.7 are

dummy variables used to indicate some points used to define the angles. The model purpose is to correlate θ_w^P and M_S in a Regular Reflection, and therefore it is valid for $\phi \in \left[\phi^{LE}, \pi/2\right]$.

To express the angle θ_w^P as a function of the two angles λ and ϕ, some intermediate steps are required.

With reference to the nomenclature introduced in fig. 3.7, the line $\overline{IE}$ is the tangent line to the shock wave at the Reflection Point.$\overline{SI}$ connects the focus point to the Reflection Point, and therefore it is also a radius of the circumference representing the shock wave. For this reason, the two segments $\overline{SI}$ and $\overline{IE}$ are perpendicular. The line $\overline{FI}$ is the tangent line of the obstacle at the reflection point I, and divides the right angle $S\hat{I}E$ into two parts. Therefore, θ_w^P is the complementary of the angle $F\hat{I}E$, termed ε,

$$\overline{SI} \perp \overline{IE} \Longrightarrow \theta_w^P = \frac{\pi}{2} - \varepsilon. \tag{3.3}$$

The point A is in the intersection between the line $\overline{FI}$ and the lower symmetry line. Therefore, the points F, I and A belong to the straight line $\overline{FA}$. The segment $\overline{IB}$ is a horizontal line passing by the reflection point. Therefore, the angle $F\hat{I}A = \pi$ can be expressed as the sum of three angles, i.e. ε, $B\hat{I}A$ and their supplementary, named υ,

$$F\hat{I}A = \pi \Longrightarrow \varepsilon = \pi - \upsilon - B\hat{I}A. \tag{3.4}$$

The two lines $\overline{SA}$ and $\overline{IB}$ are parallel by definition, and they are crossed by the line $\overline{IA}$. The two angles $B\hat{I}A$ and $I\hat{A}S$ are alternate interior angles, and therefore they have equal values. For this reason, they will be both referred to as ω,

$$\overline{IB} \parallel \overline{SA} \Longrightarrow B\hat{I}A = I\hat{A}S =: \omega. \tag{3.5}$$

The combination of eqs. (3.4) and (3.5) provides the expression of ε as a function of υ and ω,

$$\varepsilon = \pi - \upsilon - \omega. \tag{3.6}$$

It is now necessary to evaluate the angles υ and ω. The line $\overline{DI}$ is adjacent to the line $\overline{OI}$, which is the radius of the

obstacle passing by the Reflection Point. For this reason the lines $\overline{DI}$ and $\overline{IA}$ are perpendicular, and the line $\overline{IB}$ subdivides the right angle $D\hat{I}A$ into two,

$$\overline{DI} \perp \overline{IA} \Longrightarrow \omega = \frac{\pi}{2} - D\hat{I}B. \tag{3.7}$$

Since $\overline{IB}$ and $\overline{OH}$ are horizontal lines, the two angles $D\hat{I}B$ and $I\hat{O}H$ are corresponding angles of the two parallel lines $\overline{IB}$ and $\overline{OH}$ cut by the transversal line $\overline{DO}$. Therefore, $D\hat{I}B$ and $I\hat{O}H$ are equal angles of value ϕ,

$$\overline{OH} \parallel \overline{IB} \Longrightarrow D\hat{I}B = I\hat{O}H =: \phi. \tag{3.8}$$

Eqs. (3.7) and (3.8) provide the correlation between the dummy angle ω and the obstacle polar angle ϕ,

$$\omega = \frac{\pi}{2} - \phi. \tag{3.9}$$

The other angle used to define ε, i.e. υ, corresponds to the angle delimited by the segments $\overline{IB}$ and $\overline{EI}$. This angle $E\hat{I}B$ is crossed by the segment $\overline{IC}$ and subdivided into the two angles $E\hat{I}C$ and $C\hat{I}B$. Moreover, $\overline{IC}$ is also adjacent to $\overline{SI}$, and therefore perpendicular to the shock tangent line $\overline{EI}$. For this reason, the angle υ is obtained by the sum of the right angle $E\hat{I}C$ and the angle $C\hat{I}B$,

$$\overline{EI} \perp \overline{IC} \Longrightarrow \upsilon = \frac{\pi}{2} + C\hat{I}B. \tag{3.10}$$

The horizontal lines $\overline{IB}$ and $\overline{SA}$ are cut by the transversal line $\overline{BS}$, which defined the corresponding—and therefore congruent—angles $C\hat{I}B$ and $I\hat{S}A$. The latter is the shock polar angle λ, and therefore also $C\hat{I}B = \lambda$,

$$\overline{IB} \parallel \overline{SA} \Longrightarrow C\hat{I}B = I\hat{S}A =: \lambda. \tag{3.11}$$

This result, together with the expression of υ from eq. (3.10), correlates the dummy variable υ with the polar coordinate of the shock evaluated at the Reflection Point λ,

$$\upsilon = \frac{\pi}{2} + \lambda. \tag{3.12}$$

The correlation between the angle ε and the two polar angles is obtained by substituting the expressions of ϕ and λ (pro-

vided by eqs. (3.9) and (3.12)) in eq. (3.6),

$$\left.\begin{aligned} \varepsilon &= \pi - \upsilon - \omega \\ \upsilon &= \frac{\pi}{2} + \lambda \\ \omega &= \frac{\pi}{2} - \phi \end{aligned}\right\} \Longrightarrow \varepsilon = \phi - \lambda. \tag{3.13}$$

Finally, the expression of ε as a function of ϕ and λ is used to define the perceived wedge angle θ_w^P:

$$\theta_w^P = \frac{\pi}{2} - \phi + \lambda. \tag{3.14}$$

The correlation between geometrical and kinematic parameters is due to the parametrization in polar coordinates of the shock wave (which geometry time dependent) and the obstacle (which is fixed, instead), by means of ϕ and λ:

$$\text{Obstacle:} \qquad \overline{z_o} = \begin{cases} x_o = x_0 + R_o \cos\phi, \\ y_o = y_0 + R_o \sin\phi, \end{cases} \tag{3.15}$$

$$\text{Shock:} \qquad \overline{z_s} = \begin{cases} x_s = R_s(\tau) \cdot \cos\gamma, \\ y_s = R_s(\tau) \cdot \sin\gamma. \end{cases} \tag{3.16}$$

At the point I, where the shock and the obstacle intersect, their coordinates are coincident, i.e. $\overline{z_s} = \overline{z_o}$,

$$\begin{cases} x_0 + R_o \cos\phi = R_s \cos\gamma, \\ y_0 + R_o \sin\phi = R_s \sin\gamma, \end{cases} \tag{3.17}$$

Eq. (3.17) contains the three unknowns R_s, λ and ϕ. In this framework R_s is not known because the goal is not the determination of the shock position at a given time, but the definition of a correlation describing a temporal evolution, and therefore $R_s(\tau)$ must be considered an unknown variable.

The squares of the right and of the left hand sides of each row of the system $\overline{z_s} = \overline{z_o}$ (eq. (3.17)), that is $(\overline{z_s})^2 = (\overline{z_o})^2$ are computed,

$$x_0^2 + y_0^2 + R_o^2 \underbrace{\left(\cos^2\phi + \sin^2\phi\right)}_{1} + 2R_o \underbrace{\left(x_0\cos\phi + y_0\sin\phi\right)}_{f(\phi)} = R_s^2 \underbrace{\left(\cos^2\lambda + \sin^2\lambda\right)}_{1}. \tag{3.18}$$

The Pythagorean identity [I] allows to drop the mutual dependence of ϕ and R_s from λ. Moreover, as resulting from eq. (3.18), all the terms containing the unknown ϕ are merged in the generic expression $f(\phi)$, and disengaged from the remaining unknown R_s. Therefore, eq. (3.18) is manipulated to separate $f(\phi)$, in the left hand side, from R_s in the right hand side,

$$f(\phi) = \left(x_0\cos\phi + y_0\sin\phi\right) = \frac{R_s^2 - x_0^2 - y_0^2 - R_o^2}{2R_o}. \tag{3.19}$$

$f(\phi)$ is decomposed into the product of two terms, the variables q and q_0. The latter is defined as

$$q_0 := \sqrt{x_0^2 + y_0^2}, \tag{3.20}$$

and therefore $f(\phi)/q_0$ is rewritten as

$$\frac{x_0}{q_0}\cos\phi + \frac{y_0}{q_0}\sin\phi =: q. \tag{3.21}$$

Since

$$\frac{x_0^2}{q_0^2} + \frac{y_0^2}{q_0^2} = 1, \tag{3.22}$$

a dummy variable ν is introduced, that satisfies the following relations,

$$\left(\frac{x_0}{q_0}, \frac{y_0}{q_0}\right) = (\cos\nu, \sin\nu)\ . \tag{3.23}$$

Therefore, the variable q is rewritten as a function of ϕ (from eq. (3.21)) and of ν (from eq. (3.23)) in the compact form

[I] $\cos^2\varpi + \sin^2\varpi = 1 \qquad \forall\varpi \in \mathbb{R}$

provided by Addition formulas [II],

$$\begin{aligned} q &= \cos\nu\cos\phi + \sin\nu\sin\phi \\ &= \cos\left(\pm\left(\phi - \nu\right)\right). \end{aligned} \tag{3.24}$$

By reversing the dependence of the variables in eq. (3.24), and maintaining both the positive and the negative arguments in the cosine, one has

$$\phi = \pm\arccos(q) + \nu \tag{3.25}$$

The sign of ϕ is determined as follows: the ordinate of the obstacle osculating circle is negative, and therefore also $\sin\nu$ and ν are. On the contrary, $\phi \geq 0$ for definition, because the obstacle is described by a polar angle $\phi \leq \phi^{LE}$. For this reason, from eq. (3.25), one has

$$(\pm\arccos(q)) = \phi - \nu \geq 0 \tag{3.26}$$

The codomain of the arccosine function is non-negative for definition, i.e.

$$\arccos(\varkappa) \geq 0 \quad \forall\varkappa \in [-1, 1], \tag{3.27}$$

and therefore $\arccos(q) \geq 0$. By recalling the definitions of q (eq. (3.21)) and of ν (eq. (3.23)), ϕ is explicitly correlated to R_s,

$$\begin{aligned} \phi &= \arccos(q) + \arcsin\left(\frac{y_0}{q_0}\right) \\ &= \arccos\left(\frac{R_s^2 - x_0^2 - y_0^2 - R_o^2}{2R_o\sqrt{x_0^2 + y_0^2}}\right) + \arcsin\left(\frac{y_0}{\sqrt{x_0^2 + y_0^2}}\right). \end{aligned} \tag{3.28}$$

The expression of λ is obtained substituting eq. (3.28) into

[II] $\cos\varpi\cos\varrho + \sin\varpi\sin\varrho = \cos\left[\pm\left(\varpi - \varrho\right)\right] \quad \forall\varpi, \varrho \in \mathbb{R}$

eq. (3.17):

$$\lambda = \arcsin\left(\frac{y_0 + R_o \sin\phi}{R_s}\right) = \tag{3.29}$$

$$= \arcsin\left\{\frac{y_0 + R_o \sin\left[\arccos\left(\frac{R_s^2 - x_0^2 - y_0^2 - R_o^2}{2R_o\sqrt{x_0^2+y_0^2}}\right) + \arcsin\left(\frac{y_0}{\sqrt{x_0^2+y_0^2}}\right)\right]}{R_s}\right\}.$$

With this expression, ϕ and λ are functions only of R_s and are parametrized on the obstacle geometry. Combining eq. (3.14) with eqs. (3.28) and (3.29), the expression is obtained for

$\theta_w^P = \theta_w^P\,(R_s;\ \text{obstacle geometry})$ (3.30)

To express $R_s = R_s\,(M_s)$, Guderley's self similar law applies to describe the position of the cylindrical shock versus time for a given set of initial conditions,

$$R_s = \tilde{r}\left(1 - \frac{\tau}{\tilde{\tau}}\right)^{\alpha}, \tag{3.31}$$

where α is the self similarity exponent (characteristic of the problem symmetry and of the thermodynamic model) and $\tilde{r}$, $\tilde{\tau}$ are constants of the problem satisfying the condition

$$\left[\,\tilde{r} = r(\tau = 0)\,\right] \iff \left[\,r(\tau = \tilde{\tau}) = 0\,\right]. \tag{3.32}$$

Provided $R_s\,(\tau)$ by means of Guderley's model, the shock speed s is computed as the time derivative of R_s:

$$\begin{aligned} s = \dot{R_s} &= \tilde{r}\alpha\left(1 - \frac{\tau}{\tilde{\tau}}\right)^{\alpha-1} \cdot \left(-\frac{1}{\tilde{\tau}}\right) \\ &= \underbrace{\tilde{r}\left(1 - \frac{\tau}{\tilde{\tau}}\right)^{\alpha}}_{R_s} \cdot \frac{-\alpha}{\tilde{\tau}\,(1 - \tau/\tilde{\tau})} \\ &= R_s \cdot \frac{-\alpha}{\tilde{\tau} - \tau}, \end{aligned} \tag{3.33}$$

and its Mach number is calculated as

$$M_s = \frac{\left|\dot{R_s}\right|}{w_i} = R_s \cdot \frac{\alpha}{w_i\left(\tilde{\tau} - \tau\right)}. \tag{3.34}$$

If the initial time is set in correspondence of the shock impingement, the value of $\widetilde{r}$ is known, but $\widetilde{\tau}$ is not, and it depends on the evolution of the shock. However, in the following it will assumed that $\widetilde{\tau}$ is very close to the one of a cylindrical shock [III], and that therefore it can be calculated as follows:

$$\left.\begin{aligned}\widetilde{M_s} &= M_s\,|_{\tau=0}\\ \widetilde{r} &= R_s\,|_{\tau=0}\end{aligned}\right\} \implies \widetilde{M_s} \approx \widetilde{r}\cdot\frac{\alpha}{w_i\widetilde{\tau}} \implies \widetilde{\tau} \approx \frac{\alpha\widetilde{r}}{w_i\widetilde{M_s}}. \tag{3.35}$$

The mutual dependence of the variables in eq. (3.31) is reversed to express $\tau = \tau(R_s)$,

$$\tau(R_s) = \left[1 - \left(\frac{R_s}{\widetilde{r}}\right)^{\frac{1}{\alpha}}\right]\widetilde{\tau}, \tag{3.36}$$

and therefore $\tau(R_s)$ (from eq. (3.36)) and $\widetilde{\tau}$ (from eq. (3.35)) are substituted into eq. (3.34),

$$M_s = \frac{\alpha R_s}{w_i\widetilde{\tau}\left\{1 - \left[1 - \left(\frac{R_s}{\widetilde{r}}\right)^{\frac{1}{\alpha}}\right]\right\}} = \left(\frac{\alpha\widetilde{r}^{\frac{1}{\alpha}}}{w_i\widetilde{\tau}}\right)R_s^{\frac{\alpha-1}{\alpha}}, \tag{3.37}$$

to obtain

$$R_s = \left(\frac{M_s}{\widetilde{M_s}}\right)^{\frac{\alpha}{\alpha-1}}\widetilde{r}. \tag{3.38}$$

Eq. (3.38) is then substituted into the expressions of ϕ (eq. (3.28)) and λ (eq. (3.29)), so that the final expression of the correlation between the local values of M_s and θ_w^P is:

[III] See sec. 3.3.2 for details

$$\theta_w^P = \frac{\pi}{2} - \arccos\left[\frac{\left(\frac{M_s}{\widetilde{M}_s}\right)^{\frac{2\alpha}{\alpha-1}}\tilde{r}^2 - x_0^2 - y_0^2 - R_o^2}{2R_o\sqrt{x_0^2+y_0^2}}\right] - \arcsin\left(\frac{y_0}{\sqrt{x_0^2+y_0^2}}\right)$$

$$+\arcsin\left\{\frac{y_0}{\left(\frac{M_s}{\widetilde{M}_s}\right)^{\frac{\alpha}{\alpha-1}}\tilde{r}} + \frac{R_o}{\left(\frac{M_s}{\widetilde{M}_s}\right)^{\frac{\alpha}{\alpha-1}}\tilde{r}}\sin\left\{\arccos\left[\frac{\left(\frac{M_s}{\widetilde{M}_s}\right)^{\frac{2\alpha}{\alpha-1}}\tilde{r}^2 - x_0^2 - y_0^2 - R_o^2}{2R_o\sqrt{x_0^2+y_0^2}}\right]\right.\right.$$

$$\left.\left. + \arcsin\left(\frac{y_0}{\sqrt{x_0^2+y_0^2}}\right)\right\}\right\}. \tag{3.39}$$

3.3.2 Discussion on the model validity

The description of the implosion propagation by means of eq. (3.31) is correct only for truly self-similar cases, such as the cylindrical implosion, for which $\alpha = 0.834$.

It is however known [79] from approximate theoretical considerations and numerical simulations on cylindrical implosions that

$$\forall\left(M_s,\ \theta_w^{LE} \geq \theta_w^{cr}\right) \quad \exists\ \theta_w^{tr} < \theta_w^{cr} \ \left|\ \left[\left(\theta_w^P \leq \theta_w^{tr}\right) \Longleftrightarrow (RR \longrightarrow MR)\right]\right. . \tag{3.40}$$

It is therefore expected that, regardless of the obstacle thickness and of local shock concavity, when $x_s \approx x_0$, $\theta_w^P \approx 0$ and, therefore, the Regular Reflection must become a Mach Re-

flection . This will cause the shock to depart from the cylindrical shape and, therefore, not to obey to eq. (3.31).

However, far from the obstacle, the shock shape still obeys axisymmetrical conditions, and therefore the overall time-to-focusing $\tilde{\tau}$ and convergence rate α remain the same. The only limitation would occur in case of more than one obstacle: in this case the multiple Mach Reflections would influence all the shock front shape. It was however verified [88] that if the reshaped shock conserves a high level of symmetry (i.e. if obstacles are symmetrically arranged along azimuth, so that the reshaped shock is a symmetric polygon), the shock position with respect to time still follows a power-law trend, even though with different constants. Moreover, the higher is the number of edges of the polygon, the closer the propagation will remain to that of the axisymmetric cylindrical shock in terms of values of α, $\tilde{r}$ and $\tilde{\tau}$. In this framework, it is assumed that the values of the three constants do not vary with respect to the axisymmetric problem, and that therefore other phenomena, such as the RR $\longrightarrow$ MR transition or the trailing edge flow separation, can be neglected.

3.3.3 Comparison of eq. (3.39) with numerical results

The accordance of the analytic law (3.39) with numerical results is reported in fig. 3.8, concerning a Regular Reflection over one circular obstacle. The propagation along time is from top ($\theta_w^{LE} = \pi/2$) to bottom ($\theta_w^{LE} > 0$ when $\phi = \pi/2$). During the evolution of the Regular Reflection, θ_w^P spans from θ_w^{LE} till the value of the perceived angle when the Regular Reflection terminates and the transition into a Mach Reflection occurs.

The average trajectory along the θ_w^{LE}-M_s plane is well captured, even though a dispersion of the sampled values id observed. The error is possibly due to the technique adopted to evaluate the numerical M_s. Indeed, it is assumed to be proportional to the difference between the shock radii at different time steps: this means that the error on M_s includes the contributions of two measurements and propagates towards the following time step.

A persistence of Regular Reflection is observed for θ_w^{LE} <

θ_w^{cr}, in accordance with the observations performed in [79].

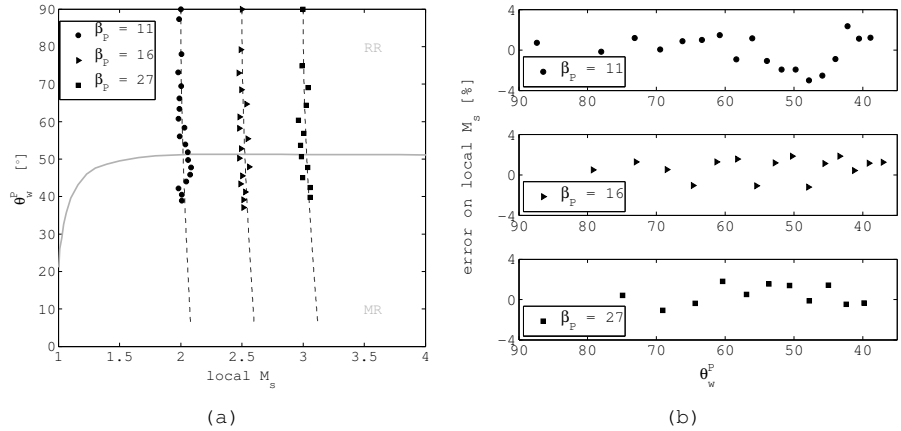

Figure 3.8: (a) Predicted evolution of the combinations between M_S and θ_w^P in Regular Reflections (dashed line) and numerical results (●, ►, ■) for diverse initial conditions. Time increases from top to bottom. (b) Percentage deviation between theoretical and numerical values. Axes are reversed because of the more visible effect on M_S of measurement errors.

3.4 Transition from Regular to Mach Reflection

As observed by several theoretical and experimental works dealing with the reflection of weak planar shocks over cylindrical obstacles [78, 79, 83], due to the loss of self similarity with respect to the pseudo-steady problem, θ_w^P varies along time, and therefore the reflection may change from Regular to Mach-type during the shock propagation. Authors assessed the effect of the initial wedge angle and of the radius of curvature of the obstacle.

In this work, the RR ⟶ MR transition is observed also for cylindrical shocks. Moreover, after the RR ⟶ MR transition, also the transition among diverse Mach Reflection types, hereafter defined "internal" transition, can be observed. Figs.

3.9 and 3.10 report two temporal evolution of these internal transitions, after the transition from a Regular Reflection. In particular, fig. 3.9 represents the case of a shock generated by an initial pressure ratio β_P = 130, and therefore the strong shock with M_S^{LE} = 6.5 undergoes a DMR → TMR. On the contrary, the shock depicted in fig. 3.10 has M_S^{LE} = 2.0, which causes its transition from Transitional Mach Reflection to Pseudo-Transitional Mach Reflection to Single Mach Reflection. It is worth noticing that both patterns in fig. 3.9(b) and in fig. 3.10(b) are Transitional Mach Reflections but the kink is much more evident in the first case: it is observed that, in general, shock structures are more defined for strong shocks.

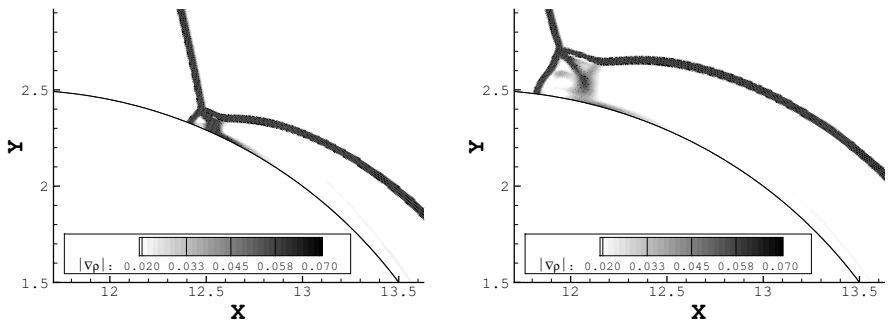

Figure 3.9: Transition after the RR ⟶ MR transition, internal Mach Reflection transitions: from (a) Double Mach Reflection to (b) Transitional Mach Reflection for a shock impinging on a cylindrical obstacle with M_S = 6.5 (β_P = 130) at twice the reference distance.

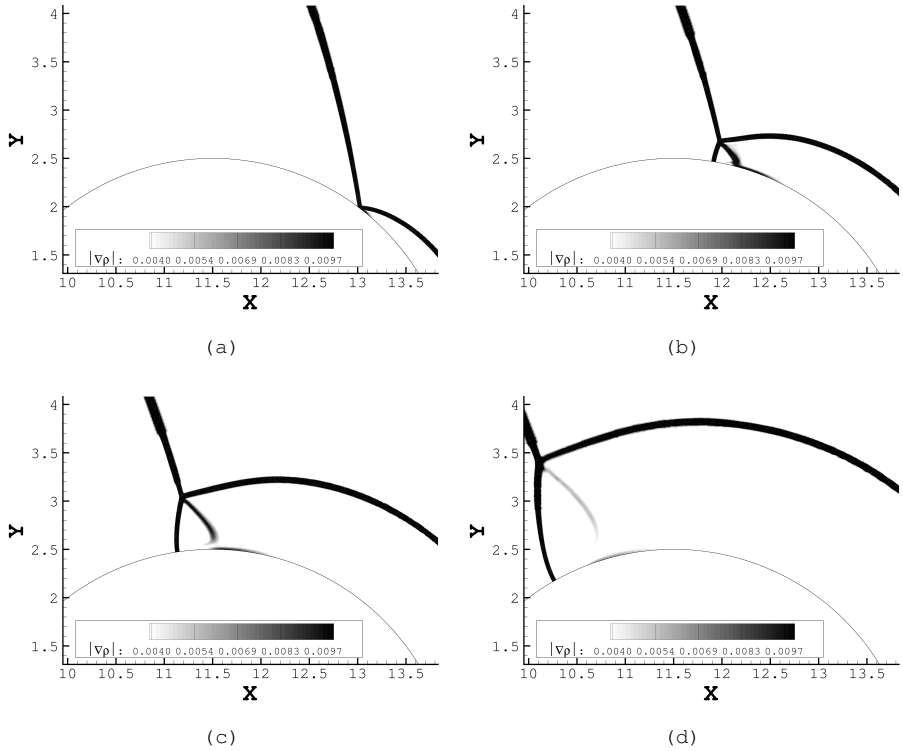

Figure 3.10: Transition from (a) Regular Reflection to (b) Transitional Mach Reflection to (c) Pseudo-Transitional Mach Reflection to (d) for a shock impinging on a cylindrical obstacle with $M_S = 2.0$ ($\beta_P = 11$) at twice the reference distance.

In the following, the RR $\longrightarrow$ MR transition will be discussed for obstacles which can produce a Regular Reflection at the leading edge. With reference to numerical results reported in fig. 3.6, a Regular Reflection occurs for obstacles with $t/c = 0.445$, 0.49, 0.56, 0.63, 0.77, 0.91 and 1.0.

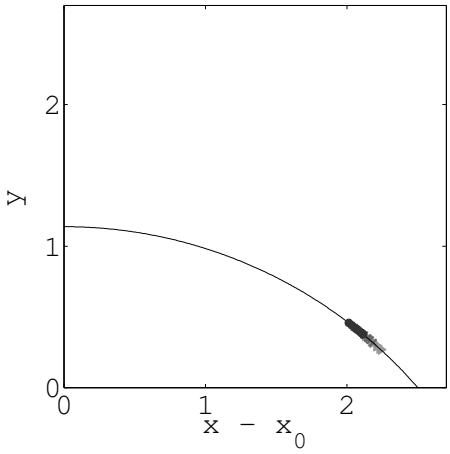

(a) $t/c = 0.445$

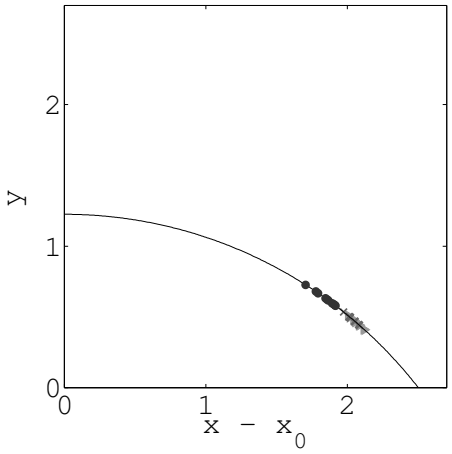

(b) $t/c = 0.49$

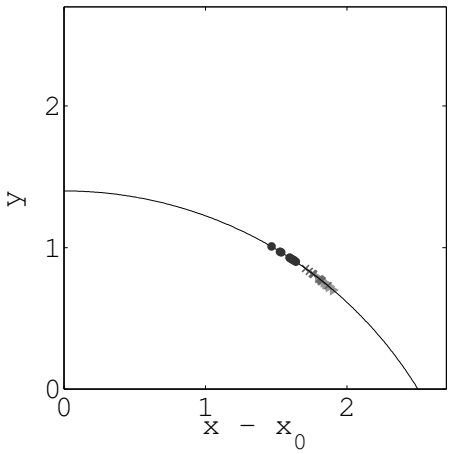

(c) $t/c = 0.56$

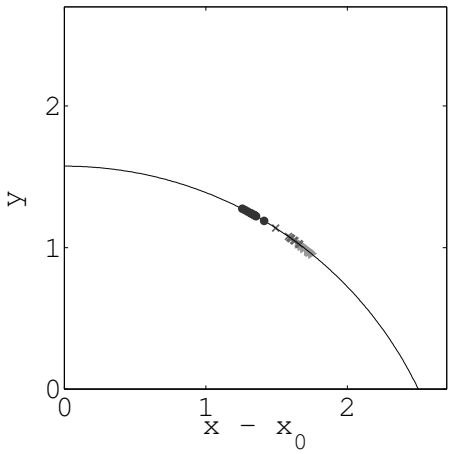

(d) $t/c = 0.63$

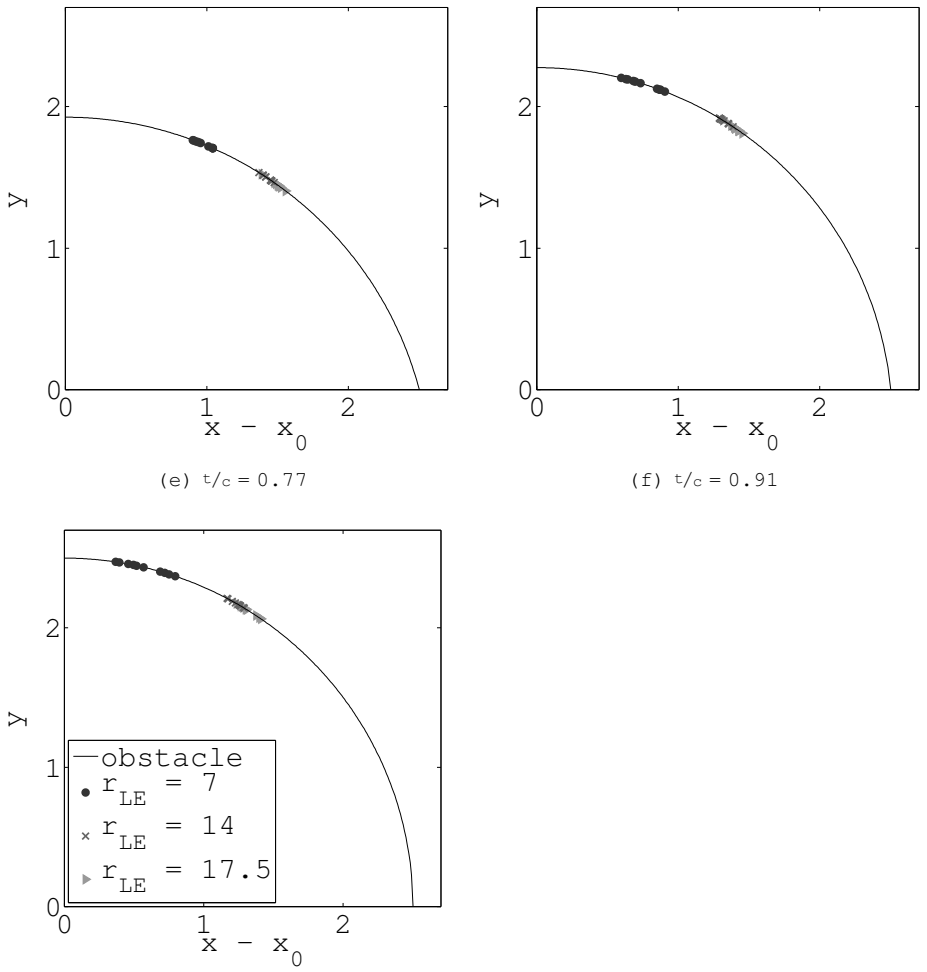

(e) $t/c = 0.77$ (f) $t/c = 0.91$

(g) $t/c = 1.0$

Figure 3.11: RR $\longrightarrow$ MR transition points for increasing t/c and r_{LE}. Each picture depicts the transitions over a diverse-t/c obstacle, represented by the solid line. Symbols represents the transition points, and each marker is associated to a diverse r_{LE} value: $r_{LE} = 7$ (●), $r_{LE} = 14$ (✕) and $r_{LE} = 17.5$ (▶). The 10 symbols in each group of similar markers represent the sampled values of the transition points for diverse M_s. The effect of the shock Mach number is not made explicit for visual clarity.

Fig. 3.11, on pages 114–115, illustrates the RR $\longrightarrow$ MR transition points along the obstacle boundaries. On each picture, data indicated with the same marker represent reflections over obstacles with an equal r_{LE} value, regardless of the value of the shock Mach number. Two trends are evident: on one hand, the larger is t/c, the lower is θ_w^{tr} and, on the other hand, the larger is r_{LE}, the higher is θ_w^{tr}. The effect of r_{LE} is in accordance with reference results, because the reflection of weak planar shocks over convex obstacles represents a limit of the present case, that is for $r_{LE} \to \infty$.

The detection of the transition points was achieved by means of simple visual observation of the computed flow fields, and did not require the development of an automatic procedure.

For each analyzed configuration, the value of the coordinates of the transition point $\left(x^{tr}, y^{tr}\right)$ are directly sampled. The "absolute transition angle" θ_w^{tr} is defined here as the angle between the local obstacle tangent line and the chord direction. θ_w^{tr}, therefore, is simply evaluated as

$$\theta_w^{tr} = \frac{\pi}{2} - \arctan\left(\frac{y^{tr} + y_0}{x^{tr} - x_0}\right). \tag{3.41}$$

On the contrary, the perceived transition angle $\theta_w^{tr,P}$ and the local shock Mach number at the transition are calculated by means of eq. (3.39).

The main error source in the measurement can be attributed to the observation that, immediately after the RR $\longrightarrow$ MR transition, the growth of the Mach stem is much slower than during the following evolution of the Mach Reflection: this causes a non negligible difficulty in detecting the exact termination of the Regular Reflection and the rising of the Mach Reflection, resulting in a maximum measurement error of $\pm 2.0^{\circ}$ in the determination of θ_w^{tr} and, therefore, of $\theta_w^{tr,P}$.

In fig. 3.11 the dependence of the transition points on the shock Mach number is not explicit, since all the configurations with the same geometry are represented by means of the same marker for visual clarity. The effect of the shock Mach number, on the contrary, is shown in fig. 3.12.

Each row of the array of pictures in fig. 3.12 is associated to a diverse r_{LE} value. The left column represents the transi-

tion points in terms of absolute values, i.e. θ_w^{tr} and M_s^{LE}. On the contrary, the pictures on the right column depict the local values of wedge angle $\theta_w^{tr,P}$ and M_s at the transition. Each line represents the transition angle as a function of the shock Mach number for a diverse obstacle t/c.

With reference to figs. 3.12(a) – (c) – (e) (left column of fig. 3.12), it is observed that the absolute θ_w^{tr} is affected mainly by the obstacle thickness, and less by shock intensity, as in the self-similar case. The shock Mach number, indeed, does not induce neither a specific trend nor a relevant variance of the transition angles belonging to the same curve. On the contrary, for a given combination of r_{LE} (picture) and β_P (curve), it can be observed that, in general, the larger is t/c, the lower θ_w^{tr} is. Therefore, the so-called "Regular Reflection persistence", that is the existence of a Regular Reflection in presence of wedge angles which would generate leading edge Mach Reflections, is more relevant for larger t/c values. The effect of r_{LE} is to qualitatively determine the range of variability of the transition angles for diverse t/c values: θ_w^{tr} ranges about from 10° to 40° for $r_{LE} = 7$, from 27° to 41° for $r_{LE} = 14$ and from 30° to 43° for $r_{LE} = 17.5$.

The trend between t/c and θ_w^{tr} can be expressed also as a trend between R_o and θ_w^{tr} or between θ_w^{LE} and θ_w^{tr}, in accordance with eq. (3.1). In particular, θ_w^{tr} is higher when R_o is larger and therefore when θ_w^{LE} is smaller. The first result—the correlation between the transition angle and the obstacle curvature—is in accordance with the observations in Refs. [79, 78] on the reflection of planar shock waves over convex obstacles. In these works, indeed, an increasing trend between R_o and θ_w^{tr} was observed. The second result, i.e. the decreasing trend between θ_w^{LE} and θ_w^{tr}, seems to be in contradiction with the results of the same works [79] where, on the contrary, an increasing trend between θ_w^{LE} and θ_w^{tr} was observed. In the reference works, however, the effects of R_o and θ_w^{LE} were assessed independently. On the contrary, in this work both R_o and θ_w^{LE} are summarized by the parameter t/c, and therefore their effects cannot be observed separately. Therefore, it cannot be determined yet whether the two different observed trends are due to physical reasons, i.e. the influence of the shock wave curvature, or to an interaction between the two factors R_o and θ_w^{LE}.

When local values of the wedge angle and shock Mach number are observed, i.e. the perceived angle $\theta_w^{tr,P}$ and the transition M_S, (figs. 3.12(b) - (d) - (f), the right column of fig. 3.12), the effect of t/c is significantly weaker than in the case of the absolute transition angle. The separation among all the lines, indeed, becomes comparable with the separation among the data of the same curve, and a very reduced variability of $\theta_w^{tr,P}$ is observed for different t/c values. Moreover, the effect of r_{LE} becomes almost negligible, since the range of variability of $\theta_w^{tr,P}$ remains the same—about from 37^o to 43^o—for all the diverse investigated r_{LE} values.

Unlike geometric factors, the shock Mach number appears to have a weak or negligible influence on both θ_w^{tr} and $\theta_w^{tr,P}$ in the considered range of parameters. Therefore, to better assess the effects of the most relevant factors, i.e. t/c and r_{LE}, on the RR $\longrightarrow$ MR transition, the effect of the shock Mach number is neglected. In fig. 3.13, each point of the diagram represented the average transition angle for a given combination of t/c and r_{LE}, and therefore it does not account for the shock Mach number. Fig. 3.13(a) represents the absolute and fig. 3.13(a) the perceived transition angles. For each obstacle geometry (combination of t/c and r_{LE}), the range of variability of the transition angle due to the shock Mach number is represented by a vertical bar.

As observed above, θ_w^{tr} exhibits a monotonically decreasing trend versus t/c, whose average slope is influenced by r_{LE}.

On the contrary, $\theta_w^{tr,P}$ does not present a significant dependence on t/c, being the average slopes of the curves almost null. Moreover, all the three curves associated to the three values of r_{LE} become completely overlapped. This fact indicates that $\theta_w^{tr,P}$ is not influenced by r_{LE}, that is, the shock curvature, in a first degree of approximation.

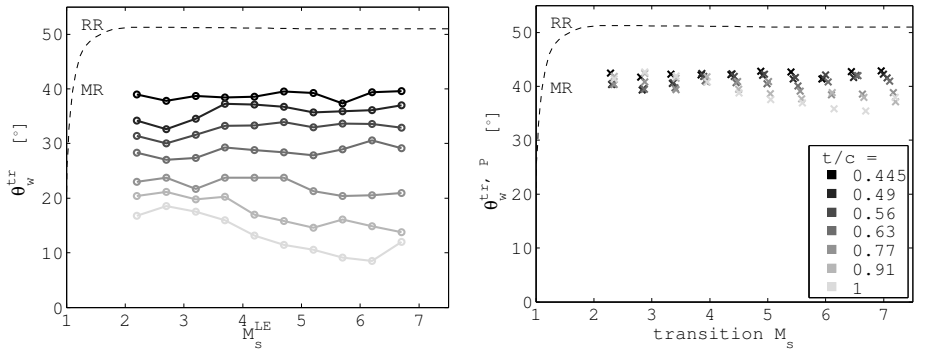

(a) $r_{LE} = 7$ (b) $r_{LE} = 7$

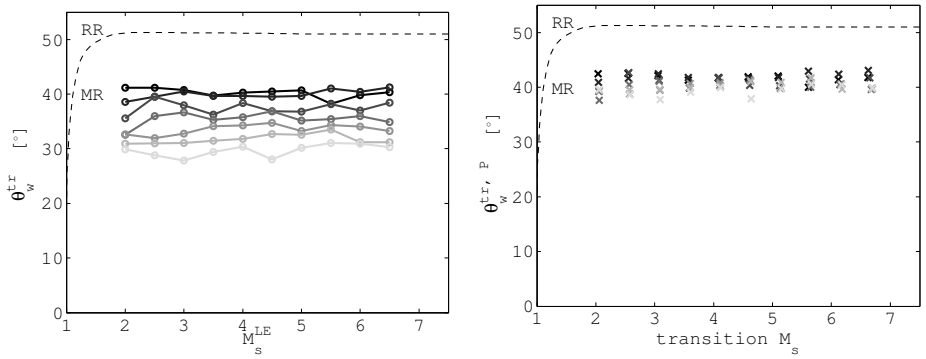

(c) $r_{LE} = 14$ (d) $r_{LE} = 14$

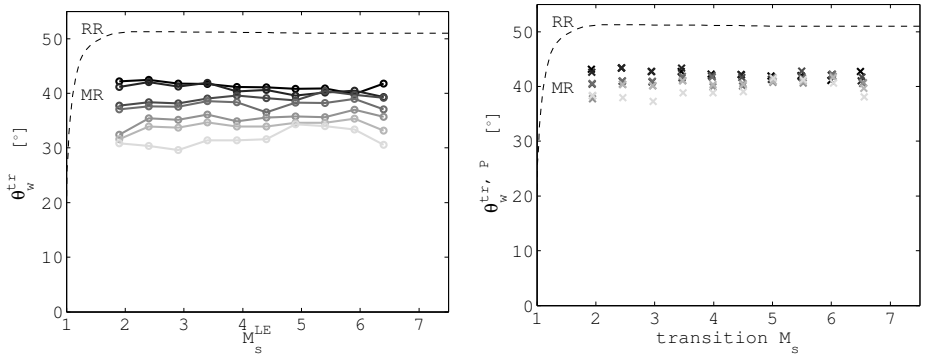

(e) $r_{LE} = 17.5$ (f) $r_{LE} = 17.5$

Figure 3.12: Transition angles versus shock Mach number parametrized on t/c and r_{LE}: absolute values (left column, —o—) and values perceived at the transition (right column, ✖).

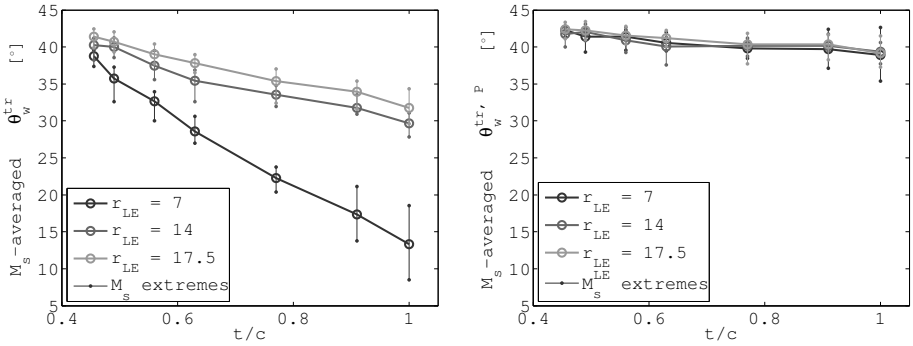

Figure 3.13: Average (a) absolute and (b) perceived transition angles versus t/c and parametrized on r_{LE} (—o—). For each point, the range of variability due to M_s is indicated by the bar I.

3.5 Triple Point trajectories

In steady reflections, the coordinates of a Triple Point are, of course, constant. Similarly, in pseudo-steady reflections the self-similar coordinates of the Triple Point remain constant. On the contrary, in the reflection of genuinely unsteady shocks, the Triple Point moves in a genuinely unsteady fashion, and therefore its coordinates vary with time. Former works on the reflection of planar shocks over cylindrical obstacles determined the trajectory of the Triple Point of a Mach Reflection arisen after the termination of a Regular Reflection occurred at the leading edge. [45] and [78] theoretically analyzed the Triple Point path by means of the characteristics method, while [83] performed an experimental campaign which confirmed their results.

In this work, only "genuine" Mach Reflections are considered, that is reflections which are of Mach-type immediately from the leading edge reflection, as opposed to Mach Reflections generated by the RR $\longrightarrow$ MR transition. To attain the shock reshaping, indeed, Mach Reflections are required. Reflections of regular type at the leading edge are observed [79], also

in this work, to often turn into Mach Reflections during the shock convergence. However, this empirical evidence is not supported by a physical model, and therefore some conditions may exist which do not cause the RR $\longrightarrow$ MR transition. For this reason, only genuine Mach Reflections are observed.

The investigated Triple Point paths, therefore, are assumed to always start from the obstacle leading edge. However, the assumption on the onset of a Mach Reflection exactly in correspondence of the leading edge is known to be an approximation of the local physics of the reflections. Both theoretical (see, e.g., [133]) and experimental works ([134] and [84]) performed on pseudo-steady reflections, indeed, highlighted a distance of the order of some free mean paths from the wedge leading edge to the actual point of detachment of the Triple Point from the reflecting surface. Therefore, on a "macroscopic" scale, genuine Mach Reflections exist and are investigated in this section, whereas on a "microscopic" scale, Mach Reflections do not arise in correspondence of the leading edge.

In the reference papers [133, 134, 84], the delay in the onset of Mach Reflections was attributed to viscous effects, which become relevant in small-scale experimental investigations. In the present work, therefore, this delay can be neglected. Reynolds number, indeed, is between 10^6 and 10^7 and Knudsen number Kn is always lower that 10^{-5} in all the computational domain. The latter is defined as the ratio between the molecules free mean path and the characteristic lengths, and therefore it indicates the order of magnitude of resolved scales [IV].

Also other viscous effects can be neglected: in a recent work [85] on the reflection of planar shocks over convex obstacles, no measurable effect of viscosity was recorded for streams characterized by Reynolds number of 10^6 and larger.

[IV] For a polytropic ideal gas, the definition of Reynolds, Mach and Knudsen numbers allows to evaluate the latter from the first two, without computing the exact value of the free mean path:

$$\mathrm{Kn} = \frac{\mathrm{M_f}}{\mathrm{Re}} \sqrt{\frac{\left(\delta_\gamma + 1\right)\pi}{2}},$$

where $\mathrm{M_f}$ is the flow Mach number. $\left(\delta_\gamma + 1\right)$ is the ratio of the specific heats at constant pressure and volume for a polytropic ideal gas. In this work, air is modeled as a binary mixture of diatomic gases, i.e. N_2 and O_2, and therefore $\left(\delta_\gamma + 1\right) = 1.4$.

The separation of genuine Mach Reflections is performed by means of the map of leading edge reflections reported in fig. 3.6. The obstacle t/c values, therefore, are respectively of 0.07, 0.14, 0.21, 0.28, 0.35 and 0.42. β_P ranges from 11 to 130 on ten levels, generating as many shock Mach numbers for each one of the three r_{LE}, thus 7, 14 and 17.5.

In the following, the coordinates of the Triple Point will be indicated as (x, y), and refer to a right-hand oriented reference system with the origin in the focus point and an abscissa axis aligned with the obstacle chord. In analogy to the detection of the RR $\longrightarrow$ MR transition, the tracing of the Triple Point trajectories is performed by means of a simple visual analysis of the flow field at diverse time steps; no algorithm for the automatic measurement of the Triple Point coordinates was developed.

The adopted procedure introduces a relevant variance in data, due on the first hand to the human factor on the measurement and, on the other hand, to the lack of a unique criterion which defined the exact position of a Triple Point computed by means of numerical simulation (see for analogy the problem of the detection of the shock position, sec. 2.2.1). Three replications of the measurements were performed. Data reported in the following represent the average values of the three replications samples. It is observed that the uncertainty on both x and y is ± 0.02.

3.5.1 Preliminary observations on the Triple Point trajectories

In this section, the trajectories of the Triple Points generated by the diffraction of the shock waves over obstacles with diverse geometries are shown. Preliminary observations on the trajectories and on the influential factors on the shapes will be reported in sec. 3.5.1.1.

Moreover, some considerations will be performed on the offset of the Triple Point from the reflecting surface in sec. 3.5.1.2.

3.5.1.1 Triple Point coordinates

Fig. 3.14 reports all the trajectories of the Triple Point sampled at constant time intervals for the obstacles with $t/c = 0.28$. Different curve colors indicate different r_{LE} values, whereas each symbol represent a specific β_P. It is well evident that all the trajectories show an arched trend and are grouped on the basis of r_{LE}, regardless of β_P. This event occurs just as clearly also for the other five t/c levels.

The independence on β_P of the trajectory shape is unexpected, since theoretical models and experimental results on pseudo-steady reflections (e.g. [82]) predicted a dependence of χ—the angle between the Triple Point path and the reflecting wall—on θ_w, P_i, T_i and M_s.

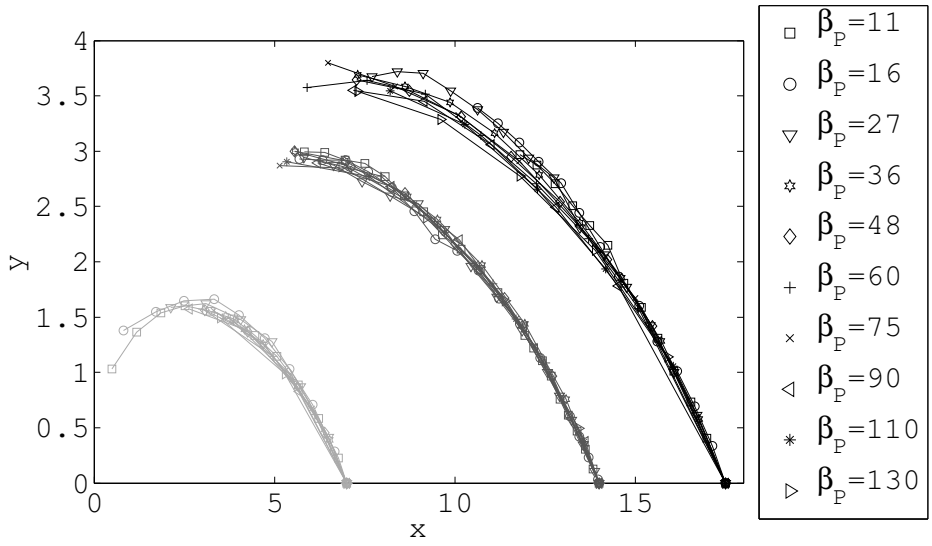

Figure 3.14: Triple Point trajectories for Mach Reflections over obstacles with the same $t/c = 0.28$. Each group of curves represents the trajectories due to the diffractions over obstacles located at the same r_{LE}, whereas the single lines indicate trajectories of Triple Points belonging to shock waves generated by diverse β_P.

In addition to the disengagement of the trajectory shape from the shock Mach number, another common feature is observed among the thirty paths plotted in fig. 3.14. Especially in

the beginning, indeed, all the three groups of trajectories appear to be homogeneous dilations of the same curve. A homothetic transformation centered in the focus point (0, 0) and with ratio corresponding to r_{LE} is applied to numerical data. The resulting transformed Triple Point positions are reported in fig. 3.15.

All the trajectories normalized on r_{LE} overlap in proximity of the leading edge, regardless of r_{LE} and M_S, but exhibit an incipient divergence in correspondence of the peak value. This behavior of the curves near the peaks is caused by two factors: the first one is the unavoidable error measurement, and the second one is a probable weak but physical influence of r_{LE} on the path shape. The error measurement is slightly increasing with r_{LE} (see fig. 3.14) due to the peculiar shapes of the shock system: the local slopes of the incident shock and the Mach stem in correspondence of the triple point, indeed, become very similar for large values of r_{LE}. The detection of the Triple Point exact position, therefore, suffers from the difficulty to distinguish the two shock waves, increasing the variance of the results.

The observations on the weak influence of M_S and r_{LE} are confirmed by the analysis of the trajectories of the Triple Point for all the values of t/c. It must be noted that in the following, for clearer visibility, figures reporting clustered data will be plotted only for the three cases of β_P = 11, 16 and 27 and for the extreme values of r_{LE} = 7 and 17.5, albeit calculations and quantitative considerations are performed including results all the treatments.

Figs. 3.16 reports the non-normalized Triple Point position: as observed for the case with $t/c = 0.28$, the effect of M_S is null or negligible and, moreover, all the groups of curves in each picture exhibit a similar trend.

The same homothetic transformation as before (with center in (0, 0) and ratio r_{LE}) is applied to numerical data. Results for r_{LE} = 7 and 17.5 and for β_P = 11, 16 and 27 are reported in fig. 3.17. From the comparison among the pictures in fig. 3.17—each associated to a diverse t/c value—, it is apparent that the curve shapes depend most on t/c, whereas the influence

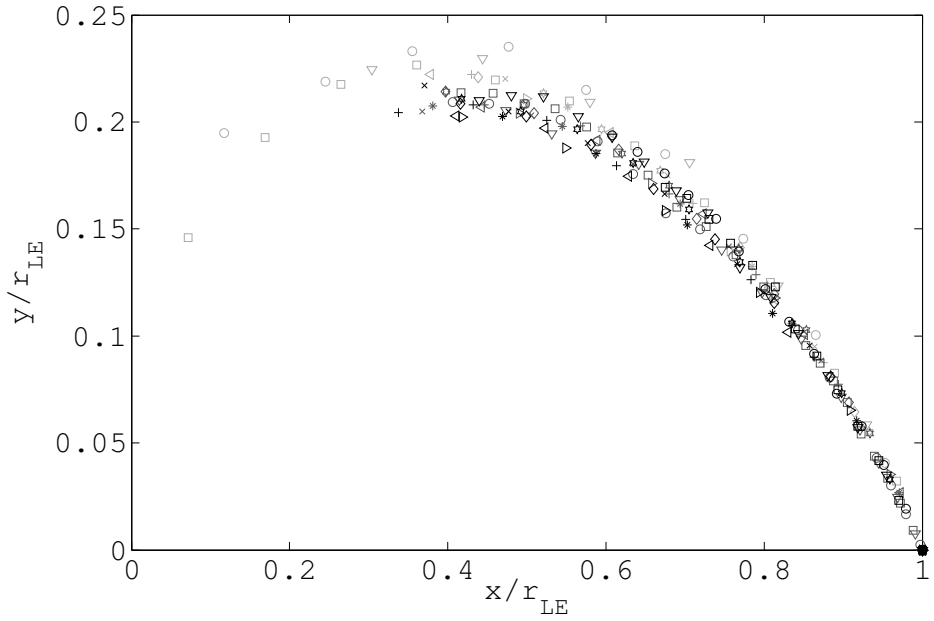

Figure 3.15: Triple Point trajectories normalized with r_{LE} for Mach Reflections over obstacles with the same t/c but different r_{LE} values and for shocks generated by diverse β_P.

of r_{LE} is almost completely negligible.

On the contrary, effects of r_{LE} appear on the long-term behavior of the trajectories, and only for certain t/c values. Indeed, no relevant difference is observed among the normalized data on each picture for $t/c = 0.07$, 0.14 and 0.21, whereas a separation between the two groups of curves with different r_{LE} appears in the other three cases. Moreover, in a first degree of approximation, this separation increases with t/c.

Data present a larger dispersion for $t/c = 0.07$ with respect to other values of obstacle thickness. This must be attributed to the difficulty in detecting the exact location of the Triple Point in Irregular Reflections whose pattern is very close to von Neumann Reflections, as observed in sec. 3.2. To overcome this difficulty, the adopted procedure is to trace the trajectory of the so-called "equivalent Triple Point". Literature

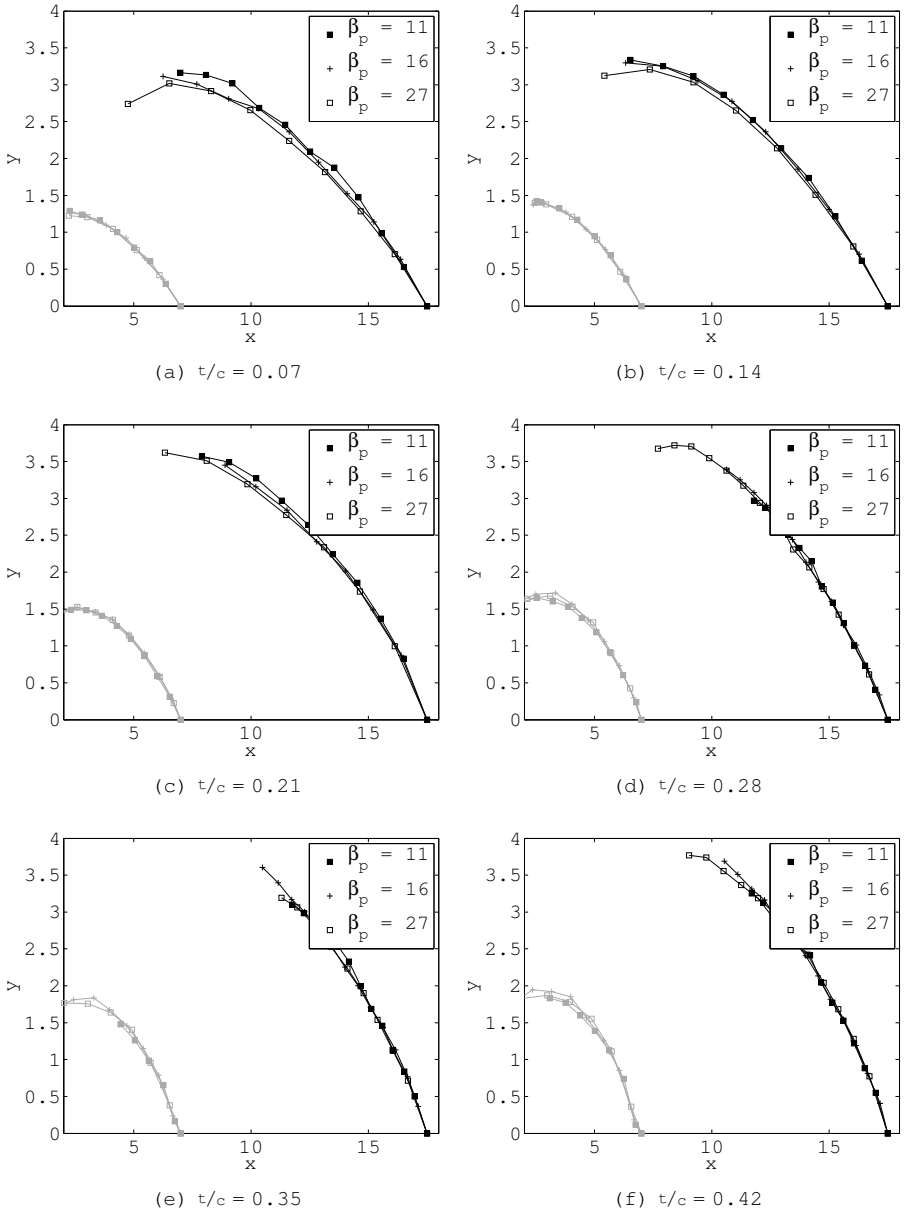

Figure 3.16: Trajectories of the Triple Point generated at the leading edge for obstacle aspect ratios ranging from (a) 0.07 to (f) 0.42 for diverse initial pressure ratios and obstacle leading edge radii (gray markers for $r_{LE} = 7$, black markers for $r_{LE} = 17.5$).

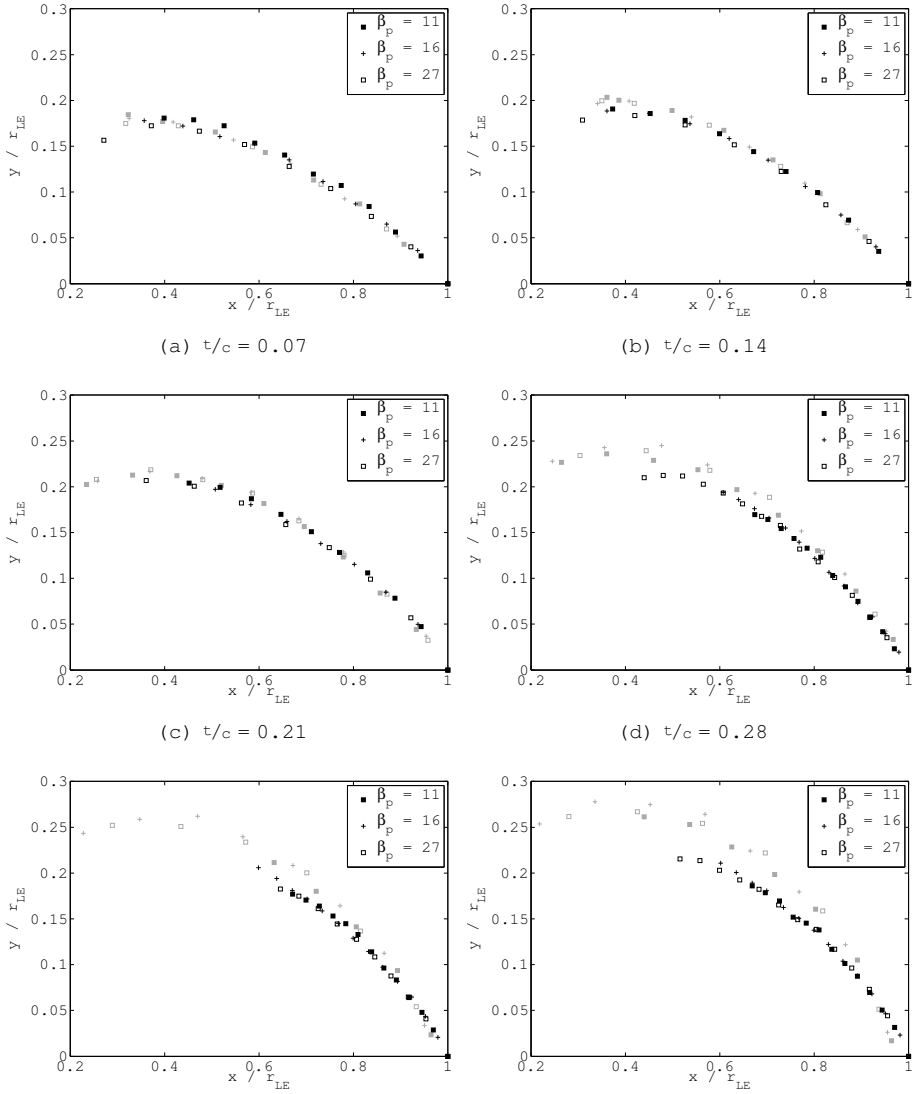

(a) $t/c = 0.07$ (b) $t/c = 0.14$

(c) $t/c = 0.21$ (d) $t/c = 0.28$

(e) $t/c = 0.35$ (f) $t/c = 0.42$

Figure 3.17: Normalized trajectories of the Triple Point on r_{LE} generated at the leading edge for obstacle aspect ratios ranging from (a) 0.07 to (f) 0.42 for diverse initial pressure ratios and obstacle leading edge radii (gray markers for $r_{LE} = 7$, black markers for $r_{LE} = 17.5$).

suggests to set the equivalent Triple Point of a von Neumann Reflection in correspondence of the intersection between the incident shock and the end of the compression band which substitutes the reflected wave. The advantage of this procedure is that it identifies both the equivalent Triple Point of a von Neumann Reflection and the true Triple Point of a Single Mach Reflection.

However, due to the non-uniqueness in the detection of the leading compression band, this procedure introduces a degree of inaccuracy in the detection of the Triple Point, and therefore the data dispersion appears larger than in other cases.

This is evident in fig. 3.18, which compares the trajectories of Triple Points generated by the reflection over obstacles with $t/c = 0.07$, $r_{LE} = 17.5$ and $t/c = 0.21$, $r_{LE} = 7$. r_{LE} is varied between the two groups of curves to have a weak shock for $t/c = 0.07$—and, therefore, a possible weak reflection—and a strong shock for $t/c = 0.21$—causing a Single Mach Reflection.

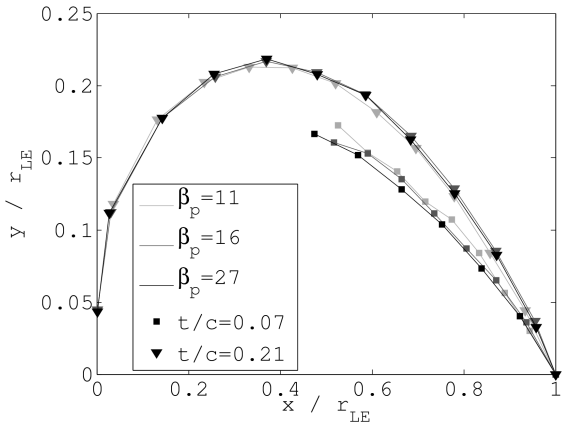

Figure 3.18: Comparison between trajectories of Triple Point generated by obstacles with diverse t/c and r_{LE} highlighting the diverse data dispersion. r_{LE} is varied between the two groups of curves in order to further stress the difference in shock intensity and make the data dispersion more evident.

3.5.1.2 Triple Point offset from the reflecting surface

The vertical offset Δy of the Triple Point position with respect to the reflecting surface is computed. It is recalled that with "reflecting surface" both the obstacle and the trailing edge symmetry line are indicated. Therefore, the ordinate of whole reflecting surface is evaluated as $y_{RS} = \max(0, y_o)$, where y_o is the ordinate of the obstacle surface, introduced in sec. 3.3. In this section, non-normalized data on r_{LE} will be used, because the obstacle chord is fixed ($c = 5$) and its normalization would alter the extent of the range where $y_{RS} \equiv y_o$.

A phenomenological survey is performed in the beginning.

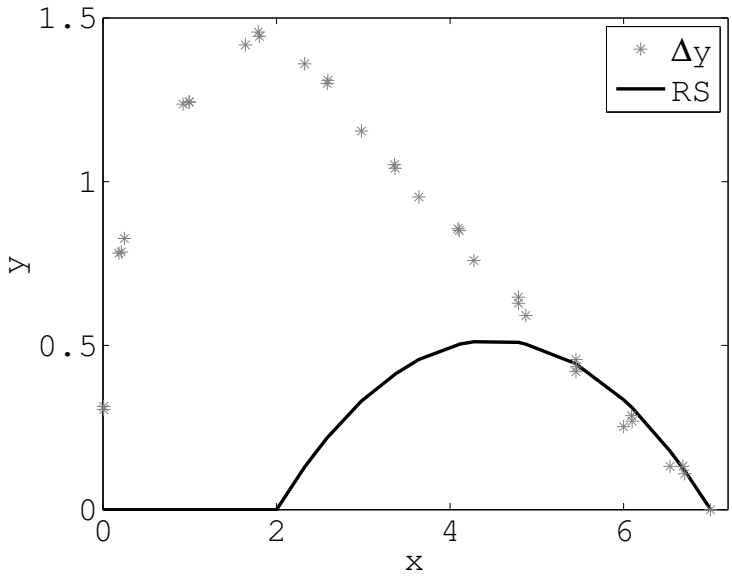

Figure 3.19: Offset of the Triple Point trajectory (*) from the reflecting surface (black line) for $t/c = 0.21$ and $r_{LE} = 7$, showing a quasi-linear trend (image not in scale).

Fig. 3.19 shows the Triple Point offset $\Delta y = y - y_{RS}$ for the case with $t/c = 0.21$ and $r_{LE} = 7$. It clearly exhibits that, after the obstacle trailing edge, the offset of the Triple Point

trajectory abruptly abandons the monotone trend and the Triple Point moves towards the reflecting surface. This consideration is easily explained because $y_{RS} \equiv 0$ for $x \leq x_{TE}$.

Results of numerical simulations carried out within this work show a peculiar fact. Theoretical [66] and experimental [86, 79] works on the unsteady reflection of straight shock waves over concave obstacles, indeed, demonstrate the existence of the so-called "Inverse Mach Reflection" (InMR). An Inverse Mach Reflection presents three features:

1a The distance between the Triple Point and the reflecting surface decreases during the shock propagation;

2a The slipstream originated at the Triple Point moves away from the reflecting surface;

3a Inverse Mach Reflections are intrinsically unstable, and terminate into a "Transitioned Regular Reflection" (TRR) [75], a complex shock system described in ref. [86].

Most shock wave reflections, in the parameter ranges considered in literature, are of Direct Mach Reflection type—like the ones depicted in figs. 3.3 and 3.4, with a Triple Point moving away from the reflecting surface. Therefore the occurrence of Inverse Mach Reflections is a rare phenomenon, usually limited to the reflection over concave obstacles [79].

In the reference literature [79], concerning the diffraction of planar shock waves by means of curved obstacles, either all the three conditions 1a-2a-3a are observed—in an Inverse Mach Reflection—or none of them is verified—i.e. in Direct Mach Reflections. Numerical results presented in this work, on the contrary, demonstrate a higher level of complexity in the distinction between Direct and Inverse Mach Reflections in the diffraction of curved shock waves. Indeed, only some features correspond to the conditions 1a-2a-3a for the identification of an Inverse Mach Reflection:

1b The offset Δy is non-monotone in space, in accordance with the criterion 1a. This fact implies that, after a transient, the distance between the Triple Point and the re-

flecting surface decreases in space (and time). This is peculiar, because Inverse Mach Reflection was previously observed and analytically derived only for concave obstacles. In the present work, on the contrary, a Triple Point converging towards convex obstacles is observed.

However, it is also true that the reversal of the offset slope—if present—occurs only in correspondence of the trailing edge. This implies that, to detect the offset slope reversal, it is mandatory to include in the reflecting surface both the obstacle and the trailing edge symmetry line. This global reflecting surface, even though it is made up of two convex profiles, is, however, concave.

2b The direction of the slipstream is in partial accordance with the Inverse Mach Reflection one, because for $t/c = 0.07$ and $t/c = 0.14$ the slipstream moves away from the obstacle.

3b The transition from Mach Reflection to Transitioned Regular Reflection can never be observed in the reflection of cylindrical converging shock waves over circular-arc obstacles. Indeed, two impediments can occur, as depicted in fig. 3.20. The first one causes the shock focusing—and therefore the termination of the existence of the imploding wave—to occur when the Triple Point is still moving towards the lower symmetry line. The second one is associated to trailing edge shock reflections. The Triple Point, indeed, belongs to the leading-edge generated Mach stem. Therefore, when $x = x_{TE}$, also the leading-edge generated Mach stem is diffracted over the trailing edge discontinuity into a further Mach stem and a reflected wave. The Triple Point under scrutiny—i.e. the leading-edge generated one—can be observed only before its interaction with these additional waves. Since this interaction necessarily occurs before the Triple Point reaches the trailing edge symmetry line, the Transitioned Regular Reflection cannot take place.

In conclusion, the behavior of the trajectory the Triple Point during the convergence of a cylindrical shock wave appears to be a more complex phenomenon than in the case of a planar shock. Therefore, it cannot be determined whether Inverse Mach Reflections can occur also over circular-arc convex obstacle,

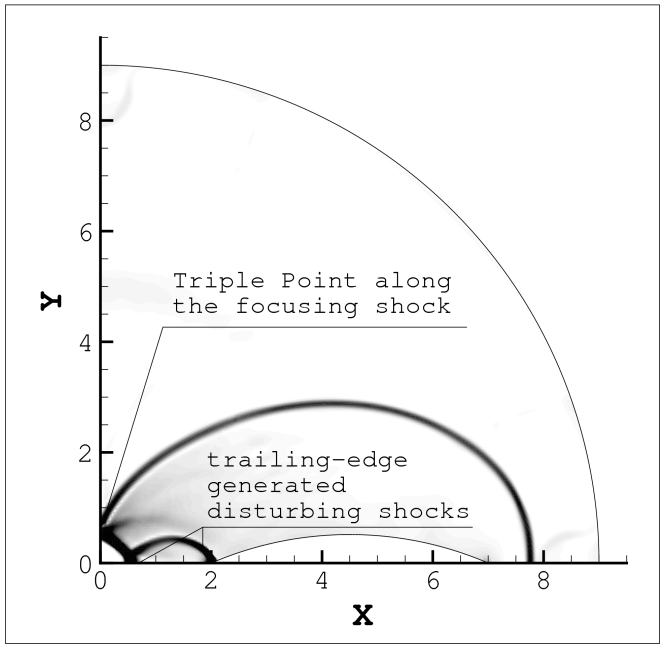

Figure 3.20: Numerical Schlieren of the reflection of a shock with M_s^{LE} = 2.2 over an obstacle characterized by t/c = 0.21 and r_{LE} = 7. The onset of disturbing shock waves at the trailing edge and the simultaneous focusing of the converging shock before the termination of the InMR are visible.

because the classical criteria, i.e. the ones adopted to classify the diffraction of planar shock waves, do no apply.

3.5.2 Propagation of the Triple Point over the complete computational domain

In this section, the propagation of the Triple Point over the whole computational domain is observed. In analogy to sec. 3.5.1, both the trajectories and the offset from the reflecting surface of the Triple Point are analyzed.

3.5.2.1 Triple Point coordinates

The goal of this section is to determine an empirical law which correlates the Triple Point x and y coordinates. In the beginning, polynomial fitting are investigated.

As observed in sec. 3.5.1, in the considered range of initial conditions, the incident shock Mach number appears to have no relevance in determining the Triple Point trajectory, and therefore it will not considered among the influential parameters. On the contrary, a twofold dependence on the obstacle leading edge radius is observed: in a first degree of approximation, only the macroscopic effect of r_{LE} is accounted for, that is its role in the normalization of the Triple Point trajectory. The secondary effect, that is the separation of the groups of curves in correspondence of their peak, is weaker, and therefore it will be neglected in the following.

Therefore, the goal is to provide a correlation between coordinates normalized on r_{LE} and parametrized on t/c,

$$y/r_{LE} = f\,(x/r_{LE};\ t/c)\ . \tag{3.42}$$

Two data fitting are performed: the first will be called "simple interpolation", and consists of a linear regression on all the polynomial coefficients of diverse degree, and will be represented in figures by full lines. The second fitting will be indicated as "constrained interpolation", that is the linear regression on the polynomial coefficients except one, that is evaluated in accordance to the aforementioned assumption (detailed at the beginning of sec. 3.5) that the Triple Point originates at the obstacle leading edge.

To easily deal with the results of the interpolations, the coordinates are transformed, so that the obstacles leading edge—that is the origin of the Triple Point trajectory—becomes coincident with the origin of the Cartesian axes:

$$\begin{cases} x \longrightarrow 1 - x/r_{LE}, \\ y \longrightarrow y/r_{LE}. \end{cases} \tag{3.43}$$

The correlation is therefore in the form

$$y/r_{LE} = f\,(1 - x/r_{LE};\ t/c) \tag{3.44}$$

for both the simple and the constrained interpolation. The constraint becomes

$$f\left(1 - x/r_{LE};\ t/c\right)\Big|_{\substack{x = x_{LE} \\ \forall\, t/c}} = f\left(0;\ t/c\right) = y_{LE}/x_{LE} = 0, \qquad (3.45)$$

resulting in forcing the constant term of the fitting to be null, regardless of the interpolating polynomial degree.

With reference to fig. 3.21, polynomial interpolations of second, third and fourth orders are performed on transformed data. The trajectories are analyzed from the onset of the Triple Point to the focusing, that is $1 - x/r_{LE} \in [0, 1]$. The trajectory exhibits a relevant skewness, which implies that the second order polynomial fitting is not suitable to the description of the Triple Point path.

The fourth degree polynomial appears to capture the Triple Point propagation better than the second and third degree. However, the fourth order degree polynomial can provide at most an "empirical" description of the Triple Point trajectory. Indeed, high order polynomials present several oscillations which are not explained by a model. Therefore, high-order polynomials do not represent the "physics" of the Triple Point propagation.

It must be observed that the description of the trajectory cannot be, in general, performed on the whole domain $1 - x/r_{LE} \in [0, 1]$. Indeed, each time the Triple Point reaches a reflecting surface, its trajectory presents a wedge which cannot be described by a regular function. Moreover, depending on the combination of parameters, when the Mach stem is reflected over the obstacle trailing edge discontinuity, a further Triple Point may arise and possibly disturb the propagation of the observed leading edge Triple Point.

3.5.2.2 Triple Point offset from the reflecting surface

With reference to fig. 3.19, a feature resulting from the observation of the Triple Point offset is a quasi-linear trend between Δy and x while the shock is propagating along the obstacle. Fig. 3.19 represents the case with the best adhesion

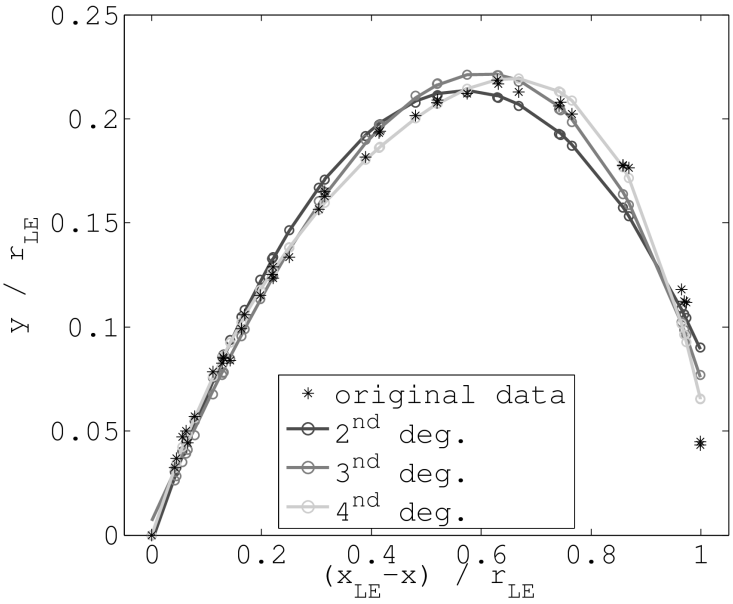

Figure 3.21: Diverse degrees of polynomial used to interpolate the whole TP trajectory ($t/c = 0.21$, $r_{LE} = 7$ case)

to the linear trend, while, on the contrary, fig. 3.22 depicts some cases where the linearity of the correlation is worse.

A linear regression is performed on the data to obtain a law in the form

$$\Delta\widehat{y} = \widehat{h}\,(x - x_{LE})\,, \tag{3.46}$$

where $\widehat{h} < 0$ is the estimated slope of the trajectory offset with respect to $(x - x_{LE})$. After the obstacle trailing edge, since $y_{RS} \equiv 0$, the offset is coincident with the position of the Triple Point, and therefore the variables dependence cannot be linear. For this reason, the regression is performed only on data with $x \in [x_{LE} - c;\ x_{LE}]$.

To quantify the importance of measurement errors on the deviation of numerical results from the linear trend, a goodness-of-fit test is performed on the result of the linear regression reported in eq. (3.46). For all the observed cases, the coefficient PPC is evaluated. This coefficient, namely the Pearson

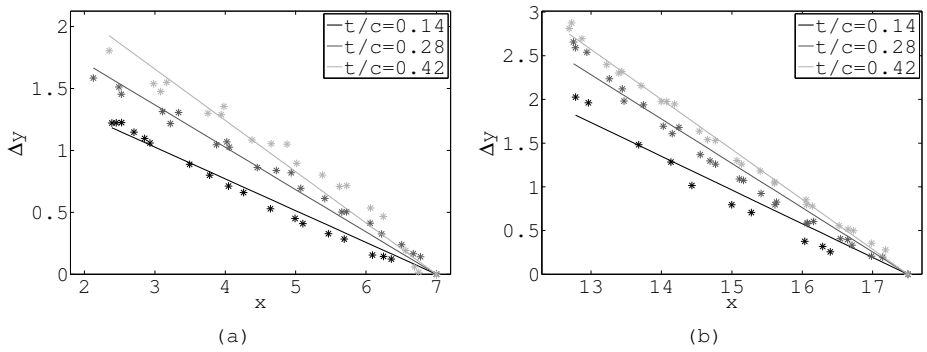

Figure 3.22: Offset of the Triple Point trajectory from the reflecting surface for diverse t/c and r_{LE} values.

product–moment correlation coefficient, indicates the presence of a linear correlation between two groups of data and it is defined as

$$PPC = \frac{Cov(x, \Delta y)}{\sqrt{Var(x)\,Var(\Delta y)}}, \tag{3.47}$$

where Cov and Var indicate the covariance and the variance of the sets of samples [135]. The closer to 1 (the highest admissible value) $|PPC|$ is, the stronger is the correlation; in particular, $|PPC| > 0.7$ suggests the presence of a strong correlation. For all the eighteen sets of data, $PPC < -0.98$, which indicates, indeed, a strong linear correlation.

A second way to test the supposed linearity of Δy versus x consists in using the predicted value of the offset to trace the Triple Point trajectory. Indeed, from the definition of offset, one has:

$$\begin{aligned} y &= \Delta y + y_{RS} \\ &= h\,(x - x_{LE}) + y_0 + \sqrt{R_O^2 - \left(x - x_0\right)^2}, \end{aligned} \tag{3.48}$$

where $y_{RS} \equiv y_o$ because the linear trend of Δy is observed only before the Triple Point reaches the trailing edge.

After a few algebraic passages, the above equation can be rewritten in the form of a generic conic curve

$$\Xi_1 y^2 + \Xi_2 xy + \Xi_3 x^2 + \Xi_4 y + \Xi_5 x + \Xi_6 = 0, \tag{3.49}$$

where the coefficients are defined as:

$$\begin{aligned} &\Xi_1 = 1; && \Xi_2 = -2h; && \Xi_3 = h^2 + 1; \\ &\Xi_4 = 2\left(hx_{LE} - y_0\right); && \Xi_5 = -2\left(h\Xi_4 + x_0\right); && \Xi_6 = \Xi_4^2 - R_o^2 + x_0^2. \end{aligned} \tag{3.50}$$

The type of resulting conic can be determined by discussing the sign of $\left(\Xi_1\Xi_3 - \Xi_2\right)$: the trajectory is hyperbolic for $h < {}^{-1}/\sqrt{3}$, parabolic for $h = {}^{-1}/\sqrt{3}$ and elliptic for $h \in \left({}^{-1}/\sqrt{3}, 0\right)$. Unfortunately, numerical results from the linear regression show that $\widehat{h} = \widehat{h}\,(t/c, r_{LE})$, resulting in values of $\widehat{h}$ larger or smaller than ${}^{-1}/\sqrt{3}$, depending on the obstacle geometry. This result is not compatible with the observation of pseudo-homothetic data with respect to r_{LE} performed in sec. 3.5.1, because the homothetic behavior implies that the analytic expression of $y/r_{LE}\,(x/r_{LE})$ cannot depend on r_{LE}.

In conclusion, the results of this analysis suggest that, despite the qualitative and quantitative indications provided by fig. 3.19 and by the PPC coefficient respectively, the trend Δy with respect to x cannot be linear.

3.5.3 Regression on partial Triple Point trajectories

The analysis of both the trajectories and of the offset of the Triple Point over the whole domain performed in sec. 3.5.2 indicate that the Triple Point path cannot be described by means of polynomial or conic functions; similarly, the Triple Point offset from the reflecting surface does not follow a linear trend.

Therefore the domain of observation of the Triple Point trajectory is restricted to the initial part of the Triple Point propagation, where effects of r_{LE} are negligible (see fig. 3.15) and, therefore, a simple correlation can be found between the Triple Point coordinates.

A second degree polynomial law is used to describe the trajectory, using data sampled during the shock propagation over a restricted domain, that is the obstacle first half-chord. Coefficients are obtained by a least-squares interpolation on

normalized data. The obtained fitting is in the form

$$y/r_{LE} = \Upsilon_2 \, (1 - x/r_{LE})^2 + \Upsilon_1 \, (1 - x/r_{LE}) + \Upsilon_0, \qquad (3.51)$$

where the three coefficients $(\Upsilon_2, \Upsilon_1, \Upsilon_0)$ depend on t/c.

Also for the regression over the restricted domain, simple and constrained interpolations are performed. For the constrained interpolation, coefficient $\Upsilon_0 \equiv 0$ by virtue of the constraint expressed in eq. (3.45). On the contrary, for the simple interpolation, coefficient Υ_0 results from the regression. However, from the analysis of numerical results of the regression, it is verified that Υ_0 remains very close to zero, i.e. $\Upsilon_0/\min(|\Upsilon_2|, |\Upsilon_1|) = \mathcal{O}(10^{-3})$ and furthermore it does not exhibit any dependence on t/c. This result is in agreement with the assumption that the Triple Point trajectory begins in correspondence of the obstacle leading edge, that justifies the constrained interpolation.

Figure 3.23 reports the two coefficients Υ_1 and Υ_2 as functions of the parameter t/c. For both the computational methods—the simple and the constrained interpolations, indicated respectively by a gray full line and the symbol o—the coefficient exhibit a pseudo-linear trend with respect to t/c.

For this reason, a linear fitting is performed on $\Upsilon_2(t/c)$ and $\Upsilon_1(t/c)$. The interpolation is performed on the two coefficients obtained from the constrained data fitting, which allows to neglect the analysis of Υ_0, which is defined null. The linear fitting is depicted in fig. 3.23 by means of a black dashed line. Each of the two coefficients is therefore expressed as a linear function of t/c:

$$\begin{cases} \Upsilon_1 = \Lambda_{1,1} \cdot t/c + \Lambda_{1,0}, \\ \Upsilon_2 = \Lambda_{2,1} \cdot t/c + \Lambda_{2,0}, \end{cases} \qquad (3.52)$$

where Λ are the coefficients of the linear regression reported in fig. 3.23. The first subscript of each Λ indicates the associated Υ and the second represents the corresponding order of the term in the linear correlation.

Therefore, in accordance to the assumption underlying the constrained interpolation, the Triple Point trajectory during

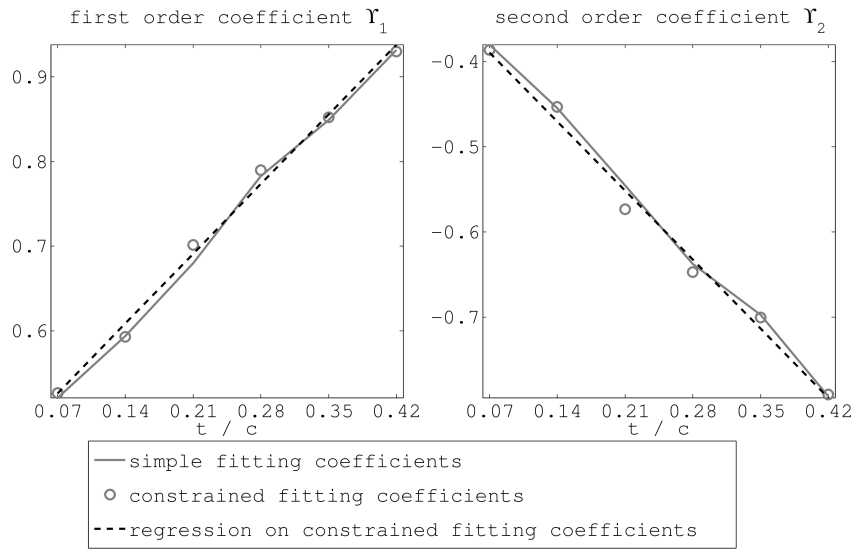

Figure 3.23: Coefficients Υ_1 (left) and Υ_2 (right) of the correlation $y/r_{LE} = \Upsilon_2 (1 - x/r_{LE})^2 + \Upsilon_1 (1 - x/r_{LE}) + \Upsilon_0$.

the first part of the propagation follows a law in the form

$$y/r_{LE} = \left(\Lambda_{2,1} \cdot t/c + \Lambda_{2,0}\right) \cdot (1 - x/r_{LE})^2 + \left(\Lambda_{1,1} \cdot t/c + \Lambda_{1,0}\right) \cdot (1 - x/r_{LE}) , \tag{3.53}$$

which describes a sheaf of vertical-axis parabolas passing by the two base points $(0; 0)$ and $-\Lambda_{1,1}/\Lambda_{2,1}\left(1; \Lambda_{1,0} - (\Lambda_{2,0}\Lambda_{1,1})/\Lambda_{2,1}\right)$, as reported in fig. 3.24.

The suitability of the parabolic function to the description of the Triple Point trajectory in its initial part is verified by comparing numerical data to analytically predicted trajectories. In fig. 3.25, the two levels of regression are exposed: the first level, i.e. the second order polynomial fitting on samples is indicated by gray lines (for the simple interpolation) and by the symbol ○ (for the constrained interpolation). The second level of regression, that is the linear interpolation over parabolic coefficients, as indicated by eq. (3.53), is depicted by means of a black dashed line. For the second level of regression, only results for the constrained

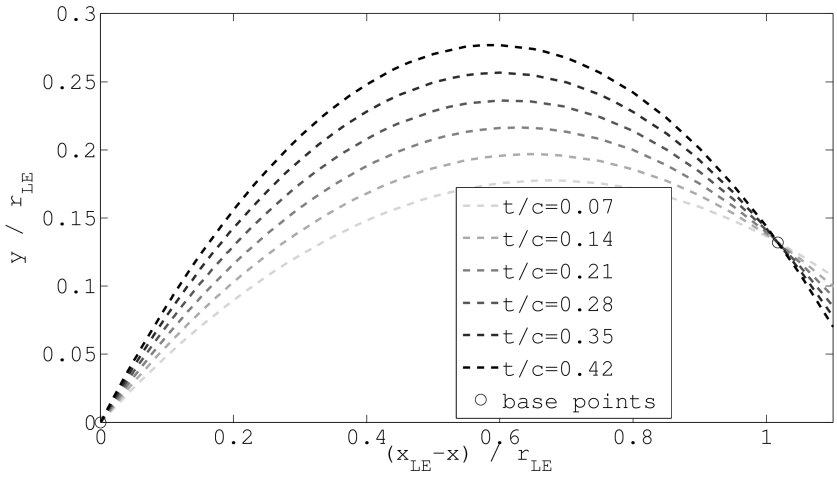

Figure 3.24: Extrapolated Triple Point trajectories after the regression performed on the parabolic coefficients.

interpolation are reported for higher clarity. The results for the simple interpolation, however, present an excellent overlapping with the constrained interpolation ones.

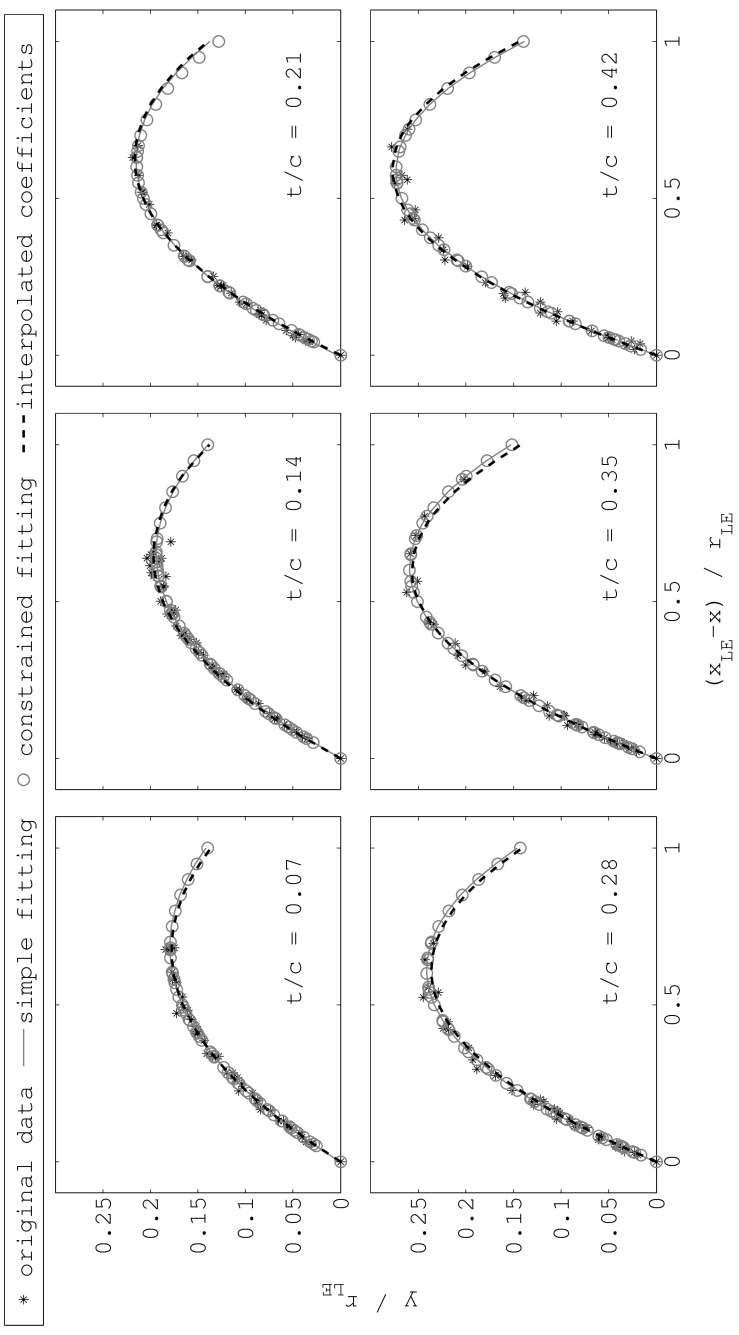

Figure 3.25: TP trajectories data relative to the first half-chord: original data (*), simple regression on original data (gray full line), constrained regression (gray circles) and plot of the curve $y/r_{LE} = a\,(1 - x/r_{LE})^2 + b\,(1 - x/r_{LE})$ with a and b obtained from the linear regression (black dashed line).

Final remarks

It is worth noticing that results reported in this chapter have been derived under strong assumptions, and therefore they represent an empirical description of cylindrical shocks reflections over circular-arc obstacles without performing an insight on the physics of the shock diffraction. In the detail of the RR $\longrightarrow$ MR transition, indeed, the dependence of the transition angle on the shock Mach number is assumed to be a second-order effect, and therefore it was not further detailed. Moreover, the slight dependence of the Triple Point trajectory shape on the leading edge radius r_{LE}, observed for obstacles with $t/c \in [0.28, 0.42]$, was neglected and following computations were performed over normalized data.

On the contrary, the advantage of this approach is that it covers the whole range of admissible obstacle thickness: with reference to fig. 3.6, for $M_s^{LE} \approx 2$ and higher, the dependence of the RR $\longrightarrow$ MR transition wedge angle on the incident shock Mach number is negligible, let alone null. Therefore, the effects of all the possible t/c values which generate a leading edge Regular Reflection are explored in sections 3.3 and 3.4.

Similarly, the correlation between the Triple Point position and the obstacle thickness (sec. 3.5) covers all the admissible values of t/c which produce a Mach Reflection at the leading edge.

This implies that the correlations derived in secs. 3.3, 3.4 and 3.5 can be adopted, even if they are known in advance to be able to provide only a phenomenological description. The reason is that their predictive ability is expected to be fairly good albeit their simpleness, because the domain on which they can be applied is coincident with the one used to define them.

The only parameter whose effect is neglected, due to its weak effect, is the (local or incident) shock Mach number. However, for shocks stronger than the explored ones, high temperature effects become non-negligible, and therefore the polytropic ideal gas model cannot apply. On the contrary, if weaker shocks are considered, it is necessary to keep into account that the physics of weak shock reflections [128] is much more

complex than the one used to describe Regular and Mach Reflections. Therefore, different computational methods and assumptions would be required to describe the reflection of weak or very strong shocks.

In conclusion, the domain of shock Mach numbers where the proposed correlations are valid cannot be further extended.

Chapter 4

Shock reshaping and focusing in dilute gas

> [. . .] systems are never in equilibrium. They are inherently unstable. They may seem stable, but they're not. Everything is moving and changing. In a sense, everything is on the edge of collapse.
> — MICHAEL CRICHTON, JURASSIC PARK

This chapter describes the interaction between a cylindrical converging shock wave and an array of symmetrically-arranged aerodynamic obstacles. The outcome of this interaction is the shock reshaping, i.e. the transformation of the front shape into a pseudo-polygonal, more stable one. The shock stability is of fundamental importance considering the possible applications of converging shock waves, e.g. Inertial Confinement Fusion and Sonoluminescence, which require extremely high temperature and pressure at the focus point.

The goal is to find the configurations which provide the optimal level of energy concentration. Alternative experimental configurations are therefore devised from the reference one described in sec. 1.1 ($n_{obs} = 8$, $t/c = 0.14$, $r_{LE} = 7$, $M_s^{LE} = 2.7$, cf. [97]) by varying both the obstacle layout and the operating conditions. Other parametric studies have been performed on the interaction between shock waves and reflecting walls, as in [59] and in the more recent [136, 59], but never in the perspective of an empirical optimization of the energy focus-

ing by means of a cylindrical converging shock wave. Numerical simulations are performed, whose results are exposed in this chapter, to explore a wider range of geometrical configurations and operational parameters, with the purpose of finding alternative, more efficient, solutions. As in the reference case, the polytropic ideal gas model is adopted.

Numerical simulations are also used to explore in detail the reflection patterns generated by the multiple reflections of shock waves over material and symmetry boundaries. The effect of the diverse factors is assessed both on the final shock effectiveness and on the flow structures generated during the convergence.

4.1 Numerical simulations setting

The setting of the numerical simulations is described in this section. In sec. 4.1.1 the design of experiments is described: the investigated parameters, the considered values of each parameter and the preliminary analysis which allowed to restrict the factorial design with respect to the one adopted in chap. 3. In sec. 4.1.2, the adopted spatial and temporal discretization are described and justified by numerical results. Eventually, the position of the shock wave computed by means of numerical simulations is compared with reference values of R_S to verify numerical results.

4.1.1 Design of experiments

Numerical simulations are performed over a factorial design including all the factors investigated in chap. 3 (incident shock Mach number M_S^{LE}, obstacle thickness-to-chord ratio t/c and leading edge radius r_{LE}) and the number of obstacles n_{obs}. Recalling that the final goal is to obtain high values of pressure and temperature, a preliminary investigation is performed to restrict the factorial design to the most relevant region, and reduce the computational cost.

Thickness-to-chord ratios are set respectively equal to $t/c = t/c^{ref}$, ±50%, that is $t/c = 0.14$, 0.21 and $t/c = 0.07$, corresponding to the three lowest t/c values investigated in chap. 3. The choice is motivated by the symmetry with respect to reference conditions, and the boundary of this range are selected to respond to two a priori requirements. The first one stems from an observation derived from a preliminary analysis, that the reshaped shock effectiveness decreases for increasing t/c (upper t/c limit). The second one is the need of obtaining Mach Reflections at the leading edge—which are used to ignite the reshaping process—which is guaranteed only by obstacles with a t/c ratio between 0.07 and 0.42, in accordance with the results presented in chap. 3.

The reference Mach number of the shock M_s^{LE}, evaluated at a brief distance from the obstacle leading edge at reference distance, is 2.7. This value is varied on three levels (reference M_s^{LE}, ±20% corresponding respectively to 2.7, 3.2 and 2.2). Therefore only initial pressure ratios β_P of 11, 16 and 27 are considered. It is true, indeed, that stronger shocks can produce higher energy concentration at the focus point, resulting in higher pressure and temperature values, but considering shock waves generated by β_P up to 130, as in chap. 3, would present two limitations. The first one is that the shock Mach number, and therefore its intensity, have a less-than-linear growth with β_P, as reported in fig. 4.1. The second limitation is that the stronger is the shock, the higher are density and temperature in the flow field, resulting in a loss of accuracy of the results if computations are performed under the polytropic ideal gas assumption.

The various numbers of obstacles n_{obs} are selected after a preliminary analysis over a wide range. Results for $t/c = 0.21$ and $r_{LE} = 7$ are reported in fig. 4.2, which confirms the goodness of the choice performed in reference works [97] to use an array of 8 obstacles. Arrays of six, eight and sixteen obstacles are therefore investigated. It must be noticed that a similar trend was found in [94] while investigating the reshaping induced by cylindrical obstacles, as depicted in fig. 4.3

Obstacles are arranged at once, twice and 2.5 times the

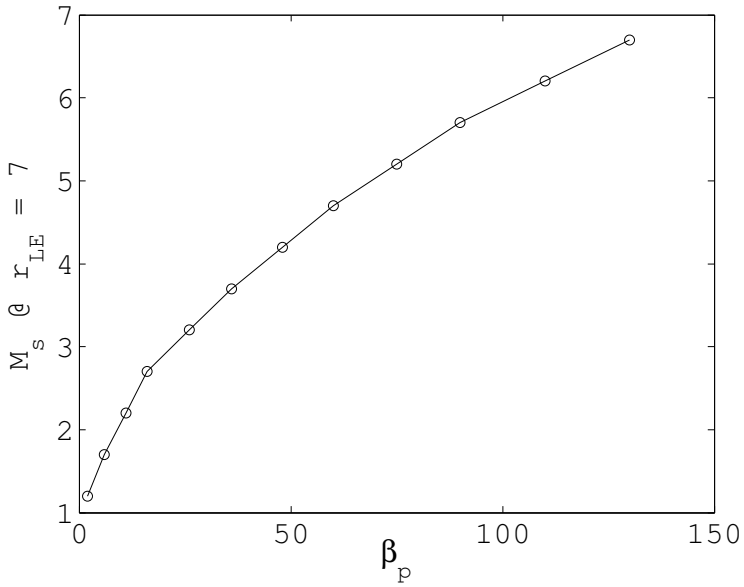

Figure 4.1: Shock Mach numbers obtained at a small distance upstream the obstacle leading edge (r_{LE} = 7) versus the initial pressure ratio that generates the shock. The decreasing efficiency of the shock generation can be observed.

reference value r_{LE}^{ref}, corresponding respectively to 7, 14 and 17.4. For this case, the range is maintained equivalent to the one explored in chap. 3, because the preliminary analysis show that also pressure and temperature attained at the focusing present a slight dependence on r_{LE}. Cases with a leading edge radius lower than r_{LE}^{ref} are not considered, because this would result in reciprocal geometric interferences between adjacent obstacles, for the considered n_{obs}.

The considered parameter ranges are listed in table 4.1, generating a full factorial design including 81 treatments [135]. Local extensions of the full factorial design are considered: the case with no obstacles is also investigated for reference, the 24-obstacle case is partially explored to gain a better insight of the physics of the flow in the channel between two obstacles, and the flow induced by the interaction

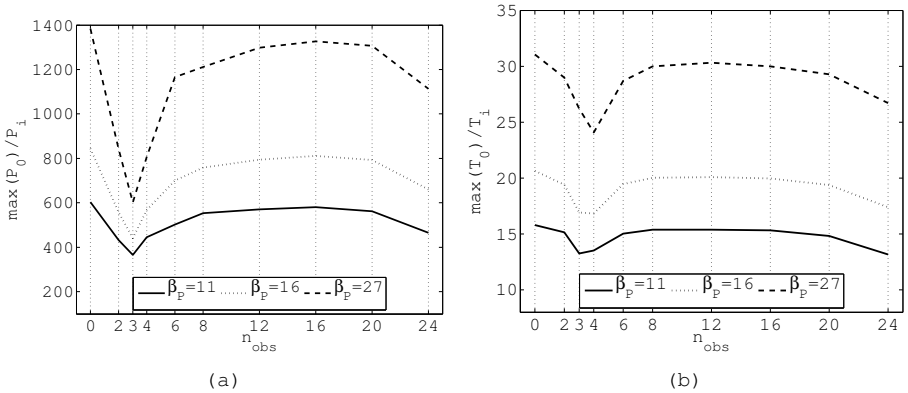

Figure 4.2: (a) Pressure and (b) temperature at the origin as functions of the number of obstacles, parametrized on the leading edge Mach number, for obstacles with $t/c = 0.21$ and $r_{LE} = 7$. Please compare the trend of pressure and temperature at the focus point versus n_{obs} with results obtained with cylindrical obstacles in fig. 4.3

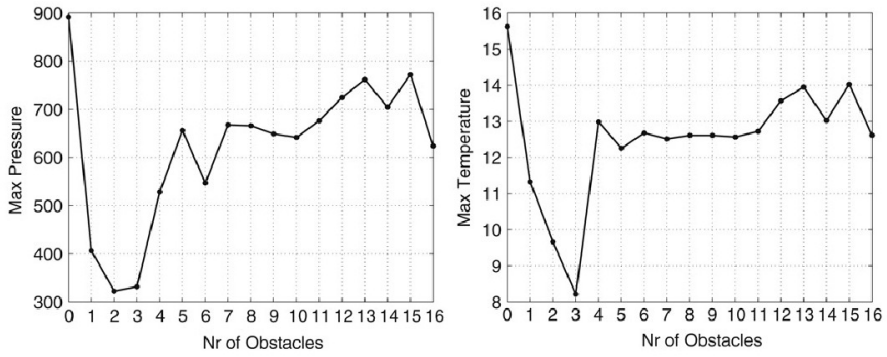

Figure 4.3: Maximum pressure and temperature near the focal point as s function of the number of cylinders (initial $M_S = 2.4$, $\widehat{r}_{LE} = 46.25\,mm$, $\widehat{c} = 15\,mm$). (Image and caption source: V. Eliasson, W.D. Henshaw, D. Appelö, "On cylindrically converging shock waves shaped by obstacles", Physica D (2008).)

Number of obstacles	n_{obs}	6	8	16
Thickness-to-chord ratio	t/c	0.07	0.14	0.21
Leading edge coordinate	r_{LE}	7	14	17.5
Initial pressure ratio	β_P	11	16	27

Table 4.1: Test matrix for the numerical experiments. Considered parameters are the number of obstacles n_{obs}, the thickness-to-chord ratio t/c, the radial coordinate of the obstacle leading edge r_{LE} and the initial pressure ratio β_P. In all tests, the operating fluid is air in standard conditions, with $\gamma = 1.4$. The value that the parameter assumes in the reference configuration in ref. [97] is evidenced.

between the shock and cylindrical obstacles is described.

4.1.2 Assessment on grid spacing and time step

Numerical simulations are carried out with the application of the multi-domain approach described in chap. 2. In the obstacle region, the simulations are performed on a fixed grid with a number of grid nodes ranging from 50000 to 400000, depending on the computational domain size, with an a priori refinement in correspondence of the regions of interest, which include the obstacles leading and trailing edges, the shock reflection region and the focusing region.

The grid and time-step dependence is verified for a range of grid element sizes and time step levels, as reported in figures 4.4 and 4.5, respectively. The above simulations were carried out considering $n_{obs} = 16$, reference r_{LE} and t/c, and an initial pressure ratio $\beta_P = 60$, a condition that is more demanding in terms of space and time resolution than all cases considered in the present study.

In figure 4.4, the non dimensional pressure profile over the bottom symmetry line and the obstacle surface is reported at four relevant time level, corresponding to the impinging shock being located at 25% (figure 4.4(a)), 50% (figure 4.4(b)),

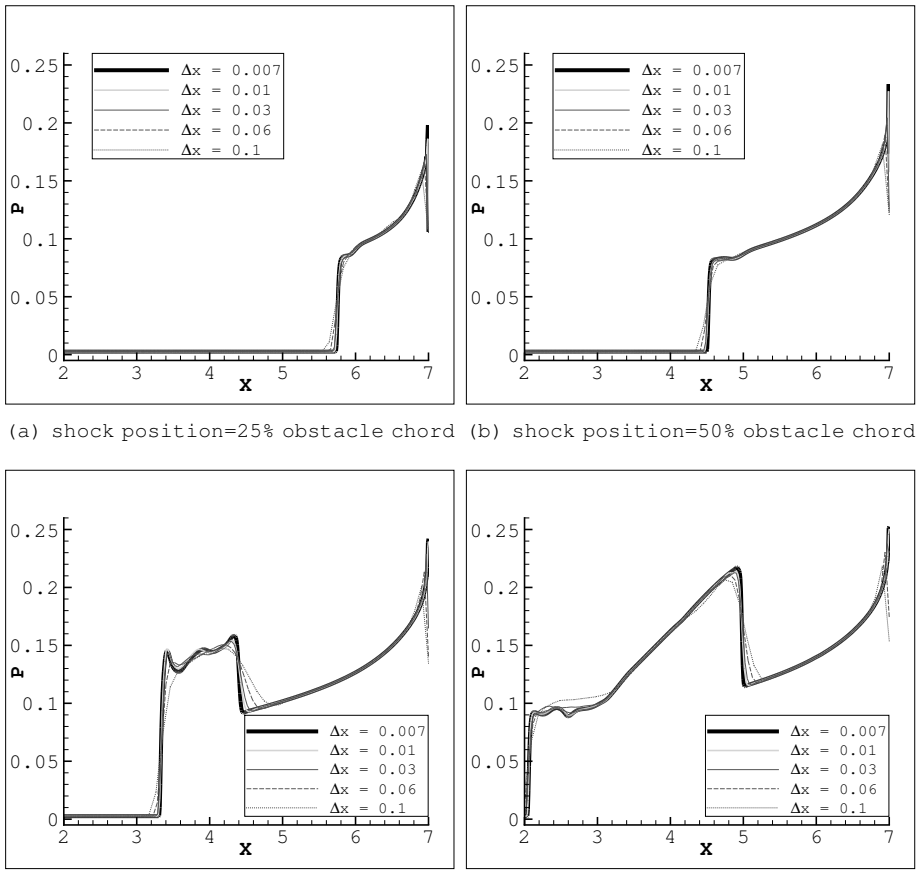

(a) shock position=25% obstacle chord (b) shock position=50% obstacle chord

(c) shock position=75% obstacle chord (d) shock position=obstacle trailing edge

Figure 4.4: Pressure—obtained with different meshes—on the obstacle during the propagation of a shock with Mach number of 4.7 at r_{LE}^{ref}. The time step is $\Delta\tau = 6 \times 10^{-4}$ in all simulations. The shock advancement at each figure corresponds to 25% of the obstacle chord.

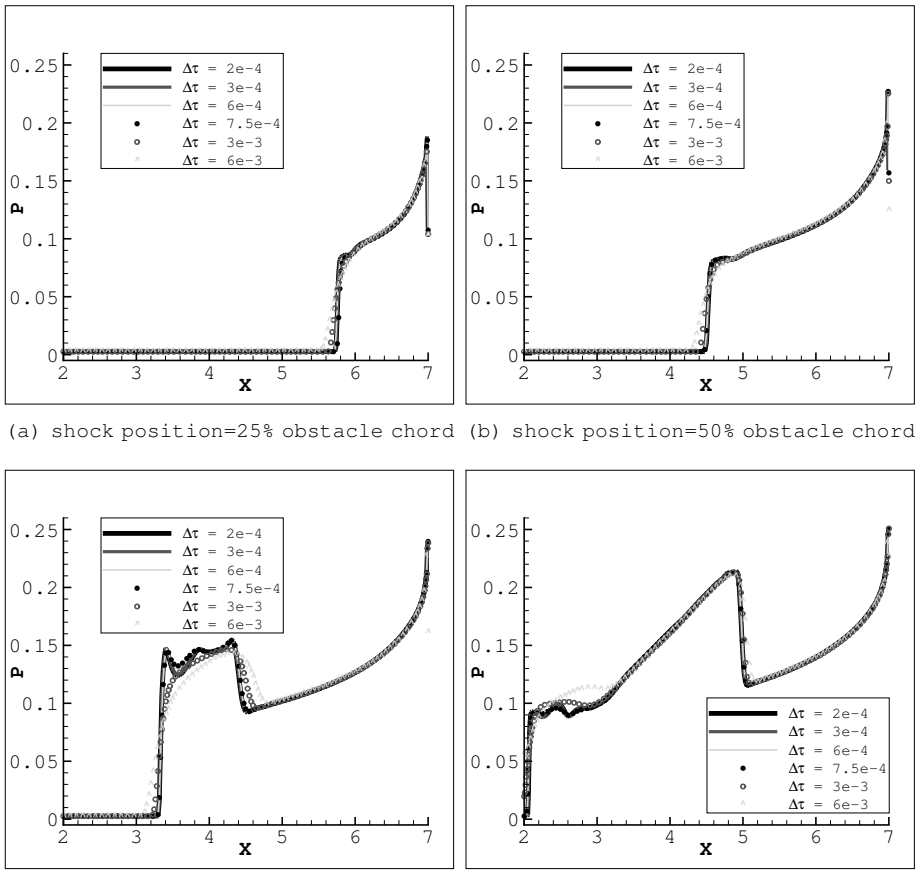

(a) shock position=25% obstacle chord (b) shock position=50% obstacle chord

(c) shock position=75% obstacle chord (d) shock position=obstacle trailing edge

Figure 4.5: Pressure—obtained with different time steps—on the obstacle during the propagation of a shock with Mach number of 4.7 at r_{LE}^{ref}, over a grid made of 56000 nodes ($\Delta x = 0.01$). The shock advancement at each figure corresponds to 25% of the obstacle chord.

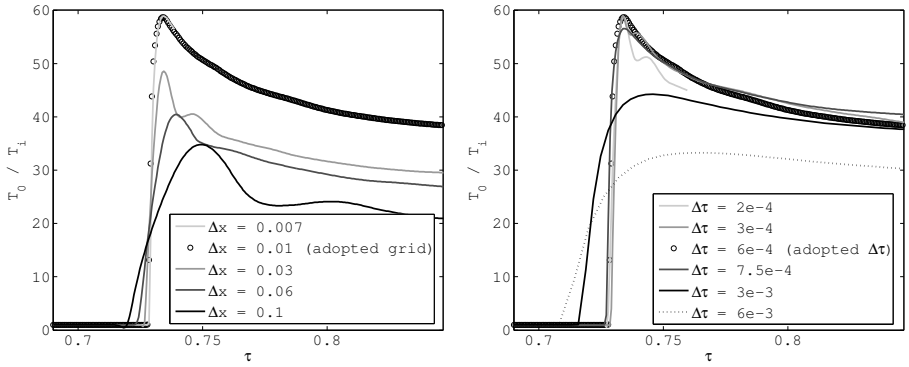

(a) Constant time step $\Delta\tau = 6 \times 10^{-4}$ (b) Constant grid spacing $\Delta x = 0.01$

Figure 4.6: Temperature value at the focus point versus time for different space (a) and time (b) discretizations.

75% (figure 4.4(c)) and 100% (figure 4.4(d)) of the obstacle chord. Five different grids are considered, with reference grid length Δx scaling from 0.1 to 0.007, with Δx being the maximum element linear size. All simulations in figure 4.4 were carried out with a time step $\Delta\tau = 6 \times 10^{-4}$, that is the one adopted for all the simulations.

The pressure profiles in figure 4.4 are found to be almost independent from the grid spacing for the three most refined grids, namely, $\Delta x = 0.03$, 0.01 and 0.007.

In figure 4.5, the pressure profile over the bottom symmetry line and the obstacle surface is reported the the same four time levels as in figure 4.4 for six different values of the time-step $\Delta\tau$, ranging from 6×10^{-3} to 2×10^{-4}. All simulations in figure 4.5 were carried out over a grid made of 56000 nodes ($\Delta x = 0.01$). The pressure profiles obtained with the three smallest time steps, $\Delta\tau = 2 \times 10^{-3}$, 4×10^{-3} and 6×10^{-3} exhibit a satisfactory overlap.

Finally, figure 4.6 illustrates the focus point temperature-internal temperature ratio over time for different time and space discretizations. In particular, results in figure 4.6(a) are computed for different grids resolution using the same time step of $\Delta\tau = 6 \times 10^{-4}$; results in figure 4.6(b) are computed for different time steps over a grid with 56000 nodes ($\Delta x = 0.01$). Not surprisingly, the accurate determina-

tion of the temperature profile at the focus point is the most demanding quantity in terms of grid and time-step resolution. Therefore, it is used here to select the grid and the time-step to be used in the following.

The selected grid spacing and time step are the aforementioned $\Delta x = 0.01$ and $\Delta\tau = 6 \times 10^{-4}$ respectively. It must be noted that the same grid spacing (with the proper local refinements) adopted for the simulation of the leading edge reflection patterns in chap. 3 (sec. 3.1.2.2) represents a valid spatial discretization also when the focusing must be observed. On the contrary, the time step requires a further refinement, as the $\Delta\tau = 10^{-3}$ selected in chap. 3 does not allow to correctly capture the temperature profile at the focus point.

4.1.3 Comparison to self-similar solutions and experimental results

To test the reliability of numerical results, a comparison with the self-similar solution proposed by Guderley is provided [39]:

$$R_s = \tilde{r}\left(1 - \frac{\tau}{\tilde{\tau}}\right)^{\alpha}, \tag{4.1}$$

where quantities $\tilde{r}$, $\tilde{\tau}$ and α have been introduced in sec. 3.3. The value of the self similarity exponent α can be obtained by means of different methods, as discussed in refs. [39, 63, 48, 47]. Details on the applicability of the law are discussed in sec. 3.3. One of the assumptions which allow to perfectly apply the self-similar model is that the shock is "near" its focus point. In the following, in accordance with the approach adopted in the main reference paper [97], the shock average position is evaluated after the shock wave has passed the trailing edge, that is for $r \leq 2$.

Figure 4.7 reports the shock dimensional radii in time, and compares numerical results to experimental one available in ref. [97] ($n_{obs} = 8$, $r_{LE} = 7$, $t/c = 0.14$, $M_s^{LE} = 2.7$) evaluated at the same dimensional times. Furthermore, analytical power-law curves are depicted, for both cylindrical and octagonal-like shocks.

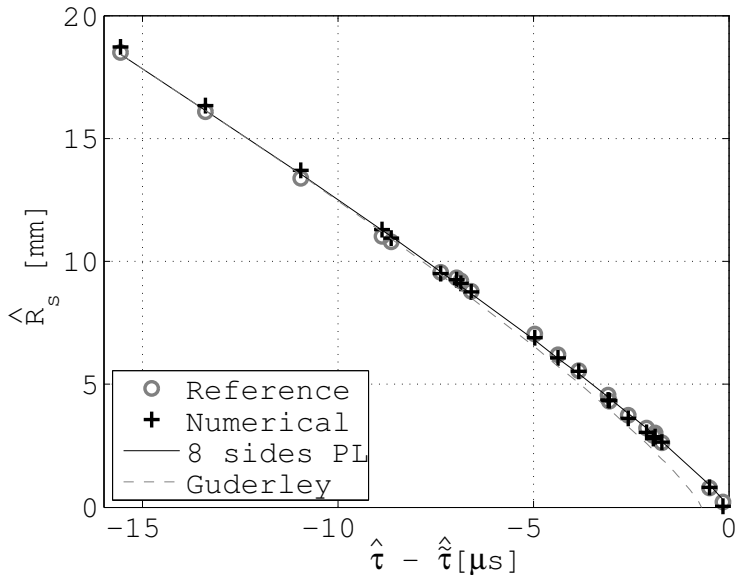

Figure 4.7: Experimental (○) and numerical (+) results of the shock position for the reference case and analytical power laws: cylindrical shock (dashed line) and octagonal-like shock (full line) exponents.

In figure 4.8, the average radii of polygonal shocks are plotted versus time for diverse values of n_{obs} with respect to the reference condition. The shocks are generated by the reflection of cylindrical shocks with M_s^{LE} = 2.7 over arrays of 6, 8, and 16 obstacles with r_{LE} = 7 and t/c = 0.14. Results for cylindrical shocks are reported for comparison. As demonstrated in ref. [88], polygonal shocks exhibit a self-similar behavior and therefore a power law can be used to represent the data, provided that the so-called Schwendeman's conditions are satisfied, namely, that the shock front has a regular polygonal shape. As discussed in sec. 1.1, only in the reference case the reshaping is regular enough to satisfy Schwendeman's conditions. However, due to the high radial symmetry of the problem, it is still possible to to apply a power-law fit to the other configurations as well. Self-similarity exponents obtained with the fitting are 0.836 for the cylindrical shock (which is in good accordance with the theoretical value of 0.834), 0.879 for n_{obs} = 6, 0.873 for n_{obs} = 8 (which is in agreement to the reference value of 0.875 reported in ref. [97]) and 0.858 for n_{obs} = 16.

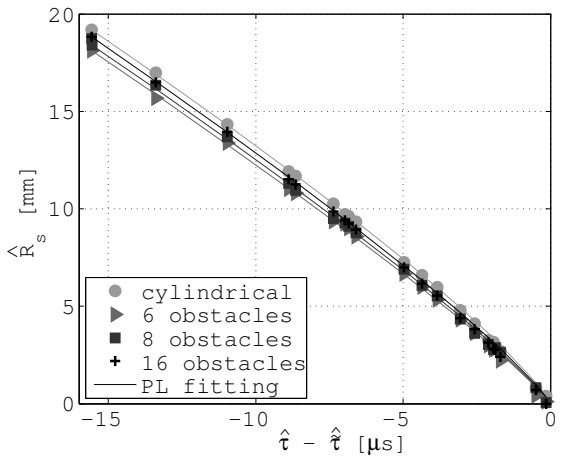

Figure 4.8: Shock position versus time for cylindrical (●) and reshaped shocks obtained with arrays of 6 (▶), 8 (■), and 16 (✚) obstacles. Power law fittings is shown in solid lines.

Shock Mach numbers are compared with available experimental data [97] and are reported in figure 4.9. The average shock

Mach number is computed as the ratio of the front speed s and the speed of sound in the unperturbed region. The shock speed s is obtained by means of three methods. In the first approach, the shock speed is computed as the analytical derivative of the power law (PL). In the second one, s is obtained by means of centered finite differences (FD) of the shock position in time as follows

$$M_s^{PL}(\tau_k) = \frac{1}{w_i} \left. \frac{dR_s^{PL}}{d\tau} \right|_{\tau_k}, \tag{4.2}$$

$$M_s^{FD}(\tau_k) = \frac{1}{w_i} \frac{R_s(\tau_{k+1}) - R_s(\tau_{k-1})}{\tau_{k+1} - \tau_{k-1}}. \tag{4.3}$$

The last method moves from the mass conservation law across the shock front. In a reference frame moving at the flow velocity in the unperturbed state, from the Rankine–Hugoniot conditions one has

$$M_s^{RH}(\tau_k) = \frac{1}{w_i} \frac{\left|\underline{m}\left(R_e(\tau_k)\right)\right|}{\rho\left(R_e(\tau_k)\right) - \rho_i}, \tag{4.4}$$

where it is recalled that w and $\underline{m}$ indicate the flow speed of sound and momentum and subscripts $_i$, $_e$ denote the internal and the external conditions of the imploding shock. Since the fluid is at rest ahead of the shock front, the above relation is valid here in the laboratory reference as well.

Results are reported in figure 4.9(a), where the three criteria are compared to the power-law fit. Notably, M_s^{FD} shows a reasonable agreement with the reference. Note that to reduce the dispersion in the numerical evaluation of the derivatives, only data set with a significant separation in time were considered. A comparable dispersion is observed for the so-called Rankine–Hugoniot method ((4.4)), which probably suffers from the high spatial variability of the quantities behind the reflected shock, in particular near the focusing.

A quantitative comparison is performed for the reference case ($n_{obs} = 8$, $t/c = 0.14$, $r_{LE} = 7$, $M_s^{LE} = 2.7$). In this case, it is possible to use the theory in ref. [88] to compute the ratio between the Mach number $M_{s,n}$ of the polygon edges generated at the n – th reflection and $M_{s,n-1}$. Similarly to ref. [97], the average shock Mach number between two consecutive reflection

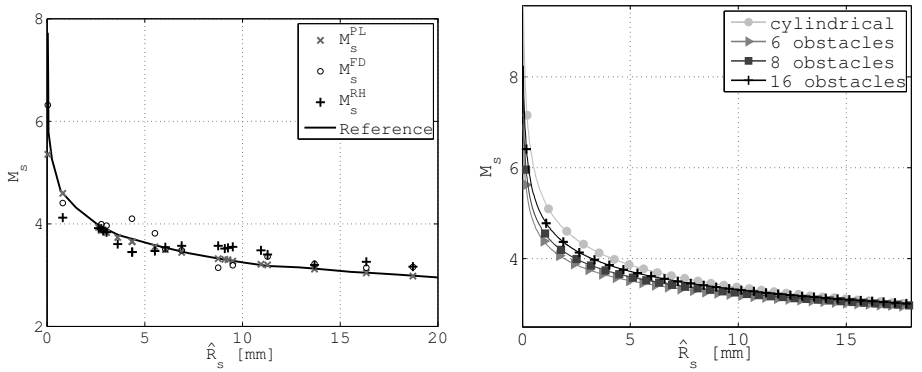

Figure 4.9: (a) Shock Mach number at diverse radial positions calculated with diverse estimation methods for the shock speed. Analytical derivative of Guderley's law (✖), centered finite differences (○), Rankine–Hugoniot relations (+). Reference value from ref. [97] is in bold full line (——). (b) Mach numbers versus radius from fitting for diverse n_{obs} for the reference M_s^{LE} and geometry.

	$M_{s,1}/M_{s,cyl}$	$M_{s,2}/M_{s,1}$	$M_{s,3}/M_{s,2}$
Theory (ref. [88])	–	1.201	1.201
Experim. (ref. [97])	–	1.20±0.02	1.19±0.03
Simul. (Present)	1.190	1.200	1.207

Table 4.2: Ratios of the Mach numbers of shock edges generated between consecutive reflections. Theoretical predictions are from ref. [88], experimental data from ref. [97] and present numerical simulations.

is estimated by means of a stepwise linear regression on the shock radius. Theoretical,[88], experimental [97] and numerical results are reported in table 4.2 for three reflections. A very good agreement is found for the reference configuration. Note that in the first reflection, the incident shock front is cylindrical and therefore the theory could not be fully applicable.

4.2 Maximum pressure and temperature at the focus point

Results of numerical simulations are reported in current and next section. The most relevant quantities in shock focusing are the maximum values of the pressure and temperature factors attained at the focus point. The compression factor and the temperature factor are defined as

$$c_P = P_0^M(k)/P_i, \tag{4.5a}$$

$$c_T = T_0^M(k)/T_i, \tag{4.5b}$$

where $P_0^M(k)$ and $T_0^M(k)$ are respectively the minimum-time pressure and temperature values in the origin such that

$$P_0^M(k) \geq \max\left(P_0(k+1), P_0(k-1)\right), \tag{4.6a}$$

$$T_0^M(k) \geq \max\left(T_0(k+1), T_0(k-1)\right). \tag{4.6b}$$

The condition on the minimum time is introduced because of the complex flow structure behind the reshaped shock, where several reflected waves are present: as reported also in fig. 4.6, after the shock focusing a number of reflected waves reaches the origin and may possibly cause a further increase in pressure and temperature. However, only the P and T peak values due to the main shock are relevant for applications.

Figure 4.10 reports c_P (a) and c_T (b) at the origin as functions of the shock Mach number M_s at r_{LE}^{ref}, as well as the obstacles aspect ratio. The curves are parametrized by the number of obstacles. The shock Mach number at the impingement is considerably more influential than the number of obstacles, for reference obstacle shape and position. Moreover, the pressure

peak attained present in general a non monotone trend with respect to the number of obstacles.

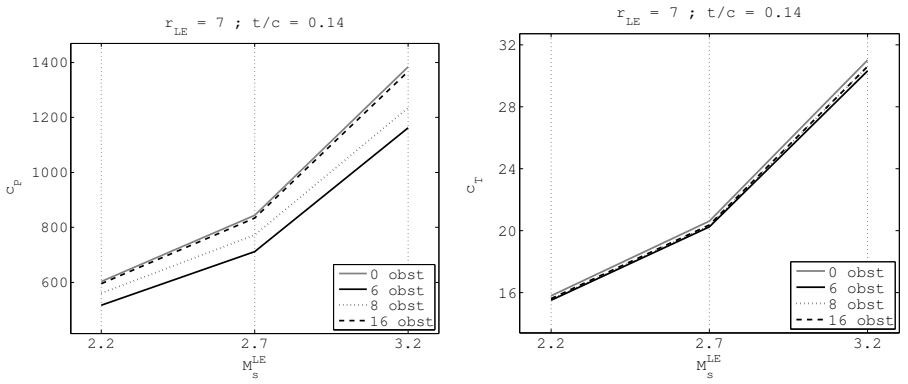

Figure 4.10: Maximum pressure (a) and temperature (b) attained at the origin after a reshaping obtained by means of obstacles with reference aspect ratio.

Figures 4.11 and 4.12 illustrate the same quantities, but for higher and lower t/c values, respectively. For both types of obstacles the monotone increasing trend is preserved with respect to the shock Mach number.

Figs. 4.10 to 4.12 show that the separation of the curves related to temperature is negligible. This corresponds to the non-monotone trend of c_P and c_T with respect to n_{obs} observed in fig. 4.2.

The effects of the obstacle position and aspect ratio are reported in figure 4.13: even for diverse combinations of M_S^{LE} and number of obstacles, the highest temperature values are obtained for obstacle with thickness-to-chord ratio of 0.07, with no relevant exceptions. The temperature dependence on the leading edge radius is generally non-monotone.

According to the present simulations, the configuration producing the highest temperature at the focus point is the combination of sixteen obstacles with $t/c = 0.07$ located at

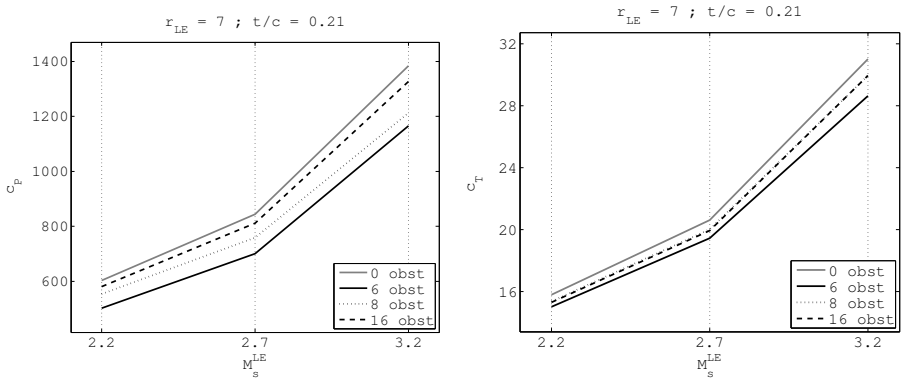

(a) (b)

Figure 4.11: Maximum pressure (a) and temperature (b) attained at the origin after a reshaping obtained by means of obstacles with thickness-to-chord ratio of 0.21, corresponding to 150% of the reference value.

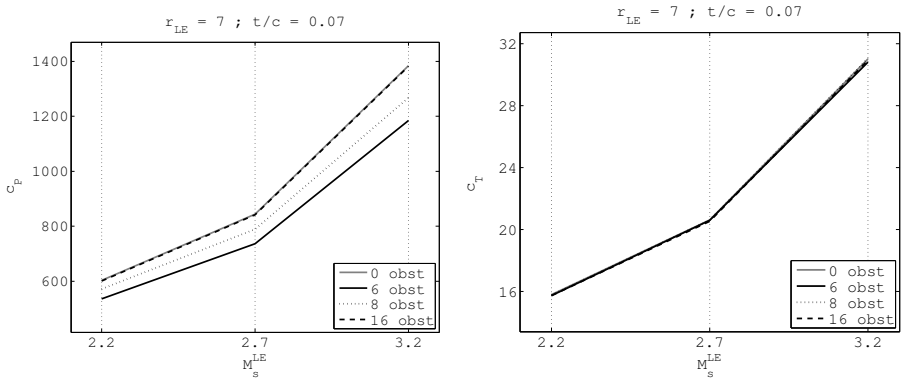

(a) (b)

Figure 4.12: Maximum pressure (a) and temperature (b) attained at the origin after a reshaping obtained by means of obstacles with thickness-to-chord ratio of 0.07, corresponding to 50% of the reference value.

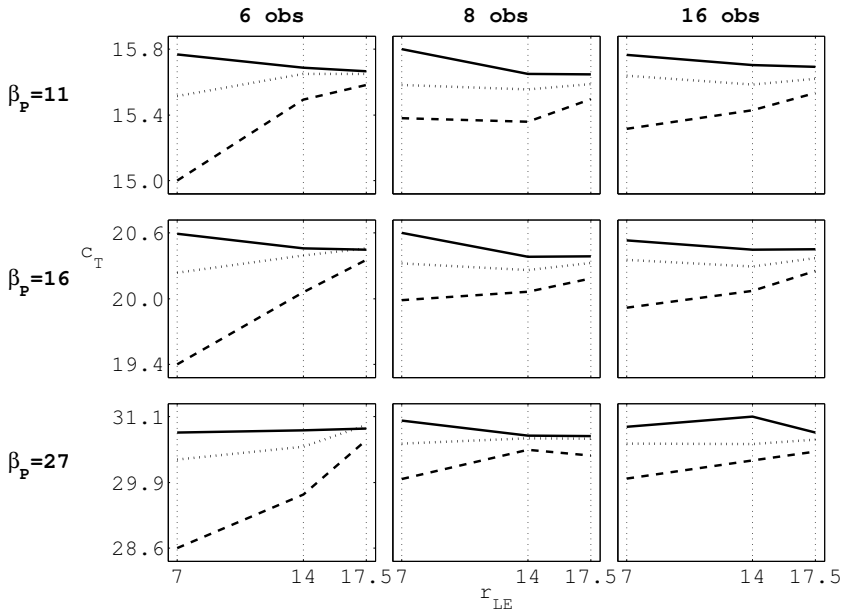

Figure 4.13: Maximum temperature value attained at the focus point for reference shaped obstacles versus leading edge radius for diverse M_s^{LE} and n_{obs}, parametrized by the obstacle thickness-to-chord ratio: 0.07 (full line), 0.14 (dotted line), 0.21 (dashed line).

twice the reference distance and overrun by a shock generated by an initial pressure ratio $\beta_P = 27$. For this case, the temperature peak interval, defined as the time interval along which the temperature remains within the 90% of the maximum value, is approximately $\Delta\tau/\tilde{\tau} = 0.013$. It is remarkable that this new configuration delivers a focus efficiency that is only slightly better (2 – 3%) than the reference one at the same Mach number, thus confirming the goodness of the obstacle arrangement proposed in ref. [97].

4.3 Non-leading edge reflection patterns

Shock reflection patterns are described in this section. Sec. 4.3.1, describes the pseudo-polygonal shocks resulting

from the reshaping, highlighting the possible formation of shocks with more edges than the theoretical expected value of n_{obs} and $2n_{obs}$. The features of the reflections occurring downstream the leading edge are the topic of the following three sections. In particular, the reflection of wave A over the upper symmetry boundary is discussed in sec. 4.3.2, the effect of the obstacle concavity and leading edge position on the interaction of the multiple-waves systems is presented in sec. 4.3.3 and the overall number of reflections of the shock before its focusing is reported in sec. 4.3.4. Eventually, section 4.3.5 discusses the results of numerical simulations applied to the case of cylindrical obstacles.

4.3.1 General shock reshaping process

Past the leading edge reflection, that is the first step in accordance to the nomenclature in section 1.1, diverse patterns can be identified depending on the obstacle arrangement and geometry.

Indeed, the shock reshaping process described in section 1.1, where four distinct steps take place and the final shock consists of a regular polygonal front, is not the most recurrent in the considered range of design parameters, since it occurs only for peculiar combinations of the shock speed and the geometry. More frequent is the occurrence of further intermediate reflections, which cause a distortion of the reshaped polygon and hence modify the effectiveness of the shock wave. As an example, figure 4.14 illustrates the numerical Schlieren of the solution on an elementary domain and the reconstructed polygonal shock on the basis of symmetry considerations. Dashed lines and circles represent the polygon edges and vertexes, respectively. The sequence of pictures in figure 4.14, therefore, depict a sudden switch from a $3n_{obs}$ polygonal shock (a) to n_{obs} one (b) at the conclusion of the step 3. The following reflection occurring downstream the obstacle causes the onset of a shock in correspondence of the trailing edge, as well as a Mach stem which increases the number of edges from n_{obs} (b) to $2n_{obs}$ (c). The evolution of the latter reflection results in a “reshaping cascade”, which produces a continuous

transformation of the shock from a n_{obs}-edges to a $2n_{obs}$-edges to a n_{obs}-edges again, even though rotated (d), and so on. The reshaping cascade was predicted by Schwendeman et al. [88], who demonstrated the onset of a continuous $n_{obs} - 2n_{obs}$ transition until the focusing. The present numerical simulations show that the phenomenon can become much more complex. As experimentally confirmed also in ref. [91] for cylindrical obstacles, this is related to the type of reflection (regular or Mach-type) occurring in correspondence of symmetry surfaces. It is worth noticing that the aforementioned Direct Mach Reflection causes the Mach stems to present a slight curvature. In fig. 4.14(b) it is apparent that the edges of the 8-sides polygon representing the shock are curved. Therefore the numerical secondary Mach stem and the approximating polygon side differ significantly. However, the absence of additional reflections of the secondary Mach stem over the symmetry surface preserve the shock topology and no additional vertexes are introduced.

Reflections occurring downstream the obstacle satisfying conditions in ref. [88] are not the only cause for the departure from the regular polygonal shock shape. For instance, if the trailing edge is not along the trajectory of the secondary triple point, that is the first Mach stem reaches the obstacles trailing edge before the conclusion of the shock reshaping, the non orthogonality between the first Mach stem and the symmetry line causes a further reflection: in this case, if the latter reflection is of Mach type, the number of edges, in addition to the aforementioned n_{obs} and $2n_{obs}$, becomes $3n_{obs}$ and $4n_{obs}$ (figure 4.15).

As detailed in the following paragraphs, other non-simple interactions of the waves generated by the reflections causes a variety of final configurations and intermediate patterns.

4.3.2 Secondary reflection

The secondary reflection, taking place on the symmetry lines not intersecting the obstacles during the second reshaping step, is indeed a complex process. As a matter of facts,

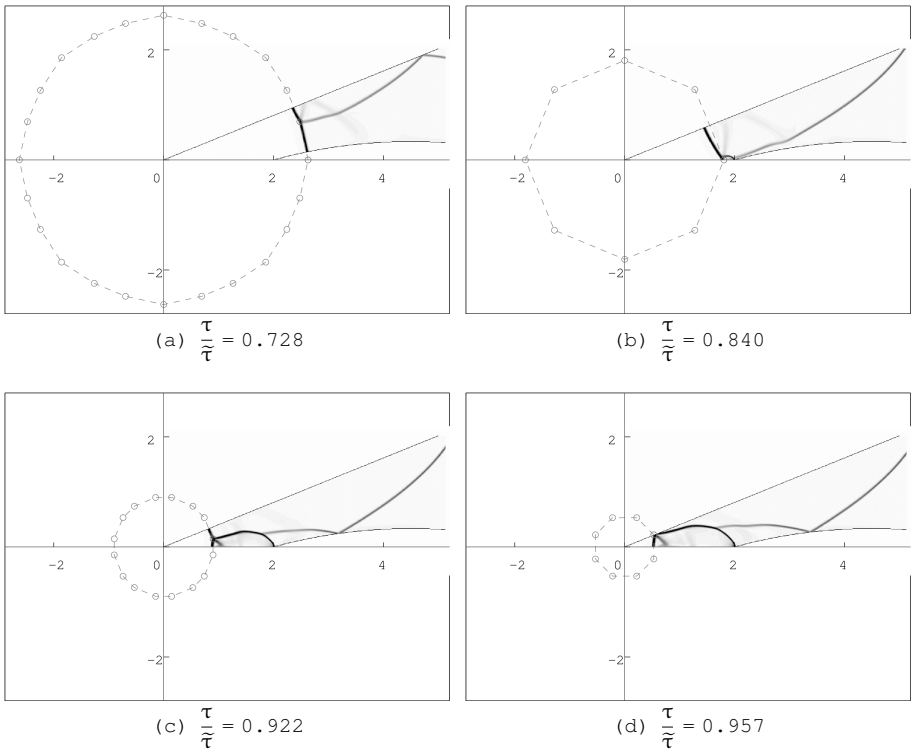

Figure 4.14: Numerical Schlieren of the shock reshaping process in reference conditions, showing the reshaping cascade. The 2π polygonal shape is reconstructed from the numerical simulations carried out in the elementary $\pi/8$ subdomain. (a) During step 3, the number of edges is three times the number of obstacles. (b) The number of edges equals the number of obstacles, vertices are along symmetry lines crossing the trailing edges. (c) The number of edges is twice the number of obstacles. (d) The number of edges equals the number of obstacles, vertices are aligned with other symmetry lines. The indicated time advancement is computed from the shock impingement over the obstacle leading edge till the focusing.

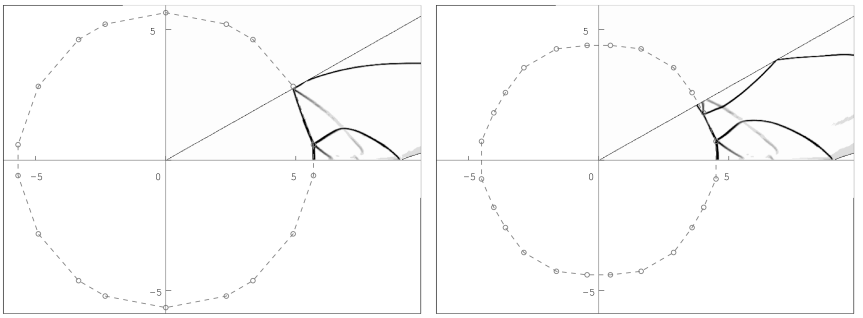

(a) $\frac{\tau}{\tilde{\tau}} = 0.665$ (b) $\frac{\tau}{\tilde{\tau}} = 0.743$

Figure 4.15: Numerical Schlieren after the interaction with 6 obstacles of $t/c = 0.21$ at twice the reference distance ($r_{LE} = 14$) and initial pressure ratio of 27. The shock becomes (a) an optadecagon ($3n_{obs}$) and (b) an icosikaitetragon ($4n_{obs}$). The deviation of the reflected wave from the classical SMR shape is due to the interaction with contact discontinuities generated during previous reflections, and it is not due to an actual TMR. The indicated time advancement is computed from the shock impingement over the obstacle leading edge till the focusing.

unlike the leading edge reflection, it involves the reflection of two waves. The first one, the Mach stem generated by the leading edge reflection, undergoes a Mach Reflection. This is in accordance with the three-shock theory, which can now fully applies, since the reflecting surface is straight and the incident shock is a pseudo-straight wave moving at approximately constant speed. The second shock which is reflected on the symmetry surface is wave A, which undergoes either a Regular Reflection or a Mach Reflection (figure 4.16).

With reference to table 4.3, Mach Reflections are concentrated in correspondence of larger obstacle numbers and thickness. For a given set of parameters, in fact, the secondary perceived wedge angle $\theta^{P}_{w,s}$—i.e. the angle of the diffracting wall perceived by wave A at its reflection over the upper symmetry surface—is lower for a larger number of obstacles, as sketched in figure 4.16. Moreover, the higher is the obstacle thickness, the stronger is the curvature of wave A, which contributes to reducing the value of the secondary $\theta^{P}_{w,s}$ too. Therefore, the most relevant parameters influencing the secondary reflection type are n_{obs} and t/c.

However, the type of secondary reflection seems not to significantly affect the following reflection patterns.

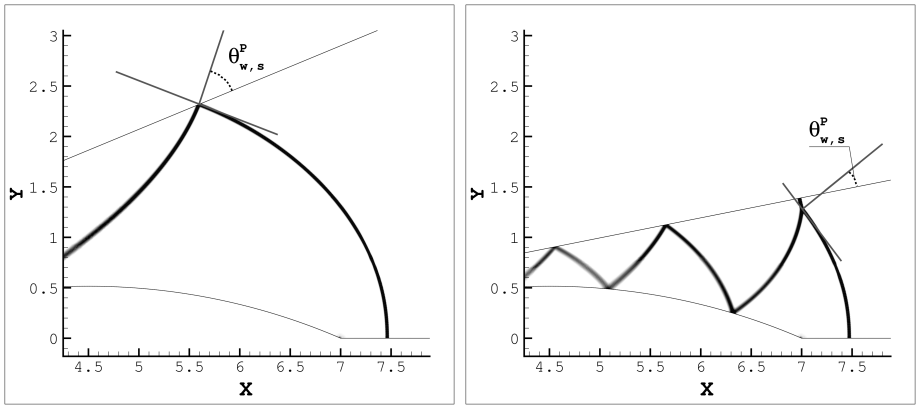

(a) (b)

Figure 4.16: Numerical Schlieren of the secondary reflection caused by thick obstacles at reference distance (β_P = 16): (a) Regular (8 obstacles) and (b) Mach type (16 obstacles) caused by diverse values of the angle of the diffracting corner perceived by wave A during the secondary reflection, thus the secondary perceived wedge angle $\theta^P_{w,s}$.

	r_{LE}	7			14			17.5		
β_P	n_{obs} \ t/c	0.07	0.14	0.21	0.07	0.14	0.21	0.07	0.14	0.21
11	24			MR	MR	MR	MR			
	16	?R	RR	MR	?R	RR	MR	?R	MR	MR
	8	?R	RR	RR	?R	RR	RR	?R	RR	RR
	6	?R	RR	RR	?R	RR	RR	?R	RR	RR
16	24			MR	MR	MR	MR			
	16	RR	RR	MR	RR	RR	MR	RR	MR	MR
	8	RR	RR	RR	RR	RR	RR	RR	RR	RR
	6	RR	RR	RR	RR	RR	RR	RR	RR	RR
27	24			MR	MR	MR	MR			
	16	RR	RR	MR	RR	RR	MR	RR	MR	MR
	8	RR	RR	RR	RR	RR	RR	RR	RR	RR
	6	RR	RR	RR	RR	RR	RR	RR	RR	RR

Table 4.3: Secondary reflection types: Mach Reflections are concentrated in the top-right part of each block, corresponding to higher t/c and n_{obs}.

4.3.3 Trailing edge reflections dynamics

The obstacle arrangement strongly influences the dynamics of the reflections after the shock reaches the obstacle trailing edge. In particular, the obstacle thickness and position are observed to influence the curvature of wave A (cf. section 1.1) and the triple point trajectory, and therefore to condition also the following reflections.

Figures 4.17 and 4.19 depict the reshaping of a cylindrical shock generated by an initial pressure step $\beta_P = 11$ for two configurations, namely ($n_{obs} = 8$, $t/c = 0.21$, $r_{LE} = 14$) and ($n_{obs} = 6$, $t/c = 0.21$, $r_{LE} = 7$), respectively. The diverse obstacle arrangements cause the onset of different shock patterns. The non-linear interaction between the shock wave and the reflecting walls results in an increasing complexity of the flow field during the shock convergence. In sec. 1.1, the reference configurations was shown to produce a relatively simple pattern: the reshaped polygonal shock has a number of edges switching from n_{obs} to $2n_{obs}$ and back during the shock propagation, see figure 4.14. In fig. 4.17, a more complex case is represented. The leading edge Mach reflection of the cylindrical shock results in the three-shock structure consisting of the incident shock i_s, in the reflected wave A (defined in sec.1.1) and in the leading edge Mach stem m_{LE} (fig. 4.17(a)). This configuration is well known from previous theoretical, numerical and experimental studies on shock reflection, see e.g. ref. [70]. When the shock reaches the trailing edge, m_{LE} is diffracted into the trailing edge Mach stem m_{TE} and wave C, which intersect at the trailing edge triple point TP_{TE} (fig. 4.17(b)). Afterwards, the secondary reflection of the first, leading-edge triple point over the upper symmetry line occurs (cf. figure 1.3), resulting in the onset of wave B and of the secondary Mach stem m_{sec} (fig. 4.17(c)). Eventually (fig. 4.17(d)), a head-on collision between waves B and C occurs; the resulting shocks then interacts with the upper and lower symmetry lines. Because of the comparable intensity and size of waves B and C, a symmetric reflection system is observed. The sequence of the reflections of waves B and C over the upper and lower symmetry lines is denoted by waves B^I, B^{II}, etc. and C^I, C^{II}, etc. respectively, as illustrated in fig. 4.18.

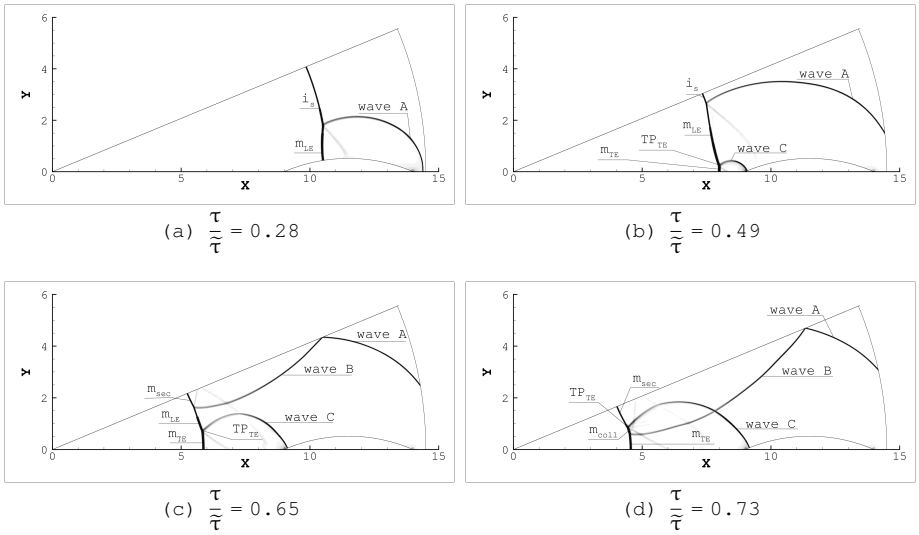

Figure 4.17: Numerical Schlieren images representing the reshaping of a shock generated by an initial pressure ratio $\beta_P = 11$ over an array of 8 obstacles with $r_{LE} = 14$ and $t/c = 0.21$. (a) Mach reflection of the incident shock i_s and formation of the leading edge Mach stem m_{LE} and of wave A. (b) Mach reflection of m_{LE} at the trailing edge and formation of the trailing edge Mach stem m_{TE} and of wave C, merging at the triple point TP_{TE} (c) Secondary reflection over the upper symmetry line, resulting in the onset of wave B and of the secondary Mach stem m_{sec} (d) Head-on collision of waves B and C, resulting in a weak distortion of the two waves and in the formation of the collision Mach stem m_{coll} (The indicated time advancement is computed from the shock impingement over the obstacle leading edge till the focusing).

In fig. 4.19, a small variation in the obstacle arrangement is seen to cause a significantly different final pattern, thus pointing to highly non-linear nature of the problem. Indeed, in fig 4.19(a), the leading edge reflection is a Single Mach Reflection as in the previous case (cf. fig. 4.17(a)). In the present configuration, wave A reaches the upper symmetry line while the shock is still crossing the obstacle (fig. 4.19(b), to be confronted with fig. 4.17(b)), and wave B is generated. Wave C is generated at the trailing edge reflection of m_{LE} (fig. 4.19(c)) as in the previous case. Its interaction with waves B, again a head-on collision, takes place when wave C is still

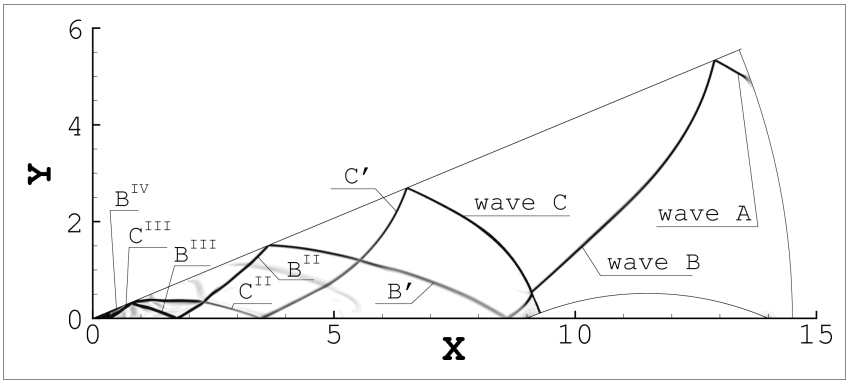

Figure 4.18: Evolution of the reflections of waves B and C, which remain independent waves almost until the shock focusing (n_{obs} = 8, t/c = 0.21, r_{LE} = 14, β_P = 11, $\frac{\tau}{\tilde{\tau}}$ = 0.87).

a small-amplitude shock. As a result, wave B is only slightly affected by the interaction with wave C and eventually reflects into wave B^I over the lower symmetry boundary. The reflected wave B^I propagates towards the upper symmetry line and coalesce with wave C (fig. 4.19(d)). From this moment, one complex wave termed "multiple wave", consisting of the overlapping of waves B^I and C, is observed (fig. 4.20).

The diverse interactions between the reflected waves downstream the trailing edge result in polygonal shocks with variable edges numbers and intensity and, in general, in a more complex flow field with respect to the reference configuration in ref. [97]. Indeed, the presence of several single waves rather than one multiple wave causes further reflections. Fig. 4.21(a) details the flow field near the trailing edge for the first case described in this section (n_{obs} = 6, t/c = 0.21, r_{LE} = 7, β_P = 11) at an intermediate time between those depicted in figs. 4.17(d) and 4.18: it is apparent that wave C reaches the symmetry surface before the triple point, and undergoes two regular reflections. On the contrary, the above is not observed in 4.21(b) (n_{obs} = 6, t/c = 0.21, r_{LE} = 14, β_P = 11, intermediate time between 4.19(d) and 4.20), where the triple point reaches the reflecting surface first. Therefore, the above interaction sequence is chosen as the criterion to

distinguish the two reflection patterns.

Numerical simulations reveals that a larger obstacle distance and thickness cause the reflected wave to approach the symmetry surface before the triple point, as illustrated in table 4.4, thus resulting in the reflection pattern described in fig. 4.21(a). Obstacles with larger thickness, indeed, generate reflected shocks (wave A) with larger curvature, which extend more significantly towards the upper symmetry line. As a consequence, for thick obstacles the reflected shock waves reaches the symmetry line before the triple point, as in figure 4.21(a).

The effect of the parameter r_{LE} on the shape of the trailing edge reflection is indirect. Indeed, wave C always interacts with wave B before reflecting at the upper symmetry line. Hence, the stronger wave B is, the more significant is the deformation of the trailing-edge reflected wave resulting from their interaction (as it is evident in fig. 4.21(b)). Therefore, the trailing-edge triple point TP_{TE} is more likely to reach the reflecting surface before wave C. The effect of r_{LE} on the intensity of wave B is twofold. On one hand, for a given β_P, a larger r_{LE} implies a lower shock Mach number M_S of the incident shock, resulting in a weaker leading edge reflection. Therefore, wave B is less intense as well. Moreover, the larger is r_{LE} (for a given n_{obs}), the longer is the distance between the obstacle leading edge and the upper reflecting surface. Therefore a stronger attenuation of wave A is observed as it diffracts from the leading edge. Note that the distance between the leading edge and the upper reflecting surface depends also on the number of obstacles. However, a clear dependence of the reflection patterns on n_{obs} was not observed.

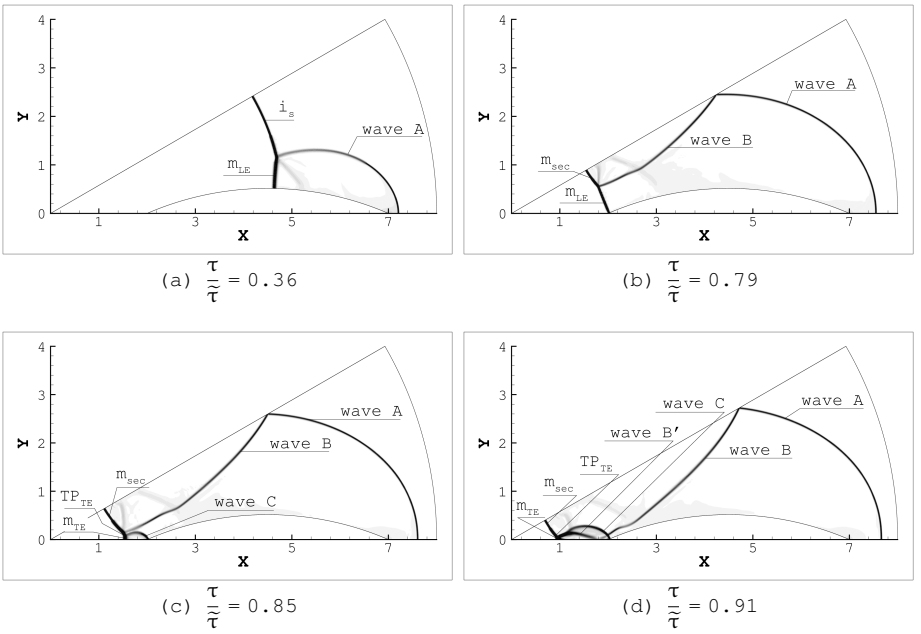

(a) $\frac{\tau}{\tilde{\tau}} = 0.36$ (b) $\frac{\tau}{\tilde{\tau}} = 0.79$

(c) $\frac{\tau}{\tilde{\tau}} = 0.85$ (d) $\frac{\tau}{\tilde{\tau}} = 0.91$

Figure 4.19: Numerical Schlieren images representing the reshaping of a shock generated by an initial pressure ratio $\beta_P = 11$ over an array of 6 obstacles with $r_{LE} = 7$ and $t/c = 0.21$. (a) Mach reflection of the incident shock i_s and formation of the leading edge Mach stem m_{LE} and of wave A. (b) Secondary reflection over the upper symmetry line, resulting in the onset of wave B and of the secondary Mach stem m_{sec} (c) Mach reflection of m_{LE} at the trailing edge and formation of the trailing edge Mach stem m_{TE} and of wave C, merging at the triple point TP_{TE} (d) Coalescence of waves C and B^I (the reflection of wave B over the lower symmetry surface) resulting in a strong distortion of the two waves (The indicated time advancement is computed from the shock impingement over the obstacle leading edge till the focusing).

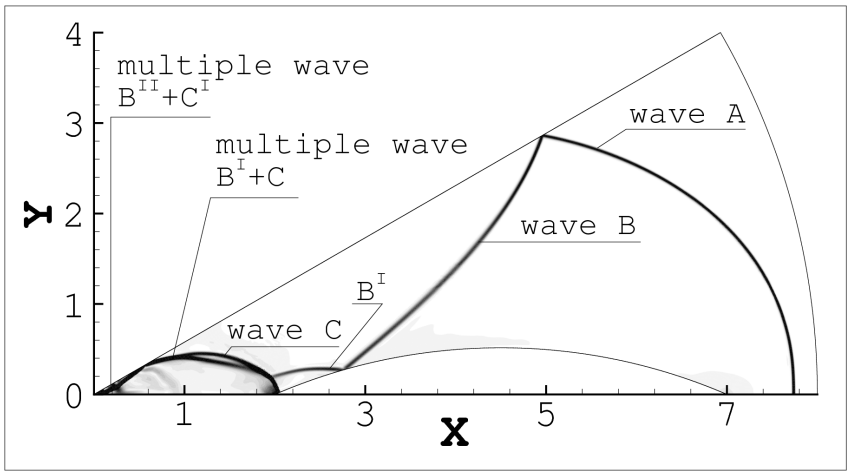

Figure 4.20: Evolution of the reflections of waves B and C, which merge together before the shock focusing (n_{obs} = 6, t/c = 0.21, r_{LE} = 7, β_P = 11, $\frac{\tau}{\tilde{\tau}}$ = 0.99).

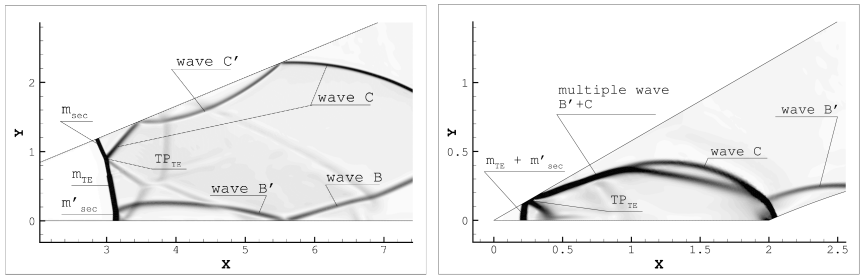

(a) $\frac{\tau}{\tilde{\tau}}$ = 0.83 (b) $\frac{\tau}{\tilde{\tau}}$ = 0.98

Figure 4.21: Reflection at the trailing edge approaching the symmetry line after the interaction with thick obstacles (β_P = 11): (a) reflected wave preceding the triple point (n_{obs} = 6, r_{LE} = 14) and (b) vice-versa (n_{obs} = 8, r_{LE} = 14).

	r_{LE}	7			14			17.5		
β_P	n_{obs} \ t/c	0.07	0.14	0.21	0.07	0.14	0.21	0.07	0.14	0.21
11	24			TP	TP	TP	RSW			
	16	TP	TP	TP	TP	TP	RSW	RSW	RSW	RSW
	8	TP	TP	TP	TP	TP	RSW	TP	RSW	RSW
	6	TP	TP	TP	TP	TP	RSW	TP	TP	TP
16	24			TP	TP	TP	RSW			
	16	TP	TP	TP	TP	TP	RSW	RSW	TP	RSW
	8	TP	TP	TP	TP	TP	RSW	TP	RSW	TP
	6	TP	TP	TP	TP	TP	TP	TP	TP	RSW
27	24			TP	TP	TP	RSW			
	16	TP	TP	TP	TP	TP	RSW	TP	RSW	TP
	8	TP	TP	TP	TP	TP	RSW	TP	RSW	TP
	6	TP	TP	TP	TP	TP	TP	TP	TP	RSW

Table 4.4: Element which first reaches the symmetry surface: the reflected shock (RSW) or the triple point (TP).

4.3.4 Total number of shock reflections

Table 4.5 reports the overall number of reflections affecting the shock before its focusing.

With the only exception of the 24-obstacle configuration, the number of total reflections before focusing increases with the number of obstacles. It is remarkable that the number of reflections appears to be almost independent on the initial pressure ratio β_P and on the obstacle thickness-to-chord ratio. For 24 obstacles at twice the reference distance, the number of reflections is lower than in the corresponding 16-obstacle cases. This is possibly due to the strong blockage effect which produces a nozzle-like flow in between each pair of obstacles. The supersonic flow in the divergent portion of the channel results in the onset of a new shock wave, termed "nozzle shock", as reported in figure 4.22. The new shock wave converges towards the focus and coalesces with the polygonal reshaped shock. After the coalescence, the shock undergoes a very limited number of reflections.

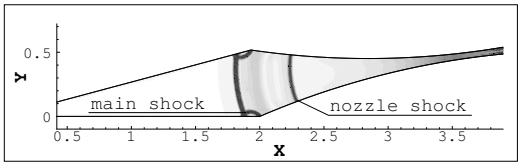

(a)

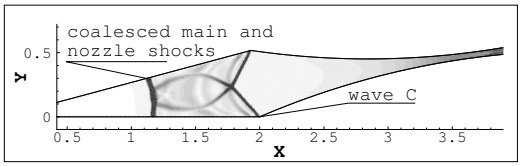

(b)

Figure 4.22: Numerical Schlieren representing (a) the onset of a shock due to the nozzle effect behind the converging shock wave and (b) its coalescence with the converging shock reflections. The shock is depicted over a computational domain including two obstacles to highlight the nozzle effect ($\beta_P = 27$, $r_{LE} = 7$, $n_{obs} = 24$, $t/c = 0.21$).

	r_{LE}	7			14			17.5		
β_P	t/c / n_{obs}	0.07	0.14	0.21	0.07	0.14	0.21	0.07	0.14	0.21
11	24			21	10	7	11			
	16	11	12	11	8	8	11	13	8	10
	8	7	7	6	7	7	8	8	8	8
	6	5	6	5	6	7	7	5	8	6
16	24			16	11	10	9			
	16	11	11	11	12	12	10	12	8	10
	8	5	6	5	7	7	7	9	7	7
	6	6	6	5	7	6	6	5	6	6
27	24			14	10	9	13			
	16	12	10	10	12	11	8	11	13	8
	8	5	6	5	7	7	7	7	7	6
	6	4	6	4	6	6	6	6	6	5

Table 4.5: Global number of shock reflections (not including the focusing).

4.3.5 Circular obstacles patterns

It is shown by preliminary investigations that circular obstacles cause relevant losses in the interaction with shock waves [37]. On the contrary, circular geometries allow to observe peculiar patterns. The flow across the obstacle undergoes very strong deflections, and therefore different flow patterns are observed with respect to the ones induced by aerodynamic obstacles. Due to geometrical interference, the case of $n_{obs} = 16$ is substituted with $n_{obs} = 4$.

It must be noted that numerical results presented in this section cannot be intended as an accurate description of the phenomena occurring during the reshaping of a cylindrical implosion by means of circular obstacles. Indeed, as it is well known, behind a bluff body—such as cylindrical obstacles—flow separation occurs and therefore the flow cannot be described in detail by means of numerical simulations performed with a solver for Euler equations. However, reference experimental works show that, or length scales of interest for applications, the recirculation region remains small with respect to the reference geometrical scale, and that it does not jeopardize the shock wave reshaping. Fig. 4.23 reports an experimental Schlieren image of a cylindrical imploding shock wave diffracted by four cylindrical obstacles: it can be observed that the shape of the polygonal shock wave is not affected by the wake downstream the obstacles.

Figure 4.24 illustrates a sequence of the reshaping of a shock generated by a β_P of 16. In 4.24(a) wave B, already described in section 1.1, is visible in the top of the figure. Meanwhile, the Mach stem generated at the leading edge has overpassed the obstacle and undergoes a reflection—Regular, in the present case—in correspondence of the lower symmetry line, generating the aforementioned wave C. The size of wave C increases along time, and therefore it intersects the obstacle with a variable slope (fig. 4.24(b)). This causes wave C to undergoes a Mach Reflection in correspondence of the obstacle trailing edge (fig. 4.24(c)).

In the shock-circular obstacle reflection framework, three

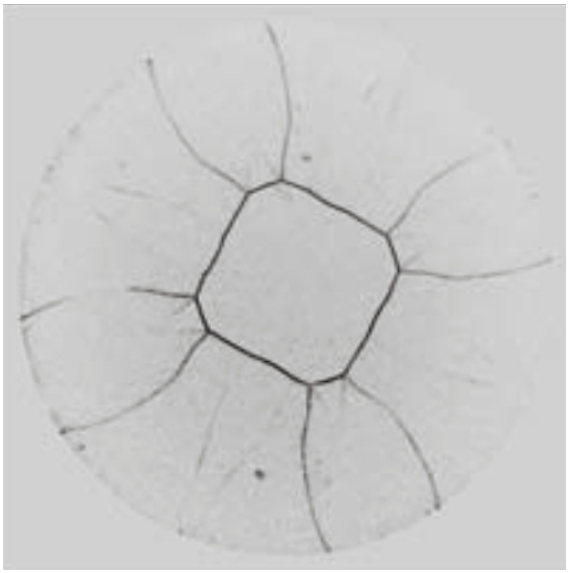

Figure 4.23: Schlieren photograph of converging shock wave reshaped by an array of four cylinders, with diameters of 15 mm and located at 61.5 mm from the focus point. (Inverted colors, image source: V. Eliasson, M. Kjellander, N. Apazidis, "Regular versus Mach reflection for converging polygonal shocks", Shock Waves (2007).)

main waves can be detected, and their interactions described: they are wave B, wave C—introduced in sec. 4.3.3—and the expansion across he obstacle induced by the shock passage. Their paired interactions are described in the following; however, it must be noticed that the interaction are observed only in a subset of all the explored configurations.

The first interaction, involving wave B and the expansion—fig. 4.24(c)—results in the local reversal of the concavity on the first wave—figs. 4.24(d) to (f)—and therefore in a modification of the reflection of wave B onto the obstacle. In fact, in fig. 4.24(f) it takes place in correspondence of the obstacle trailing edge, whereas it would occur elsewhere along the obstacle—or far downstream—if wave B were without inflection points.

The second interaction, between wave C and the expansion

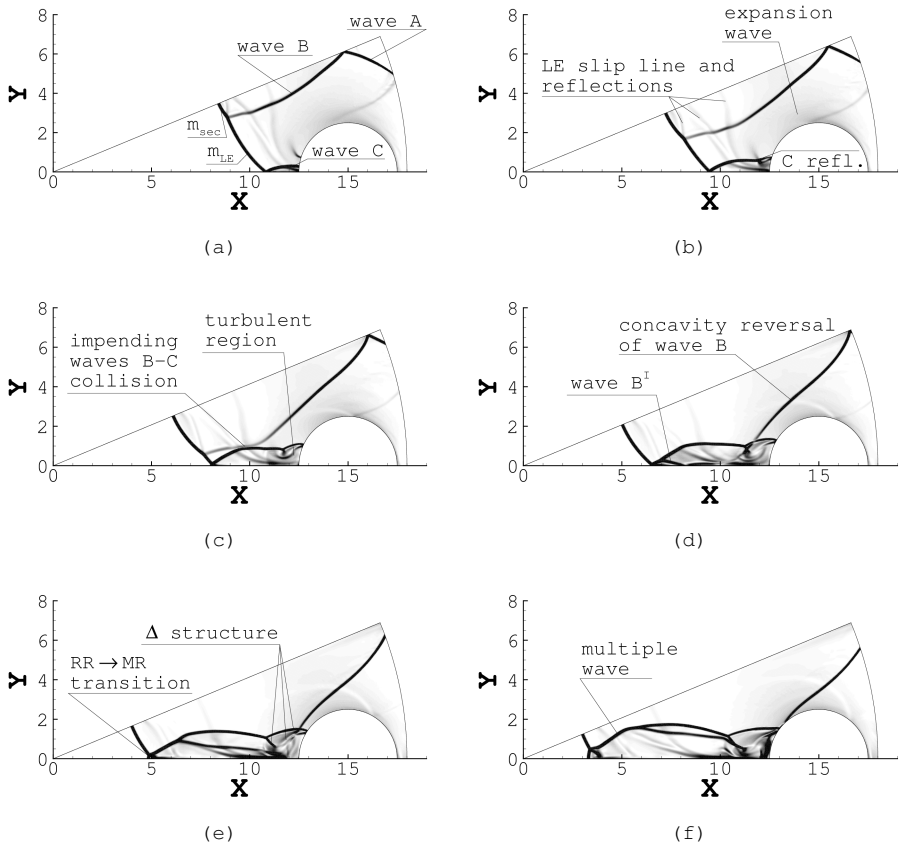

Figure 4.24: Flow field generated by the interaction between eight circular obstacles and a shock generated by a β_P of 16, equally distanced in time. The mutual interaction among wave C, wave B and the expansion wave is visible from (b) to (f).

wave, is caused by their opposite relative motion: while the Mach stem generated by the reflection of wave C onto the obstacle trailing edge moves upwards, it encounters the expansion—fig. 4.24(b) and following. At their interface, their respectively induced flows encounter with opposite velocities, generating a recirculating region at the obstacle trailing edge. The size and the vorticity intensity of this turbulent region cannot be correctly resolved without a Navier-Stokes solver, but in this framework it is only possible to observe its existence.

The third interaction is close to the one described in sec. 4.3.3 and it is caused by a possible reflection of wave B over the lower symmetry line (fig. 4.24(d)), which generates wave B^I. The complexity of the flow field and the variable slope of wave B do not allow to perform theoretical predictions on the type of reflection, but all the explored configurations report a coalescence (fig. 4.24(e)) of vave C and wave B^I, resulting either in a Regular Reflection or in a Mach Reflection. For the case illustrated in 4.24(f), the peculiar structure generated after the shocks coalescence consists of four straight waves at the triple point: (moving counterclockwise from the top) the secondary reflection Mach stem m_{sec}, the Mach stem attributed to the reflection of wave B over the lower symmetry line, the contact discontinuity and the wave enveloping waves C and B^I (thus the multiple wave introduced in sec. 4.3.3). This wave presents two (or more, in general) kinks—for the case in fig. 4.24, at $x \approx 4.5$ and $x \approx 5$. This structure is very similar to the so-called "Transitional-Double Mach Reflection", a shock system whose existence was originally suggested by [70] but later proved to be impossible in accordance with the shock diffraction theory [73]. However, this detection of this wave does not contradict theoretical results, because the multiple wave shape is due to the several and non-simple waves interactions, and is not generated by a single reflection.

Figure 4.25 details the passage of wave B across the turbulent region and how its reflection affects the shape of the multiple wave after the coalescence with wave C. Moreover, a deformation of density contours is visible at $x \approx 7.5$ under the multiple wave, which is the heritage of the reflection of

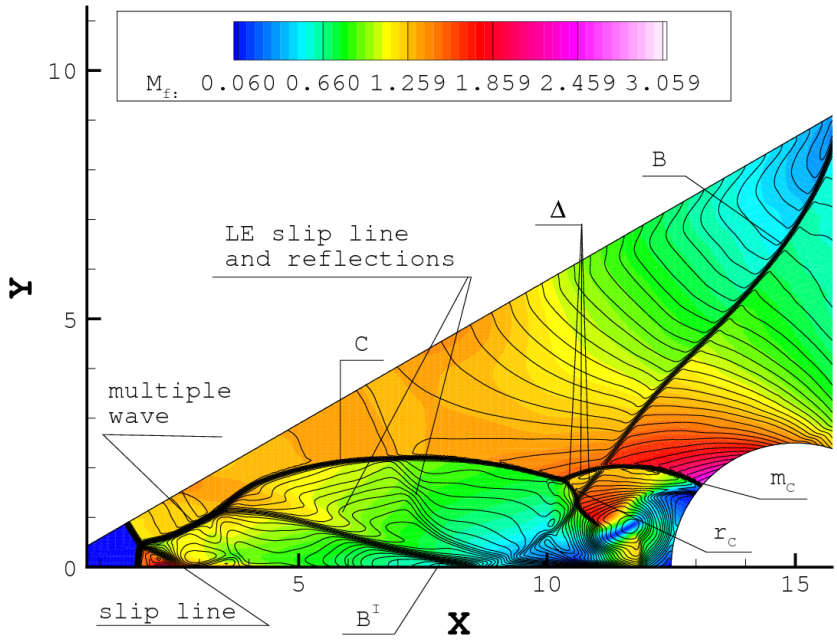

Figure 4.25: Mach number contours and isopycnics highlighting the interactions between the reflected waves downstream the obstacle ($\beta_P = 11$, $n_{obs} = 6$, $r_{LE} = 17.5$).

previous contact discontinuities.

Figure 4.25 illustrates also the mutual interaction among all the three observed waves, thus waves B, C and the expansion. In correspondence of the turbulent region, a triangular structure (following, the "Delta-structure") is delimited by wave B and the two shock waves originated by the reflection of wave C over the obstacle trailing edge—namely the "reflected wave C" r_C and the "wave C-originated Mach stem" m_C—both distorted by the interaction with the expansion. It is observed that the presence of the Delta-structure, observed also in figures 4.24(e)-(f) is not mandatory. Indeed, wave B can be reflected also over the obstacle profile, as well as over the lower symmetry line. In the first case, if the reflection of wave B over

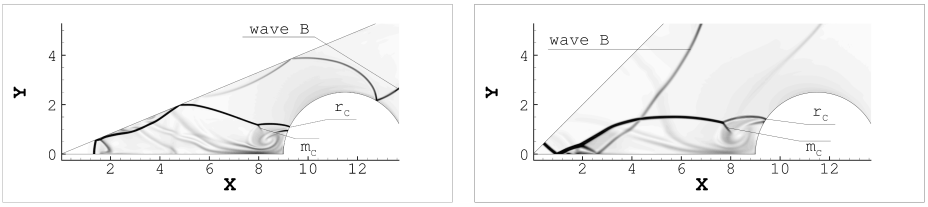

Figure 4.26: Absence of the Delta-structure: (a) premature (n_{obs} = 8) (b) and missing (n_{obs} = 4) wave B reflection over the obstacle. (β_P = 11, r_{LE} = 14).

the obstacle is premature (fig. 4.26(a)) or, on the contrary, if it does not occur (fig. 4.26(b)), the Delta-structure is missing.

Eventually, figure 4.27(a) represents the advancement of the reshaped shock front. The stepwise acceleration of the shock front after each reflection can be inferred by the different average distance between two adjacent fronts. This implies that the Mach stem of the reflection generated by circular obstacles present a relevant curvature, which cannot be neglected as in the three-shock theory.

Moreover, a peculiar transition is observed. Indeed, when the leading edge-generated Mach stem m_{LE} reaches the obstacle trailing edge, it undergoes a reflection, as described in sec. 4.3.3, resulting in the onset of wave C and, possibly of the trailing edge Mach stem m_{TE}. The latter is present only if the reflection is of Mach-type. In this framework, in correspondence of the lower symmetry line, the reflection of the leading edge-generated Mach stem starts as a Regular Reflection , then turns into a Mach Reflection (whose Mach stem m_{TE} is visible between r = 4.5 and r = 2), and eventually terminates into a Regular Reflection after the interaction between waves B and C. Figure 4.27(b) represents the flow field associated to an intermediate state, represented by a bold line in figure (a), highlighting the effect of reflected contact discontinuities on the deformation of both waves B and C.

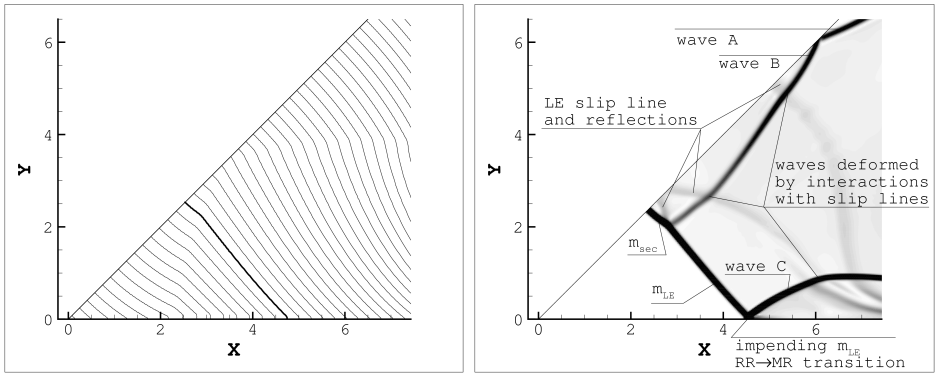

(a) (b)

Figure 4.27: Shock generated by $\beta_P = 11$ after the interaction with 4 circular obstacles arranged at twice the reference distance: (a) Advancement of the shock front (the non-dimensional time step between two adjacent fronts is $\tau/\tilde{\tau} = 0.016$); (b) flow field corresponding to an intermediate state (the bold one in the twin picture).

Chapter 5

Non-ideal fluid effects

> The atom we are speaking about [...] enters [...], colliding with innumerable, but here useless, molecules of Nitrogen and Oxygen.
> — PRIMO LEVI, IL SISTEMA PERIODICO, "CARBONIO"

Due to the high values of temperature and density attained by the gas during the reshaping, the polytropic ideal gas model presents some limitations, as introduces in sec. 1.2.2. Therefore, alternative thermodynamic models are explored in the present chapter. This results in different expressions of the two equations describing the thermodynamics of the problem, i.e. the pressure equation of state and the specific heat equation.

The thermal equation, i.e. the equation of state for pressure, is varied from the ideal gas one (eq. (1.12)), in favor of the van der Waals gas model (eq. (1.16)). For the treatment of the specific heat, a diverse model is devised from the polytropic one adopted in chaps. 3 and 4: a temperature-dependent term is added to the constant one in the expression of c_v, in accordance to the harmonic oscillator model [116].

Numerical simulations allow us to observe the effects of diverse thermodynamic models on the shock propagation, reshaping and focusing. Indeed, for all the thermodynamic models,

the pressure and temperature coefficients are provided, along with the efficiency of the shock. To describe the kinematics of the shock convergence, self-similarity exponents are calculated for diverse obstacle arrangements, equations of state and c_v expressions. The evolution of physical quantities during the implosion is assessed by means of the representation on the P–v plane of the locus of fluid states immediately behind the shock during time.

5.1 Description of the numerical experiments

The setting of the numerical experiments is described here. In sec. 5.1.1, the adopted factors and the levels of each one are described. The choice of the initial conditions is briefly recalled in sec. 5.1.2, in accordance with sec. 1.2.3. Eventually, an assessment on the adopted grid spacing and time step is detailed in sec. 5.1.3.

5.1.1 Design of experiments

With reference to tab. 5.1, numerical simulations are performed varying the factors described in sections 3.1.1 and 4.1.1, thus the initial pressure ratio β_P, the number of obstacles n_{obs}, their distance from the focus point r_{LE} and their thickness-to-chord ratio t/c.

In addition, four different models are provided for the description of the fluid thermodynamics. The other considered model for the thermal equation—in alternative to the polytropic ideal gas one—is the van der Waals equation of state [117], defined in sec. 1.2.2,

$$\widehat{P} + \frac{a}{\widehat{v}^2} = \frac{R\widehat{T}}{\widehat{v} - b}. \tag{5.1}$$

High temperature effects are accounted for by adopting the harmonic oscillator law for c_v in addition to the polytropic one,which includes also the contribution of vibrational motions of the molecules to internal energy. In the current

model of air as a binary mixture of diatomic gases, there is one vibrational temperatures for each chemical element, respectively $\widehat{T}_{vib,O2} = 2273K$ and $\widehat{T}_{vib,N2} = 3393K$.

The combinations between the two equations of state and the two c_v models result in four possible descriptions of the thermodynamic behavior of the shock-induced flow field. In accordance to the the notation adopted in sec. 1.2.2, the thermodynamic model is indicated by a letter code: the first letter is a "P" or a "H" for polytropic and harmonic oscillator models for c_v, respectively. The second group of letter, separated from the first by a "-" symbol, is either "IG" or "VdW" depending on the selected equation of state, i.e. ideal gas or van der Waals.

Eventually, a further factor is introduced: in addition to the "dilute" gas conditions, explored in chapters 3 and 4, the so-called "dense" gas conditions are investigated too.

For all the thermodynamic models, the levels of β_P of 11, 16, 27 and 36 are explored. For the polytropic ideal gas, they correspond respectively to $M_S = 2.2$, 2.7 (the reference value), 3.2 and 3.7 at $r_{LE} = 7$. Moreover, in the case of simulations involving polytropic and harmonic ideal gas, additional levels of β_P are included, i.e. 48, 60, 75, 90, 110 and 130, which extend the M_S^{LE} upper limit to 6.7. Problems of computational stability are observed in simulations involving shock waves propagating in van der Waals gases and generated by $\beta_P \geq 48$. This setup generates a globally factorial design consisting of two fully crossed designs (one for ideal gas, including 1440 treatments, and one for van der Waals gas, for 560 treatments), resulting in an overall number of 2000 investigated cases. The investigated fractional factorial design is summarized in tab. 5.1:

5.1.2 Initial conditions setting

To assess real gas effects, results are compared with the ones obtained with the polytropic ideal gas model. Therefore, the same initial conditions are adopted. The internal pressure, for gas in dilute conditions, is $\widehat{P}_i^0 = 10^4$ Pa—in accor-

Number of obstacles (n_{obs})	4 levels	0, 6, 8, 16
Thickness-to-chord ratio (t/c)	3 levels	0.07, 0.14, 0.21
Leading edge coordinate (r_{LE})	3 levels	7, 14, 17.4
Initial pressure ratio (β_P)	4 or 10 levels	11, 16, 27, 36 (48, 60, 75, 90, 110, 130)
Thermodynamic model	4 levels	P-IG, P-VdW, H-IG, H-VdW
Gas conditions	2 levels	dilute, dense

Table 5.1: Test matrix for the numerical experiments. Considered parameters are the number of obstacles n_{obs}, the thickness-to-chord ratio t/c, the radial coordinate of the obstacle leading edge r_{LE}, the initial pressure ratio β_P, the thermodynamic model and the gas conditions. In all tests, the operating fluid is air.

dance with [97]—whereas, for gas in dense conditions, it is $\widehat{P}_i^0 = 10^6\,\mathrm{Pa}$. The imposed internal density values, respectively in the dilute and dense gas cases, are $\widehat{\rho}_i^0 = 0.1168\,\mathrm{kg/m^3}$ and $\widehat{\rho}_i^0 = 11.684\,\mathrm{kg/m^3}$. The external pressure is obtained as $\widehat{P}_e^0 = \widehat{P}_i^0 \cdot \beta_P$, and—being the fluid initial velocity everywhere null—the corresponding density is computed from the shock adiabat for polytropic ideal gas.

Initial pressure and temperature are evaluated by in accordance with the polytropic ideal gas model. Therefore, the same initial values are imposed to all the simulations with the same β_P and gas conditions, regardless of the thermodynamic model.

Different temperature values are originated by this set of initial conditions. Indeed, for ideal gas, the external temperature is $\widehat{T}_i^0 = \widehat{P}_i^0/\widehat{R}\widehat{\rho}_i^0$, which corresponds, in the case of $\beta_P = 36$, to $2077.43\,\mathrm{K}$ for both the dilute and the dense gas. On the contrary, the temperature evaluated in accordance with the van der Waals gas model depends on the gas conditions: for dilute gas and $\beta_P = 36$, one has $\widehat{T}_i^0 = 2076.22\,\mathrm{K}$ whereas, for dense gas, $\widehat{T}_i^0 = 1954.01\,\mathrm{K}$. It can be observed that the difference between

the ideal and the van der Waals models is negligible in dilute conditions ($\Delta\widehat{T}_i^0 = 1.2\,K$), whereas it is more relevant in dense conditions ($\Delta\widehat{T}_i^0 = 122\,K$). Fig. 5.1 depicts the diverse initial internal and external states on the P-v plane, depending on β_P and on the gas conditions.

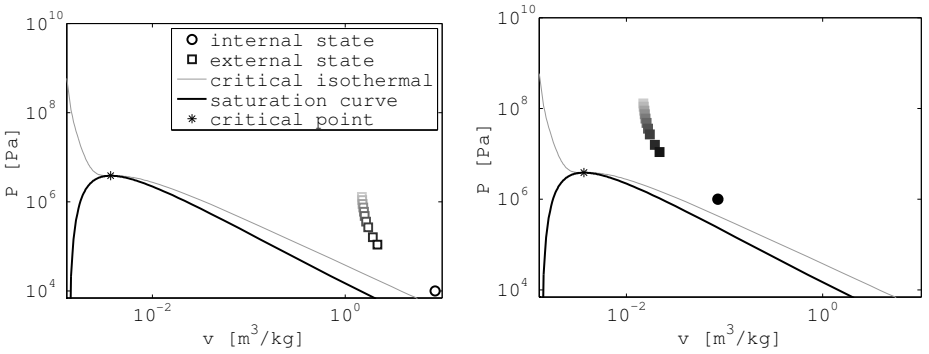

(a) dilute conditions (b) dense conditions

Figure 5.1: Initial conditions adopted for the numerical simulations represented in the P-v plane. The thick solid line represents the saturation curve, and the thin solid line is the critical isothermal curve, computed in accordance with the van der Waals gas model. The internal state is represented by a circle, whereas the external ones are indicated by squares. Each color of the squares is associated to a diverse β_P. Empty markers (fig. (a)) are adopted for dilute gas, full ones (fig. (b)) for dense gas.

5.1.3 Assessment on grid spacing and time step

Similarly to the case of polytropic ideal gas, simulations are performed on a triangular fixed grid with a maximum element length $\Delta x = 0.01$. Local grid refinements are performed a priori in correspondence of the obstacle surface, leading edge and trailing edge. The overall number of nodes is between 50000 and 400000, depending on r_{LE}, n_{obs} and t/c, which determine the area of the computational domain.

Fig. 5.2 reports the pressure profiles over the obstacles for polytropic van der Waals gas in dilute conditions, obtained with diverse grid spacing ($\Delta x = 0.1$, 0.06, 0.03, 0.01

and 0.007, respectively). On each picture the shock propagation increases of of the 25% of the obstacle chord. Calculations are performed over an array of 16 obstacles in reference geometrical conditions, that is $r_{LE} = 7$, $t/c = 0.14$ and with $\beta_P = 27$.

The selected time step is $\Delta\tau = 6 \times 10^{-4}$, which is the same as the one adopted for the simulation of the reshaping and focusing in polytropic ideal gas. Results of an analysis carried out to test the dependence of the solution on the time step are reported in fig. 5.3. The pressure profiles are obtained for the same geometrical and operating conditions adopted to assess the effect of the grid spacing (fig. 5.2), on a mesh of 56000 nodes with a maximum node spacing $\Delta x = 0.01$. The investigated time step value are $\Delta\tau = 2 \times 10^{-4}$, 3×10^{-4}, 6×10^{-4}, 7.5×10^{-4}, 3×10^{-3} and 6×10^{-3}.

The ratio between the focus point temperature and the internal temperature is illustrated in fig. 5.4 for diverse space (fig. 5.4(a)) and time (fig. 5.4(b)) resolutions. The reported temperature profile is attained after the focusing of the polygonal shock caused by the set of conditions and parameters described above. The temperature curves in fig. 5.4 confirm that a maximum node spacing $\Delta x = 0.01$ with local refinements and a time step $\Delta\tau = 6 \times 10^{-4}$ provide the correct discretization.

All the results and figures in the following concern simulations performed with a grid spacing $\Delta x = 0.01$ and time step $\Delta\tau = 6 \times 10^{-4}$.

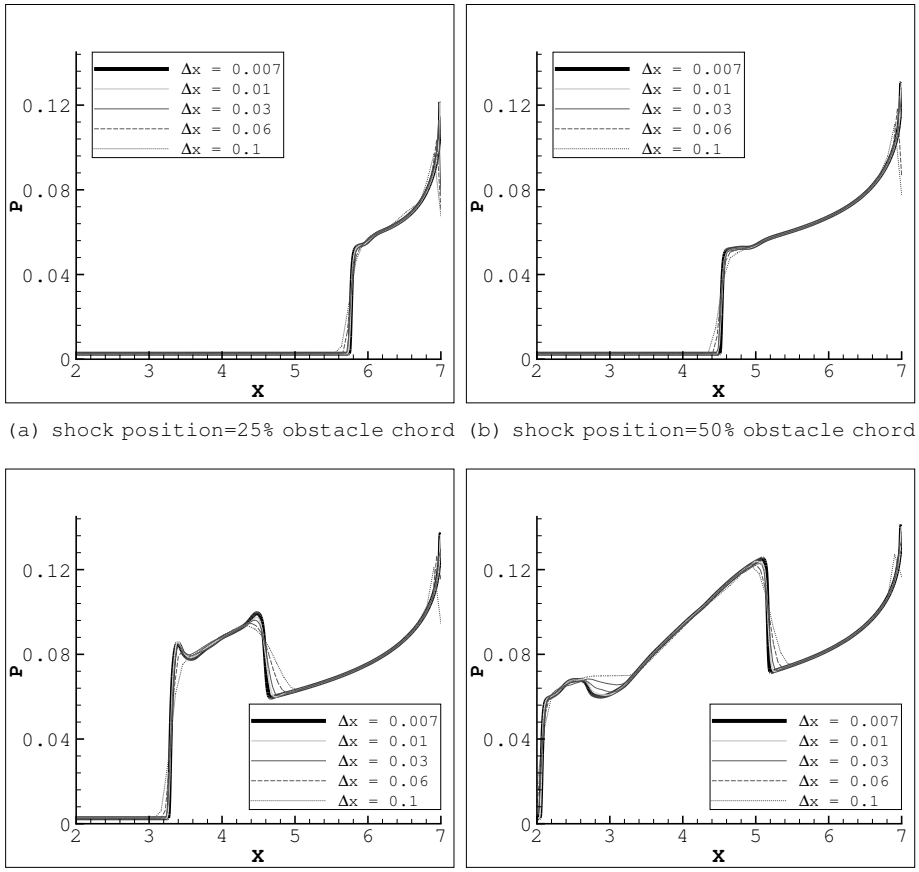

(a) shock position=25% obstacle chord (b) shock position=50% obstacle chord

(c) shock position=75% obstacle chord (d) shock position=obstacle trailing edge

Figure 5.2: Pressure—obtained with different meshes—on the obstacle during the propagation of a shock with initial pressure step $\beta_P = 27$ and reshaped by 16 obstacles with reference t/c and r_{LE}. The solution is computed by means of a polytropic van der Waals model. The time step is $\Delta\tau = 6 \times 10^{-4}$ in all the simulations. The shock advancement at each figure corresponds to 25% of the obstacle chord.

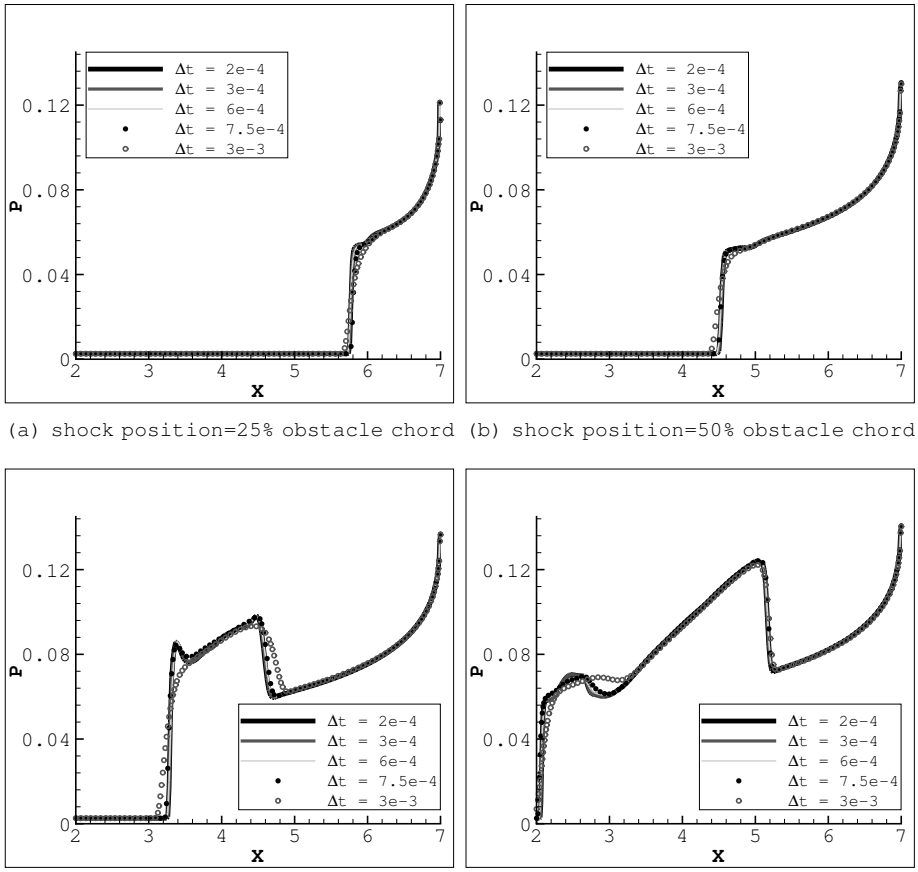

(a) shock position=25% obstacle chord (b) shock position=50% obstacle chord

(c) shock position=75% obstacle chord (d) shock position=obstacle trailing edge

Figure 5.3: Pressure—obtained with different time steps—on the obstacle during the propagation of a shock with initial pressure step $\beta_P = 27$ and reshaped by 16 obstacles with reference t/c and r_{LE}. The solution is computed by means of a polytropic van der Waals model, over a grid made of 56000 nodes ($\Delta x = 0.01$). The shock advancement at each figure corresponds to 25% of the obstacle chord.

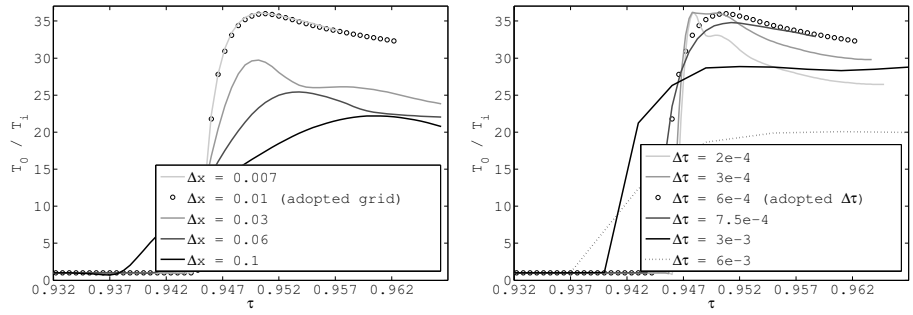

(a) Constant time step $\Delta\tau = 6 \times 10^{-4}$ (b) Constant grid spacing $\Delta x = 0.01$

Figure 5.4: Temperature value at the focus point versus time for different space (a) and time (b) discretizations. The temperature peak is caused by the focusing of a shock wave generated by an initial pressure step $\beta_P = 27$ and reshaped by an array of 16 obstacles with reference geometry. The simulations concern dilute gas governed by a polytropic van der Waals model.

5.2 Non-ideal fluid effects during shock convergence

Figs. 5.5(a) and 5.5(b) report the specific internal energy e versus the temperature T of a cylindrical shock generated by an initial pressure ratio $\beta_P = 16$, respectively in dilute and dense conditions. The specific internal energy is plotted versus temperature for all the nodes of the computational domain for the considered equations of state and c_v laws. High temperature effects are evident in terms of separation between the polytropic (represented by full lines in fig. 5.5) and the harmonic curves (indicated by symbols in the same figure), regardless of the pressure equation of state. The harmonic curves depart from polytropic ones in correspondence of $T \approx 0.25 \cdot T_{vib,O2}$ (first vertical dashed line in figure) and increases theis mutual distance at about $T \approx 0.25 \cdot T_{vib,N2}$ (second vertical dotted line). It must be noted that non-ideal effects are negligible in dilute conditions depicted fig. 5.5(a) (the ideal gas and the van der Waals gas curves are overlapped, for each of the two c_v models), whereas they become more relevant in dense conditions (fig. 5.5(b)). In the second case, indeed, the maximum attained temperature (end, therefore, internal specific

energy) are lower when van der Waals model applies with respect to the ideal gas case.

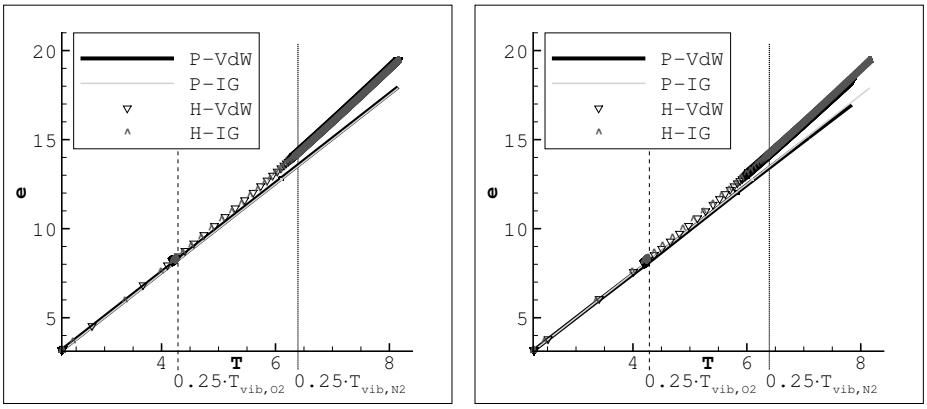

(a) dilute conditions (b) dense conditions

Figure 5.5: Specific internal energy versus temperature of an axisymmetrical shock generated by a $\beta_P = 16$ for four diverse combinations of thermodynamic models, illustrating the curves separation in correspondence of vibrational temperatures: 5.5(a) dilute and 5.5(b) dense gas conditions ($\Delta x = 0.01$, corresponding to 2300 nodes, and $\Delta\tau = 6 \times 10^{-4}$).

Figure 5.6 depicts the radial distribution of density, compressibility factor, temperature and specific internal energy for an axisymmetrical shock generated by $\beta_P = 16$ in dilute conditions at $\tau = 0.01625$ after the initial time.

The effect of the equation of state is negligible in the explored, dilute-gas conditions. The compressibility factor, defined as $Z = P/\rho T$, is a measure of the relevance of non-ideal gas effects: with reference to fig. 5.6(b), it is evident that Z evaluated for the van der Waals gas remains very close to 1 in the whole domain (the maximum difference between Z evaluated for the ideal gas and Z computed for van der Waals gas is of 0.04%). A magnification in fig. 5.6(c) illustrates a slight difference of temperature depending on the adopted equation of state, i.e. the ideal gas (represented by —— and ^) or van der Waals gas (indicated with ▬ and ∇).

On the contrary, high temperature effects begin to arise

in the region downstream the shock. Indeed, the effect of the shock passage is to increase the flow temperature: therefore, it is observed that, for the explored conditions—that is for shocks generated by initial pressure ratios $\beta_P \geq 11$—the temperature behind the shock is higher than $0.25 \cdot T_{vib,O2}$ by the time the shock reaches the obstacle leading edge. This is visible in fig. 5.6(c), where the horizontal dashed line indicates the temperature value of $0.25 \cdot T_{vib,O2}$, for which the temperature-dependent term of the specific heat becomes relevant in the gas governed by the harmonic oscillator model. The dotted horizontal line indicates the other threshold, that is $0.25 \cdot T_{vib,N2}$. It is observed that, contrary to the oxygen one, the nitrogen vibrational degree of freedom contributes to the specific heat only for stronger shocks, that is for $\beta_P \geq 27$.

The same quantities are reported in fig. 5.7 for gas in dense conditions. The difference of the compressibility factor computed with ideal and van der Waals models becomes slightly larger than 4% whereas, in dilute gas conditions, the differences are within 0.04%. Non-ideal gas effects can be clearly observed also in the density profile: behind the shock, indeed, the thermodynamic model affects the solution. The effect of the pressure equation of state on T and e is also present, even if it is weaker than on density.

Fig. 5.8 reports the two-dimensional spatial distributions of density, compressibility factor, temperature and specific internal energy ($\beta_P = 27$, dilute conditions) after the interaction with obstacle in a reference geometrical arrangement. The picture suggest that, for dilute gas, real gas effects remain very weak even after the leading edge reflection (see e.g. fig. 5.8(b)).

As reported in fig. 5.8, the speeds of the shock waves computed with diverse thermodynamic models do not differ significantly at the beginning of the reshaping, in dilute conditions.

On the contrary, when the polygonal shock wave is in proximity of the focus point, the difference becomes more important. Fig. 5.9 reports result of the reshaping of a cylindrical shock wave generated by $\beta_P = 16$ by means of reference obstacles. The only difference among the four pictures consists in the adopted thermodynamic model, as the polygonal shock wave is depicted

at $\tau = 1.3605$ after the diaphragm breaking. It can be observed that the shock waves simulated with the polytropic c_v model (top row) are slower than the ones with a harmonic c_v model (bottom row), regardless of the form of the thermal equation. Moreover, when the van der Waals gas model applies (right column), the resulting shock speed is lower than in case of ideal gas (left column) for both polytropic and harmonic gas.

The effect of the parameters, including the thermodynamic model, on the increasing departure of the shock pattern from the reference one is two-fold. The first effect is "direct": since all the parameters affect the physics of the reflections, the adoption of each thermodynamic model results in a diverse shock pattern. The difference introduced by the direct effect is mainly quantitative, as it can be observed, e.g. in fig. 5.6, where the shapes of the radial distributions do not vary with the thermodynamic model. The second effect is "indirect": in the reshaping of cylindrical converging shock waves, a series of reflections occurs, which bring the original, unperturbed cylindrical shock wave to become a pseudo-polygonal shock before the focusing. At each reflection, the conditions of the incident shock are the result of the previous reflection. The complex shock-induced flow field, therefore, is the result of a recursive, non-linear process. The latter two features, i.e. recursiveness and non-linearity, are typical of chaotic systems as pointed out e.g. in [137]. This suggest that also qualitative differences (e.g. the type of shock-approximating polygon, the periodicity of the reshaping, ...) may be detected when observing a shock wave which is the result of a recursive, non-linear process, such as the reshaping.

Fig. 5.10 reports a direct comparison among the four aforementioned cases, both at the same physical time after the shock generation (fig. 5.10(a)) and at different times, each corresponding to the shock focusing (fig. 5.10(b)). These pictures show that the main difference introduced by the thermodynamic model, in the explored range of parameters, concerns mainly the shock speed, and therefore intensity. On the contrary, the flow field downstream the polygonal shock wave is not significantly influenced by the thermodynamic model, as reported in fig. 5.10(b).

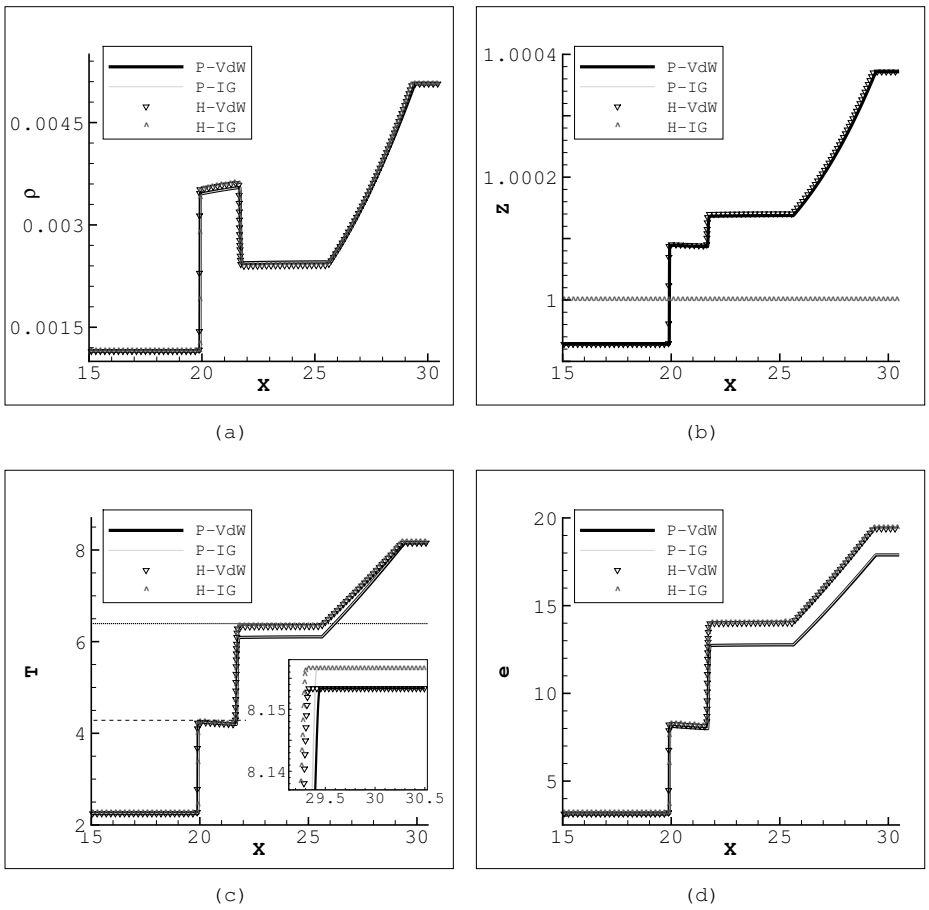

Figure 5.6: Radial distributions of (a) density, (b) compressibility factor, (c) temperature and (d) specific internal energy in an axisymmetrical shock-induced flow field in dilute conditions generated by a $\beta_P = 16$ and obtained with four different thermodynamic models ($\Delta x = 0.01$, corresponding to 2300 nodes, and $\Delta\tau = 6 \times 10^{-4}$).

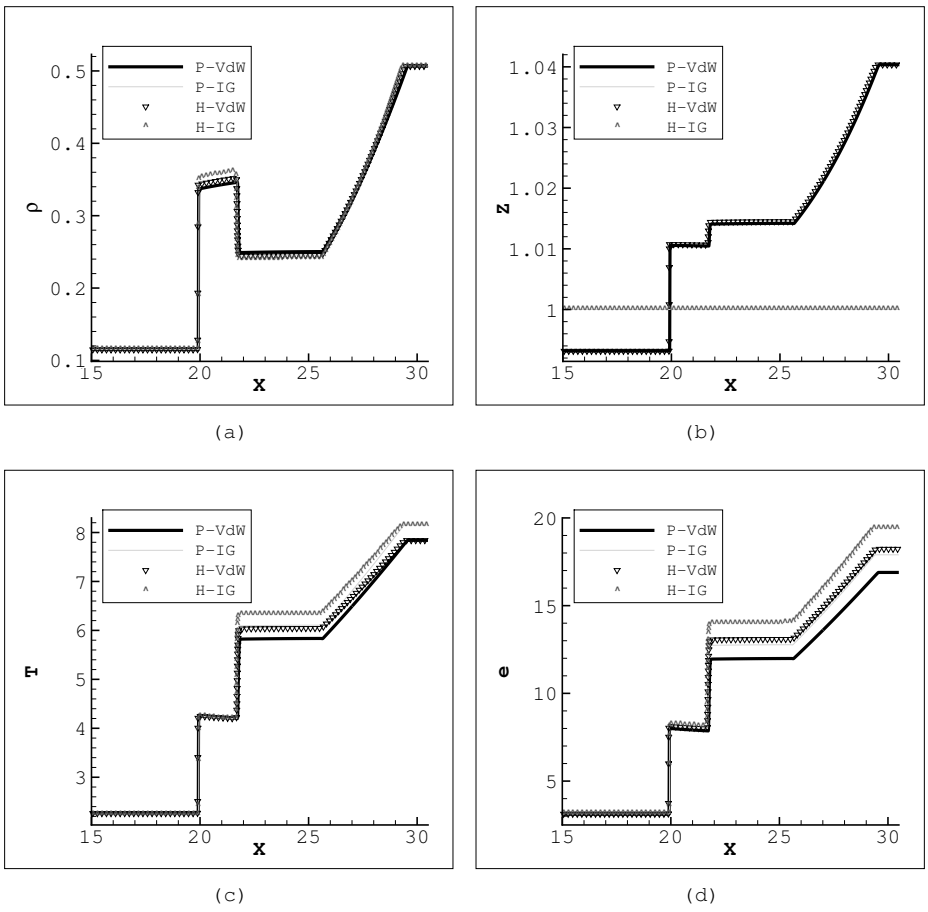

Figure 5.7: Radial distributions of (a) density, (b) compressibility factor, (c) temperature and (d) specific internal energy in an axisymmetrical shock-induced flow field in dilute conditions generated by a $\beta_P = 16$ and obtained with four different thermodynamic models ($\Delta x = 0.01$, corresponding to 2300 nodes, and $\Delta\tau = 6 \times 10^{-4}$).

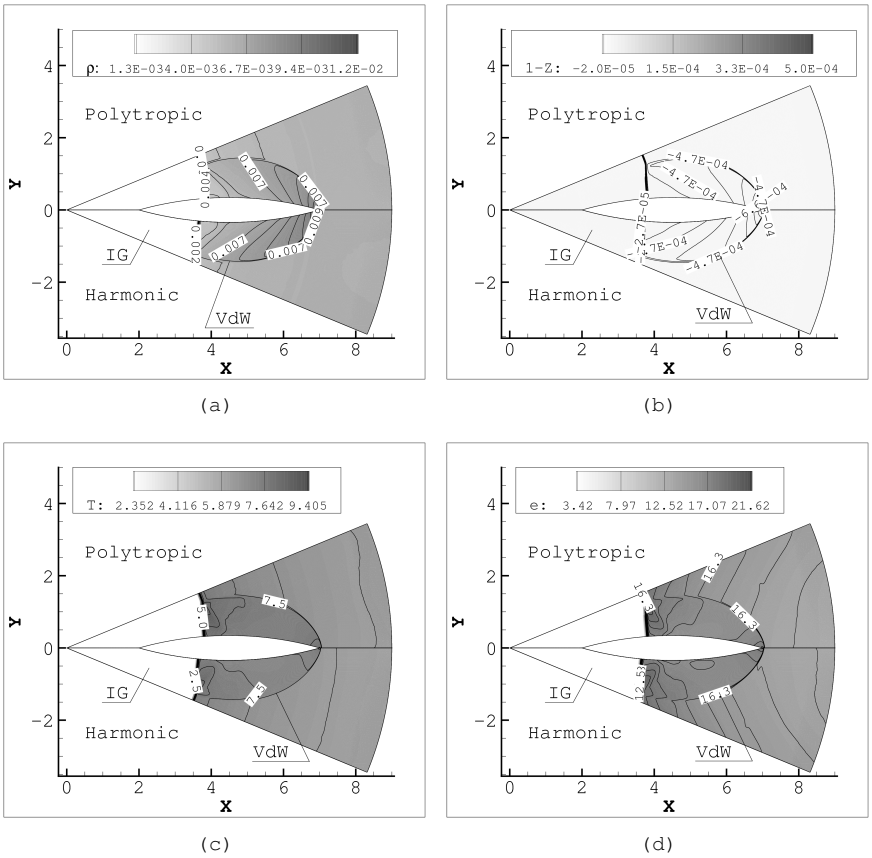

Figure 5.8: Spatial distributions of (a) density, (b) compressibility factor, (c) temperature and (d) specific internal energy in a reshaped shock-induced flow field in dilute conditions generated by a $\beta_P = 27$ and obtained with four different thermodynamic models (reference geometry, time from the impinging to the focusing $\tau/\tilde{\tau} = 0.472$, $\Delta x = 0.01$, corresponding to about 100000 nodes, and $\Delta\tau = 6 \times 10^{-4}$).

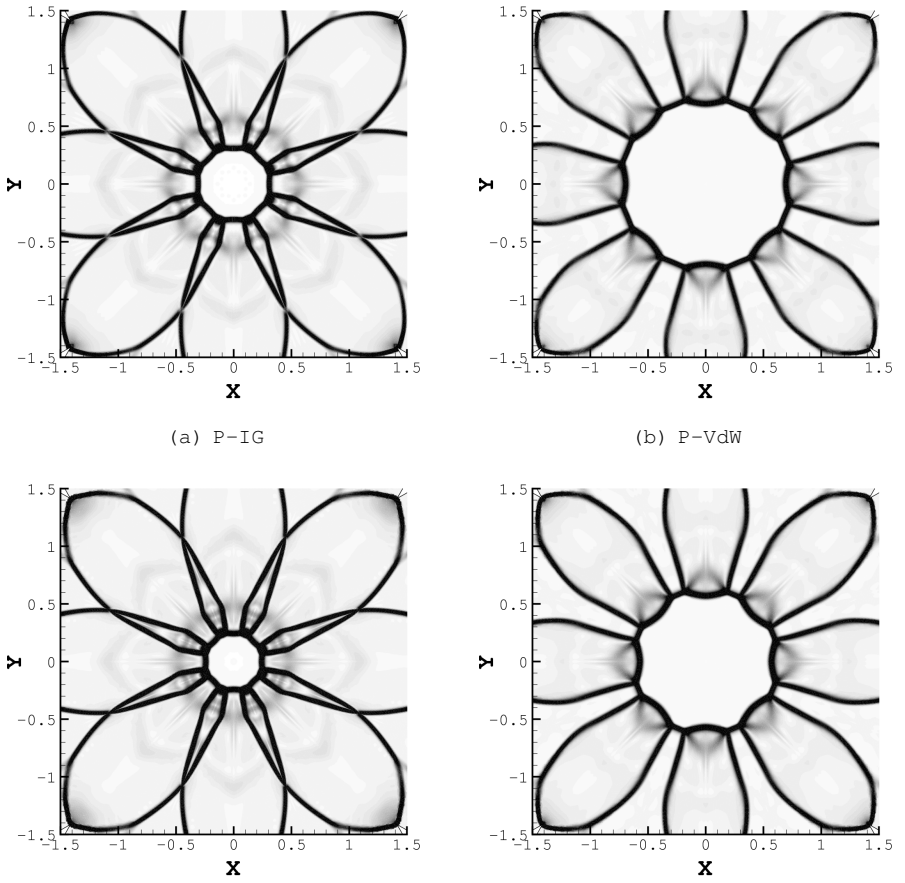

(a) P-IG (b) P-VdW

(c) H-IG (d) H-VdW

Figure 5.9: Comparison among the diverse shock shapes in correspondence of the focus point for diverse thermodynamic models: (a) P-IG, (b) P-VdW, (c) H-IG and (d) H-VdW. The polygonal shock waves are reported at a time $\tau = 1.3605$ from the initial diaphragm breaking. The shock waves simulated with the polytropic c_v model (top line) are slower than the ones with a harmonic c_v model (bottom line). Moreover, when the van der Waals gas model applies (right column), the resulting shock speed is slower that in case of ideal gas (left column). The shocks are generated by an initial $\beta_P = 16$ and they are reshaped by an array of 8 obstacles in reference geometry. Numerical simulations are performed over a grid with $\Delta x = 0.01$, corresponding to about 100000 nodes, and $\Delta\tau = 6 \times 10^{-4}$).

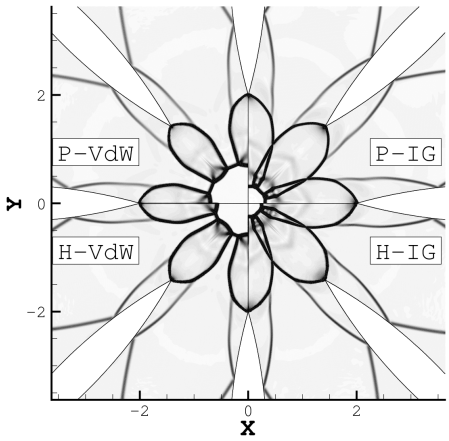

(a) $\tau = 1.3605$

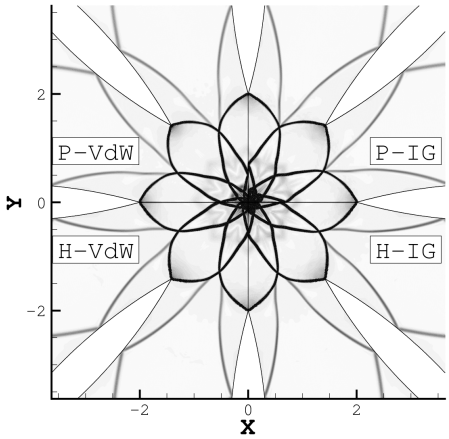

(b) $\tau = \tilde{\tau}$

Figure 5.10: Comparison among the shock waves near the focus point in the same configuration (reference conditions) simulated with different thermodynamic models: (a) at time $\tau = 1.3605$ after the diaphragm breaking and (a) at different times, i.e. when each shock wave reaches the focus point. Numerical simulations are performed over a grid with $\Delta x = 0.01$, corresponding to about 100000 nodes, and $\Delta\tau = 6 \times 10^{-4}$).

5.3 Pressure and temperature at the focus point

The values of pressure and temperature attained at the origin after the shock focusing are reported in this section. An assessment between the pressure and temperature factors c_P and c_T—defined in sec. 4.2—obtained with diverse thermodynamic models is reported in sec. 5.3.1. The most relevant differences between the results obtained in dense and dilute gas conditions are discussed in sec. 5.3.2.

5.3.1 Dilute gas conditions

Fig. 5.11 compares the pressure factors versus number of obstacles obtained with diverse thermodynamic models. As expected, c_P in general increases with the shock strength (summarized by the initial pressure ratio β_P) and with the number of obstacles, in accordance with the preliminary analysis performed on polytropic ideal gas (cf. fig. 4.2).

The thermodynamic model appears to have a large influence, in terms of both quantity and quality.

It can be observed that results obtained with the ideal gas model (gray line in fig. 5.11) presents higher pressure values than the corresponding ones obtained with the van der Waals model (black line in fig. 5.11), for a given specific heat model. This is qualitatively in accordance with results in fig. 5.5: non-ideal gas effects cause the maximum internal energy values to decrease with respect to the ideal gas case. It must be noted that in fig. 5.5, this effect is observable only in dense gas, whereas the results under scrutiny concern the dilute gas case. However, the shock intensity increase during the shock convergence: the pressure, temperature and density at the focusing (depicted in fig. 5.11), therefore, are so high to be comparable to the initial conditions of the shock convergence in dense conditions (reported in fig. 5.5). For this reason, non-ideal effects become observable at the focusing of a shock wave generated in dilute conditions.

Similarly, considering pairs of configurations responding to the same equation of state, c_P appears to be higher when the

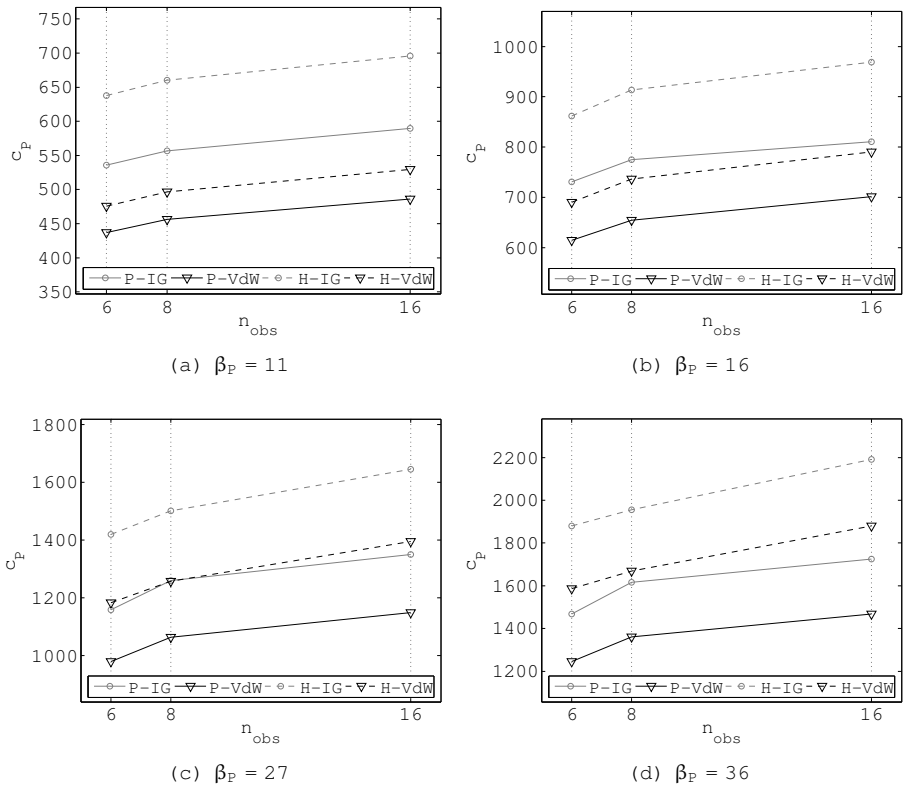

(a) $\beta_P = 11$ (b) $\beta_P = 16$

(c) $\beta_P = 27$ (d) $\beta_P = 36$

Figure 5.11: Pressure factor versus obstacles number with diverse thermodynamic models for air in dilute conditions and increasing β_P ($r_{LE} = 17.5$, $t/c = 0.21$). The interaction effect, i.e. the switch between the curves convernong the P-IG and the H-VdW models triggered by the shock intensity, occurs at $\beta_P = 27$, but it can be observed from the lower to the upper β_P value. Numerical simulations are performed with $\Delta x = 0.01$, corresponding to about 400000 nodes, and $\Delta\tau = 6 \times 10^{-4}$.

harmonic term is considered in the c_v model (dashed line versus full line in fig. 5.11). These two effects, as well as those occurring in all the configurations regardless of the values of other factors, will be referred to as "simple", because they depend on one factor only.

In opposition to simple effects, "interaction" effects can be observed, too. Indeed, the relative importance of the equation of state and the c_v model changes when the shock intensity is considered. Indeed, for the case of $\beta_P = 11$ reported in fig. 5.11(a), the effect of the equation of state is more relevant that the one of the c_v model. In this operating condition, regardless of n_{obs}, the values of c_P in ascending order are provided by the following thermodynamic models:

P-VdW H-VdW P-IG H-IG

On the contrary, for $\beta_P = 36$ a larger separation is observed between pairs of curves sharing the same equation of state. In this case, c_P in ascending order is provided by the diverse thermodynamic models as follows:

P-VdW P-IG H-VdW H-IG

This implies that, even though the two simple effects are preserved, an interaction occurs between the equation of state and the c_v model, triggered by β_P. Result of this interaction is a switch (termed "inversion", in the following) between the P-IG and H-VdW curves of c_P, occurring at $\beta_P = 27$ for all the obstacle configurations.

The examination of the effects of the factors on the temperature, represented by the coefficient c_T in fig. 5.12, confirms the observation performed in sec. 4.2 for the polytropic ideal gas. Indeed, the temperature attained at the focus point increases more than proportionally with M_S^{LE}, but presents much weaker dependence on single geometric factors and on their mutual interactions. Fig. 5.12 reports c_T versus M_S^{LE} for diverse thermodynamic models in a test matrix where rows indicate levels of r_{LE} and columns of n_{obs} (the obstacle thickness-to-chord ratio is fixed to $t/c = 0.21$). For higher visual clarity, only

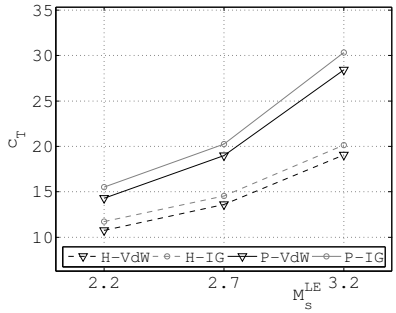

(a) $r_{LE} = 7$, $n_{obs} = 6$

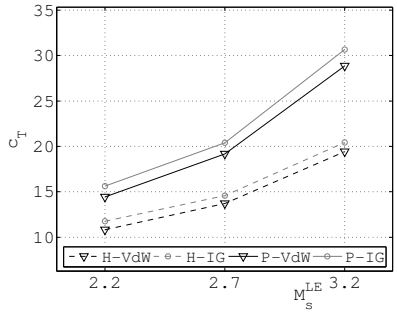

(b) $r_{LE} = 7$, $n_{obs} = 16$

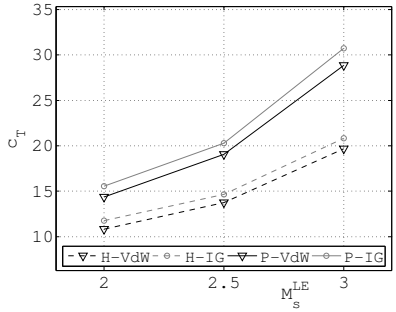

(c) $r_{LE} = 14$, $n_{obs} = 8$

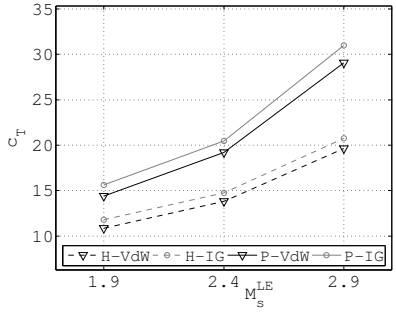

(d) $r_{LE} = 17.5$, $n_{obs} = 6$

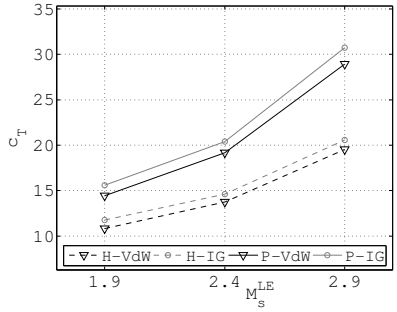

(e) $r_{LE} = 17.5$, $n_{obs} = 16$

Figure 5.12: Temperature factor versus shock Mach number at the leading edge with diverse thermodynamic models for air in dilute conditions and diverse combinations of r_{LE} and n_{obs} ($t/c = 0.21$). Numerical simulations are performed with $\Delta x = 0.01$ and $\Delta\tau = 6 \times 10^{-4}$.

results belonging to the diagonals of the test matrix are reported.

It is observed that the computed c_T is higher when polytropic models for c_v are adopted, with both ideal and van der Waals equations of state. Similarly, both in the polytropic and in the harmonic case, simulations performed with the ideal gas equation of state provide higher values of c_T. Between these two simple effects, the most relevant is the one due to the constant-volume specific heat model for all the geometric configurations and operating conditions.

Unlike what observed for the pressure coefficient, no mutual interaction—between the equation of state and the c_v model or among geometric factors—is observed.

5.3.2 Dense gas conditions

Numerical experiments are performed also in dense gas conditions. It is recalled that the numerical values of the initial pressure and density do not depend on the thermodynamic model. Moreover, for the simulations performed with a given β_P value, the ratio between the external and the internal values of pressure and density is the same as in the corresponding dilute gas case with the same β_P value. Therefore, the initial temperature evaluated for the ideal gas case is the same as in dilute gas conditions. On the contrary, a very slight variation in the temperature initial values is observed for van der Waals gas. Therefore, real gas effects are expected to be more relevant than in dilute gas conditions, whereas high temperature effects are considered comparable.

The case of shock waves interacting with eight obstacles at reference distance is detailed in the following. Considerations derived for $n_{obs} = 8$ and $r_{LE} = 7$ may be extended to all the other configurations.

Fig. 5.13 compares the shock effectiveness on the compression of the gas at the focus point obtained in dilute and dense gas conditions, both for $t/c = 0.21$. In the first row of pictures (figs. 5.13(a) and 5.13(b)), the pressure factor is plotted versus the incident shock Mach number; in the second (figs.

5.3(a) and 5.13(d)), it is represented in function of the initial pressure ratio. Eventually, in figs. 5.13(e) and 5.13(f), the trend of the pressure ratio normalized with the initial pressure ratio—assumed as an indicator of the shock compression efficiency—is reported versus β_P.

In accordance with theory, the comparison indicates that c_P for the ideal gas model does not present relevant differences between the dilute and the dense conditions, in particular for the polytropic case, which remains the same. The simple effects of the thermodynamics highlighted for the dilute gas can be observed also for the dense gas: the pressure factor is higher when computed with a harmonic model for c_v or with an ideal gas equation of state. The most relevant difference concerns the effectiveness and efficiency of the implosion when computed by means of a van der Waals equation of state: for dense gas conditions, indeed, the pressure factor presents only a weak dependence on the shock intensity, and therefore the compression efficiency decreases with increasing β_P. Eventually it is observed that the interaction between the equation of state and the c_v model—which in dilute conditions causes the crossing between the curves of harmonic ideal gas and polytropic van der Waals gas at $\beta_P = 27$—does not occur in the observed range of β_P in dense conditions.

Similarly, the curves depicting the trend of c_T show a weak or null variation for ideal gas between dilute and dense conditions. For van der Waals equation of state, on the contrary, relevant differences appear. Indeed, for $M_s^{LE} \leq 3.7$, van der Waals curves present higher values of c_T, both for the polytropic and for the harmonic case. Moreover, an interaction between the initial pressure ratio and the specific heat model is observed, resulting in the systematic inversion of the two van der Waals curves at $M_s^{LE} \approx 3.2$ for all the t/c values.

The two trends of c_P and c_T confirm the qualitative considerations performed for the dilute gas case. Of course, the difference between results obtained with different pressure equations of state is much more relevant, due to the higher importance of non-ideal effects in dense conditions.

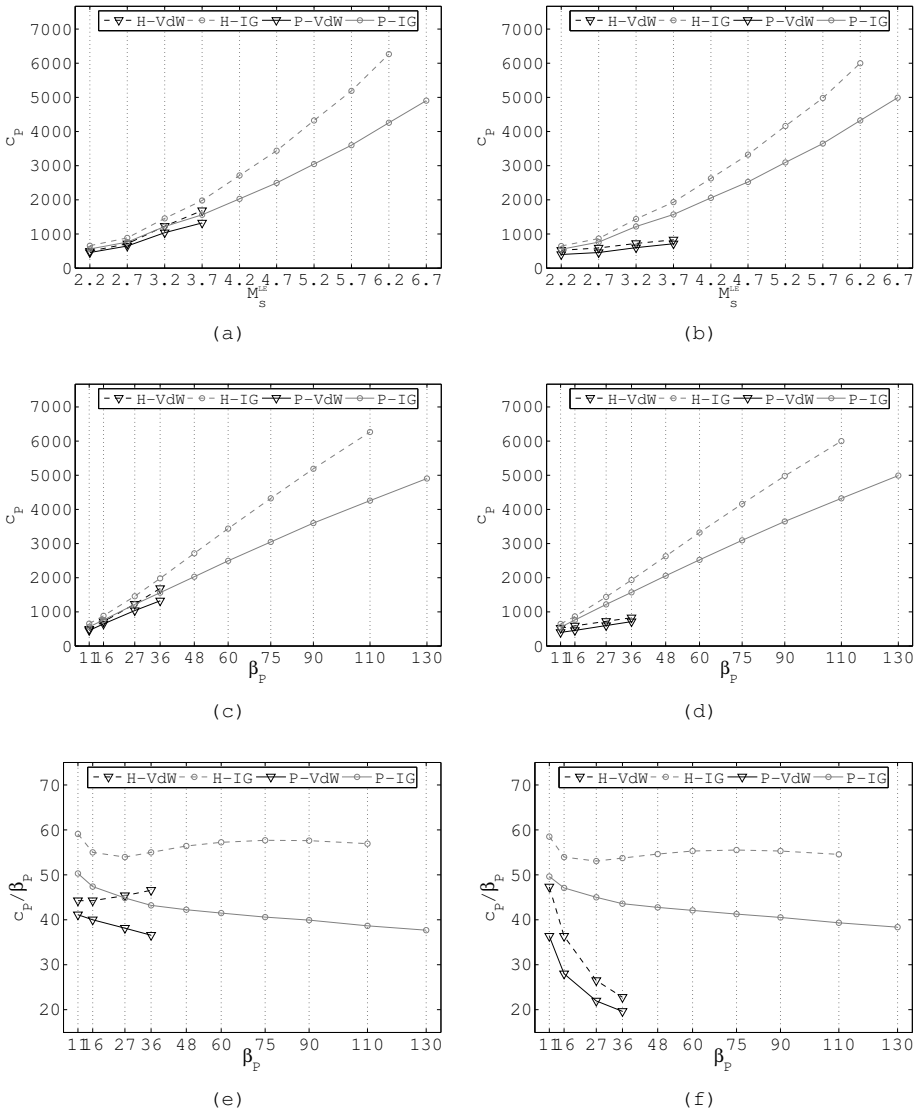

Figure 5.13: Pressure factor for diverse thermodynamic models in (a)-(a)-(e) dilute and (b)-(d)-(f) dense gas conditions ($r_{LE} = 7$, $n_{obs} = 8$, $t/c = 0.21$).

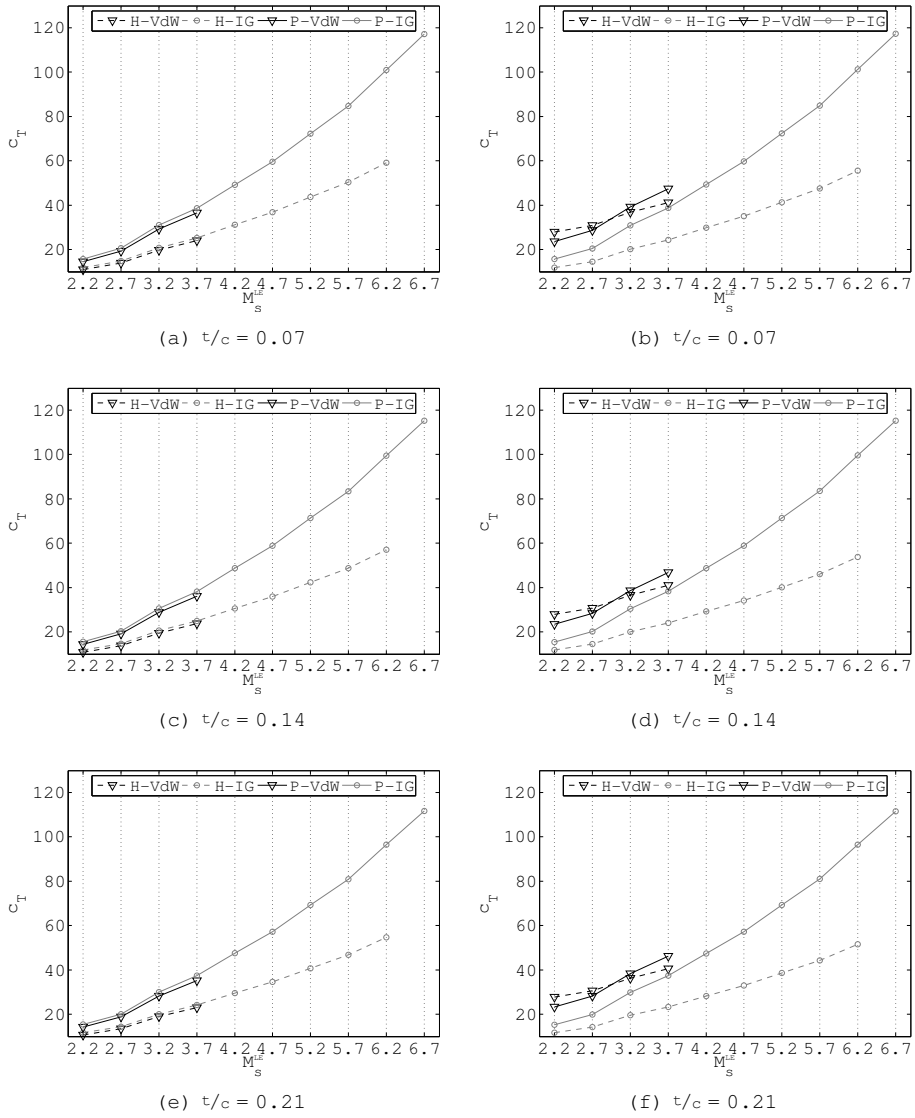

(a) $t/c = 0.07$ (b) $t/c = 0.07$

(c) $t/c = 0.14$ (d) $t/c = 0.14$

(e) $t/c = 0.21$ (f) $t/c = 0.21$

Figure 5.14: Temperature factor versus M_s^{LE} for diverse thermodynamic models and t/c values in (a)-(c)-(e) dilute and (b)-(d)-(f) dense gas conditions ($r_{LE} = 7$, $n_{obs} = 8$). Numerical simulations are performed with $\Delta x = 0.01$, corresponding to about 100000 nodes, and $\Delta\tau = 6 \times 10^{-4}$.

5.4 Pseudo-self similarity exponents

In this section, a linear regression on the shock position is performed in order to estimate the self-similarity exponent α in the power-law function that correlates the shock position with time. This function, introduced in sec. 3.3 (eq. (3.31)) and detailed in sec. 4.1.3 (eq. (4.1)) is in the well known form

$$R_S = \tilde{r}\left(1 - \frac{\tau}{\tilde{\tau}}\right)^{\alpha}. \qquad (5.2)$$

According to theoretical works [39, 88], the power law strictly applies to genuinely self-similar phenomena, that is cylindrical shocks and shock fronts undergoing the reshaping cascade whose initial shape is a regular polygon. However, a fair accordance to a power-law function is observed also for polygonal shocks, as detailed in sec. 4.1.3, provided a certain level of symmetry.

The analytical derivation of the power-law for genuinely self-similar phenomena, as reported by [41, 49], shows that the functional form of the equation does not depend on the thermodynamic model; on the contrary, the numerical value of α requires the knowledge of both the shock front shape and of the thermodynamic model.

For shocks converging in polytropic ideal gas, and generated by a piston in cylindrical symmetry, the characteristics method allowed to obtain an analytical expression for of α. Details on the hypotheses underlying the method, procedure, and results can be found in [41, 42, 54, 39, 63, 48, 47]. The shock waves analyzed in this work do not satisfy some of the criteria: their propagation is genuinely unsteady, most of the reshaped shock have symmetrical but irregular polygonal shape, the shock onset is due to different initial conditions (the numerical diaphragm instead of the cylindrical piston), the length scales of R_S and of the diaphragm position are comparable. It is recalled that the problem of the initial conditions is due to the physical transient which leads from the compression band caused by the piston to the onset of the real shock wave: during this transient, the phenomenon is not self-similar. Therefore, analytical works based on the cylindrical piston model assume that the self-similar solution is a "limit-

ing solution". This implies that the length scale of the shock radius where the power law applies must vary significantly from the scale associated to the piston position or, in general, to the initial conditions radius.

Moreover, the treatment of the thermodynamic model appears to be a very hard issue. The "CCW" method (from Chester [43], Chisnell [44] and Whitham [45, 46]) provides an analytic expression for α for cylindrical shock waves. The method is based on the polytropic ideal gas model, and therefore the expression can be manipulated thanks to its linearity. Unfortunately, the procedure cannot be—in general—extended to a case whose thermodynamics is described by means of an alternative, more complex model.

In conclusion, a simple least-square interpolation is performed on numerical data (in dilute gas conditions), to provide transformed as follows:

$$\ln\left(\frac{R_s}{\tilde{r}}\right) = \alpha \cdot \ln\left(1 - \frac{\tau}{\tilde{\tau}}\right). \tag{5.3}$$

5.4.1 One-dimensional shock exponents

For one-dimensional axisymmetrical shock waves, genuine self-similarity applies. Therefore, the power-law function represents the exact correlation between the shock radius and time. Indeed, the maximum relative error between the sampled R_s^{samp} and the predicted radius among all the observed configurations remains negligible,

$$\max_{config}\left(\frac{\left|R_s^{samp}(\tau) - R_s^{PL}(\tau)\right|}{R_s^{PL}(\tau)}\right) = \mathcal{O}\left(10^{-3}\right). \tag{5.4}$$

The solution was not analyzed in the initial transient, i.e. a few time steps after the diaphragm breaking. The reason is two-fold. On the one hand, the numerical procedure which allows to detect the shock position described in sec. 2.2.1 becomes inaccurate if the spatial separation between the shock wave and the collateral waves is too small. During the first time steps of the numerical simulation, of course, the three

waves are confined within a small number of nodes. Therefore, the pressure along the shock profile does not follow any of the distributions reported in fig. 2.19, but a more complex one.

On the other hand, as described at the beginning of sec. 5.4, self-similarity applies to shock waves in correspondence of the focus point. In this work, this condition is violated, because the shock wave is observed on a larger spatial range. Therefore, a preliminary analysis was performed on the shock wave propagating in polytropic ideal gas to determine the range of applicability of eq. (3.31). The fitting was indeed performed on data sampled over intervals ranging from the focus point to a variable maximum radius, and the self-similarity exponents were computed and compared to the theoretical value, 0.834. The preliminary analysis allowed to determine the maximum R_s for which the convergence of the cylindrical shock wave still exhibits a self similar behavior, that is about 24.

The values of α resulting from the linear regressions are reported in tab. 5.2

1D	P-IG	P-VdW	H-IG	H-VdW
α	0.836	0.849	0.850	0.853

Table 5.2: Self-similarity exponents of one-dimensional shock waves for diverse thermodynamic models.

As discussed in sec. 4.1.3, the value of α in the polytropic ideal gas case is in good accordance with the results of theoretical models and experimental results. For the other thermodynamic models, α is slightly larger, but still comparable with the polytropic ideal gas one.

Fig. 5.15 depicts the shock position for the four different thermodynamic models: numerical data are represented by symbols (each symbol is associated to a different shock intensity), while the fitting curve is depicted as a full line. Time is normalized on the overall convergence time from the diaphragm breaking to the shock focusing, and in abscissa its complementary to one is reported to highlight the term reported

in eq. (5.3). The similar values of the self-similarity exponents reported in tab. 5.2 imply that the propagation of the one-dimensional shock is not significantly influenced by the thermodynamic model; indeed, the four curves of fig. 5.15 appear to be very similar to each other.

The fitting is performed without separating data concerning shock waves with different β_P. Indeed, it is known [42] that the value of the shock Mach number is not influential either on the functional form of the power-law function or on the self-similarity exponent, but only, at most, in the combination between the parameters $\tilde{r}$ and $\tilde{\tau}$.

5.4.2 Two-dimensional shock exponents

As detailed in sec. 2.2 during the description of the method adopted to detect the shock position, in a two-dimensional framework R_S actually indicates the shock average radius, as the shock front consists in a polygonal wave. The average shock radius in time can still be conveniently described by means of a power-law function. The new self-similarity exponent depends on the shock symmetry, and the parameters $\tilde{r}$ and $\tilde{\tau}$ must be modified to fit the polygonal shock propagation.

When the cylindrical shock is reflected over the obstacle leading edge, the Mach stem size gradually grows from zero to the maximum size, and then it is reflected over the upper symmetry surface. Therefore, between the leading edge and the secondary reflections, the shock front consists in both cylindrical and polygonal shock waves, and therefore the function $R_S(\tau)$ assumes intermediate values between the power laws adopted to describe the one- and two-dimensional propagations.

Fig. 5.16 illustrates $R_S(\tau)$ for the reference case (dilute gas conditions, polytropic ideal gas model, $\beta_P = 16$, $n_{obs} = 8$, $r_{LE} = 7$, $t/c = 0.14$): the two curves representing the one- and the two-dimensional shock waves propagation are reciprocally tangent at $r \approx 7$ which is the region where the transition occurs. This indicates the smoothness of the transition from the one- to the two-dimensional curves.

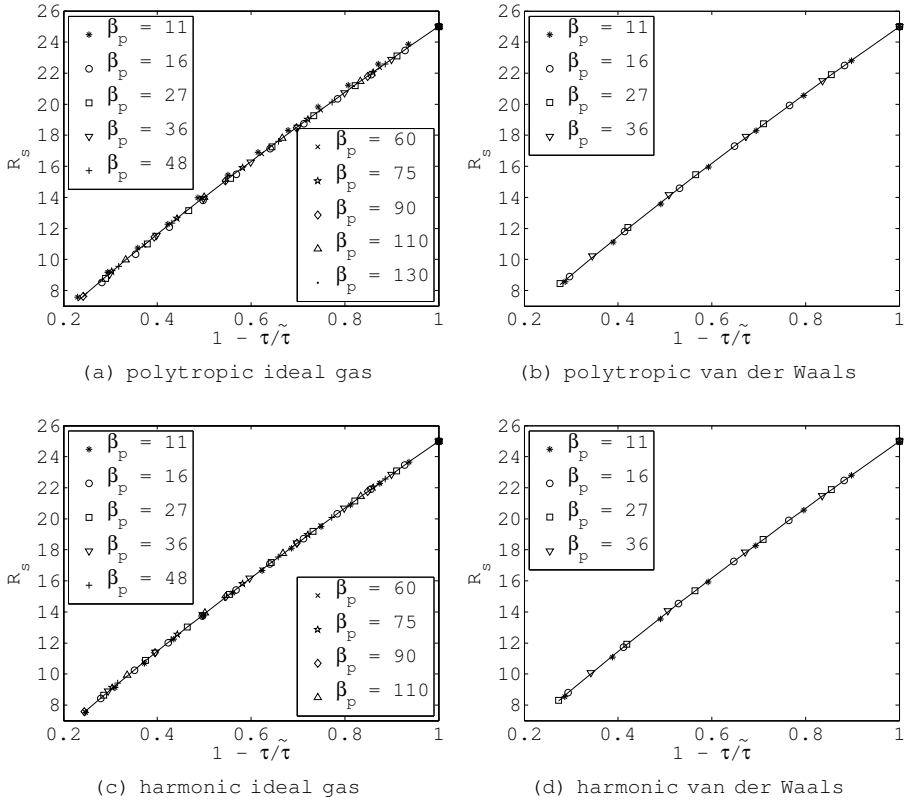

(a) polytropic ideal gas

(b) polytropic van der Waals

(c) harmonic ideal gas

(d) harmonic van der Waals

Figure 5.15: One-dimensional shock waves propagation for diverse thermodynamic models: (a) P-IG (10 β_P levels), (b) P-VdW (4 β_P levels), (c) H-IG (9 β_P levels) and (d) H-VdW (4 β_P levels). Numerical data are represented by symbols, the fitting curves by a full line. Numerical simulations are performed with $\Delta x = 0.01$, corresponding to about 2300 nodes, and $\Delta\tau = 6 \times 10^{-4}$.

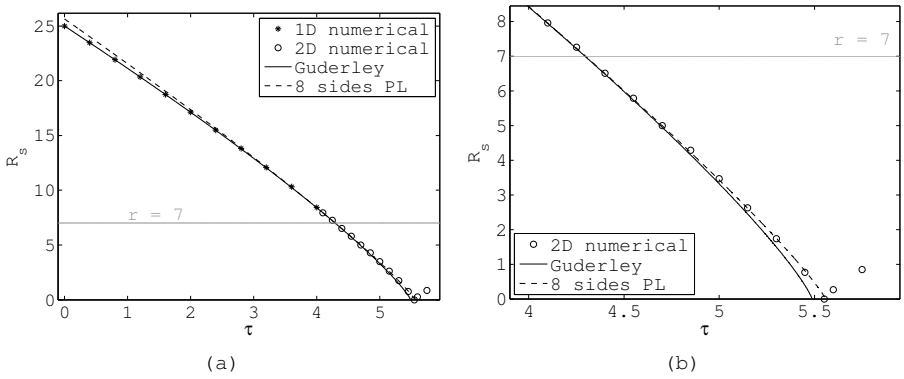

Figure 5.16: Transition from the one-dimensional (∗ symbol for numerical data, full line for the fitting curve) to two-dimensional (o symbol for numerical data, dashed line for the fitting curve) shock propagations: (a) full interval and (b) close-up in correspondence of the transition and focusing (dilute gas conditions, P-IG model, $\beta_P = 16$, $n_{obs} = 8$, $r_{LE} = 7$, $t/c = 0.14$). Numerical simulations are performed with $\Delta x = 0.01$ and $\Delta\tau = 6 \times 10^{-4}$.

A linear regression is performed on the average R_S of polygonal shocks. Figs. 5.17 to 5.20 show the shock advancement for diverse thermodynamic models and obstacle numbers. After the time normalization, the curves regarding diverse β_P, represented by different symbols, become coincident, as expected on the basis of theoretical considerations. Data are shown only for $\beta_P \leq 27$ for visual clarity.

Note that plots in figs. 5.17 to 5.20 concern only obstacle configurations with $t/c = 0.14$ and $r_{LE} = 7$. However, as discussed in the following, these two factors are not influential on α. Indeed, among all the explored configuration, only the reference one has been observed to produce a reshaping cascade in accordance with Schwendeman description [88], that is a continuous self-similar reshaping from a n_{obs}- to a $2n_{obs}$- polygonal shape and vice versa. For this reason, the pseudo-self similarity exponent α for polygonal shock must rely with the general non self-similarity of the reshaping cascade. Therefore, each power-law function of $R_S(\tau)$ is assumed to describe

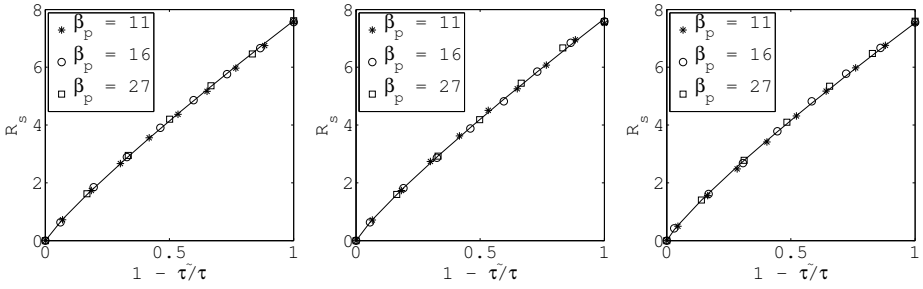

(a) P-IG, $n_{obs} = 6$ (b) P-IG, $n_{obs} = 8$ (c) P-IG, $n_{obs} = 16$

Figure 5.17: Polygonal shock average radius in polytropic ideal gas for diverse obstacle numbers: (a) $n_{obs} = 6$, (b) $n_{obs} = 8$ and (c) $n_{obs} = 16$. The shock intensity is reported for three levels, $\beta_P = 11$ (∗), $\beta_P = 16$ (○) and $\beta_P = 27$ (□) (dilute gas conditions, $r_{LE} = 7$, $t/c = 0.14$). Numerical simulations are performed with $\Delta x = 0.01$ and $\Delta\tau = 6 \times 10^{-4}$.

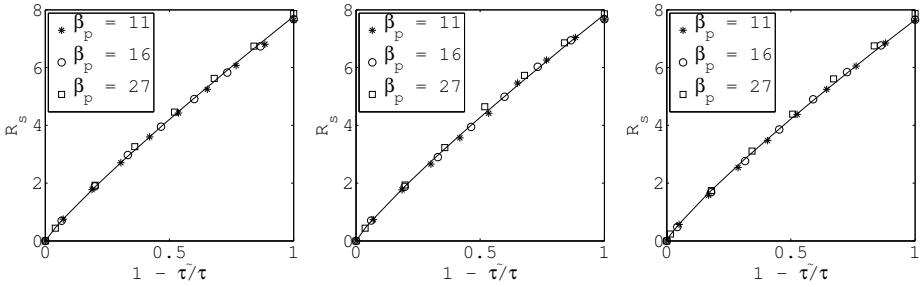

(a) P-VdW, $n_{obs} = 6$ (b) P-VdW, $n_{obs} = 8$ (c) P-VdW, $n_{obs} = 16$

Figure 5.18: Polygonal shock average radius in polytropic van der Waals gas for diverse obstacle numbers: (a) $n_{obs} = 6$, (b) $n_{obs} = 8$ and (c) $n_{obs} = 16$. The shock intensity is reported for three levels, $\beta_P = 11$ (∗), $\beta_P = 16$ (○) and $\beta_P = 27$ (□) (dilute gas conditions, $r_{LE} = 7$, $t/c = 0.14$). Numerical simulations are performed with $\Delta x = 0.01$ and $\Delta\tau = 6 \times 10^{-4}$.

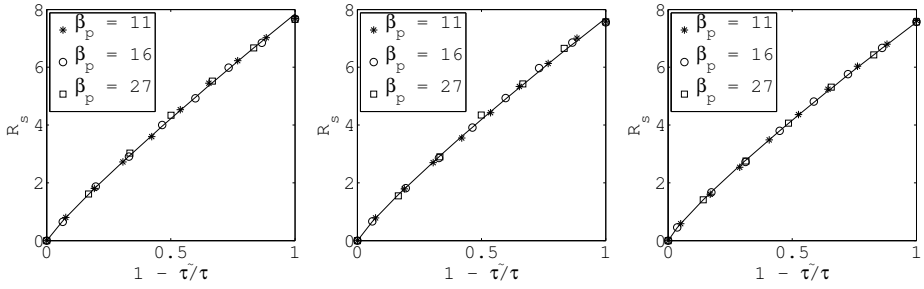

(a) H-IG, $n_{obs} = 6$ (b) H-IG, $n_{obs} = 8$ (c) H-IG, $n_{obs} = 16$

Figure 5.19: Polygonal shock average radius in harmonic ideal gas for diverse obstacle numbers: (a) $n_{obs} = 6$, (b) $n_{obs} = 8$ and (c) $n_{obs} = 16$. The shock intensity is reported for three levels, $\beta_P = 11$ (∗), $\beta_P = 16$ (o) and $\beta_P = 27$ (□) (dilute gas conditions, $r_{LE} = 7$, $t/c = 0.14$). Numerical simulations are performed with $\Delta x = 0.01$ and $\Delta\tau = 6 \times 10^{-4}$.

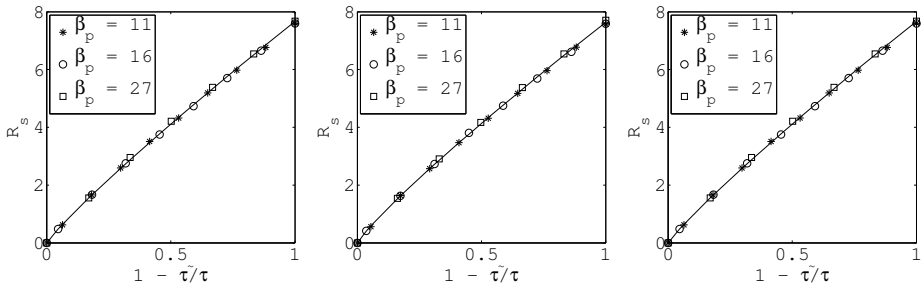

(a) H-VdW, $n_{obs} = 6$ (b) H-VdW, $n_{obs} = 8$ (c) H-VdW, $n_{obs} = 16$

Figure 5.20: Polygonal shock average radius in harmonic van der Waals gas for diverse obstacle numbers: (a) $n_{obs} = 6$, (b) $n_{obs} = 8$ and (c) $n_{obs} = 16$. The shock intensity is reported for three levels, $\beta_P = 11$ (∗), $\beta_P = 16$ (o) and $\beta_P = 27$ (□) (dilute gas conditions, $r_{LE} = 7$, $t/c = 0.14$). Numerical simulations are performed with $\Delta x = 0.01$ and $\Delta\tau = 6 \times 10^{-4}$.

the convergence of a polygonal shock with "periodic symmetry", instead of the classical polygonal regularity.

As described in sec. 4.3, the polygonal shock varies unsteadily the number of edges during the convergence; it ranges from n_{obs} to the maximum number of edges, which can be $2n_{obs}$, $3n_{obs}$ or $4n_{obs}$ depending on the combination of geometrical factors and operating conditions. For each configuration, the set of the number of edges belonging to the polygonal shock during time can be defined. This set is always coprime, being n_{obs} the greatest common divisor of the element of this set, i.e. $2n_{obs}$, $3n_{obs}$ and $4n_{obs}$. Therefore, the periodic symmetry of each polygonal shock depends on n_{obs} only, and the effects of t/c and r_{LE} can be neglected.

This assumption is verified by comparing the values of α obtained for a number of geometrical conditions. Considering the case of $n_{obs} = 8$, results for diverse obstacle distance and thickness are reported. Tab. 5.3 lists the values of α, and fig. 5.21 depicts the curves for the diverse obstacle distance ((a)-(b)) and thickness ((c)-(d)).

t/c	0.14	0.14	0.14	0.07	0.21
r_{LE}	7	14	17.5	7	7
α	0.87296	0.87304	0.87265	0.87369	0.87300

Table 5.3: α values for diverse geometrical configurations for P-IG and $n_{obs} = 8$: no relevant difference can be observed.

The values of α of polygonal shock waves are summarized in tab. 5.4. Fig. 5.4(a) plots the self-similarity exponents versus the obstacles number (fig. 5.22(a)) and the periodicity of the polygonal shock (fig. 5.22(b)), and assesses them with the cylindrical shock α. The periodicity of the polygonal shock is defined as ξ/π, that is equivalent to $1/n_{obs}$.

The close-up in correspondence of the polytropic ideal gas curves in correspondence of $n_{obs} = 8$ shows the values of α for diverse geometrical conditions, i.e. those reported in tab. 5.3. It can be observed that the difference between the self-similarity exponents of each single condition and the global one is negligible with respect to the distinction due to n_{obs}

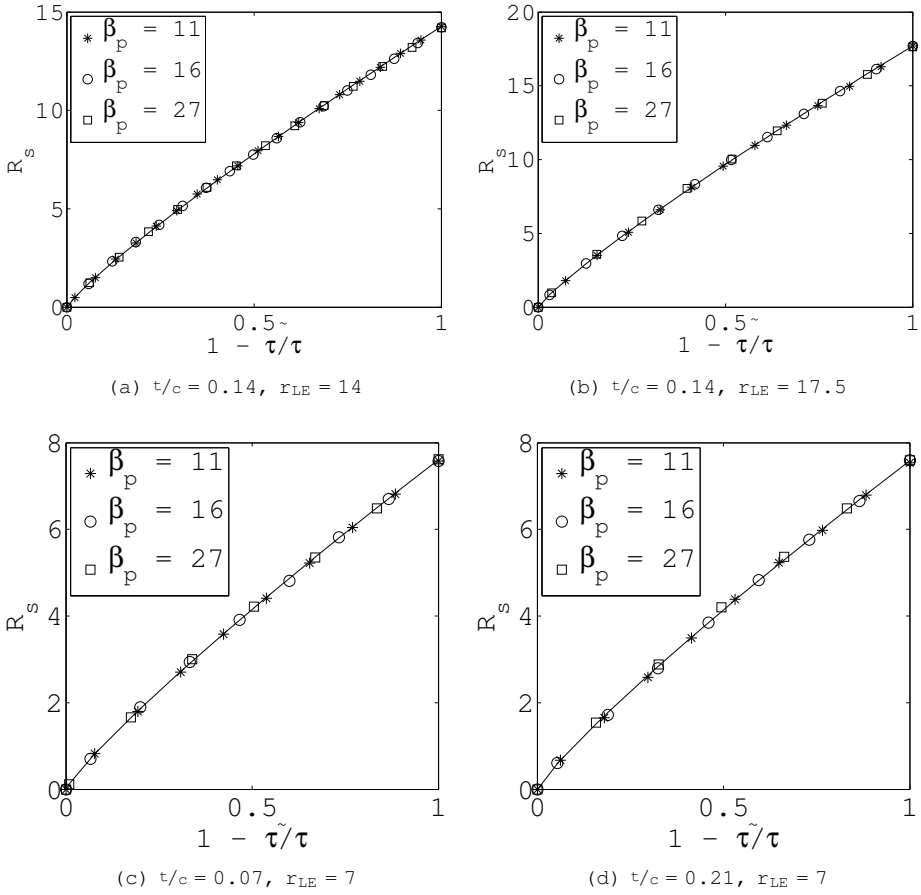

(a) $t/c = 0.14$, $r_{LE} = 14$

(b) $t/c = 0.14$, $r_{LE} = 17.5$

(c) $t/c = 0.07$, $r_{LE} = 7$

(d) $t/c = 0.21$, $r_{LE} = 7$

Figure 5.21: Polygonal shock average radius in polytropic ideal gas for $n_{obs} = 8$ and diverse obstacle geometries: (a) $t/c = 0.14$, $r_{LE} = 14$, (b) $t/c = 0.14$, $r_{LE} = 17.5$, (c) $t/c = 0.07$, $r_{LE} = 7$ and (d) $t/c = 0.21$, $r_{LE} = 7$. The shock intensity is reported for three levels, $\beta_P = 11$ (∗), $\beta_P = 16$ (o) and $\beta_P = 27$ (□).

or to the thermodynamic model.

α, 2D	P-IG	P-VdW	H-IG	H-VdW
$n_{obs} = 6$	0.878	0.888	0.895	0.900
$n_{obs} = 8$	0.873	0.876	0.878	0.883
$n_{obs} = 16$	0.858	0.860	0.861	0.873

Table 5.4: Self-similarity exponents of two-dimensional shock waves for diverse thermodynamic models and obstacle numbers.

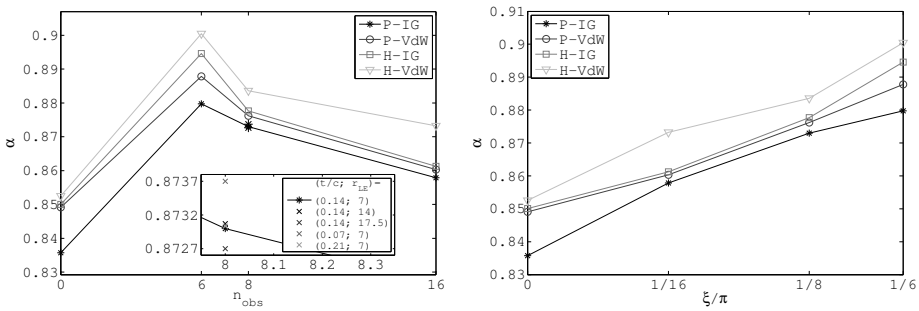

Figure 5.22: α versus (a) the number of obstacles and (b) the periodicity of the symmetrical polygonal shock for diverse thermodynamic conditions. The close-up in correspondence of the P-IG curves at $n_{obs} = 8$ shows the values of α for diverse geometrical conditions.

5.5 Shock propagation in the P-v plane

It is well known that the conditions behind a shock wave depend on the state of the flow ahead of the shock, in accordance to the Rankine-Hugoniot conditions and hence the thermodynamic model. For a planar shock, the flow behind the shock is uniform and it does not depend on time. Therefore, on the thermodynamic plane P-v it is represented by a single point. This point belongs to the shock adiabat, which is unique for each set of thermodynamic conditions in front of the shock, defined the

"pivots" of the adiabat. The position of the point representing the post-shock state along the adiabat depends on the shock intensity.

On the contrary, due to its unsteady nature, the Mach number of a cylindrical shock varies along time in accordance with eq. (3.38) derived from Guderley's formula. For this reason, also the pressure and specific volume immediately behind the shock are time-dependent. Therefore the point on the plane P-v characterizing the condition of the flow immediately behind th shock moves along the shock adiabat which is pivoted in the point (v_i, P_i).

Rankine-Hugoniot conditions are valid across normal shock waves. However, it is also known that any shock wave can be locally recast to a normal one to determine Rankine-Hugoniot conditions [138], as they derive from the local enforcement of the conservation laws expressed in integral form. Therefore, the unsteady and geometrical source terms—which are non-null in the conservation laws in cylindrical symmetry—become negligible when the control volume adopted for the derivation of algebraic jump relations goes to zero.

For polytropic ideal and van der Waals gas, c_v remains constant, and therefore it is possible to define the constant quantity

$$\delta_\gamma = \frac{\widehat{R}}{\widehat{c}_v}. \tag{5.5}$$

For a polytropic ideal gas, $\delta_\gamma = \gamma - 1$, where γ is the ratio of specific heats at constant pressure and constant volume. On the contrary, for a van der Waals gas, Mayer relation [100] does not apply, and therefore $\delta_\gamma + 1$ does not indicate the specific heats ratio.

For cylindrical shock waves in polytropic gas, classical relations between pressure and specific volume, i.e. the shock

adiabat, apply

$$P_b\left(v_b; P_i, v_i\right) = P_i \cdot \frac{\left(\frac{\delta_\gamma+2}{\delta_\gamma}\right) - \frac{v_b}{v_i}}{\left(\frac{\delta_\gamma+2}{\delta_\gamma}\right)\frac{v_b}{v_i} - 1} \tag{5.6a}$$

(polytropic ideal gas),

$$P_b\left(v_b; P_i, v_i\right) = \frac{\frac{1}{\delta_\gamma}\left(P_i + \frac{a}{v_i^2}\right)\left(v_i - b\right) - \frac{P_i}{2}\left(v_b - v_i\right) + \frac{a}{v_b\delta_\gamma}\left(\frac{b}{v_b} - 1\right)}{\left(\frac{1}{2} + \frac{1}{\delta_\gamma}\right)v_b - \left(\frac{v_i}{2} + \frac{b}{\delta_\gamma}\right)} \tag{5.6b}$$

(polytropic van der Waals gas).

The relations above are defined also for non-polytropic gas, but the evaluation of post-shock conditions requires a numerical procedure. The derivation of the shock adiabat also for gas which are not governed by a polytropic ideal gas model is described in [139].

The tracing of the locus of point describing the post shock conditions in time in the P-v plane is performed by evaluating P_b as $P(R_e)$ and v_b as $v(R_e)$ at each time step. R_e is the radius of the node immediately behind the shock wave defined is sec. 2.2.1, and therefore it is measured by means of the procedure described in chap. 2. The time history is filtered to reduce high frequency oscillations introduced by local errors in the shock position detection. The measurement error is particularly relevant at the beginning of the one-dimensional simulation, when all the three waves generated by the solution of Riemann problem are confined within few nodes.

5.5.1 One-dimensional cylindrical shock

Fig. 5.23 represents the cylindrical shock trajectory in the P-v plane in dilute conditions, with time monotonically increasing in the direction of higher pressure and density. Different line styles represent different thermodynamic models:

each curve is obtained as the envelope of all the curves associated to different β_P and computed with the same thermodynamic model. Fig. 5.23(a) provides a close up of the region where curves representing shock waves generated by $\beta_P \leq 36$ are depicted, to compare results associated to ideal gas and van der Waals gas models. Fig. 5.23(b) illustrates the same curves in bi-logarithmic scale to better understand the relative position between the shock trajectories and the saturation curve. The latter is traced in accordance to the procedure described in [116] by imposing thermal and chemical equilibrium.

The same results are reported in fig. 5.24 for dense gas conditions.

For both dilute and dense gas conditions, relevant differences in the specific volume can be observed if high temperature effects are considered for both thermal equations of state. In particular, the specific volume computed by means of a polytropic model is always larger that the corresponding one for harmonic c_v. On the contrary, modest separations are observed between the curves computed with different equations of state but the same c_v model, in particular in dilute conditions. In a first degree of approximation, the ranges of pressure attained by the shock during the propagation depend slightly on the thermodynamic model, and more significantly on β_P.

The gas conditions (dilute or dense) causes the inversion between van der Waals and ideal gas curves for each c_v model, that is the switch between pairs of data lines defined in sec. 5.3.1. Indeed, for each pressure level, in dilute conditions one has specific volume arranged in ascending order for

H-VdW H-IG P-VdW P-IG,

whereas for dense conditions the order is

H-IG H-VdW P-IG P-VdW.

Numerical data for polytropic gas are confronted to analytic shock adiabats (eqs. (5.6)) to check the validity of results in fig. 5.25. Fig. 5.25(a) reports data in dilute gas conditions, and confirms the observation that no relevant

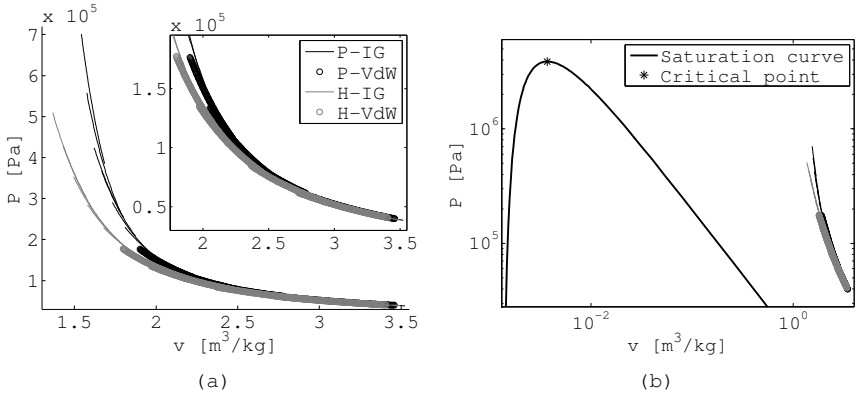

Figure 5.23: Post-shock conditions for cylindrical shocks originated by different β_P in dilute gas conditions, computed with diverse thermodynamic models.

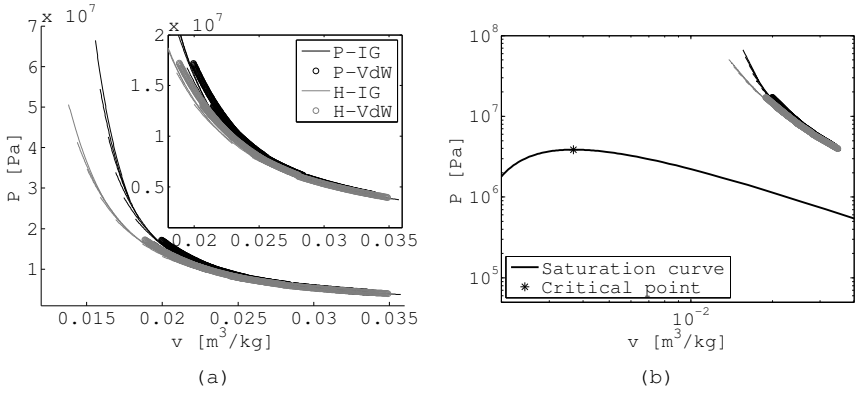

Figure 5.24: Post-shock conditions for cylindrical shocks originated by different β_P in dense gas conditions, computed with diverse thermodynamic models.

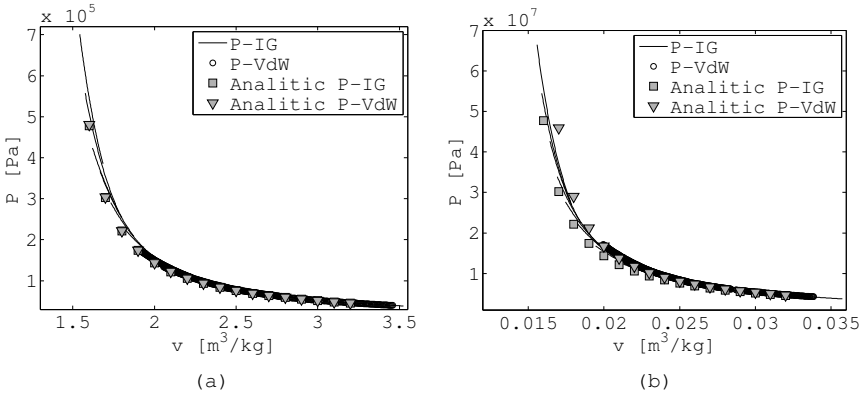

Figure 5.25: Comparison of numerical data with analytic adiabat for P-IG (full line) and P-VdW (o): (a) dilute and (b) dense gas conditions.

difference can be observed between ideal and van der Waals gas in the one-dimensional shock wave. On the contrary, for dense gas data reported in 5.25(b), the difference between the results obtained with the two equations of state is confirmed by a divergence of the analytic shock adiabats.

5.5.2 Two-dimensional polygonal shock

Similarly to the one-dimensional case, the trajectories of polygonal shocks in the P-v plane are observed. The reference analytic adiabat is the same as in the one-dimensional case for each thermodynamic model, being pivoted in (v_i, P_i).

Provided that the conditions immediately behind the polygonal shock must always belong to the adiabat [138], the numerical values of P_b and v_b at any time step not only depends on the thermodynamic model and β_P, but also on the region where data are sampled. It must be recalled that Rankine-Hugoniot conditions are valid across normal shock waves. With reference to fig. 5.26, the flow field induced by multiple reflections of converging shock waves is more complex than in the simple case of uniform flow in presence of steady, normal or oblique, shock

waves.

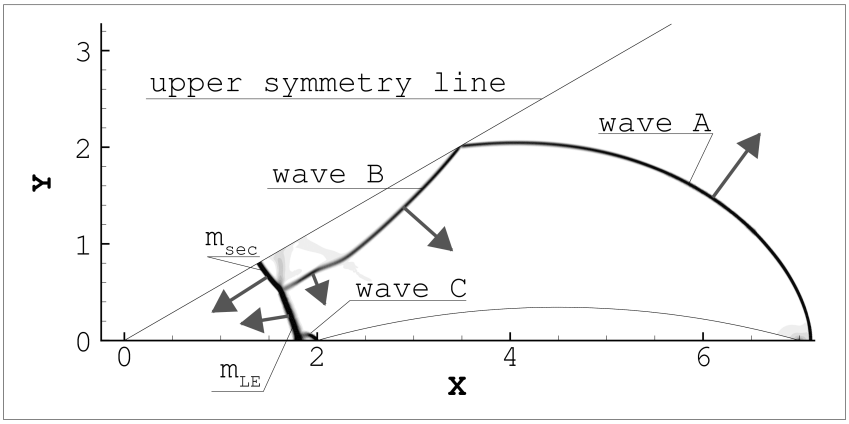

Figure 5.26: Direction of propagation of the diverse shock waves in correspondence of the secondary reflection (dilute conditions, polytropic ideal gas model, $n_{obs} = 6$, $t/c = 0.14$, $r_{LE} = 7$, $\beta_P = 27$). Numerical simulations are performed over a grid of about 120000 nodes, corresponding to a maximum $\Delta x = 0.01$, and with a time step $\Delta\tau = 6 \times 10^{-4}$.

The flow field generated by this complex shock system is characterized by three relevant features:

1. According to [138], a Galilean transformation can be applied to the the speed of the flow ahead and behind the shock wave. With reference to fig. 5.27, the relative velocity of the local flow is computed.
2. Since the flow velocity in front of the shock is zero, the speed of the show immediately behind the shock wave is coincident with the speed normal component with respect to the shock. Therefore, Rankine–Hugoniot conditions apply along each streamline.
3. Along the upper symmetry line, where slip conditions apply, the local flow is aligned with the boundary during all the shock convergence. In correspondence of the upper symmetry line, therefore, the direction of the streamline is known. Therefore, if the probes are located along the upper symmetry line, the sampled data concern always the same streamline at each time step.

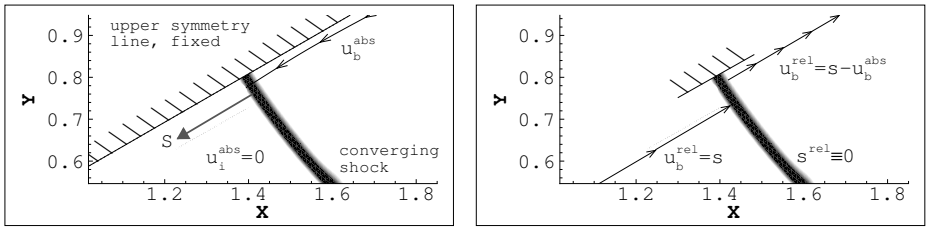

Figure 5.27: Close up of the flow field behind the polygonal shock wave in correspondence of the upper symmetry line. The velocities are expressed in the reference systems (a) of the laboratory and (b) moving with the shock wave respectively. In each picture, the bodies attached to the reference system are indicated by parallel lines. The absolute velocity of the shock wave s is indicated by the thick arrow in (a), whereas it is zero in the relative reference system. The flow speed u is represented in the absolute and in the relative reference systems along the streamlines. Numerical simulations are performed over a grid of about 120000 nodes, corresponding to a maximum $\Delta x = 0.01$, and with a time step $\Delta\tau = 6 \times 10^{-4}$ (dilute conditions, polytropic ideal gas model, $n_{obs} = 6$, $t/c = 0.14$, $r_{LE} = 7$, $\beta_P = 27$).

Moreover, to a first degree of approximation, it can be assumed that when a shock wave is diffracted by a reflecting surface, the generated Mach stem is perpendicular to the reflecting surface. For this reason, the state of the flow immediately after the shock wave computed along the upper symmetry line corresponds exactly to the flow induced by a normal shock wave.

Fig. 5.28 illustrates the trajectories in the P-v plane of polygonal shock waves in dilute gas conditions, after the interaction with an array of obstacles in reference geometrical conditions, i.e. $n_{obs} = 8$, $r_{LE} = 7$ and $t/c = 0.14$. Pictures representing data computed using the same thermodynamic model are arranged by rows, and each curve represents a shock originated by a different β_P.

The corresponding results computed for gas in dense conditions are illustrated in fig. 5.29.

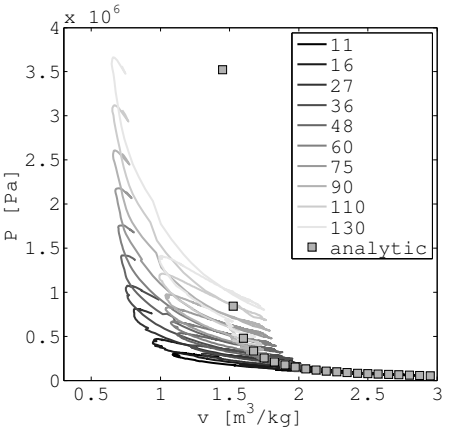

(a) P-IG

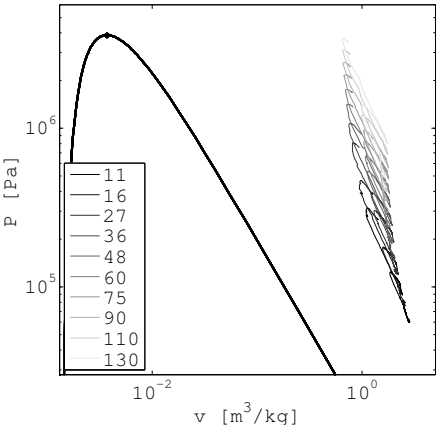

(b) P-IG

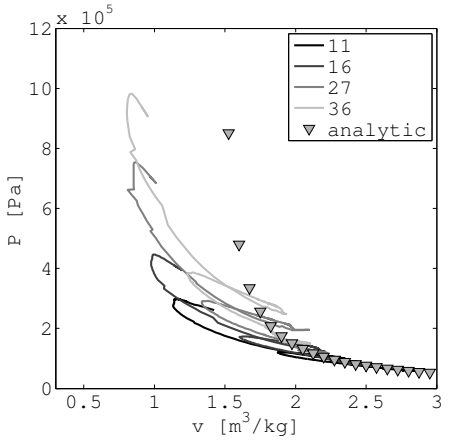

(c) P-VDW

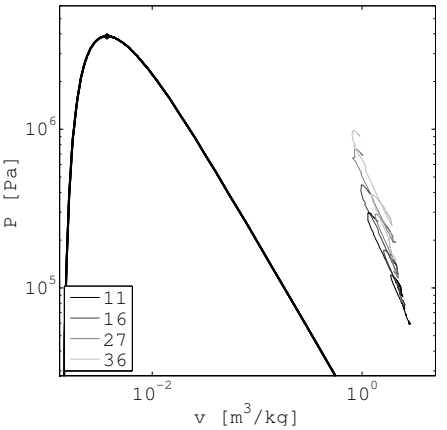

(d) P-VDW

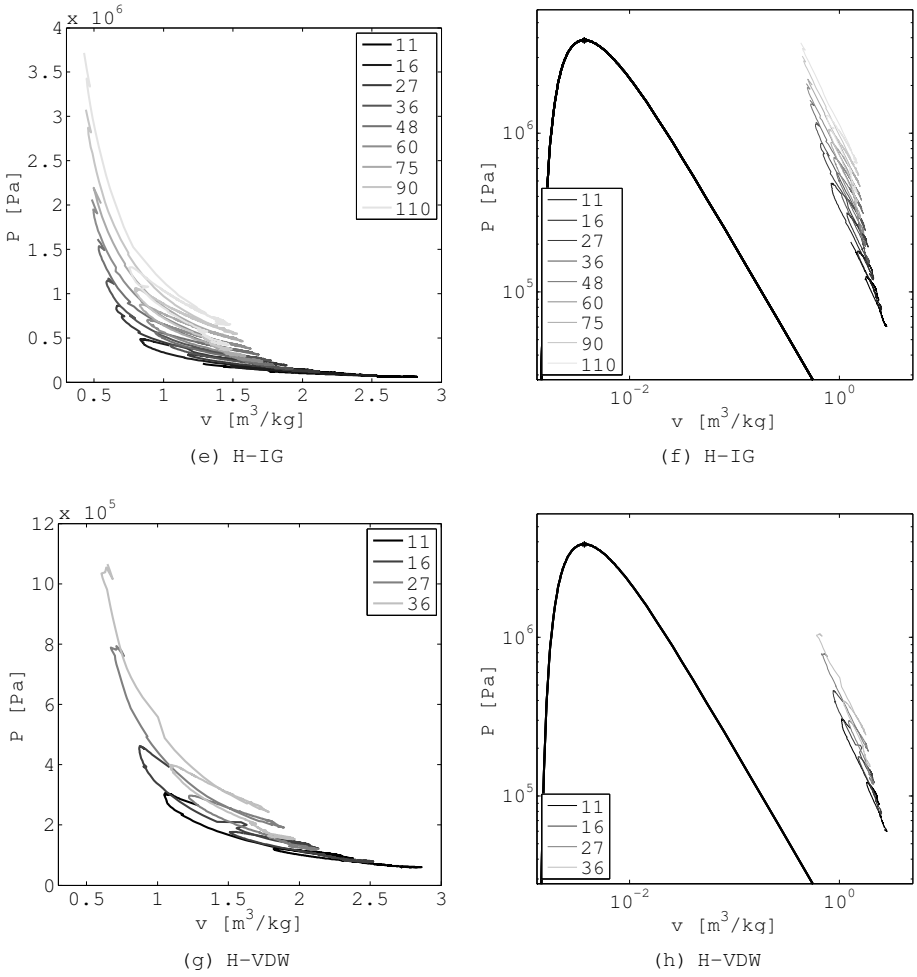

Figure 5.28: Propagation in the P-v plane of the conditions behind the polygonal shock probed along the upper symmetry line for diverse thermodynamic models (reference geometry, dilute conditions).

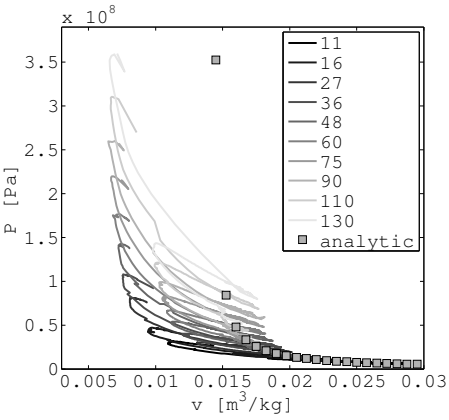

(a) P–IG

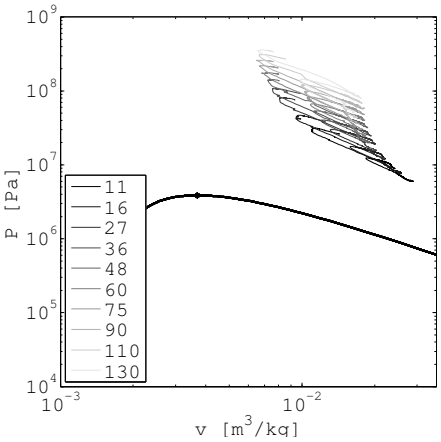

(b) P–IG

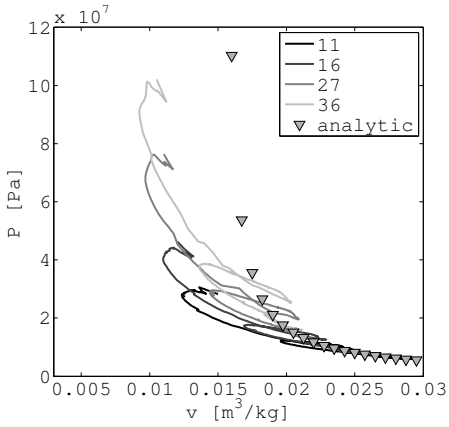

(c) P–VDW

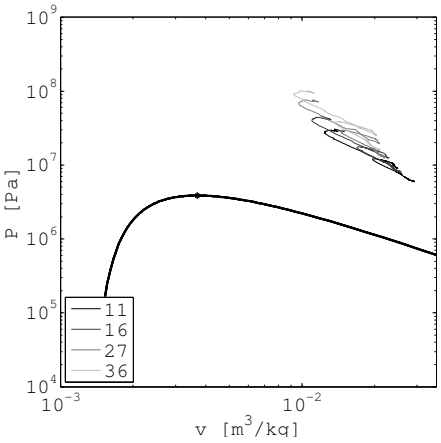

(d) P–VDW

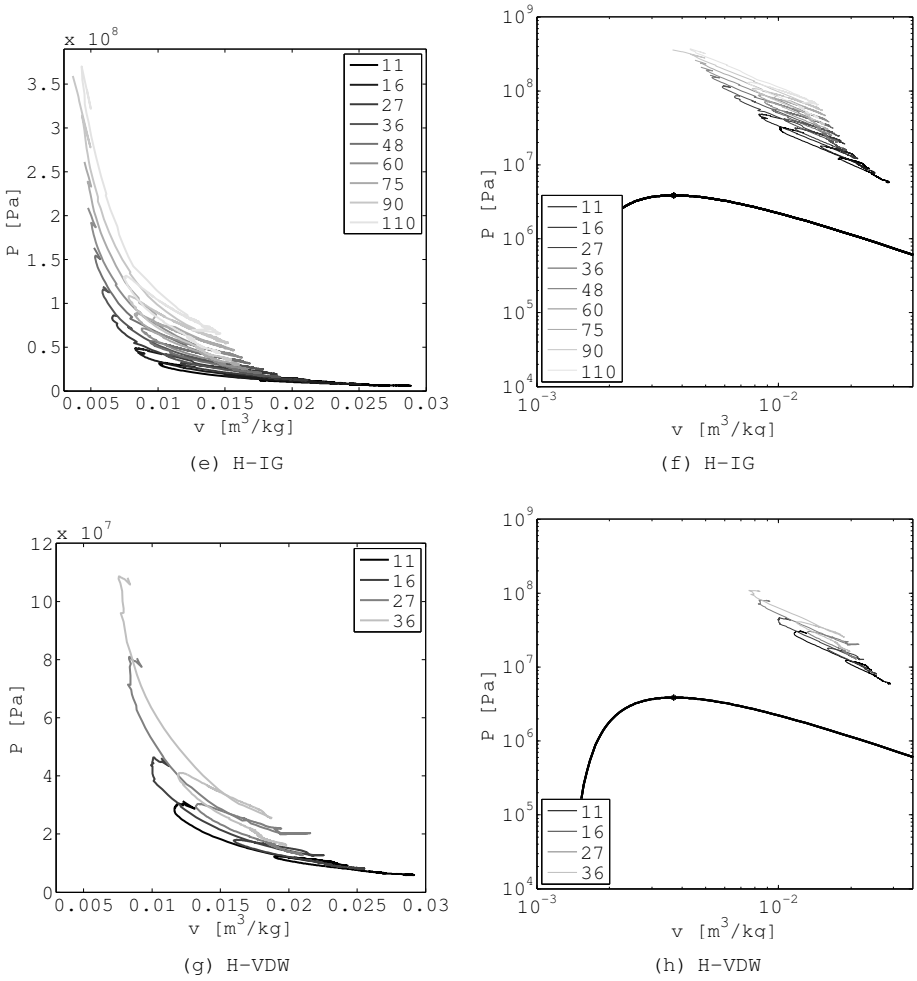

Figure 5.29: Propagation in the P-v plane of the conditions behind the polygonal shock probed along the upper symmetry line for diverse thermodynamic models (reference geometry, dense conditions).

For both dilute and dense gas results, the analytic Hugoniot adiabat is reported for comparison in figs. 5.28(a)-(c) and 5.29(a)-(c), representing the polytropic cases. A relevant deviation between analytical predictions and numerical values is observed, in terms of both numerical values and curve

topology.

Indeed, theoretical considerations imply that the specific volume behind a shock is bounded from below by the vertical asymptote of the adiabat, that is

$$v_{e,min} = \frac{v_i \delta_\gamma}{\delta_\gamma + 2} \approx 1.421 \frac{m^3}{kg} \quad \text{(dilute)} \qquad (5.7a)$$

$$\approx 1.421 \times 10^{-2} \frac{m^3}{kg} \quad \text{(dense)}$$

(polytropic ideal gas),

$$v_{e,min} = \frac{v_i \delta_\gamma + 2b}{\delta_\gamma + 2} \approx 1.423 \frac{m^3}{kg} \quad \text{(dilute)} \qquad (5.7b)$$

$$\approx 1.521 \times 10^{-2} \frac{m^3}{kg} \quad \text{(dense)}$$

(polytropic van der Waals gas).

Curves in figs. 5.28 and 5.29, on the contrary, violate this constraint, being the numerically evaluated minimum volumes approximately the half of theoretical values.

Moreover, the topology of the trajectories significantly differs from the theoretical monotone trend. Indeed, one or more “eyelets” are present where the curves self-intersect.

However, numerical results indicate that each deviation of numerical data from the analytic adiabat is a relevant but transient phenomenon occurring in correspondence of the shock reflections over the upper symmetry surfaces. The departure of numerical data from the analytic Hugoniot adiabat can be explained as follows.

With reference to fig. 5.30, which reports the discrete values in time of the points in the curve, it can be observed that outliers represent a fast transient phenomenon, which is described by a small number of data points. Indeed, most of the points are concentrated along the analytic curve (represented by the gray full line), and the two departures occur exactly in correspondence of the first and the second reflections over

the upper symmetry line.

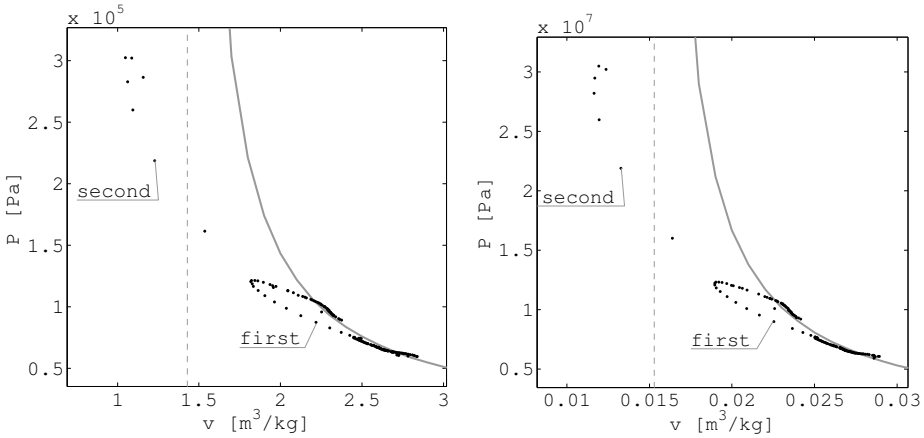

(a) dilute conditions (b) dense conditions

Figure 5.30: Comparison between the analytic adiabat (▬) and discrete values of the post-shock state (•) for (a) dilute and (b) dense gas conditions. The separation occurs only in correspondence of the (first and second) reflections and remains very limited in time (H-VdW, $n_{obs} = 8$, $t/c = 0.14$, $r_{LE} = 7$, $\beta_P = 11$)

A possible explanation to this behavior of the post-shock state is that a shock wave reflection is actually a singularity, and therefore the solution of the local flow field exactly at the time of the reflection cannot be correctly represented. The reason can be explained with the aid of fig. 5.31. As described in sec. 4.3.2, the first reflection over the upper symmetry line is actually the secondary reflection defined in sec. 1.1.2. The secondary reflection is a complex process which involves the reflection of two shock waves (wave A and the Mach stem originated at the leading edge reflection m_{LE}). In the region of the domain delimited by wave B, the secondary Mach stem m_{sec} and the upper symmetry line, hereafter termed "secondary bubble", the flow does not only depend on (v_i, P_i).

Indeed, before the occurrence of the secondary reflection (see fig. 5.31(a)), the pressure and specific volume immediately behind the one-dimensional cylindrical shock belong to the Hugoniot adiabat pivoted in (v_i, P_i), and their values are exactly P_b and v_b. Also the flow in the shock tail in vicinity

of the cylindrical shock front can be approximated with P_b and v_b.

"Significantly" after the reflection over the upper symmetry line (fig. 5.31(c))), two regions can be identified in the secondary bubble: behind m_{sec}, that is in point S^I, the thermodynamic state belongs to the Hugoniot adiabat pivoted in (v_i, P_i). On the contrary, point S^{II}, which is located at the intersection between wave B and the upper symmetry line, is reached through a new path. The type of the latter depends on the type of secondary reflection. With reference to fig. 4.16(b), if the secondary reflection is of Mach-type, the point S^{II} is reached through a new adiabat starting from a point in the shock tail. On the contrary, for Regular secondary reflections, (see fig. 4.16(a)), to get the state of the flow in S^{II}, one must first compute the flow conditions in the region between wave A and wave B (by means of an adiabat pivoted in the shock tail) and then use the latter values of pressure and density to compute the state in S^{II}, passing through wave B. The latter case is the one depicted in fig. 5.31(c). Therefore, in both cases, some time after the secondary reflection, the state in S^{II} is computed by means of one or more adiabats pivoted in $(v_{tail}, P_{tail}) \approx (v_b, P_b)$. The shock analytic Hugoniot adiabats are represented in fig. 5.31(d): both the point S^I and the state immediately behind the cylindrical shock, approximated with the flow in the shock tail, belong to the adiabat pivoted in (v_i, P_i). On the contrary, the point S^{II} lies on the adiabat originated in (v_{tail}, P_{tail}) (fig. 5.31(d), of course, represents the case of a Mach-type secondary reflection, since there is only one adiabat which leads from the state in the shock tail to S^{II}).

The numerical computation of the flow before and after the secondary reflection provides numerical results in accordance with theoretical predictions, i.e. belonging to the analytic Hugoniot adiabat. The departure of numerical results from the analytic curve is introduced exactly in correspondence of the reflection, which is depicted in fig. 5.31(b). At this time, all the secondary bubble is concentrated within a little physical space. In numerical simulations, therefore, the secondary bubble is distributed over only a few elements, and therefore the resolution is not enough to compute and represent the contact discontinuity inside the bubble. To a first degree of

approximation, this results in a computed continuous distribution of pressure and specific volume in the bubble area, instead of a discontinuous one, due to the presence of the contact discontinuity. Therefore, due to the small distance between S^I and S^{II}, the pressure and specific volume computed in correspondence of these two points do not differ significantly from each other. Indeed, according to numerical results one has $(v_{S^I}, P_{S^I}) \approx (v_{S^{II}}, P_{S^{II}})$, which contradicts the theoretical constraint that $(v_{S^I}, P_{S^I}) \neq (v_{S^{II}}, P_{S^{II}})$. For this reason, within a "small" number of time steps after the secondary reflection, before the numerical simulations can resolve the contact discontinuity, the flow in the point S^I cannot be correctly represented.

This observation is confirmed by the comparison between numerical results of pressure and specific volume in the transients after the reflections and the corresponding analytic Hugoniot adiabats pivoted in the shock tail, e.g. (v_{tail}, P_{tail}) for the secondary reflection. Fig. 5.32 reports this comparison for the case of a shock generated by $\beta_P = 11$ in dense conditions, after the interaction with eight obstacles at $r_{LE} = 7$ with $t/c = 0.14$. Fig. 5.32(a) is computed with a polytropic ideal gas model, fig. 5.32(b) with a polytropic van der Waals model. Analytic adiabats not pivoted in (v_i, P_i) (represented by gray empty circles) show a satisfactory overlapping with numerical results, in accordance with the supposition that the points S^I and S^{II} are confused during the post-secondary reflection transient.

As it is well known (see [140] and references therein), the pivot is a second-order contact point between the isentrope and the shock adiabat. For the polytropic ideal gas case reported in fig. 5.32(a), the isentropic curves are traced (gray full lines). As expected, also the isentropic curves provide a satisfactory approximation of the post-shock state during the two transients.

It must be specified that the observed departure of numerical data from the analytic curve is not due to boundary effects. Indeed, by probing the post-shock pressure and specific volume along a radius internal to the domain, the same discrepancy is observed each time a Triple Point crosses the probes line.

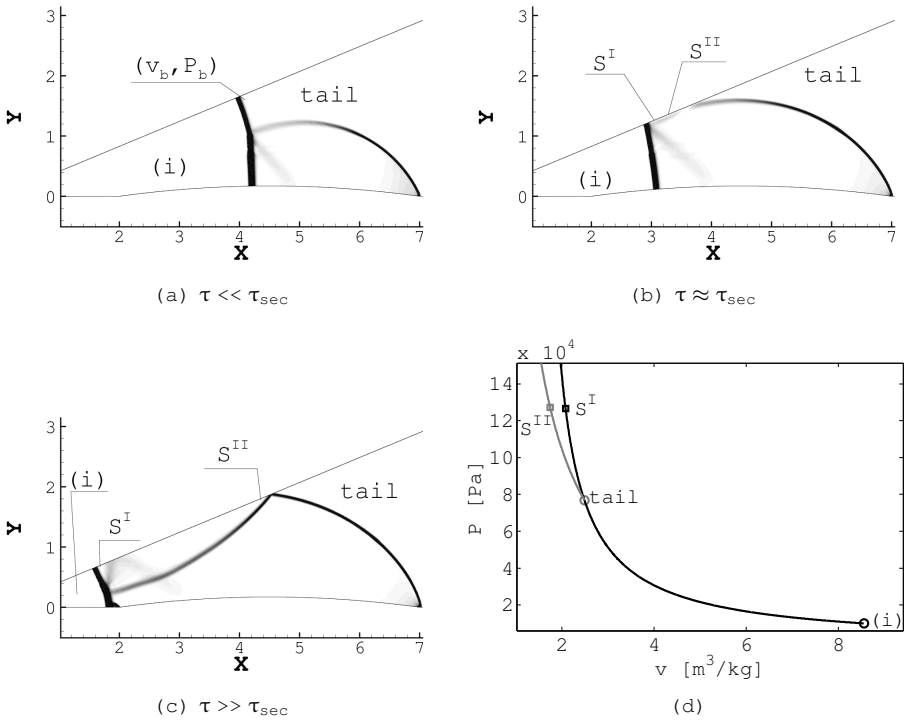

(a) $\tau << \tau_{sec}$ (b) $\tau \approx \tau_{sec}$

(c) $\tau >> \tau_{sec}$ (d)

Figure 5.31: Flow behind the shock on the upper symmetry boundary: (a) before, (b) during and (c) after the secondary reflection, showing that the points S^I and S^{II} become separated only some time steps after the occurrence of the secondary reflection. (d) Position of the highlighted points in the P–v plane. The case of a Mach-type secondary reflection is represented in the plane for visual clarity, since it requires to represent only one Hugoniot adiabat from the state in the shock tail to the point S^{II} (P–VdW in dilute conditions, $t/c = 0.07$, $r_{LE} = 7$, $n_{obs} = 8$, $\beta_P = 27$).

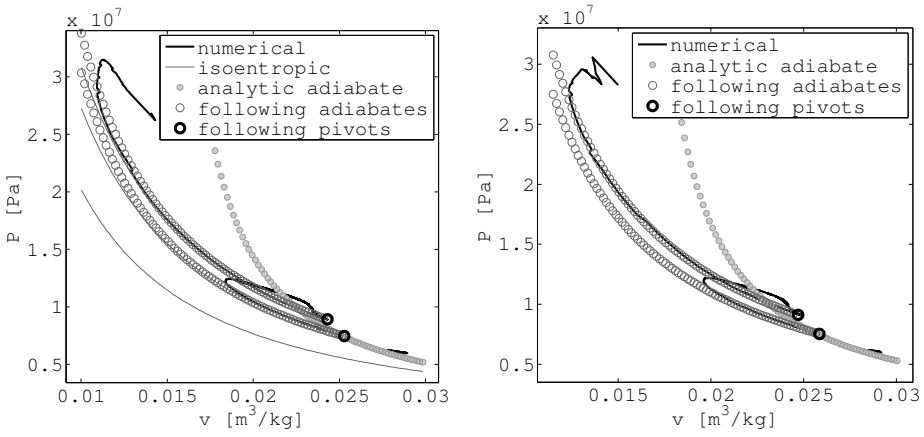

Figure 5.32: Comparison between numerical results (full black line), theoretical Hugoniot adiabat (•) and analytic adiabats (○) pivoted in the state behind the shock immediately before the reflections over the upper symmetry surface (O) for (a) P-IG and (b) P-VdW. Isentropic curves (——) are reported for the ideal gas case (dense conditions, $\beta_P = 11$, $n_{obs} = 8$, $t/c = 0.14$, $r_{LE} = 7$).

Eventually, it is known that the flow field induced by the passage of the cylindrical converging shock wave is neither uniform not constant. However, pressure and specific volume were approximated with the generic values in the shock "tail", (v_{tail}, P_{tail}). The error introduced by this approximation does not jeopardize the model adopted to explain the departure of numerical results from the analytic adiabat in correspondence of the secondary reflection.

Indeed, this model can be verified by observing the propagation in the P-v plane of the post-shock state if both the shock wave and the wedge are planar. In this configuration, depicted in fig. 5.33, a straight shock wave traveling at constant $M_S = 6$ is diffracted by a planar obstacle with wedge angle $\theta_w = 11.3^\circ$ The secondary reflection is traced along the upper boundary (fig. 5.34), where symmetry conditions are imposed. The analysis of this configuration is helpful because the pressure and specific volume in the flow in the planar shock tail are uniform in space and time. Therefore, the solution in

uniform regions is a-priori known, and the approximation of (v_b, P_b) with (v_{tail}, P_{tail}) becomes an exact equivalence.

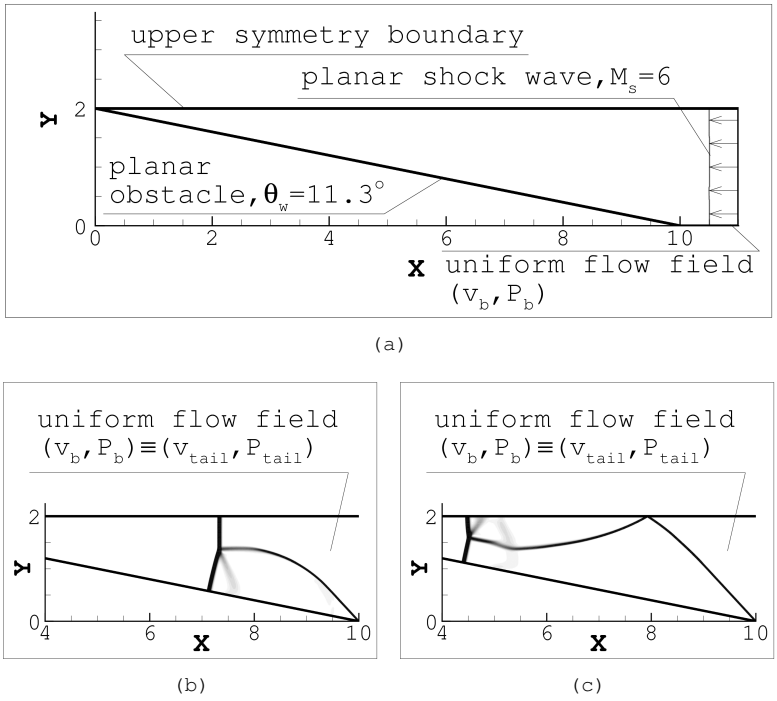

Figure 5.33: Configuration adopted for the verification of the influence of the approximation of (v_b, P_b) with (v_{tail}, P_{tail}): a planar shock wave propagating in polytropic ideal gas in dilute conditions at constant $M_s = 6$ is diffracted by a planar obstacle with wedge angle $\theta_w = 11.3^\circ$ and the secondary reflection is traced along the upper boundary, where symmetry conditions are imposed. (a) Complete domain, initial condition and close-ups in correspondence of (b) the leading edge reflection and (c) the secondary reflection. Numerical simulations are performed over a grid of about 140000 nodes, corresponding to a maximum $\Delta x = 0.01$, and with a time step $\Delta\tau = 6 \times 10^{-4}$.

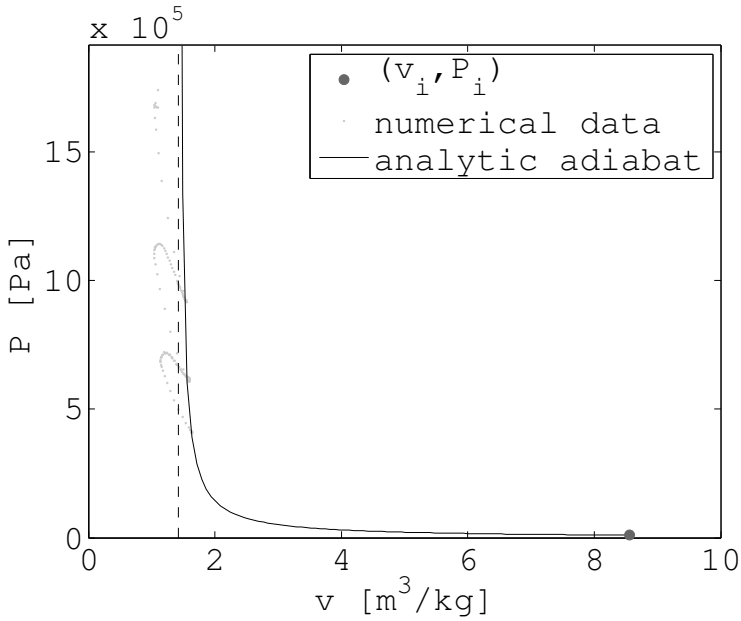

Figure 5.34: Propagation in the P–v plane of the post–shock state induced by the reflection of a straight shock wave over a planar obstacle. Also in this case, where the equivalence $(v_b, P_b) = (v_{tail}, P_{tail})$ is exact, the shape of the trajectory of the point S^I in the P-v presents the same features as in the case of the cylindrical converging shock wave reshaped by circular-arc obstacles. Numerical simulations are performed over a grid of about 140000 nodes, corresponding to a maximum $\Delta x = 0.01$, and with a time step $\Delta\tau = 6 \times 10^{-4}$ (Polytropic ideal gas in dilute conditions, $M_S = 6$, $\theta_w = 11.3^\circ$).

Conclusions

The reshaping of cylindrical converging shock waves by means of circular-arc obstacles was investigated by means of numerical simulations.

The reshaping is caused by a series of Mach Reflections of the shock wave over an array of circular-arc obstacles arranged in a symmetric fashion. Diverse geometric configurations (the obstacle number, thickness-to-chord ratio and leading edge radius), operating conditions (the pressure ratio used to generate the shock wave and the gas conditions) and thermodynamic models (ideal gas and van der Waals gas thermal equations and polytropic and harmonic constant-volume specific heat) were devised from the configuration assumed as reference, i.e. that described in the paper by M. Kjellander, N. Tillmark and N. Apazidis, "Thermal radiation from a converging shock implosion", Phys. of Fluids (2010). The reference configuration consists of an array of eight lenticular, symmetrically arranged obstacles. The leading edge radius of the obstacles is 70 mm, corresponding to a dimensionless radius $r_{LE} = 7$. The obstacle profiles consists of two equal circular arcs, symmetric with respect to the obstacle chord $\widehat{c} = 50\,\mathrm{mm}$. The obstacle thickness-to-chord value is 0.14. In the reference configuration, the cylindrical implosion is generated in a ad-hoc designed shock tube filled with air; the low-pressure side of the shock tube is at nominal pressure $\widehat{P}_i^0 = 10^4\,\mathrm{Pa}$. The Mach number of the shock wave at the inlet of the cylindrical chamber is $M_s = 2.7$.

The procedure and the developed numerical tools were described in chap. 2.

Numerical simulations were performed using Finite-Volume

solvers for Euler equations. The obtained results were demonstrated to be independent from the spatial scale. To reduce the computational cost of the simulations, a multi-domain approach was developed. The global domain where the shock converges is split into three regions, the Far Field Region, the Obstacle Region and the Focus Region, dedicated respectively to the simulation of the cylindrical shock generation, of the reshaping and of the focusing. A technique which exploits the symmetry of the reshaping process was developed for reducing the azimuthal extensions of the three regions (from a 360°-spanning domain to a $360^{\circ}/2n_{obs}$-spanning one, that is the elementary domain), and for reconstructing a-posteriori the solution outside of the boundaries (fig. C.1).

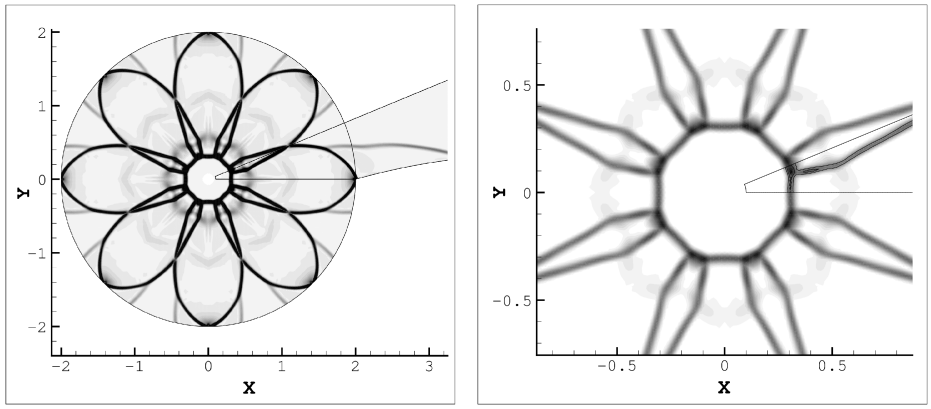

(a) (b)

Figure C.1: (a) Numerical Schlieren of the overlapping zone between the computational domains related to the Obstacle Region (sharp domain on the right, isopycnics) and the Focus Region, where the solution is reconstructed by means of the novel procedure (circular domain, contours). (b) Close-up in correspondence of the focus point (reference conditions).

A novel method to trace the shock position during the time was also developed. It applies to solutions computed by means of numerical schemes which describe the pressure across the shock wave as a continuous ramp, e.g. artificial viscosity

methods, and it accounts for the very complex shock-induced flow field in terms of both radial and azimuthal trends of quantities. Moreover, the same criterion applies both to the evaluation of the shock position at a given time and to the determination of the time associated to the shock passage by a given radius.

The solution computed using these two new tools presents the same accuracy provided by full two-dimensional simulations, but a reduction of the computational time of more than one order of magnitude is attained. Even if the current node-element tagging algorithm is fast and robust, it can be further accelerated by restricting the set of element where the correspondence is tested, for example by adding a so-called "Sweep & Prune", e.g. with two-dimensional axis-oriented bounding boxes [127].

Numerical results concern mainly two phenomena: the first one is the local interaction between the cylindrical converging shock wave and the circular-arc obstacles. The second phenomenon consists in the complete reshaping and focusing of the shock wave.

In detail, the shock-obstacle interaction was analyzed in chap. 3 by means of the observation of reflections over the leading edge of an isolated obstacle. Diverse reflection types were observed and classified in accordance to the criteria adopted for pseudo-steady reflections, highlighting the onset of similar patterns but for different configurations (fig. C.2).

For the Regular Reflection, an analytic model was proposed for the description of its unsteady evolution, which agrees fairly well with the numerical results. The conditions for the Regular Reflection transition into Mach Reflection during the propagation of the shock along the obstacle were determined. The influence of the obstacle geometry was observed on the so-called "absolute" wedge angle, whereas it appears to be absent on the "perceived" wedge angle; for both the angles, the shock Mach number presents a null or negligible effect.

The trajectory of the Triple Point was traced for genuine Mach Reflections. The independence on the shock intensity and a pseudo-homothetic behavior of the trajectories with respect to the leading edge radius were observed.The study of the com-

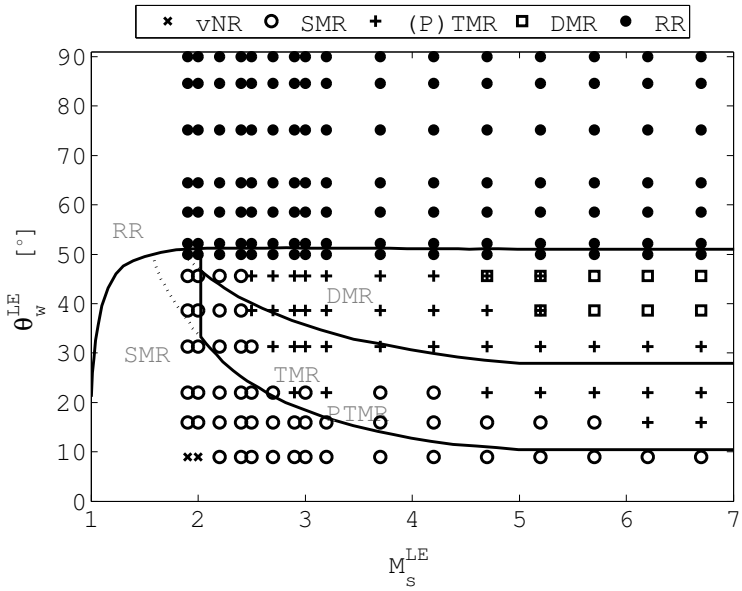

Figure C.2: Leading edge reflection types, depending on the diverse values of M_s^{LE} and θ_w^{LE}. A more detailed description of the image is provided in sec. 3.

plete propagation domain demonstrated that the trajectory cannot follow a parabolic trend; therefore, a 2^{nd} order fitting on data sampled only along the first half-chord was derived which shows a good accordance with data. Considerations on the offset of the trajectories from the reflecting surface suggest that the definition of Inverse Mach Reflection in presence of cylindrical converging shock waves and convex obstacles is more complex than for planar shocks.

The reshaping of the shock was investigated in chap. 4. The correctness of the simulation results was assessed against the Guderley self similar solution and experimental results from [97]. A grid and time step independence study was carried out.

The number of obstacles was included among the investigated factors in the study of the complete shock reshaping. Contrary to the behavior of leading edge patterns, which do not exhibit any dependence on the shock Mach number, the values of pressure and temperature attained at the focus point depend mostly

on M_S. The number of obstacles was found to be rather influential, especially on the pressure peak. The leading edge radius of the obstacles produces a weaker effect than other factors and, in addition, does not exhibit any particular trend. The obstacle thickness-to-chord ratio causes a monotone effect on the amount of focused energy: in all the explored configuration, larger thickness value cause more relevant losses, and therefore, lower values of pressure and temperature. The configuration producing the highest temperature peak at the focus point consists of 16 obstacles with $t/c = 0.07$ and $r_{LE} = 14$, associated to a shock produced by an initial pressure ratio of 27. Note that numerical results do not account for the effect of the viscosity, which in fact introduces further losses. The relevance of viscous effect increases where the local length scales are small, e.g. near the focus point or in the channel between two obstacles when n_{obs} is large. This implies that, especially when the shock wave is about to focus, the consideration of the viscosity could sensibly modify the values of the computed c_P and c_T.

Effects of interaction among thermodynamic factors triggered by the shock intensity were observed in chap. 5 on the temperature and on the pressure values in dense gas conditions. Non-ideal fluid effects, which are more relevant in the close proximity of the liquid-vapor saturation curve, cause a decreasing of the shock effectiveness and efficiency, as reported in fig. C.3.

Pseudo-self-similarity exponents were computed for diverse thermodynamic models—i.e. ideal and van der Waals gas models, each combined with a polytropic and a harmonic c_v model—and number of obstacles. A trend was observed between the value of the vertex angle of the elementary domain and α, whereas other geometric factors, i.e. the obstacle thickness and position do not significantly influence the self-similarity exponent.

The tracing of the locus of the post-shock conditions in the pressure-specific volume plane shows an excellent accordance between numerical values and analytic values of the Hugoniot adiabat. On the contrary, significant but temporary departures of numerical data from the analytic curve were observed in correspondence of each shock reflection, which locally gen-

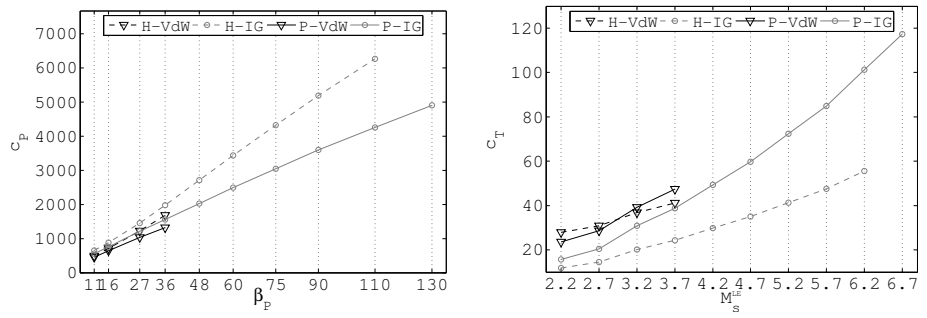

(a) $t/c = 0.07$ (b) $t/c = 0.07$

Figure C.3: Pressure and temperature factors, respectively, for diverse thermodynamic models in (a) dilute and (b) dense gas conditions (reference geometry).

erated a flow field where the conditions for the application of Rankine–Hugoniot relations do not apply.

For only the case of polytropic ideal gas, a deeper analysis of the post–leading edge reflections was performed, including secondary reflections over the upper symmetry boundary, post–trailing edge patterns, the nozzle effect, and the relation between the number of edges of the polygonal shock wave and n_{obs}. A qualitative description of the flow field induced by the diffraction over cylindrical obstacles was provided.

Future developments and recommendations

The improvement of the numerical results presented in this work can be performed in three directions.

The first one concerns the numerical investigation of the physics of the reshaping of cylindrical converging shock waves. The influence of the thermodynamic mode was assessed in the present work in terms of shock effectiveness/efficiency and of average influence of the shock convergence. On the contrary, the thermodynamics effect were not studied on the leading edge reflection. Therefore, an analysis of the

shock-induced flow field and of the leading edge reflection patterns—e.g. RR $\longrightarrow$ MR transition boundaries and Triple Point trajectory—is recommended. The influence of θ_w^{LE} and R_O on the RR $\longrightarrow$ MR transition angle remains an open issue.

Moreover, the effectiveness of the converging shock wave, some observed patterns and the transition boundaries between the diverse reflection types should be studied accounting for two important factors which have been neglected in the present work. The first one consists of transport phenomena, such as viscosity, diffusion and thermal conduction. The second factor concerns other high temperature effects, including the models of the dissociations, electronic excitation and ionization in correspondence of the focus point.

The second possible improvement consists in the development of numerical tools for a faster and more accurate analysis of the leading edge patterns. The setup of an automatic procedure to locate the point of intersection between the incident and the reflected shock wave (the Reflection or the Triple Point) could help achieving two goals. Indeed, such a procedure would allow on the one hand to trace the Triple Point Trajectory and on the other hand to detect the RR $\longrightarrow$ MR transition. Indeed, the RR $\longrightarrow$ MR occurs at the detachment of the Reflection Point from the obstacle surface.

Finally, an experimental verification of the numerical results is required. According to the authors of [97], the reference test rig provides a high repeatability of the tests. Therefore, the adoption of an experimental setup for both the generation and the reshaping of converging shock waves like the reference one is suggested.

The experimental activity is envisaged to confirm the results reported in chap. 3 concerning the leading edge reference patterns. Moreover, a further investigation on the RR $\longrightarrow$ MR transition where the parameters θ_w^{LE} and R_O are varied independently from each other could help solving the open issue described in chap. 3. This problem concerned the different computed trends of θ_w^{tr} with respect to the two factors, which appear to be partially in contradiction with the results obtained for the diffraction of planar shock waves. For the setup of the experiments, a procedure similar to the one described in [79]

is suggested, which allows to consider the parameters as independent.

The effects of the viscosity on the shock reshaping can be determined by exploring configurations with a variable obstacles number, resulting in a different width of the channel between the obstacles.

Non-ideal gas effects can be determined by performing a fitting on experimental data and by comparing the resulting values of the self-similarity exponent α with each of the ones obtained by numerical simulations with different thermodynamic models. Since all the curves in fig. C.4 do not intersect in the observed range of n_{obs}, departure of the values of α from the experimental one should provide an indication of the relevance of non-ideal fluid effects. The comparison of the experimental value α to the diverse numerical values provides a more robust indication than other parameters do. Indeed, it is known that further real gas effects are observed in correspondence of the focusing, in addition to the investigated ones. Because of these high temperature effects, the experimental values of c_P and c_T are expected to show some discrepancies from numerical ones.

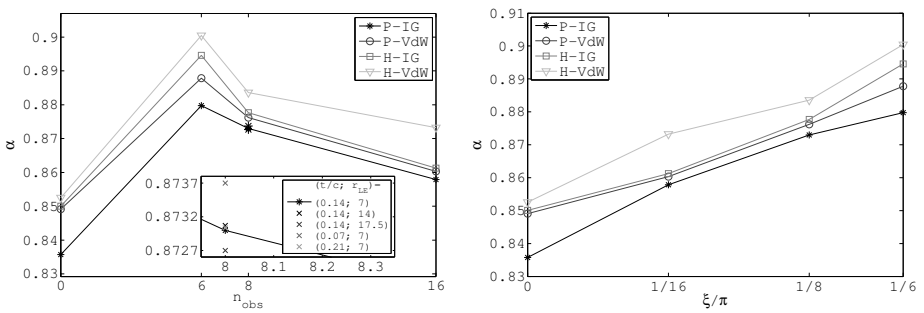

Figure C.4: α versus (a) the number of obstacles and (b) the periodicity of the symmetrical polygonal shock for diverse thermodynamic conditions.

Bibliography

[1] J.A. Maniscalco, "Inertial Confinement Fusion", Annual Review of Energy, v. 5, pp. 33–60 (1980).

[2] J.D. Lindl, L.R. McCrory, E.M. Campbell, "Progress Toward Ignition and Burn Propagation in Inertial Confinement Fusion", Phys. Today, pp. 32–40 (1992).

[3] J.W. Bates, A.J. Schmitt, D.E. Fyfe, S.P. Obenschain, and S.T. Zalesak, "Simulations of High-Gain Shock-Ignited Inertial-Confinement-Fusion Implosions Using Less Than 1 MJ of Direct KrF-Laser Energy", High Energy Density Physics, v. 6, p. 128–134 (2009).

[4] S. Atzeni, J Meyer-ter-vehn, "The Physics of Inertial Fusion: Beam Plasma Interaction, Hydrodynamics, Hot Dense Matter", Oxford University Press (2004).

[5] P.O.K. Krell, "History of Shock Waves, Explosions and Impact - A Cronological and Biographical Reference", Springer Science & Business Media (2008).

[6] B.P. Barber, S.J. Putterman, "Light Scattering Measurements of the Repetitive Supersonic Implosion of a Sonoluminescing Bubble", Phys. Rev. Lett., v. 69, pp. 3839-3842 (1992).

[7] M.P. Brenner, S. Hilgenfeldt, D. Lohse, "Single Bubble Sonoluminescence", Rev. of Mod. Phys., v. 74 (2002).

[8] S.J. Putterman, K.R. Weninger, "Sonoluminescence: How Bubbles Turn Sound Into Light", Annu. Rev. Fluid Mech., v. 32, pp. 445–476 (2000).

[9] R. Perry, A. Kantrowitz, "The Production and Stability of Converging Shock Waves", J. of App. Phys., v. 22, p. 878 (1951).

[10] P. Thompson, "A Fundamental Derivative in Gas Dynamics", Phys of Fluids, v. 14, pp. 1843–1849 (1971).

[11] S.P. D'yakov, "On the Stability of Shock Waves", Zh. eksper. Teoret. fiz., v. 27, pp. 288–295, IN RUSSIAN (1954).

[12] V.M. Kontorvich, "Concerning the Stability of Shock Waves", Sov. Phys. JETP, v. 6, pp. 1179–1180 (1957).

[13] J.W. Bates, D.C Montgomery, "The D'yakov–Kontorvich Instability of Shock Waves in Real Gases", Phys. Rev. Lett. (2000).

[14] J.W. Bates, "Instability of Isolated Planar Shock Waves", Phys. of Fluids. (2007).

[15] R. Betti, V.N. Goncharov, R.L. McCrory, C.P. Verdon, "Growth Rates of the Ablative Rayleigh–Taylor Instability in Inertial Confinement Fusion", Phys. of Plasmas, v. 5, pp. 1446–1454 (1998).

[16] V.A. Thomas, R.J. Kares, "Drive Asymmetry and the Origin of Turbulence in an ICF Implosion", Phys. Rev. Lett., v. 109 (2012).

[17] V.A. Smalyuk, D.T. Casey, D.S. Clark, M.J. Edwards, S.W. Haan, A. Hamza, D.E. Hoover, W.W. Hsing, O. Hurricane, J.D. Kilkenny, J. Kroll, O.L. Landen, A. Moore, A. Nikroo, L. Peterson, K. Raman, B.A. Remington, H.F. Robey, S.V. Weber, K. Widmann, "First Measurements of Hydrodynamic Instability Growth in Indirectly Driven Implosions at Ignition–Relevant Conditions on the National Ignition Facility", Phys. Rev. Lett., v. 112 (2014).

[18] G.I. Taylor, "The Instability of Liquid Surfaces When Accelerated in a Direction Perpendicular to Their Planes, I", Proc. R. Soc. Lond. A, v. 201 (1950).

[19] Lord Rayleigh, "Investigation of the Character of the Equilibrium of an Incompressible Heavy Fluid of Variable Density", Scientific Papers, v. 2, p. 200 (1883).

[20] J.W. Miles, "On the Generation of Surface Waves by Shear Flows - Part 3: Kelvin-Helmholtz Instability", J. of Fluid Mech., v. 6, pp. 583-598 (1959).

[21] Lord Kelvin, "Mathematical and Physical Papers", Cambridge univ press, v. IV, pp. 76-86 (1871).

[22] R.D. Richtmyer, "Taylor Instability in Shock Acceleration of Compressible Fluids", Commun. on Pure and Appl. Math., v. 13, p. 297 (1960).

[23] E.E. Meshkov, "Instability of the Interface of Two Gases by a Shock Wave", Izv. Acad. Sci. USSR Fluid Dynamics, v. 4, p. 101 (1969).

[24] A.K. Evans, "Instability of Converging Shock Waves and Sonoluminescence", Phys. Rev. E, v. 54, pp. 5004-5011 (1996).

[25] J.H. Gardner, D.L. Book, Ira B. Bernstein, "Stability of Imploding Shocks in the CCW Approximation", J. Fluid Mech., v. 2, pp. 41-58 (1982).

[26] Z. Somogyi. P.H. Roberts, "Stability of an Imploding Spherical Shock Wave in a Van Der Waals Gas, II", Quarterly J. of Mech. & App. Maths., v. 60, pp. 289-309 (2006).

[27] M. Watanabe, K. Takayama, "Stability of Converging Cylindrical Shock Waves", Shock Waves, v. 1, pp. 149-160 (1991).

[28] S.H.R. Hosseini, K. Takayama, "Experimental Study of Richtmyer-Meshkov Instability Induced by Cylindrical Shock Waves", Phys. of Fluids, v. 17, (2005).

[29] A.G. Bashkirov, "Influence of Viscous Stresses on Shock Wave Stability in Gases", Phys. of Fluids, v. 3 (1991).

[30] T. Itoh, K. Abe, "Simulation of Instability of Cylindrically Converging Shock Waves", Nagoya Univ. Workshop

Rept. on Simulation Tech. for Shock Wave Phenomena and Characteristics of Plasma in Inertial Confinement Fusion, pp. 115–119, (1985).

[31] K. Fong, B. Ahlborn, "Stability of Converging Shock Waves", Phys. of Fluids, v. 2 (1979).

[32] K. Takayama, H. Kleine, H. Grönig, "An Experimental Investigation on the Stability of Converging Cylindrical Shock Waves in Air", Exper. in Fluids, v. 5, pp. 315–322 (1987).

[33] K. Takayama, O. Onodera, Y. Hoshizawa, "Experiments on the Stability of Converging Cylindrical Shock Waves", Theor. Appl. Mech. v. 32, pp. 117–127 (1984).

[34] M. Lombardini, D.I. Pullin, "Small-Amplitude Perturbations in the Three-Dimensional Cylindrical Richtmyer-Meshkov Instability", Phys. of Fluids, v. 21 (2009).

[35] V. Eliasson, N. Apazidis, N. Tillmark, "Controlling the Form of Strong Converging Shocks by Means of Disturbances", Shock Waves, v. 17, pp. 29–42 (2007).

[36] N. Apazidis, M. Kjellander, N. Tillmark, "High Energy Concentration by Symmetric Shock Focusing", Shock Waves, v. 23, v. 361–368 (2013).

[37] H. Shi, K. Yamamura, "The Interaction Between Shock Waves and Solid Spheres Arrays in a Shock Tube", Acta Mech. Sinica, v. 20, pp. 219–227 (2004).

[38] S. Sha, Z. Chen, X. Jiang, "Influences of Obstacle Geometries on Shock Wave Attenuation", Shock Waves, v. 24, pp. 573–582 (2014).

[39] G. Guderley, "Starke Kugelige Zylindrische Verdichungsstöße in Der Nähe Des Kugelmittelpunktes Bzw. Der Zylinderachse", Luftfahrtforschung v. 19 (1942).

[40] D.S. Butler, "Converging Spherical and Cylindrical Shocks", 54/54 Armament Res. & Dev. Est., Ministry of Supply (1954).

[41] B. Zel'dovich Ya., P. Raizer Yu., "Physics of Shock Waves and High-Temperature Hydrodynamic Phenomena", Academic Press Inc., New York, v. 2, chap. 12: "Some Self-Similar Processes in Gasdynamics" (1967).

[42] L.I. Sedov, "Similarity and Dimensional Methods in Mechanics", Academic Press Inc., New York, chap. 4: "One-Dimensional Unsteady Motion of a Gas" (1959).

[43] W. Chester, "The Quasi-Cylindrical Shock Tube", Phil. Mag., v. 45, pp. 1293-1301 (1954).

[44] R.E. Chisnell, "The Formation of a Shock Wave in a Channel", J. Fluid Mech., v. 2, pp. 286-298 (1955).

[45] G.B. Whitham, "A New Approach to the Problems of Shock Dynamics, Part 1. Two-Dimensional Problems", J. Fluid Mech., v. 2, pp. 146-171 (1957)

[46] G.B. Whitham, "Linear and Nonlinear Waves", John Wiley & Sons, New York (1973).

[47] H. Matsuo, "Cylindrically Converging Shock and Detonation Waves", Phys. of Fluids v. 26, pp. 1755-1762 (1983).

[48] M. Van Dyke, A. J. Guttmann, "The Converging Shock Wave From a Spherical or Cylindrical Piston", J. Fluid Mech. v. 120, pp. 451-462 (1982).

[49] G. Ben-Dor, O. Igra, T Elperin, "Handbook of Shock Waves", Academic Press Inc., New York, chap. 11: F. Higashino, "Shock Wave Focusing" (2000).

[50] H. Matsuo, "Converging Shock Waves Generated by Instrantaneous Energy Release Over Cylindrical Surfaces", Phys. of Fluids, v. 22 (1979).

[51] J. H. Lee, B. H. K. Lee, "Cylindrical Imploding Shock Waves", Phys. of Fluids v. 8, pp. 2148-2152 (1965).

[52] K. Hatanaka, T. Saito, K. Takayama, "Numerical Studies of Shock Focusing Induced by Reflection of Detonation Waves Within a Hemispherical Implosion Chamber", Shock Waves v. 22, pp. 567-578 (2012).

[53] H. Matsuo, K. Fujiwara, "Explosive-Driven Cylindrical Imploding Shocks", Phys. of Fluids A, v. 2, pp. 266-273 (1990).

[54] K. P. Stanyukovich, "Unsteady Motion of Continuous Media", Gostekhizdat, Moscow, pp. 804-878 (1955).

[55] R.C. Srivastava, D. Leutloff, K.G. Roesner, "Numerical Investigations of Converging Cylindrical and Spherical Shock Waves", Astrophys. and Sp. Sci., v. 192, pp. 1-9 (1992).

[56] Y.G. Jung, K.S. Chang, "Shock Focusing Flow Field Simulated by a High-Resolution Numerical Algorithm", Shock Waves v. 22, pp. 641-645 (2012).

[57] Y. Saillard, H. Barbry, C. Mournier, "Transformation of a Plane Uniform or Spherical Shock by Wall Shaping", In Shock waves and shock tubes, Proc. 15th Intern. Symp., Stanford, CA, pp. 147-154 (1985).

[58] Z. Zhai, C. Liu, F. Qin, J. Yang, X. Luo, "Generation of Cylindrical Converging Shock Waves Based on Shock Dynamics Theory", Phys. of Fluids v. 22 (2010).

[59] Z. Zhai, T. Si, X. Luo, J. Yang, C. Liu, D. Tan, L. Zou, "Parametric Study of Cylindrical Converging Shock Waves Generated Based on Shock Dynamics Theory", Phys. of Fluids v. 24 (2012).

[60] L.Z. Dumitrescu, "Efficient Shock-Focusing Configurations", In 11th Australasian Fluid Mechanics Conference, Hobart, Tasmania, pp. 723-725 (1992).

[61] R.B. Payne, "A Numerical Method for a Converging Cylindrical Shock", J. Fluid Mech. v. 2-02, pp. 185-200 (1957).

[62] A. Amirfazli, "Numerical Simulation of Imploding Shock Waves", Ph.D. dissertation, Department of Mechanical Engineering, Concordia University, Sweden (1994).

[63] J. Tyl, E. Włodarczyk, "Analysis of Imploding Shock Waves by the Chester-Chisnell-Witham Method", J. de Phys. Colloques, v. 45-C8, pp. 267-272 (1984).

[64] M. Kjellander, "Energy Concentration by Converging Shock Waves in Gases", Ph.D. dissertation, Department of Mechanics, KTH, Sweden (2012).

[65] E. Mach, "Über Den Verlauf Von Funkenwellen in Der Ebene Und Im Raume", Sitzungsbr. Akad. Wiss. Wien, v. 78, pp. 819–838 (1878).

[66] R. Courant, K. O. Friedrichs, "Supersonic Flow and Shock Waves", ed. Wiley Inc., New York (1948).

[67] L. G. Smith, "Photographic Investigation of the Reflection of Plane Shocks in Air", OSRD Rep. 6271, Off. Sci. Res. Dev., Washington DC (1945).

[68] D. R. White, "An Experimental Survey of the Mach Reflection of Shock Waves", Princeton Univ., Dept. Phys., Tech. Rep. II–10 (1951).

[69] G. Ben–Dor, "Relations Between First and Second Triple Point Trajectory Angles in Double Mach Reflection", AIAA J., v. 19, pp. 531–533 (1981).

[70] G. Ben–Dor, "Shock Wave Reflection Phenomena", ed. Springer (1995).

[71] M.J. Lighthill, "The Diffraction of Blast I", Proc. Roy. Soc. A. v. 198, pp 454–470 (1948).

[72] P. Colella, L.F. Henderson, "The Von Neumann Paradox for the Diffraction of Weak Shock Waves", J. Fluid Mech. v. 213, pp. 71–94 (1990).

[73] H. Li, G. Ben–Dor, "Reconsideration of Pseudo–Steady Shock Wave Reflections and the Transition Criteria Between Them", Shock Waves, v. 5, pp. 59–73 (1995).

[74] H.G. Hornung, H. Oertel, R.J. Sandeman, "Transition to Mach Reflexion of Shock Waves in Steady and Pseudosteady Flow with and Without Relaxation", J. Fluid Mech., v. 90, pp. 541–560 (1979).

[75] L. F. Henderson, A. Lozzi, "Experiments on Transition of Mach Reflection", J. Fluid Mech., v. 68, pp. 139–155 (1975).

[76] J. von Neumann, "Collected Works", v.6, pp. 238-299 (1963).

[77] J.M. Dewey, G.D. Lock, "An Experimental Investigation of the Sonic Criterion for Transition From Regular to Mach Relection of Weak Shock Waves", Expts. in Fluids, v. 7, pp. 282-292 (1989).

[78] S. Itoh, N. Okazaki, M. Itaya, "On the Transition Betwen Regular and Mach Reflection in Truly Non-Stationary Flows", J. Fluid Mech., v. 108, pp.383-400 (1981).

[79] K. Takayama, M. Sasaki, "Effects of Radius of Curvature and Initial Angle of the Shock Transition Over Concave and Convex Walls", Rep. Inst. High Speed Mech., v. 46, pp. 1-30 (1983).

[80] G. Ben-dor, K. Takayama, "Analytical Prediction of the Transition From Mach to Regular Reflection Over Cylindrical Concave Wedges", J. Fluid Mech., v. 158, pp.365-380 (1985).

[81] G. Ben-Dor, K. Takayama, "Application of Steady Shock Polars to Unsteady Shock Wave Reflections", AIAA J., v. 24, pp. 682-684 (1986).

[82] C. K. Law, I. I. Glass, "Diffraction of Strong Shock Waves by a Sharp Compressive Corner", CASI Trans., v. 4, pp. 2-12 (1971).

[83] W.H. Heilig, "Diffraction of a Shock Wave by a Cylinder", The Phys. of Fluids Suppl. I, v. 12, pp. 154-157 (1969).

[84] B. Schmidt, "Structure of Incipient Triple Point at the Transition From Regular Reflection to Mach Reflection", in "Rarefied Gas Dynamics: Theoretical and Computational Techniques", Progress in Astronautics and Aeronautics, v. 118, pp. 597-607 (1989).

[85] H. Kleine, E. Timofeev, A. Hakkaki-Fard, B. Skews, "The Influence of Reynolds Number on the Triple Point Trajectories at Shock Reflection Off Cylindrical Surfaces", J. Fluid Mech., v. 740, pp. 47-60 (2014).

[86] G. Ben-Dor, K. Takayama, "The Dynamics of the Transition From Mach to Regular Reflection Over Concave Cylinders", Israel J. Tech, v. 23, pp. 71-74, (1986-7).

[87] A. M. Tesdall, R. Sanders, B. Keyfitz, "Self-Similar Solutions for the Triple Point Paradox in Gasdynamics", J. Appl. Math., v. 68 (5), pp. 1360-1377 (2008).

[88] D. W. Schwendeman, G. B. Whitham, "On Converging Shock Waves", Proc. Roy. Soc. A. v. 413, pp 297-311 (1987).

[89] D.W. Schwendeman, "On Converging Shock Waves of Spherical and Polyhedral Form", J. Fluid Mech., v. 454, pp. 365-386 (2002).

[90] N. Apazidis, M.B. Lesser, "On Generation and Convergence of Polygonal-Shaped Shock Waves", J. Fluid Mech., v. 309 (1996).

[91] V. Eliasson, M. Kjellander, N. Apazidis, "Regular Versus Mach Reflection for Converging Polygonal Shocks", Shock Waves v. 17, pp. 43-50 (2007).

[92] V. Eliasson, N. Apazidis, N. Tillmark, "Focusing of Strong Shocks in an Annular Shock Tube", Shock Waves (2006).

[93] V. Eliasson, "On Focusing of Shock Waves", Ph.D. dissertation, Department of Mechanics, KTH, Sweden (2007).

[94] V. Eliasson, W.D. Henshaw, D. Appelö, "On Cylindrically Converging Shock Waves Shaped by Obstacles", Physica D, v. 237, pp. 2203-2209 (2008).

[95] W.D. Henshaw, N.F. Smyth, D.W. Schwendeman, "Numerical Shock Propagation Using Geometrical Shock Dynamics", J. Fluid Mech., v. 171, pp. 519-545 (1986).

[96] T.V. Bazhenova, L.G. Gvozdeva, M.A.Nettleton, "Unsteady Interactions of Shock Waves", Prog. Aerosp. Sci., v. 21, pp. 249-331 (1984).

[97] M. Kjellander, N. Tillmark, N. Apazidis, "Thermal Radiation From a Converging Shock Implosion", Phys. of Fluids v. 22 (2010).

[98] H. Schlichting, "Boundary-Layer Theory", McGraw-Hill series in mechanical engineering (1979).

[99] F. Vignati, A. Guardone, "Multi-Domain Simulations of Shock Wave Interaction with Aerodynamic Obstacles in Cylindrical Implosions", accepted by J. Comp. and Appl. Math. (2013).

[100] H. B. Callen, "Thermodynamics and an Introduction to Thermostatistics", ed. John Wiley and sons, New York, (1985).

[101] M. Kjellander, N. Tillmark, N. Apazidis, "Shock Dynamics of Strong Imploding Cylindrical and Spherical Shock Waves with Real Gas Effects", Phys. of Fluids v. 22 (2010).

[102] E.A. Mishkin, Y. Fujimoto, "Analysis of a Cylindrical Imploding Shock Wave", J. Fluid Mech., v. 89-I, pp. 61-78 (1978).

[103] T. de Neef, C. Hechtman, "Numerical Study of the Flow Due to a Cylindrical Implosion", Computers and Fluids, v. 6, pp. 185-202 (1978).

[104] R.J. Le Veque, "Numerical Methods for Conservation Laws", ed. Birkhauser Verlag (1992).

[105] A. Guardone, D. De Santis, G. Geraci, M. Pasta, "On the Relation Between Finite Element and Finite Volume Schemes for Compressible Flows with Cylindrical and Spherical Symmetry", J. Comp. Phys. v. 230 (3), pp. 680-694 (2011).

[106] D. Isola, A. Guardone, G. Quaranta, "Arbitrary Lagrangian Eulerian Formulation for Two-Dimensional Flows Using Dynamic Meshes with Edge-Swapping", J. Comp. Phys. v. 230, pp. 7706-7722 (2011).

[107] FlowMesh Solver Website, www.aero.polimi.it/flowmesh.

[108] C.C. Wu, P.H. Roberts, "Structure and Stability of a Spherical Shock Wave in a Van Der Waals Gas", Q. J. Mech. Appl. Meth., v. 49-IV, pp. 501-543 (1996).

[109] M.M. Kamel, A.F. Ghoniem, M.I. Rashei, A.K.O.K. Oppenheim, "Blast Waves in Real Gases", Acta Astronautica, v. 4, pp. 439–458 (1977).

[110] H. Steiner, W. Gretler, "The Propagation of Spherical and Cylindrical Shock Waves in Real Gases", Phys. of Fluids, v. 6 (1994)

[111] R.K. Anand, "Shock Dynamics of Strong Imploding Cylindrical and Spherical Shock Waves with Non–Ideal Gas Effects", Wave Motion (2013).

[112] F. Higashino, N. Oshima, "Real Gas Effects on Converging Shock Waves", Astron. Acta, v. 15, pp. 523–529 (1970).

[113] M. Kjellander, N. Tillmark, N. Apazidis, "Experimental Determination of Self–Similarity Constant for Converging Cylindrical Shocks", Phys. of Fluids, v. 23 (2011).

[114] M. Yousaf, "Imploding Spherical and Cylindrical Shocks", Phys. of Fluids, v. 29, pp. 680–684 (1986).

[115] L. Galgani, A. Scotti, "On Subadditivity and Convexity Properties of Thermodynamic Functions", Pure App. Chem., v. 22, pp. 229–235, (1970).

[116] G. Emanuel, "Advanced Classical Thermodynamics", AIAA Education Series, AIAA, New York (1987).

[117] J.D. van der Waals, "Over De Continuiteit Van Der Gas– En Vloeistoftoestand", Ph.D. dissertation, Leiden, Netherlands (1873).

[118] National Institute of Standards and Technology, NIST Chemistry WebBook, www.nist.gov.

[119] R.J. Le Veque, "Nonlinear Conservation Laws and Finite Volume Methods for Astrophysical Fluid Flow", in Nonlinear Conservation Laws and Finite Volume Methods for Astrophysical Fluid Flow, ed. Springer–Verlag (1998).

[120] D. De Santis, G. Geraci, A. Guardone, "Equivalence Conditions Between Linear Lagrangian Finite Element and Node–Centred Finite Volume Schemes for Conservation Laws in Cylindrical Coordinates", Int. J. Num. Meth. in Fluids, v. 74, pp. 514–542 (2014).

[121] P. Woodward and P. Colella, "The Numerical Simulation of Two-Dimensional Fluid Flow with Strong Shocks", J. Comput. Phys., v. 54, pp. 114-173 (1984).

[122] C.B. Laney, "Computational Gasdynamics", Cambridge University Press (1998).

[123] S. Rebay, "Efficient Unstructured Mesh Generation by Means of Delaunay Triangulation and Bowyer-Watson Algorithm", J. Comput. Phys., v 106, pp. 125-138 (1993).

[124] P.L. George, H. Borouchaki, "Delaunay Triangulation and Meshing: Application to Finite Elements", ed Butterworth-Heinemann, (1998).

[125] J. O'Rourke, "Computational Geometry in C", Cambridge University Press (1998).

[126] R. Löhner, "Robust, Vectorized Search Algorithms for Interpolation on Unstructured Grids", J. Comp. Phys., v. 118, pp. 380-387 (1995).

[127] C. Ericson, "Real-Time Collision Detection", Elsevier (2005).

[128] E.W. Skews, J.T. Ashworth, "The Physical Nature of Weak Shock Wave Reflection", J. Fluid Mech., v. 542, pp. 105-114 (2005).

[129] K.G. Guderley, "The Theory of Transonic Flow", ed. Pergamon, New York, pp. 147-149 (1962).

[130] E. Vasil'ev, "Four-Wave Scheme of Weak Mach Shock Wave Interaction Under the Von Neumann Paradox Conditions", Fluid Dyn., v. 34, p. 421 (1999).

[131] T.C.J. Hu, I.I. Glass, "Blast Wave Trajectories From Height of Burst", AIAA J., v. 24, pp. 607-610 (1986).

[132] F. Marconi, "Shock Reflection Transition in Three-Dimensional Steady Flow About Interfering Bodies", AIAA J., v. 21 (1983).

[133] L.F. Henderson, P.M. Gray, "Experiments on the Diffraction of Strong Blast Waves", Proc. Roy. Soc. Lond. A, v. 377, pp. 363-378 (1981).

[134] H. Reichenbach, "Roughness and Heated Layer Effects on Shock Wave Propagation and Reflection — Experimental Results", Ernst Mach Inst., rep. E24-85, Freiburg (1985).

[135] D.C. Montgomery, G.C. Runger, "Applied Statistics and Probability for Engineers", John Wiley & Sons, 5th ed. (2010).

[136] J. Dowse, B. Skews, "Area Change Effects on Shock Wave Propagation", Shock Waves, v. 24, pp. 365-373 (2014).

[137] R.M. May, "Biological populations with nonoverlapping generations: stable points, stable cycles, and chaos", Science, v. 186, pp. 645-651 (1974).

[138] P.A. Thompson, "Compressible Fluid Dynamics", McGraw-Hill Inc., US, (1972).

[139] L. Quartapelle, L. Castelletti, A. Guardone, G. Quaranta, "Solution of the Riemann Problem of Classical Gadynamics", J. Comp. Phys. (2003).

[140] G. Ben-Dor, O. Igra, T. Elperin, "Handbook of Shock Waves", Academic Press Inc., New York, chap. 6: P. Roe, "Numerical Methods" (2000).